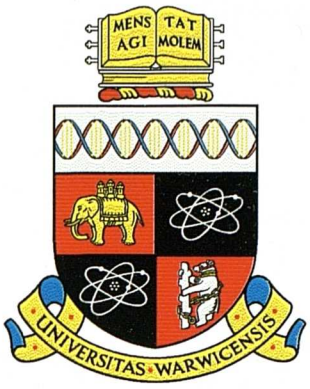

DESIGN OF CHEMORESISTIVE SILICON SENSORS FOR APPLICATION IN GAS MONITORING

by

Andrew Charles Pike

Department of Engineering

University of Warwick

A thesis submitted to the University of Warwick

for the degree of Doctor of Philosophy

June 1996

Contents

Summary

The growing concerns over our exposure to hazardous substances have been addressed by stringent legislation to ensure air quality. A wide variety of applications have therefore arisen which require the reliable detection of hazardous gases. Hence, the motivation behind the research presented in this thesis was the aim of developing a portable gas monitor to detect nitrogen dioxide, carbon monoxide and volatile organic compounds (e.g. benzene, toluene). The need to improve gas sensor technology for suitability to this demanding application has been identified. Thus, the objectives were to develop a number of ultra-low power devices consisting of an array of chemoresistive gas sensors for incorporation into an intelligent sensor system. The operation of these sensors relies on the measurement of a change in resistance of a gas-sensitive material when exposed to specific gases.

Silicon technology has been employed in order to obtain reproducible, miniaturised sensors with a low unit cost. Furthermore, chemoresistors employing metal oxide semiconductor (MOS), metal-substituted phthalocyanine (XPc) and conducting polymer (CP) materials have been used because of their sensitivity to the gases of interest.

Common problems associated with these materials are poor specificity to a target gas and poor stability. However, the approach to minimising these problems was to design arrays of cross-sensitive chemoresistors for use in a microprocessor-based intelligent sensor system. The microprocessor applies a pattern recognition algorithm to the sensor outputs to extract the required information. This thesis describes the design, fabrication and characterisation of these sensor arrays.

MOS and XPc materials have shown an optimum performance at elevated temperatures. Micromachining techniques have therefore been employed to integrate resistance heaters in a micro-hotplate structure, which can allow temperatures of 600°C to be attained in ~15 ms with a typical power consumption of ~150 mW/sensor. A pulsed mode of operation should provide average power consumptions of less than 1 mW. A low power consumption is critical for a portable battery-powered instrument. The design, modelling and characterisation of the micro-hotplate structures have also been described.

The design and development of a novel automated gas sensor test system was also fundamental to this research, in order to accurately characterise sensor responses and to validate theoretical models.

The research objectives have been fulfilled in that a number of sensor array devices have been produced, which are suitable for a portable intelligent instrument. The different designs and materials are compatible for integration into a hybrid sensor. The advancements achieved in sensor technology provide a foundation for future research into the production of a portable intelligent sensor system.

Acknowledgements

I would like to thank my academic supervisor, Dr Julian Gardner, for giving me the opportunity of studying in this field and for his guidance and tuition during my PhD. I would like to acknowledge the Health and Safety Executive (HSE) for their funding of my CASE Award. Similar gratitude is given to the Engineering and Physical Science Research Council (EPSRC) for a maintenance award.

The practical stages of my studies employed the facilities and expertise of the certain institutions. I am therefore very thankful to all the associated staff, and in particular:

Sensor Research Laboratory, Warwick University; Frank Courtney (Technician) for his practical assistance.

Institute of Microtechnology, University of Neuchâtel, Switzerland; N.F. de Rooij (Director), M. Koudelka-Hep, and P.A. Clerc who coordinated the silicon wafer processing.

Institute of Physical and Theoretical Chemistry, University of Tübingen, Germany; W. Göpel (Director), A. Hierlemann, and M. Schwiezer-Berberich for the deposition of thin and thick films of SnO_2.

Institute of Physics and Technology of Materials, Bucharest, Romania; N. Bârsan for deposition of thick SnO_2 films.

Department of Chemistry, University of Southampton, UK; P.N. Bartlett (Director), and J. Elliott for conducting polymer deposition.

HSE, Sheffield, UK; S.C. Thorpe (CASE award supervisor) for XPc deposition.

Rutherford Appleton Laboratories, Didcot, UK; J. Bryant for photolithographic mask production, and J. Watson for FIBM processing.

Finally, but most importantly, I would like to thank my family and friends for their continual support. In particular, my parents for their encouragement and support throughout my education.

Declaration

The work described in this thesis is entirely original and my own, except where otherwise indicated.

Parts of this work has been presented at international conferences:

1. *Sensors and their Applications VII, 10-13 September 1995, Dublin,* Nanoengineered Dual Sensor Device for Intelligent Monitoring of Gases, A.C. Pike and J.W. Gardner.

2. *Eurosensors VIII, 25-28 September 1994, Toulouse, France*, Integrated Array Sensor for Detecting Organic Solvents, J.W. Gardner and A.C. Pike *et al.*

Parts of the work contained in this thesis have also been published in the scientific literature:

3. J.W. Gardner, A.C. Pike, N.F. de Rooij, M. Koudelka-Hep, P.A. Clerc, A. Hierlemann and W. Göpel, Integrated Array Sensor for Detecting Organic Solvents, *Sensors and Actuators B,* **26-27** (1995) 135-139.

4. A.C. Pike and J.W. Gardner, Thermal Characterisation of Micropower Hybrid Sensor Array for Multicomponent Gas Analysis, *Under Preparation.*

List of Symbols

Symbol	Description	Units
	Roman letters:	
a	Distance across the active area	m
A	Area	m^2
A	Adsorption gas species	-
A	Constant of proportionality	-
c_p	Specific heat capacity at constant pressure	$J\ K^{-1}\ kg^{-1}$
C	Electrical capacitance	F
C	Thermal capacitance	$J\ K^{-1}$
C	Gas concentration	m^{-3}
C_{ext}	External gas concentration	m^{-3}
C_x	Local gas concentration at x	m^{-2}
D_A	Diffusion coefficient of gas species A	$m^2\ s^{-1}$
e	Electron charge	C
E	Electric field	$V\ m^{-1}$
F	Volumetric flow-rate	$m^3\ s^{-1}$
F_m	Measured volumetric flow-rate	$m^3\ s^{-1}$
F_{set}	Demanded volumetric flow-rate	$m^3\ s^{-1}$
G	Electrical conductance	S
G_c	Thermal conductance (convection)	$W\ K^{-1}$
G_r	Thermal conductance (radiation)	$W\ K^{-1}$
G_{cr}	Thermal conductance associated with convection and radiation	$W\ K^{-1}$
G_0	Base-line conductance	S
h	Heat transfer coefficient	$W\ K^{-1}\ m^{-2}$
H	Absolute humidity	mol
$H(s)$	Laplace transfer function	-
i	Current	A
I	Current	A
J	Current density	$A\ m^{-2}$
k	Boltzmann's constant	$J\ K^{-1}$

Symbol	Description	Units
k_b	Backward reaction rate	-
k_f	Forward reaction rate	-
k_r	Reaction rate of removal	-
K	Sensitivity coefficient	-
K	Arbitrary constant	-
l	Electrode length	m
L	Length of microheater	m
L_D	Debyé length	m
m	Membrane thickness	m
$M(\omega)$	Magnitude of frequency response	-
n	Electron concentration	m^{-3}
n_b	Bulk concentration of electrons	m^{-3}
N	Number of active sites	-
N_S	Electronic surface charge	$C\ m^{-2}$
N_x	Local number of active sites	-
p	Hole concentration	m^{-3}
p_o	Base-line number of electronic holes	-
P_a	Thermal convective power loss	W
P_E	Electrical power	W
P_H	Electrical microheater power	W
P_m	Thermal conductive power loss	W
P_r	Thermal radiation power loss	W
P_T	Total micro-hotplate thermal power loss	W
q	Heat flow	$W\ m^{-2}$
q^*	Heat generated per unit volume	$W\ m^{-3}$
r	Radius	m
R	Resistance	Ω
$R_{1\text{-}4}$	Thermal resistance associated with thermal conduction through the membrane	$K\ W^{-1}$
R_B	Baseline resistance	Ω
R_{cond}	Thermal resistance associated with conduction	$K\ W^{-1}$

Symbol	Description	Units
R_H	Microheater resistance	Ω
R_S	Sheet resistance	Ω/sq.
ΔR_S	Microheater resistance shift	Ω
R_T	Resistance at a specific temperature	Ω
R_{th}	Thermal resistance	K W^{-1}
R_0	Base-line resistance	Ω
$\Re$	Fractional change in resistance response	-
S	Gas-sensitivity coefficient	-
t	Time	s
t	Metallisation thickness	m
T	Temperature	K
T_1	Temperature at point '1'	K
T_2	Temperature at point '2'	K
T_a	Ambient temperature	K
T_H	Heater temperature	K
ΔT	Change in temperature	K
u	Distance across membrane	m
U	Flow rate	m s^{-1}
v_a	Voltage at node a	V
v_i	Input voltage	V
v_o	Output voltage	V
v_{SS}	Steady-state voltage	V
V	Voltage	V
V	Volume	m^3
$V_{pk\text{-}pk}$	Peak to peak voltage	V
V_S	Electronic potential barrier	eV
w	Inter-electrode gap	m
W	Width of microheater	m
x	Distance through gas-sensitive film	m
x_b	Position of moving-boundary	m
x_d	Gas-sensitive material thickness	m

Symbol	Description	Units
x'	x/x_d	-
	Greek letters:	
α	Temperature coefficient of resistivity	K^{-1}
α_P	Thermal power loss coefficient	$W K^{-1}$
β	Coefficient relating to a power law	-
β_P	Thermal power loss coefficient	$W K^{-2}$
δn	Change in number of immobilised electrons	-
δp	Change in number of holes	-
ε	Effective emissivity	$F m^{-1}$
ε_o	Vacuum permittivity	$F m^{-1}$
ε_r	Relative dielectric permittivity	-
κ	Thermal conductivity	$W m^{-1} K^{-1}$
λ_∞	Bulk mean free path	m
μ_e	Electron mobility	$m^2 V^{-1} s^{-1}$
μ_h	Hole mobility	$m^2 V^{-1} s^{-1}$
θ	Site occupancy	-
ρ	Electrical resistivity	Ω m
ρ	Density (mass)	$kg m^{-3}$
ρ_∞	Bulk electrical resistivity	Ω m
σ	Stefan-Boltzmann constant	$W m^{-2}K^{-4}$
σ	Electrical conductivity	$S m^{-1}$
σ_o	Bulk electrical conductivity	$S m^{-1}$
σ_x	Local electrical conductivity	$S m^{-1}$
τ	Time constant	s
τ_{90}	Response time of signal to reach 90 % of the final steady-state signal	s
ω	Angular velocity	$rad s^{-1}$

List of Abbreviations and Acronyms

Term	Definition
a.c.	Alternating Current
ADC	Analogue to Digital Converter
ANN	Artificial Neural Network
ASIC	Application Specific Integrated Circuit
BAW	Bulk Acoustic Wave
COSHH	Control Of Substances Hazardous to Health
CP	Conducting Polymer
CuPc	Copper Phthalocyanine
CVD	Chemical Vapour Deposition
DAC	Digital to Analogue Converter
DAQ	Data Acquisition
d.c.	Direct Current
d.i.l.	dual-in-line
DIO	Digital Input/Output
DMM	Digital Multi-Meter
FEM	Finite Element Method
FIBM	Focused Ion Beam Milling
HSE	Health and Safety Executive
IC	Integrated Circuit
I/V	Current/Voltage
LED	Light Emitting Diode
LPCVD	Low Pressure Chemical Vapour Deposition
LUT	Look-Up Table
MEL	Maximum Exposure Limit
MFC	Mass Flow Controller
MgPc	Magnesium Phthalocyanine
MHP	MicroHotplate
MOS	Metal Oxide Semiconductor
MSB	Most Significant Bit
MUX	Multiplexer

OES	Occupational Exposure Standard
PAn	Poly(Aniline)
PARC	Pattern Recognition
PbPc	Lead Phthalocyanine
PC	Personal Computer
PCB	Printed Circuit Board
Pk-Pk	Peak to Peak
PPy	Poly(Pyrrole)
PRT	Platinum Resistance Thermometer
PVD	Physical Vapour Deposition
RAM	Random Access Memory
RH	Relative Humidity
ROM	Read Only Memory
RT	Room Temperature
SAD	Sensor Array Device
SAW	Surface Acoustic Wave
SCE	Saturated Calomel Electrode
SCS	Single Crystal Silicon
TCR	Temperature Coefficient of Resistance
TEM	Transmission Electron Microscopy
TTL	Transistor-Transistor Logic
UV	Ultra-Violet
VI	Virtual Instrument
VOC	Volatile Organic Compound
XPc	Metal-Substituted Phthalocyanine

List of Chemical Symbols

Chemical Symbol	Chemical substance
Au	Gold
CH_4	Methane
Cl_2	Chlorine
CO_2	Carbon Dioxide
CO	Carbon Monoxide
F_2	Florine
Ga	Gallium
HCl	Hydrogen Chloride
H_2	Hydrogen
H_2S	Hydrogen Sulfide
KOH	Potassium Hydroxide
N_2	Nitrogen
N_2O	Nitrous Oxide
NO	Nitrogen Oxide
NO_2	Nitrogen Dioxide
NH_3	Ammonia
O_2	Oxygen
Pd	Palladium
Pt	Platinum
Si	Silicon
SiN_x	Silicon Nitride of unspecified stoichiometry
Si_3N_4	Silicon Nitride
SiO_2	Silicon Dioxide
SnO_2	Tin Dioxide
$Si_xO_yN_z$	Silicon Oxynitride of unspecified stoichiometry
Ta	Tantalum
Ti	Titanium

Chapter 1

1. Introduction

The main aim of this Chapter is to outline the desired specification of an instrument for gas sensing. One instrument of particular interest is a portable hazardous gas monitor. The sensor technologies most suited for portable instrumentation and the enabling technologies are considered and hence, the case made for investigating silicon micromachined chemoresistive gas sensors.

The research objectives and an outline of this thesis are given at the end of this Chapter.

1.1 Gas Monitoring Applications

One of the first applications identified as requiring gas monitoring was the safety-critical area of underground mines. Although there are few gases naturally present in a mine, they unfortunately tend to be hazardous and undetected by the human senses (e.g. olfaction). The hazardous gases most commonly monitored are methane (CH_4) which is explosive, carbon monoxide (CO), hydrogen sulfide (H_2S) and nitrous oxide (N_2O); the latter three are toxic. Early methods employed in dealing with an occurrence of CH_4, involved the mitigation of a spontaneous explosion in known gassy mines by igniting the build-up before it reached the critical concentration of 5 % CH_4. This technique required a miner covered in wet blankets to go around the workings at the beginning of every shift physically lighting known areas susceptible to CH_4 with a candle on a stick. Contemporary reports suggested that this was not the most popular job in the mine. The emergence of the Safety Lamp (*circa* 1800) represented a significant development in the miner's ability to monitor CH_4 in the working environment (this technique relied on an oil burning lamp in which the flame changed colour in the presence of CH_4. The flame was surrounded by a metal gauze to prevent ignition of the CH_4 build-up). By employing a canary, it was also possible

to detect toxic CO levels. However, this often led to a false sense of security because the sensitivity of the canary to CO was notoriously unreliable (ranging from 1,200 to 1,800 ppm). The strenuous work frequently carried out by the miner increased the rate of the poisoning by CO above that of the bird's (e.g. *via* increased respiration), hence the miner occasionally reached their critical level first [1.1].

The unreliability of the early techniques clearly demonstrated the need for a reliable and accurate gas monitor. Improvements made in gas-monitoring instrumentation are now capable of detecting the main hazardous gases at fixed monitoring stations, or the detection of one hazardous gas with a portable instrument. However, the occasional accident still questions the adequacy of a miner's personal protection to all hazardous gases [1.2]. Apart from the naturally occurring gases, additional hazardous gases (e.g. CO, CO_2, NO and NO_2 and sulfur compounds) are emitted from the engine exhausts of mining equipment. Furthermore, non-toxic gases like CO_2, N_2 and H_2 act as simple asphyxiants when present at high enough concentrations as to reduce the oxygen content in air by dilution. Finally, H_2 and volatile organic compounds (VOCs) e.g. benzene and toluene, have been identified as products from a mine fire. Ideally, each miner should carry a portable gas monitor which could identify and warn against all of these hazards. Unfortunately, current sensor technology is not capable of meeting this demanding specification.

Over the last 50 years there has been an increased awareness in pollution [1.3] and in particular to those substances hazardous to health. Currently, atmospheric air pollution is of concern, because it is known that many inhaled substances can have a detrimental effect on our long-term health (over several years). The known effects of air pollution has further highlighted hazards in industrial environments (e.g. mining, chemical and manufacturing industries) and in urban (domestic) environments [1.4], which has led to extensive research to determine the acceptable safe levels of known airborne hazardous substances [1.5]. Legislation has been implemented requiring that industrial activities and products cannot result in an unprotected person being exposed to harmful gas levels. Hence, there has been a sudden growth in the number of applications requiring accurate detection of a wide variety of gases and vapours. In many cases suitable methods to control or monitor these atmospheres are still limited by sensor technology. For example, the threat of CO poisoning caused by defective domestic gas appliances has been widely publicised. However, it is only in the last 5

years that a domestic CO alarm has become generally available, because of the difficulty in employing a sensor technology that fulfils the stringent requirements at a low unit cost [1.6].

The need for gas detection equipment has stimulated the development of chemical sensors that employ a wide variety of materials and technologies [1.7]. In some cases, the inadequacies of the sensor technology have been compensated for by the simultaneous development in processing power *via* microelectronics. For example, microprocessor-based instruments employing an array of non-specific sensors can apply pattern recognition (PARC) software or characteristic look-up tables (LUTs) to improve the performance of the sensor system. This approach has been commercially developed into a related instrument whose operation mimics that of the human olfaction system, it is thus referred to as an electronic nose [1.8]. These instruments allow a qualitative assessment of odours in the food, drink, medical and manufacturing industries.

The specification of a hazardous gas sensing instrument is dependent upon the safety standards relating to the gases for detection. Legislation of safety levels for occupational environments have been laid down in Control of Substances Hazardous to Health (COSHH) Regulations 1988 [1.5]. There are two types of occupational exposure limit defined in the COSHH Regulations; the maximum exposure limits (MELs) and the occupational exposure standards (OESs). The key difference between the two types of limit is that an OES is set at a level at which there is no indication of risk to health, while for a MEL there may be a residual risk. The level set for a MEL takes into account socio-economic factors. The pattern of effects on health due to exposure to hazardous gases depends on the nature of the substance and the exposure, e.g. some effects require prolonged or accumulated exposure. The OESs therefore specify a long-term (8-hour time weighted average) exposure limit which is intended to restrict the total intake by inhalation over a working shift. Other detrimental effects on health may be seen after brief exposures which have occurred once or repeatedly. Hence, short-term (10 minutes) exposure limits may be applied to such substances. Where long-term limits also apply, the short-term limit restricts the magnitude of excursions above the average concentration during longer exposures. More stringent regulations have been applied to the underground mines and domestic environments.

If a gas monitoring instrument is to be used in a potentially explosive atmosphere, then there is specific legislation that requires the instrument is intrinsically safe (British Standard BSEN 50020, BSEN 50014). The standards take into account the electronic, mechanical and operational safety considerations. The electronic standards ensure that no sparking is possible and that the maximum surface temperature exposed to the atmosphere is below that of the ignition temperature of the combustible gases.

The research reported in this thesis was supported by the Health and Safety Executive (HSE), Sheffield, who highlighted the application for a portable hazardous gas monitoring instrument to detect CO, NO_2 and VOC hazards. At this stage the VOCs of interest are limited to benzene and toluene. The exposure limits for these gases and vapours of interest are shown in Table 1.1 [1.5].

Table 1.1 Exposure limits of gases and vapours of interest. All values form the OES unless otherwise stated.

Gas/Vapour	Long-term exposure limit (ppm)	Short-term exposure limit (ppm)
NO_2	3	5
CO	50	300
Benzene	5 (MEL)	-
Toluene	50	150

Limiting the detection to a few gases of interest makes the objective of developing a suitable portable instrument a real possibility. Therefore, the next Section describes the general gas sensor characteristics that are essential for operation in a portable instrument, which provides the basis for assessment of a sensor's performance. In this way, the most suitable sensor technology for the application was selected, as described in Section 1.3.

1.2 Properties of a Gas Sensor

Figure 1.1 shows the basic functions of a gas monitoring system.

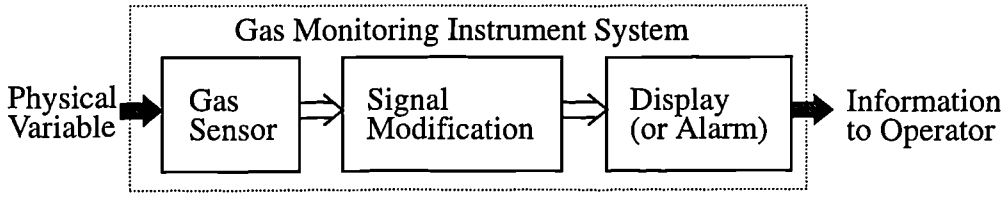

Figure 1.1 Block diagram of a gas monitoring instrument.

The sensor converts the physical gas concentration into an electrical signal. The electrical signal then has to be modified into a form which can be displayed to the operator, or in the case of hazardous gases, it may be used to give an early warning. The type of modifier depends on the sensor technology employed and the information required. During sensor testing, the function relating the electrical signal to a target gas concentration is termed the calibration function. This function should be of a form where it can be incorporated in the modifier block to determine accurately the target gas concentration. In general, a simple calibration function requires less signal processing, which has to be performed by the instrument. However, it has been found that many sensor calibration functions are far from ideal and require sophisticated mathematical processing.

The definitions of parameters describing sensor characteristics are now considered for the sensor system, as shown in Figure 1.2.

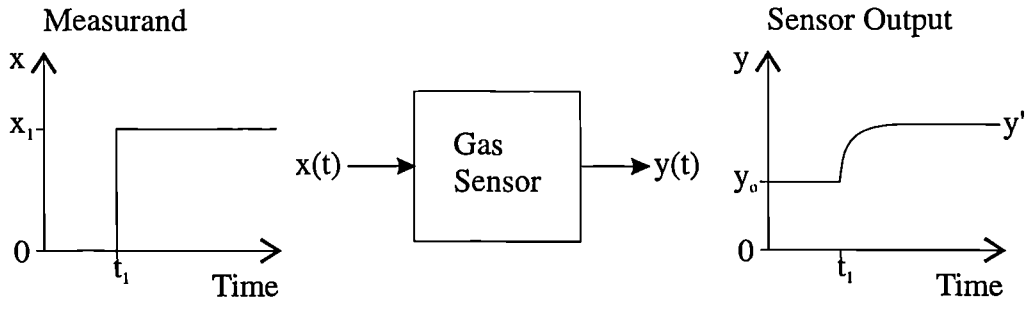

Figure 1.2 Gas sensor block diagram (centre), giving an example of a sensor output response (right) to a step change in a measurand (e.g. target gas concentration).

For an environment of clean air in the absence of the target gas (x) under constant conditions (e.g. constant pressure, humidity and temperature) the sensor output signal represents a reference or base-line value (y_o). When the sensor is exposed (at time t_1) to a target gas concentration (x_1), the change in sensor signal with respect to the base-

line is called the response (i.e. $\Delta y = y'-y_o$). The steady-state response is usually defined as a dimensionless parameter e.g. y'/y_o, or $\Delta y/y_o$. The absolute sensitivity of the sensor is the ratio of the change of the output signal to the change in the measurand (dy/dx). Alternatively, the relative sensor sensitivity is the absolute sensor sensitivity normalised by the base-line output signal (i.e. $dy/y_o.dx$). Response times are generally defined as the time to achieve a certain percentage of the final change in the sensor signal e.g. τ_{90} is defined as the time to reach 90 % of the final sensor signal. If the system is first order, a time constant defines the time taken to reach 63 % of the final sensor output. The sensor signal has to be fully reversible back to the base-line when re-exposed to clean air. Ideally the sensor should have a high sensitivity, to just the one physical variable of interest (i.e. be specific) with an instantaneous response time. Unfortunately, this is not the case for practical gas sensors. It is often found that the sensor is also sensitive to other physical variables (e.g. other gases, vapours and temperature), which causes a change in the calibration curve in the presence of these interfering components. To gauge the amount of cross-sensitivity the term specificity is used. This undesirable property is caused by the sensor's absolute sensitivities to the other physical variables. If the sensitivity is large to one measurand compared with the others, then the sensor may be regarded as specific. Selectivity is defined as the ability of a sensor to respond primarily to only one species in the presence of other species. A high selectivity means that the contribution from the gas of interest dominates and that the contribution from the interfering gases is minimal. The properties of a sensor may also be unstable and drift which are characterised by a change in output while the input conditions are kept constant. This can affect the base-line sensor output, sensitivity and repeatability and in turn can make calibration of the sensor problematic.

Ideally a portable hazardous gas monitor should be compact, lightweight, yet sufficiently sturdy to withstand use in a mining environment. If intended for operation in an explosive environment it must also be intrinsically safe (in accordance with BSEN 50020). Such an instrument would need to continuously display hazardous gas concentrations over a working shift and to sound an alarm if a potential hazard is detected. Ideally a number of specific sensors would be required, one for each of the physical variables of interest. Furthermore, the response time, τ, of the sensors should

be fast enough to allow detection well within the short-term exposure limit (e.g. $\tau <$ 60 s). The long-term exposure limit determines the sensitivity requirements for the sensor. The power requirements of such an instrument should also be very low because, for portability the instrument would need to be battery-powered.

A sensor technology does not exist that can provide all of the ideal characteristics described above, as will be outlined in the following Section. However, as is mentioned earlier the performance of many sensor systems can be improved by incorporating microelectronics with more processing power.

1.3 Identification of Suitable Sensor Technology

1.3.1 Silicon Technology

The production of gas sensors has in the past employed IC fabrication technologies with either thin film and/or thick film techniques. The difference between thin and thick films is not so much in the difference of the film thickness, but more in the difference of the deposition technique.

Thick film technology is based on screen printing techniques [1.9], usually printing on alumina substrates. The benefits with this technique are a reasonably compact sensor at a low cost. Unfortunately, the limitation on the achievable miniaturisation of the device feature size and the poor dimensional control, is due to the intrinsic resolution limitation of the screen printing technique (~ 20 μm). Reproducible film properties are also hard to control.

The advancements in microelectronics over the last 20 years have been due to the progress made in silicon technology and thin film processing techniques [1.10, 1.11]. Higher integration, faster devices and lower power have been realised by the miniaturisation of planar devices using silicon microtechnology. Extremely high device performance for a very low unit cost is now possible by the use of well defined batch-fabrication procedures. Moreover, the material properties, interfaces and surfaces can be well controlled. The potential benefits of silicon technology also satisfy the physical sensor requirements for a portable gas monitoring instrument, which are low power, miniaturisation, low weight and low unit fabrication costs [1.12]. The application of silicon technology also enables electronic circuits to be integrated onto the sensor chip, so allowing miniaturisation of the modifier, noise

reduction and on-chip compensation. Sensors with this type of integrated circuitry are referred to as intelligent sensors [1.13]. With the costs of microprocessor and Application Specific Integrated Circuit (ASIC) technology reducing each year, it is a real possibility to have a low-cost miniature hazardous gas monitor with an improved accuracy and reliability.

The suitability of silicon technology for the design of microsensors in portable instrument applications led to its selection as the enabling technology for my research.

1.3.2 Silicon Gas Sensor Technology

There are a wide variety of silicon gas sensors that are classified according to the physical parameter which is modulated by the interaction with the target gas. Using the convention employed by Göpel *et al.* [1.14] the classes of solid-state gas sensors are: electrochemical, electronic conductance and capacitance, field effect, calorimetric, mass-sensitive and optical. The initial criteria to choose a sensor technology for investigation was to ensure it could employ silicon technology and enable sensors which have a suitable performance for the detection of the gases of interest (e.g. CO, NO_2 and VOCs). Using these requirements, the class of gas sensors based on measuring electronic resistance (or conductance) were highlighted as the most suitable, as explained later in greater detail. However, the reasons for rejecting the other sensor technologies are summarised in Table 1.2, for further details on these sensors see [1.14] and the references cited therein.

The exposure of an electronic conductance sensor to a gas of interest causes a change in electrical resistance of a sensing element. Thus, they are commonly referred to as chemoresistors, which is the convention used throughout this thesis. Chemoresistors have employed a wide variety of materials which have showed sensitivity to an even wider range of gases and vapours including CO, NO_2, and VOCs. The survey by Göpel *et al.* [1.14] shows that metal-oxide semiconductors (MOS), in particular tin oxide (SnO_2) have the greatest sensitivity to CO, while the most NO_2-sensitive materials are metal-substituted phthalocyanines (XPc). More recently it has been reported by Miasik *et al.* [1.15] that conducting polymer (CP) materials are sensitive to a wide range of gases and vapours. Furthermore, Bartlett *et al.* [1.16] have demonstrated that CPs are sensitive to methanol and other organic vapours.

Table 1.2 Basis for judging sensor technologies unsuitable for the application specified in Section 1.1.

Gas Sensor Class	Unsuitable Features
Electrochemical	The number of gases showing sensitivity to this class of sensor is limited by the different types of solid electrolyte employed. Thin film processing techniques have made this technology suitable for portable instrument applications, albeit, limited to O_2 and H_2.
Field Effect	Apart from a slow response time and poor stability, the sensitivity has been limited to H_2, H_2S, NH_3, CO and larger hydrogen-containing molecules e.g. alcohols, acetylene and ethylene.
Electronic Capacitance	Sensors employing changes in the dielectric constant have only been commercially successful in determining the water partial pressure in air, i.e. humidity.
Calorimetric	This sensor type are in general limited to the detection of combustible gases e.g. H_2, CO and small hydrocarbon molecules. The most technologically mature type of calorimetric sensor is the 'Pellistor', which is prone to long-term drift effects caused by poisoning.
Mass-sensitive[†]	The operation of these devices employs a piezoelectric substrate e.g. quartz. Integration of SAW technology on silicon requires a more complex fabrication process.
Optical	The integration of optical technology with silicon technology is not appropriate for a portable instrument, because of complexity, size restraints and at present costs.

[†] This only considers surface acoustic wave (SAW) and bulk acoustic wave (BAW) type sensors.

Measuring changes in resistance has the advantage of requiring a more straightforward interface circuitry, which would be beneficial for producing a small, low-power portable instrument.

The gas-sensitive properties of MOS, XPc and CP materials coupled with their ability to be deposited in planar films makes them highly suited to silicon planar technology. Using thin film processing techniques allows a higher degree of control over the sensor structure and therefore increases reproducibility. The typical structure of a planar chemoresistor is shown Figure 1.3 that employs a constant voltage circuit.

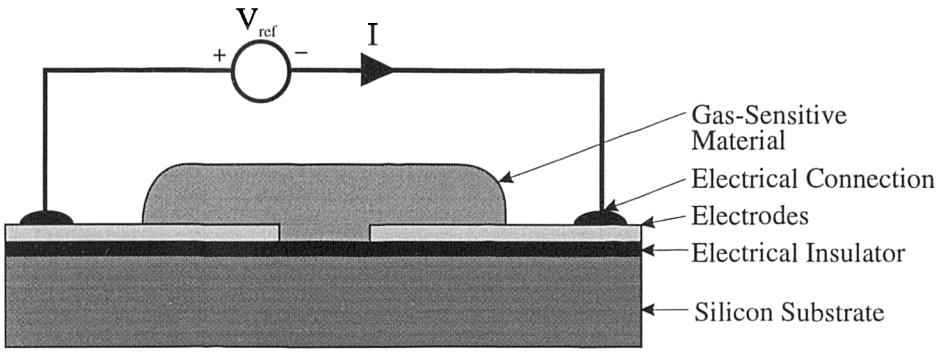

Figure 1.3 General structure of a chemoresistive gas sensor with a constant voltage supply (V_{ref}).

An electrical insulator, e.g. silicon dioxide (SiO_2) or silicon nitride (Si_3N_4) is deposited over the silicon substrate to form a suitable substrate onto which the gas-sensitive material is deposited. The resistance may be determined from the d.c. current/voltage (I/V) characteristics measured across the electrodes. Both MOS and XPc materials are known to have an optimal performance at a specific temperature. The optimum operating temperature for MOS film can range between approximately 200°C to 600°C, while XPc films operate between approximately 150°C to 200°C. Microheaters can be integrated into the sensor designs by using thin film processes and hence provide temperature control of the gas-sensitive material.

Poor specificity and long-term drift has, in the past, limited the application of these sensors. The problem of cross-sensitivity is an intrinsic property of the gas-sensitive materials, which are sensitive to groups of gases (e.g. oxidising, reducing, polar etc.) rather than one gas in particular. Drift could be caused by ageing of the sensor or desensitisation by a poisoning gas. An approach to overcoming these problems has been the continual development of new materials to give a better

performance [1.17]. However, material improvements have not totally alleviated the problems of poor specificity or long-term drift. In the mid 1980s Zaromb and Stetter [1.18] proposed a different approach to improve the selectivity of several sensor systems, which employed an array of cross-sensitive sensors in conjunction with a microprocessor. In which the microprocessor applies a pattern recognition (PARC) algorithm to the sensor outputs to extract the required information†. The sensors in the array should either be physically different or have different modes of operation to ensure that each sensor responds differently. The different outputs create a characteristic pattern or 'fingerprint' associated to different gases at specific concentrations. Assuming the sensors are highly stable, these fingerprints can be characterised and used in a PARC algorithm. A wide variety of different PARC algorithms (e.g. artificial neural networks (ANNs), principle component analysis and cluster methods [1.19]) and processing techniques have been developed to cater for this demanding application. The complexity of the PARC algorithm is proportional to the complexity of the application, which is in turn determined by the number of gases requiring detection, the characteristics of the individual sensors and the number of sensors.

Another aspect of a gas monitoring system which governs performance is the accuracy of the algorithm applied to the sensor output to extract the required information. The algorithm functions, which relate the sensor output to the physicochemical conditions, are derived from characterising the sensor outputs over controlled ranges of the measurands. The microsensor can be considered as a system, as shown in Figure 1.4.

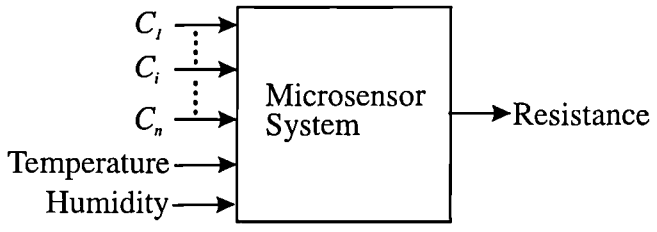

Figure 1.4 Block diagram of a microsensor system showing the input and output variables. Where C is the concentration of target gases and the subscript n refers to the number of target gases.

† This approach has been applied to the design of an electronic nose instrument as mentioned earlier.

Modelling has been used by researchers as an aid in understanding the mechanisms which produce both the desirable and undesirable sensor properties.

The approach I have taken in developing sensors for use in a portable hazardous gas monitor has been to integrate existing gas-sensitive materials into an array of sensors employing the technological benefits from silicon technology. In a potentially multicomponent gas environment, the problem exists of optimising the array of sensors and the different modes to achieve a detection, identification and quantification capability to CO, NO_2 and VOCs in the minimum time. Furthermore, a computer algorithm is needed that will permit rapid data interpretation and yet be simple enough to remain within the capabilities of a microprocessor suitable for a portable instrument. An existing PARC (i.e. back-propagation ANN) developed at Warwick University is intended to be applied.

Within this thesis is described several chemoresistor designs employing different materials and structures to establish the optimal sensor array composition with the best mode of operation. The different materials investigated were chosen on their suitable characteristics shown in the literature to the gases of interest, as is described in Chapter 2. SnO_2 was selected to detect primarily CO and NO_2, likewise XPc for NO_2 and CPs for VOCs. It is likely therefore that a multi-type (i.e. hybrid) sensor array of a particular combination of these materials could be tailored to give an optimal performance. The capability of operating each chemoresistor in the array at different temperatures also provides flexibility in the modes of operation. To simplify sensor characterisation the different gas-sensitive material technologies are investigated on separate sensor array devices (SADs). In doing this the fabrication techniques employed must enable the production of a hybrid SAD, to incorporate any of the chemoresistors investigated. The understanding of MOS and XPc material characteristics is at quite an advanced level, however this is not the case for CPs which have only emerged in the last few years as a gas-sensitive material. The variability in characteristics caused by varying the deposition conditions (as described in more detail in Chapter 4) required that a large number of discrete devices with a low fabrication cost were produced for characterisation purposes. The CP devices that are described in this thesis have been characterised as part of other research undertaken by the Universities of Warwick and Southampton. A Wheatstone sensor

bridge design is also described, to investigate minimising temperature sensitivity. The great attraction of the bridge topology is that it embodies the principle of structural compensation by simple design symmetry [1.13].

As mentioned previously, chemoresistors suffer from long-term drift. This causes inaccuracy of the sensor instrument when applying the characteristic functions at some time after the sensor characterisation occurred. This problem not only affects discrete sensor systems but also the accuracy of a PARC algorithm applied to a sensor array. This has limited the commercialisation of multicomponent gas monitors to more qualitative instruments, e.g. electronic nose instruments. However, McGeehin *et al.* [1.20] proposed a theory which has been developed further by Gardner [1.21] to describe a self-diagnostic gas sensor device, which can detect the effect of poisoning. To investigate this theory further I have incorporated the sensor design into a SAD. If the technology allows for the sensors lifetime to be calculated, it could truly be described as an intelligent sensor system.

1.3.3 Application of Silicon Micromachining

The integration of a heater into a gas sensor leads to a higher power consumption. For some commercially available gas sensors, a higher heater power consumption makes them ill-suited for use in a portable instrument (e.g. each Pellister gas sensors require 0.35 to 0.85 W to reach an operating temperature of 500°C [1.22], and Taguchi Gas Sensors, when operating at 350°C have a typical power consumption of 0.23 to 0.76 W [1.23]). Several low-power gas sensors have been researched which use micromachining techniques to fabricate free-standing [1.24] or membrane [1.25, 1.26] structures, which improve thermal insulation. The performance of a wide variety of other types microsensors have benefited from the application of micromachining [1.27]. Micromachining describes the processing techniques that together can accurately define three-dimensional structures. Micromachining fabrication techniques originate from microelectronic planar processing techniques, and so provide the same benefits of accuracy and batch processing. Generally, micromachining technology can be classified as either bulk or surface micromachining. Bulk micromachining technology is based on the anisotropic etching of the single crystal silicon (SCS) substrate used for the sensors. The well defined etch rates of different SCS planes [1.28] allow for a high degree of control

over three-dimensional structures etched in the bulk. Surface micromachining employs deposition and selective etching of sacrificial layers and thin films to produce free-standing surface microstructures. Bulk micromachining techniques was employed here to produce thermally insulated ultra-thin membrane structures. This micromachined structure is referred to as a micro-hotplate (MHP). The heater can be placed either in plane with the chemoresistor or embedded within the membrane, so allowing the chemoresistor to be superimposed above the microheater, as shown in Figure 1.5.

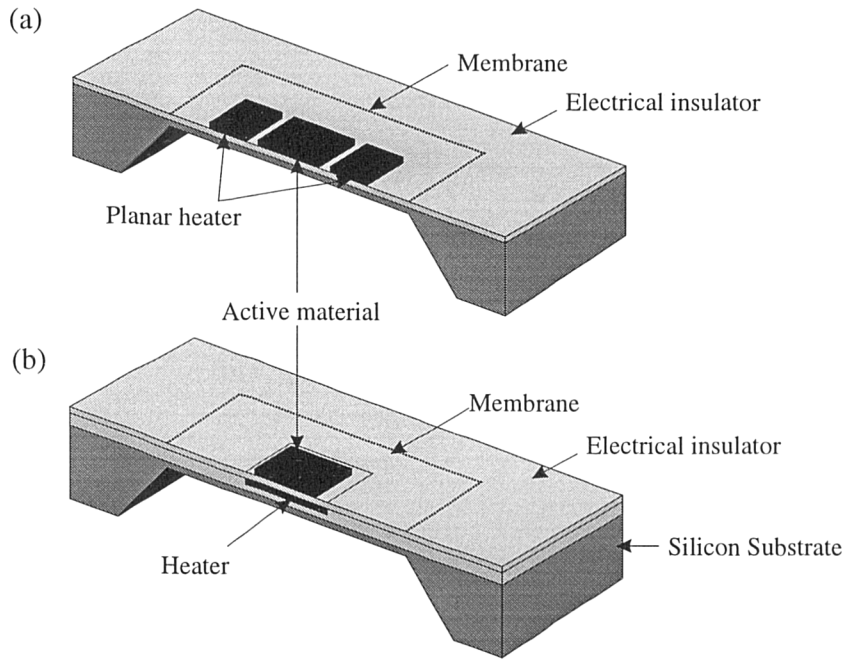

Figure 1.5 Schematic of the different MHP arrangements, (a) MHP with the heater in plane with microsensor, (b) MHP with embedded heater.

1.4 Research Objectives

The main objectives of this research are:

- To design and fabricate a number of silicon SADs for low power instruments.
- To characterise various gas-sensitive materials (e.g. MOS, XPc and CP) on these silicon sensors to the gases of interest.
- To incorporate the developed SAD technology into an intelligent portable instrument.

1.5 Outline of Thesis

My thesis describes the design, fabrication, analysis and testing of novel chemoresistor designs for low-power instruments.

In Chapter 2 I introduce the typical characteristics of the gas-sensitive materials e.g. MOS, XPc and CP. The mechanisms that lead to the gas sensitivity of the different gas-sensitive materials investigated are outlined.

In Chapter 3 I describe the design of the different chemoresistive devices and the integrated MHPs. The sensor designs and choice of materials depend greatly on the fabrication procedures to be used. These fabrication techniques are therefore outlined in Chapter 4, which introduces the conventional planar and bulk micromachining techniques used to produce the inactive[†] device structure. This Chapter also describes the techniques used to deposit the gas-sensitive materials.

In Chapter 5 I discuss the modelling of chemoresistive gas sensors. The models presented are based on previous research. A model developed by Gardner [1.21] is outlined, which describes the theoretical response from a pair of chemoresistors adapted to give a self-diagnostic for long-term drift caused by poisoning. This novel feature has been implemented in one of the SADs described in Chapter 3.

The performance of the MHP structures is described in Chapter 6. Special design considerations are taken to minimise thermal power losses. Apart from describing the mechanisms of power consumption, a novel measurement technique is employed to measure the ultra-low thermal time constants. Modelling techniques are also applied (e.g. finite element methods and lumped-element methods) in order to describe both steady-state and transient thermal properties of MHP structures.

To characterise the gas sensors I have designed and developed an automated computer-controlled test system, which is described in Chapter 7. The system controls the concentration of CO, NO_2, humidity and the operating temperature of each MHP. During the control of these variables it can measure the outputs from 12 gas sensors, the gas temperature, humidity and flow-rate. This test system is used to investigate the characteristics of chemoresistors coated with either SnO_2 or XPc. A similar rig has been constructed elsewhere to test the CP devices.

[†] Where inactive refers to the fact that the device has not been coated with the gas-sensitive material.

In Chapter 8 I discuss the results obtained for the XPc and SnO_2 chemoresistors, and the dual sensor device. In Chapter 9, I draw conclusions from the characteristics obtained for the SADs, allowing an intelligent sensor system employing a hybrid sensor to be broadly outlined. The research presented in this thesis has been the foundation for future work which is also discussed in Chapter 9.

1.6 References

1.1 Anon., Monitoring the Atmosphere in Underground Mines, *Mining Magazine*, December, 1988, 483-487.

1.2 E.R. Steyn, The Early Detection of Inflammable Gas at the Working Face, *Journal of the Mine Ventilation Society of South Africa*, July, 1985, 81-82.

1.3 N. de Nevers, *Air Pollution Control Engineering*, McGraw-Hill, New York, 1995.

1.4 R.M. Harrison, A Fresh Look at Air, *Chemistry in Britain*, December 1994, 987-1000.

1.5 Health and Safety Executive, *EH40/96 Occupational Exposure Limits 1996*, HMSO, London, 1996.

1.6 *Air Quality Guidelines for Europe*, WHO Regional Publications, European Series No. 23 (1987) 210 (WHO, Copenhagen).

1.7 R.W. Bogue, Environmental Sensors: Present Practices and Future Prospects, *Proceedings of the VII Conf. on Sensors and their Applications*, 1995, 3-11.

1.8 J.W. Gardner and P.N. Bartlett (eds.), *Sensors and Sensory Systems for an Electronic Nose*, Kluwer Academic Publishers, Dordrecht, Netherlands, 1992.

1.9 W. Göpel, J. Hesse and J.N. Zemel (eds.), *A Comprehensive Survey, Volume 1 Fundamentals and General Aspects*, VCH, Weinheim, 1989, p170-191.

1.10 J.L. Vossen and W. Kern, *Thin Film Processes*, Academic Press, Inc., London, 1978.

1.11 J.L. Vossen and W. Kern, *Thin Film Processes II*, Academic Press, Inc., London, 1991.

1.12 S. Middelhoek and S.A. Audet, *Silicon Sensors*, Academic Press, London, 1989.

1.13 J. Brignell and N. White, *Intelligent Sensor Systems*, IOP Publishing Ltd., London, 1994.

1.14 W. Göpel, J. Hesse and J.N. Zemel (eds.), *Sensors a Comprehensive Survey Vol. 2 Chemical and Biochemical Sensors Part I*, VCH, Weinheim, 1991.

1.15 J.J. Miasik, A. Hooper and B.C. Tofield, Conducting Polymer Gas Sensors, *J. Chem. Soc., Faraday Trans. 1*, **82** (1986) 1117-1126.

1.16 P.N. Bartlett and S.K. Ling-Chung, Conducting Polymer Gas Sensors Part II: Response of Polypyrrole to Methanol Vapour, *Sensors and Actuators*, **19** (1989) 141-150.

1.17 W. Göpel and K.D. Schierbaum, SnO_2 Sensors: Current Status and Future Prospects, *Sensors and Actuators B*, **26-27** (1995) 1-12.

1.18 S. Zaromb and J.R. Stetter, Theoretical Basis for Identification and Measurement of Air Contaminants Using an Array of Sensors having Partly Overlapping Selectivities, *Sensors and Actuators*, **6** (1984) 225-243.

1.19 J.W. Gardner, Detection of Vapours and Odours from a Multisensor Array Using Pattern Recognition Part I. Principle Component and Cluster Analysis, *Sensors and Actuators B*, **4** (1991) 109-115.

1.20 P. McGeehin, P.T. Moseley and D.E. Williams, Self-Diagnostic Solid State Gas Sensors Employing Both Model and Novel Materials, *6th Int. Congr. Sensors and Systems Technology (Sensor-93), Nuremberg, Germany, 11-14 Oct. 1993*, ACS, Wunstorf, 1993, 113-125.

1.21 J.W. Gardner, Intelligent Gas Sensing Using an Integrated Sensor Pair, *Sensors and Actuators B*, **26-27** (1995) 261-266.

1.22 P.T. Moseley and B.C. Tofield, *Solid State Gas Sensors*, Adam Hilger, Bristol, 1987, p 17-31.

1.23 Figaro Engineering Inc., *Figaro Gas Sensors Products Catalogue*, April 1995.

1.24 S.K.H. Fung, Z. Tand, P.C.H. Chan, J.K.O. Sin and P.W. Cheung, Thermal Analysis and Design of a Micro-Hotplate for Integrated Gas Sensor Applications, *Proc. Eurosensors IX, Stockholm, Sweden, 25-28 June 1995.*

1.25 U. Dibbern, A Substrate for Thin-Film Gas Sensors in Microelectronic Technology, *Sensors and Actuators B*, **2** (1990) 63-70.

1.26 V. Demarne and A. Grisel, An Integrated Low-Power Thin-Film CO Gas Sensor on Silicon, *Sensors and Actuators*, **4** (1991) 539-543.

1.27 L. Ristic (ed.), *Sensor Technology and Devices*, Artech House, London, 1994.

1.28 K.E. Bean, Anisotropic Etching of Silicon, *IEEE Trans. Electron Devices*, **ED-25** (1978) 1185-1193.

Chapter 2

2. Gas Sensing Materials

2.1 Introduction

The objective of this Chapter is to discuss the basic gas-sensing mechanisms of MOS, XPc and CP films, which are employed in chemoresistive gas sensors for the suitable detection of CO, NO_2 and VOCs.

The operation of a chemoresistor relies on the detection of a change in electrical resistance or conductance on exposure to particular molecules. The electrical conductance of a microsensor is the sum of the contributions from the conductances of the gas-sensitive film (bulk effect) and the interfacial region between the gas-sensitive film and both the electrodes and substrate (contact effects). A change in the environmental conditions (e.g. gas concentration, temperature and humidity) will therefore be detected when either the bulk or contact conductance is affected.

The substrate material is chosen to be electrically insulating and so the conductance of the sensor is determined by the conductivity of the gas-sensitive material and electrode structure. However, the gas-sensitive film must adhere well to the substrate and provide a mechanically-robust device.

Tan *et al.* [2.1] have shown that the choice of electrode material used with CP films (e.g. poly(pyrrole)) may either produce a rectifying or ohmic contact. The electrode material employed by chemoresistors is selected to form an ohmic contact with the gas-sensitive materials [2.2]. Hence, gold (Au) electrodes have been employed here, because the contacts formed with CP gas-sensitive materials can be ohmic at applied voltages below 1 V. In other areas of sensor research, the interface between the electrode and gas-sensitive film is designed to form a Schottky barrier with a non-linear current-voltage behaviour, which is sensitive to chemically adsorbed

(chemisorbed) molecules. In a Schottky diode sensor this interface defines the dominant gas-sensitive mechanism.

The contribution to the sensor signal by the contact resistance can be minimised by careful control of the electrode deposition conditions and by optimising the electrode geometry [2.3].

The geometry of the sensor may change due to induced stresses. However, the substrate structure, materials and fabrication techniques are selected to minimise induced stress, as described further in Chapter 3. An example of induced stress has been exhibited in CPs, which can swell when exposed to high sorbate concentrations. In this case, the internal stresses throughout the microsensor will depend upon the gas concentration and temperature, which may lead to a deformation of the microstructure.

In this Chapter only the gas-sensitive film conductance (or resistance) is considered, because careful choice of the chemoresistor structure and materials renders the other contributing conductances (e.g. contact and electrodes) either insensitive to the gases of interest or negligible compared to the gas-sensitive film. In order to understand the gas-sensing characteristics of the MOS, XPc and CP chemoresistors investigated in this research, the mechanisms suggested by other researchers are reviewed. The effect of film composition and morphology on the chemoresistor characteristics is also outlined.

2.2 Metal Oxide Semiconductor Materials

There are a wide variety of MOS materials which have shown a sensitivity to changes in particular gases [2.4, 2.5]. The group of oxides considered here are those which operate from approximately 200°C to 600°C, where the dominant gas-sensing mechanisms occur at the surface (this includes internal surfaces for porous MOS films). The most successful type of MOS material (both in terms of sensor performance and commercially) have been the oxides of transition metals, in particular tin dioxide (SnO_2). These materials have been employed in applications requiring the detection of low concentrations of potentially hazardous gases, in an atmosphere of steady partial pressure of oxygen (in air).

In an effort to improve sensor performance, early research concentrated on optimising the MOS films composition and morphology. The different mechanisms

involved have been widely investigated. SnO_2 is described as a model example, since it has been the most extensively studied and well understood of the metal oxides. SnO_2 is most commonly employed in chemoresistors as thick or thin polycrystalline films. The deposition techniques used for thin and thick SnO_2 films investigated here are discussed in Chapter 4.

As mentioned above the film morphology and composition (e.g. the effect of additives) are key parameters in determining the chemoresistor properties, as will be described in more detail later. However, to simplify the discussion involving the interaction of SnO_2 with the gases of interest, the material is first considered as a pure thin film of single crystal SnO_2.

2.2.1 Gas Sensing Mechanisms of Single Crystal SnO_2

The bulk of the thin SnO_2 single crystal is typically a *n*-type semiconductor. The intrinsic donors are connected with a stoichiometric excess of metal (Sn), generating oxygen vacancies [2.6]. At elevated temperatures, an increasing fraction of the electrons bound by the bulk defects enter the conduction band. However, it is known that, at the temperatures of interest (< 600°C), the dominant mechanism causing conduction change is gas adsorption onto the crystal surface. If the adsorbing species is an oxidising gas (i.e. electron accepting) then chemisorption produces surface acceptors which bind electrons from the bulk. This causes a surface depletion region. Conversely, the chemisorption of a reducing gas (i.e. electron donating) leads to the production of surface donors, which release electrons to the bulk, so generating an accumulation layer. It is well known that in clean air, the chemisorption of oxygen (O_2) onto SnO_2 removes electrons from the bulk, so forming negatively charged surface ions (e.g. O_2^-, O^- and O^{2-}) according to [2.7],

$$O_2 + e^- \Leftrightarrow \left(O_2^-\right)_{ads} \tag{2.1}$$

$$\left(O_2^-\right)_{ads} + e^- \Leftrightarrow \left(2O^-\right)_{ads} \tag{2.2}$$

$$(O^-)_{ads} + e^- \Leftrightarrow (O^{2-})_{lat} \tag{2.3}$$

The rates of these reactions are dependent on temperature. Above approximately 180°C O^- ions are found as the prevailing species [2.8]. At even higher temperatures, the adsorbed O^- species may form a O^{2-} which becomes stable at a lattice site.

The depletion region which is formed in air has a depth of approximately 1 to 100 nm [2.9], and tends to increase the crystal's resistance. The thickness of the depletion layer is referred to as the Debyé length (L_D). Oxygen is always present in the air, so the formation of an accumulation layer will not occur in the investigations presented here. The energy diagram, as is shown in Figure 2.1, has been used to model the surface interaction with O_2 [2.6, 2.8].

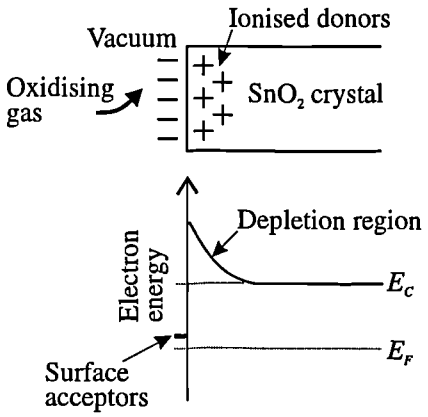

Figure 2.1 Interaction of oxidising gas species (e.g. O_2) with surface states causing depletion of surface charge. This is indicated by the schematic distribution of charge (top diagram) and the band scheme (bottom diagram) near the conduction band edge E_C, where E_F is the Fermi level.

In pure air, the effect of the resultant charge depletion layer on the single crystal thin film at a specific temperature governs the base-line resistance of the sensor. For the detection of a target gas species, the mechanisms are dominated by surface interactions, which lead to a change in the surface charge concentration. The effect on the depletion layer by the interactions with reducing (e.g. CO) and oxidising (e.g. NO_2) gases are as shown in Figure 2.2.

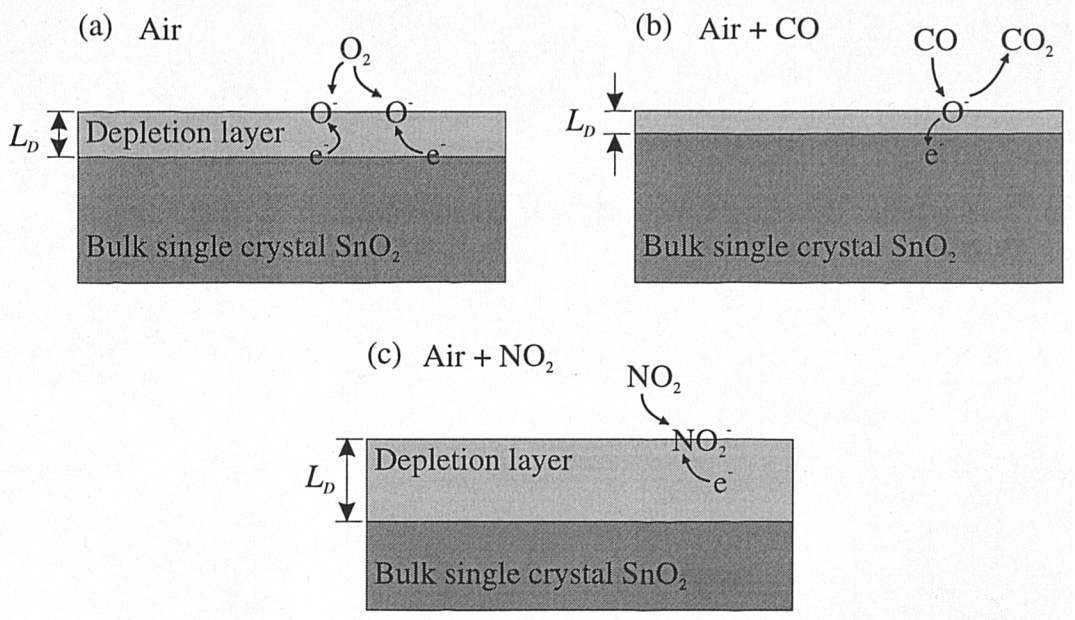

Figure 2.2 Schematic showing the depletion layer in single crystal SnO_2 in (a) air, (b) reducing gas (e.g. CO) and (c) oxidising gas (e.g. NO_2). Not all the surface interactions have been shown for the sake of clarity.

Our current understanding of surface reactions has been reviewed by Kohl [2.8].

In general, a reducing gas reacts with the adsorbed oxygen ions. The product of this reaction is desorbed from the surface, which releases electrons back to the conduction band and leaves a surface site available for further chemisorption with atmospheric oxygen. At equilibrium the concentration of adsorbed oxygen ions has been reduced and the depletion thickness falls. For example, a reducing gas of key interest here is CO. The main CO detection mechanism by the single crystal SnO_2 is an irreversible combustion process described according to [2.7],

$$CO + \left(O^-\right)_{ads} \rightarrow CO_2 + e^- \qquad (2.4)$$

Conversely, sensitivity to low concentrations of oxidising gas (e.g. NO_2) in the presence of oxygen requires that the target gas has a high electron affinity, because the processes leading to chemisorption of either the oxidising gas or atmospheric oxygen will take place competitively. If, for example, the probability of oxygen sorption is the same as that for the oxidising gas, then the difference in electron affinity produces a net change in charge. Therefore, the exposure to a stronger oxidising gas generates a

greater charge depletion which increases resistance [2.10]. For example, the chemisorption of NO_2 molecules by the capture of conduction band electrons from the single crystal SnO_2 can be expressed as,

$$NO_2 + e^- \Leftrightarrow \left(NO_2^-\right)_{ads} \tag{2.5}$$

It has been postulated by Sayago *et al.* [2.11] that the NO_2 can also be adsorbed *via* interactions with the adsorbed O_2^- and O^- species.

The effect of water vapour has been widely studied, because it is present in most applications of interest [2.12]. The effect of water is known to induce electron injection at the temperatures of interest. One such adsorption mechanism with water may proceed according to,

$$H_2O + \left(O^-\right)_{ads} \Leftrightarrow 2\left(OH^-\right)_{ads} + e^- \tag{2.6}$$

Several qualitative models have been proposed in the literature which explain the interaction of reducing gases in the presence of water [2.13, 2.8].

The gas adsorption examples presented so far are simplified atomistic models of a more complex microsystem. This is because the mechanisms also depend on a wide variety of other conditions e.g. temperature, catalytic dopants, microstructure and other species present on the surface and in the atmosphere. However, some of the interactive mechanisms are not fully understood. There may be several steps involved leading to the equilibrium with different chemisorbed gas species. Of the different reaction steps leading to the change in conductivity, the rate limiting process kinetics determine the sensor's response time. Different rate limiting process kinetics are thought to be involved during exposure and removal of the target gas, resulting in different 'on' and 'off' transients, respectively. The response time depends on many parameters, but at the temperature of highest sensitivity, MOS chemoresistors typically reach a steady-state value after a few tens of seconds.

For a single crystal SnO_2 chemoresistors to have a high sensitivity (for the detection of hazardous gases) it is essential that the Debyé length is a significant portion of the overall thickness of the bulk material. Hence, single crystals of SnO_2

have been deposited by thin film techniques (molecular beam epitaxy), but they still exhibit low sensitivities [2.14]. However, both thick and thin films of polycrystalline SnO_2 have shown high sensitivities to the gases of interest, which led researchers to postulate alternative gas-sensing mechanisms. These models are still based on the surface interactions with the gases of interest, but the importance of SnO_2 morphology is introduced in governing charge transport through the polycrystalline structure. These effects of thin and thick films of SnO_2 are outlined in the following Sections.

2.2.2 Thin Polycrystalline Films

The structure of SnO_2 deposited by thin film techniques [2.15] are in general shown to be polycrystalline with randomly orientated crystallites. The size of these crystallites are dependent on the deposition technique and any post-thermal treatment. For example, Sanjines *et al.* [2.16] have shown that as-sputtered films are initially amorphous, however, annealing the films at 550°C for 2 hours, produces crystallites with an average diameter of 15 nm (nanocrystals).

For nanocrystals with diameters greater than L_D, the depletion layer affects the local electron concentration of the conduction path between nanocrystals at the surface of the film. This mechanism of effecting conduction at the intercrystallite region has been commonly modelled as a potential barrier across which charge has to pass. This mechanism is more commonly used to model thick film SnO_2, as will be described in more detail in the following Section.

For nanocrystals with a diameter less than L_D, the depletion layer penetrates the entire nanocrystal. Therefore, electron concentration changes drastically within the nanocrystals upon exposure to adsorbing species. A thin film composed of small nanocrystals can be modelled macroscopically as a homogeneous semiconductor, in which the energy level of the conduction band edge at the surface is modulated by the charge transfer with adsorbing gas species [2.17]. This macroscopic model is equivalent to the single crystal model.

2.2.3 Thick Polycrystalline Porous Films

Porous films of polycrystalline SnO_2 deposited by thick-film deposition techniques have been shown to have very high sensitivities (where the resistance may change up to an order of magnitude) to the gases of interest (e.g. CO [2.18], NO_2

[2.19]). This sensitivity cannot be ascribed by the single-crystal thin-film model [2.8, 2.9]. Hence, as for the thin film SnO_2, other mechanisms have been postulated which are associated with the materials morphology. The structure of porous thick film SnO_2 is usually composed of grains with an average size of ~ 3 μm. These grains are themselves composed of the nanocrystals described in the previous Section [2.9]. The gas can diffuse through the porous film, whereupon, it may adsorb with internal surface sites.

Classical methods of explaining the high sensitivity to certain gases were based on the morphology of the larger grains as explained below.

It has been suggested that the conductivity is predominantly determined by the grain boundaries, the number of which is determined by the size of grains. If the grains touch but are not sintered, then the depletion layer forms a Schottky barrier, over which the charge-carriers must flow to transfer from one grain to the next, as is shown in Figure 2.3.

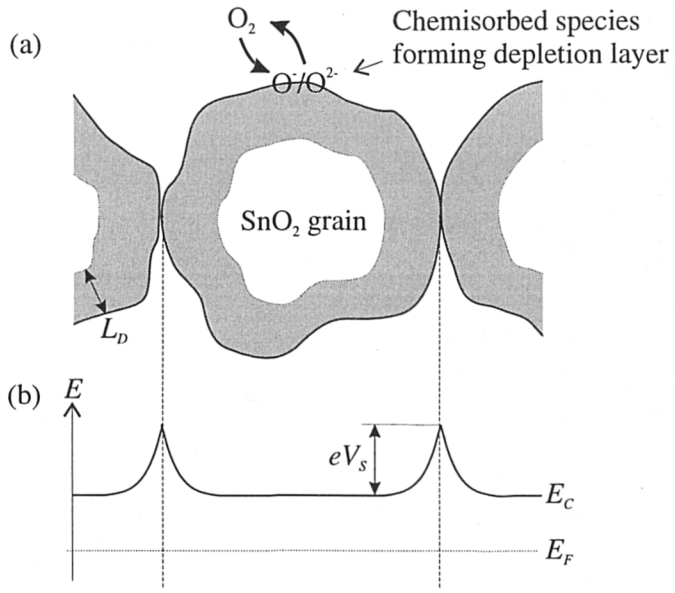

Figure 2.3 Grain boundary effects showing (a) a schematic of the grain boundaries with chemisorbed O_2 forming a depletion layer that penetrates the grain (shaded region), (b) band scheme near the conduction band showing the potential barrier (eV_S) at grain boundaries. For simplification only O^-/O^{2-} surface species are shown here.

When there is a high surface charge, the potential of the Schottky barrier, eV_S, is also high, resulting in a large resistance. However, if the surface charge density is

lowered by the chemisorption of a gas then the potential barrier is also decreased, which corresponds to a lower resistance.

The properties of a SnO_2 film are highly dependent on a high temperature (~ 600°C to 700°C) sintering stage [2.9]. Sintering increases the strength of the initially deposited material by generating "necks" between adjacent grains. If the thickness of these necks are comparable to L_D, then the adsorption of gases on the necks has the same effect on conductance as adsorption on thin single crystal SnO_2 films. An increase in L_D has an effect of restricting the width of the neck channel through which current flows, as shown in Figure 2.4. If the necks are thin enough, then all the carriers in the neck region are extracted, and the carriers must overcome a potential barrier to traverse the neck, which as before is modulated by the interaction of gas species at the surface.

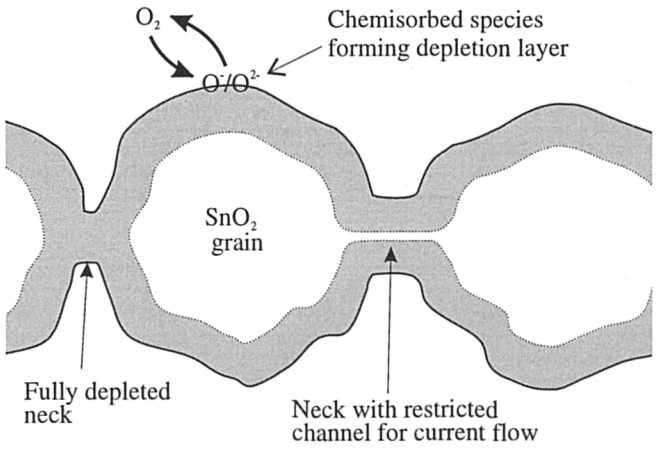

Figure 2.4 Schematic showing the surface mechanisms involving intergranular necks. For simplification only O^-/O^{2-} surface species are shown here.

More recently, Schierbaum *et al.* [2.20] have suggested possible conductance contributions by the nanocyrstals. In this case the negative surface charge due to the adsorbed negative oxygen ions causes depletion throughout entire nanocrystals at the internal surfaces.

Within a polycrystalline MOS film the morphology may consist of a range of crystallite sizes. During heat treatment the crystallite size and the amount of sintering increases. The variability involved with these processes means that more than one of the mechanisms described above may contribute to the overall microsensor

conductance. Control of these properties is dependent on the deposition processes, but in most cases the reproducibility of sensor conductance is poor. The base-line resistances for SnO_2 chemoresistors investigated in the literature therefore varies greatly (e.g. approximately 10^3 to 10^7 Ω).

2.2.4 Effects of Catalytic Additives

It is known that SnO_2 is sensitive to a wide variety of different gases, and so the poor specificity of MOS chemoresistors has limited their application. The specificity between some gases can be enhanced by careful choice of the operating temperature, but its effectiveness is limited. An alternative method to improve specificity is by the inclusion of catalytic additives or dopants [2.21, 2.22]. Two different types of sensitisation mechanism have been identified by Yamazoe *et al.* [2.22]. The first is a chemical interaction (catalytic) by which additives assist the redox processes leading to the interaction of the target gas. The second interaction is an electronic one, in which an additive behaves as a sort of electron donor or acceptor. The most commonly used additives in MOS films are palladium (Pd) and platinum (Pt), which have been shown to exhibit a catalytic chemical interaction. These additives form sites on the SnO_2 surface which may activate the gases for detection at a faster rate than at the SnO_2 surface. The ions formed on the catalyst site can then 'spillover' onto the SnO_2 surface. The catalyst additives can therefore provide an alternative reaction kinetic path for the gas adsorption at a faster rate and with different activation energies (which changes the temperature of maximum sensitivity).

Both thin SnO_2 and thick SnO_2 films have been deposited onto my chemoresistor designs and their response to CO and NO_2 studied. Moreover, the effect of adding small amounts of Pd and Pt to the pure material has been analysed.

2.3 Organic Materials

It has been known for many years [2.23] that some organic materials show a change in resistance on exposure to certain gases. The two different classes of organic material that have shown a reversible response to a number of gases are semiconducting metal-substituted phthalocyanine (XPc) materials and conducting polymers (CPs). The physical properties and gas-sensitive characteristics of these materials are described below.

2.3.1 Metal-Substituted Phthalocyanine Materials

2.3.1.1 XPc Structure

Phthalocyanines are highly coloured hetero-atom macro-cycles, in which two central hydrogen atoms can be substituted by a metal atom in the centre of a molecular ring, as shown in Figure 2.5. Where the metal species substituted into the molecule is represented by an 'X'. Note that if reference is made to a particular metal then the 'X' is replaced by the elements chemical symbol.

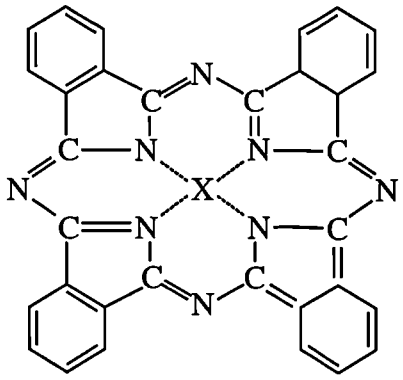

Figure 2.5 Structure of metal-substituted phthalocyanine (XPc) molecule.

The crystallinity of a XPc film is dependent upon the deposition technique and the conditions during film growth, hence, it is possible to grow XPc films into different cyrstalline phases. For example, PbPc is known to exist in monoclinic, triclinic and tetragonal phases. The different XPc deposition techniques are outlined in Chapter 4, however, at present it is sufficient to note that the most commonly employed deposition technique is vacuum sublimation (evaporation). The properties described in this Section therefore refer to evaporated thin films with a thickness of typically 1 μm. It has been shown that as-deposited films of XPc consist of fine monoclinic particles with disordered phases between the particles [2.24]. Crystallisation can be induced by thermal annealing, which may also lead to a phase transition, depending on the temperature and time of the annealing process [2.25].

2.3.1.2 Effect of Gases on Electrical Conductivity

XPcs behave in a similar manner to a *p*-type semiconductor. The actual charge carrying mechanisms associated with molecular crystals are beyond the scope of this review, the reader is refered to the work of Gutmann [2.23] and Wright [2.26] for further explanation of this topic. However, it is sufficient to note that the electrical properties and gas sensitivity of XPc films are strongly dependent on crystal structure and morphology.

The sorption of gases and vapours onto organic materials exert a profound influence on the conductivity. For XPc films the mechanisms responsible for conductivity changes are generally accepted as being dominated by gas adsorption. It is thought that oxidising gases influence conductivity *via* surface charge-transfer interactions, which generate charge carrying positive holes. For *p*-type XPcs the majority carriers in vacuum conditions are holes, so that exposure to an oxidising (i.e. electron-accepting) gas will increase the carrier concentration and hence, conductivity. As a result of these surface processes, the carrier concentration (thus the conductivity) in the bulk of the solid may change by several orders of magnitude due to the interaction of an adsorbed gas. The interactions between an oxidising gas and XPc can be described by the following general equilibria,

$$\begin{aligned} &\text{gas} + \text{XPc} \overset{\text{physisorption}}{\Leftrightarrow} \text{G} + \text{XPc} \overset{\text{charge transfer}}{\Leftrightarrow} \\ &\left[\text{G}^{-}\text{XPc}^{+}\right] \overset{\text{delocalisation}}{\Leftrightarrow} \left[\text{G}^{-}\text{XPc}\right] + \text{hole} \end{aligned} \qquad (2.7)$$

where G is a physisorbed molecule and G^- is an ionised gas molecule.

The interactions of equation 2.7 are observed when XPc films are initially exposed to air, because the electron-accepting O_2 molecules chemisorb onto the XPc surface. Thus, under normal atmospheric conditions XPc surfaces can be assumed to be completely covered with an adsorbed layer comprising mainly of O_2 ions. Note that Mocket *et al.* [2.27] have postulated that the presence of adsorbed water-derived species is also essential for reversible O_2 chemisorption.

For chemisorption to occur with another gas, an O_2 surface site must first be made available by O_2 desorption. XPc films have shown greatest sensitivity to gases with a high electron affinity, e.g. NO_2, NO, Cl_2, F_2. Their sensitivity to NO_2 is of

greatest interest, because it is a common environmental pollutant. The surface charge-transfer due to NO_2 chemisorption is stronger than existed previously with the chemisorbed O_2 leading to an increase in conductivity. In contrast, chemisorption of a reducing gas (e.g. CO) leads to the extraction of *p*-type carriers and produces a conductivity decrease [2.28]. The strength of the surface charge-transfer interactions is the most important factor controlling the change in conductivity. If the interactions are too weak (physisorption) their effect on the activation energy for carrier generation is small and conduction enhancement is small. If, however, the interactions are too strong and localised (chemical bonding) the charge carriers are bound to the adsorption sites, so conduction enhancement is again small.

The rate of conductivity change upon exposure to a gas and the rate of its reversal in clean conditions, i.e. when the target gas is removed, are optimised when the interaction with the absorbant is weak. While the reversal will be faster for more weakly-bound gases, the chemisorption of a gas is primarily limited kinetically by the ease of displacement of adsorbed O_2 from the surface. The kinetic factors that influence conductivity are temperature dependent. Archer *et al.* [2.25] suggest that thermal-treatment and gas-exposure history also contributes significantly to the response characteristics. As is mentioned earlier, thermal-treatment is known to modify the materials morphology and as a consequence changes both the conductivity and rate of sorption [2.24]. The temperature which optimises response rate, reversibility and selectivity, while retaining reasonable sensitivity and device lifetime, is usually determined experimentally.

2.3.1.3 Typical Characteristics of XPc Chemoresistors

Jones *et al.*[2.29, 2.30] have characterised the performance of different XPcs for gas sensing applications and shown that the central metal species has a significant effect on conductivity, sensitivity and selectivity. PbPc was selected for investigation with my sensor designs because it is the most sensitive to NO_2. A material showing similar sensitivity to PbPc is ZnPc, however, the poor reproducibility of this material was deemed unsuitable for investigation. The next most sensitive material, with good reproducibility is CuPc, which was also selected for investigation. MgPc was finally selected, despite its very low sensitivity to NO_2, because it has shown sensitivity to

gases other than NO_2 e.g. H_2S and HCl. All these materials were deposited at the Health and Safety Executive (HSE), Sheffield.

Typical values of XPc film conductance (G) and sensitivity to NO_2 [2.29, 2.30] are shown in Table 2.1.

Table 2.1 Typical characteristics for XPc films deposited by vacuum sublimation.

Material	Range of G in 2.8 ppb NO_2 at 170°C (Ω^{-1})	ΔG(44 ppb)/G(2.8 ppb) × 100 at 170°C (%)	Temperature of maximum sensitivity (°C)
PbPc	$1.5 - 4.5 \times 10^{-8}$	185	~ 160
CuPc	$3.0 - 4.5 \times 10^{-8}$	100	~ 160
MgPc	$5.3 - 6.9 \times 10^{-6}$	5	-

In order to ensure that the effect of the target gas is reversible and the effects of water vapour are minimised, most of the research on XPc chemoresistors has been carried out at temperatures above 100°C. However, the majority of investigations have been confined to temperatures below 200°C, because the sensitivity is known to decrease above approximately 160°C and the XPc films start to evaporate with any further increase above 200°C. In the temperature range of 150°C to 200°C, the response time (τ_{90}) of a change in conductance following a step change from pure air to a low concentration of NO_2 (~ 0.1 ppm) are in the order of 100 s [2.29]. The response to higher concentrations has been studied in detail by Archer *et al.* [2.25], who has shown that the step response takes the form of an initial fast change, followed by a slow drift to the steady-state value, which can take many minutes at these temperatures. Mrwa *et al.* [2.31] suggested that PbPc chemoresistors are physically stable at temperatures less than 250°C and at NO_2 concentrations less than 400 ppm in dry air. However, the response to NO_2 was found to be irreversible at very high concentrations (> 400 ppm). Jones *et al.* [2.32] have shown that the heat treatment of XPc films can yield sensors with very fast response times (< 10 s) at the expense of some loss of sensitivity. It should be noted, however, that some as-deposited XPc films have response times in the order of tens of minutes [2.28]. This response time

would be inadequate for an instrument warning against short term exposure hazards. Despite high sensitivity, XPc chemoresistors also suffer from poor long term stability and reproducibility, which have limited their use in commercial sensors.

2.3.2 Conducting Polymer Materials

The observation of a high electrical conductivity in doped organic polymers has been known since the late 1970s. These materials are commonly referred to as conducting polymers (CPs) and may be ionic or electronic conductors. Several applications have been envisaged for CPs (e.g. battery electrodes, electromagnetic shield, displays, and conducting plastics). The change in conductivity of electronically-conducting aromatic and heterocyclic polymers when exposed to various vapours (e.g. VOCs) has generated great interest for sensing applications [2.33]. The ease with which these kind of CPs can be electrochemically deposited as thin films and coupled with their good thermal stability makes them attractive for chemoresistive applications.

Although CP chemoresistors have a lower sensitivity (with a change in resistance up to approximately ± 10 %) when compared to MOS and XPc films, they do respond to vapours very rapidly (typically less than 10 s) at RT. However, since these materials are sensitive to a wide range of vapours, the specificity of an individual CP chemoresistor is poor. It is very easy to produce a CP chemoresistor with a base-line resistance suitable for simple interface electronics, because their conductivities are very high (in the order of 10^{-5} S/m [2.34]) and controllable by the deposition conditions.

In order to form a CP, the monomer must react to form an extended conjugate system that consists of an organic backbone based on the alternation of single and double bonds. Many CPs can be grown electrochemically, hence allowing the precise control of the polymer deposition conditions and doping during growth across the sensor electrodes. A description of the electrochemical deposition technique is given in Chapter 4. From the wide range of CPs available, materials based on poly(pyrrole) (PPy) and poly(aniline) (PAn) have been investigated here to show suitable vapour sensing performances [2.35, 2.36]. The basic composition of PPy and PAn are as shown in Figure 2.6,

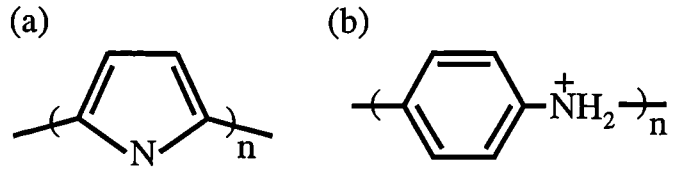

Figure 2.6 The generally accepted structures of (a) PPy, and (b) PAn.

In its oxidised state pyrrole exists as a polycation. The charge on the polymer is balanced by doping (i.e. the incorporation of anions) the film during electrochemical preparation. As a result the electrical characteristics, gas-sensing properties and structure of the final polymer depends on the choice of monomer and on the choice of counter-ion [2.37]. The counter-ions used in films that are at present being investigated (by the Universities of Warwick and Southampton Electronic Nose Group) are the alkylsulfonates (RSA, where the 'R' refers to the length of the alkyl group, e.g. pentanesulfonate becomes PSA).

The mechanisms of gas-sensitivity in CPs are, at present, poorly understood. However, a sorption model (Langmuir adsorption isotherm) has been empirically shown to be a good description [2.35]. Where the vapour species (V) interacts with internal sites, according to

$$V + \langle \text{site} \rangle \underset{k_b}{\overset{k_f}{\Leftrightarrow}} \langle V \rangle \qquad (2.8)$$

where k_f and k_b are the forward and backward reaction rates, respectively. This sorption model is described in greater detail in Chapter 5, which outlines the modelling of chemoresistive gas sensors.

Several possible theoretical mechanisms are being investigated by researchers to discover a correlation with the empirical models. The theoretical explanations have envisaged swelling of the polymer, interaction between the gas molecules and the charge carriers on the polymer chain, gas molecule/counter-ion interactions and oxidation or reduction of the polymer by the gas. Bartlett *et al.* [2.38] has suggested five possible mechanisms which might contribute to the overall observed gas-sensitivity of a CP chemoresistor, as depicted in Figure 2.7.

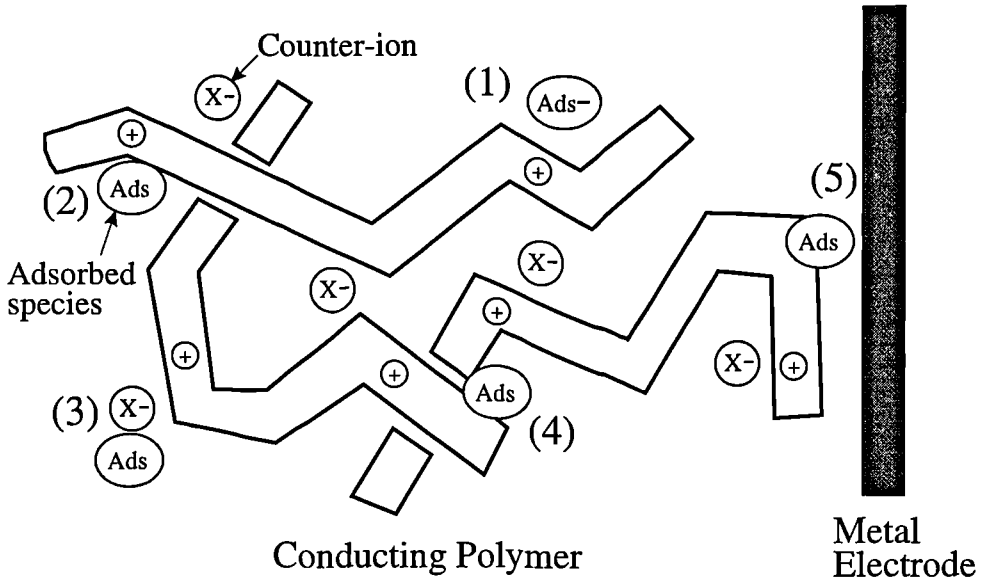

Figure 2.7 Possible mechanisms of the gas-sensitivity of CP chemoresistors caused by gas sorption, (1) direct carrier generation or removal by oxidation or reduction, (2) change in intrachain carrier mobility, (3) interaction with the counter-ion, (4) change in interchain hopping, (5) change in interfacial charge transfer.

Once a better understanding of the gas-sensing mechanisms have been established, the sensor performance can be improved by exploiting the high degree of property control with the electrochemical deposition conditions.

2.4 Chemoresistor Design Considerations

The performance of a gas-sensitive material is known to be dependent on the structure of the chemoresistor, as described below.

In many cases the performance is improved by elevating the operating temperature of the sensor to an optimal value. This is known to be true for MOS and XPc films, where an increase in temperature promotes specific chemical reactions within the film. This effect does not apply to CPs, because they possess a completely different sensing mechanism that allows optimal performance at RT. An integrated micro-heater which allows fast and accurate control of the operating temperature has been incorporated into all my microsensor designs except a CP resistor bridge sensor. The micro-heater provides a means for operating the chemoresistor at its optimum performance (i.e. a good sensitivity with a fast response time).

It is known that the response of chemoresistors based upon MOS, XPc and CP, are cross-sensitive to different gases, temperature and humidity. This poor selectivity to the variable of interest (i.e. the target gas), is reflected by interference on the measured signal. For these reasons, researchers have been investigating the use of an array of sensors in an intelligent sensor system to improve the overall system performance [2.39]. In such a system a pattern recognition program processes the output signals from the cross-sensitive elements in the sensor array to extract the required information.

Another important chemoresistor design consideration is ensuring that the chemoresistors conductance is a suitable value for interfacing with the signal conditioning circuitry. The conductance varies considerably between materials; CPs have a high conductance (typically 0.1 to 10^{-3} Ω^{-1}), MOSs tend to have a lower conductance (~ 10^{-3} to 10^{-7} Ω^{-1}), and XPcs may have a still lower conductance (~ 10^{-6} to 10^{-8} Ω^{-1}). The sensor conductance is related to different electrode geometries, as is described in Chapter 5, which can be adjusted by varying the length of electrode edge (l) and inter-electrode gap (w). To minimise the resistance of MOS and XPc chemoresistors, the aspect ratio (l/w) can be maximised (e.g. 10,000) by having an interdigitated electrode arrangement.

Finally, the structure and materials of the inactive device have to be compatible with the method employed for depositing the gas-sensitive film. It should be physically stable, without affecting the materials morphology and composition.

2.5 Conclusions

This Chapter has given an outline of the gas-sensing mechanisms suggested for MOS, XPc and CP chemoresistors. The gas detection mechanisms for each of these materials are different, and they depend on a wide variety of different properties. Table 2.2 summarises the trend in resistance change for the gas-sensitive materials to the gases of interest.

Table 2.2 Resistance change of the response of the gas-sensitive materials to the key gases of interest.

	Typical Resistance Change		
Target Species	Undoped and doped (Pd and Pt) SnO_2	XPc (PbPc, CuPc and MgPc)	CP (PPy and PAn)
CO	Large decrease	Increase	Not reported
NO_2	Large increase	Large decrease	Not reported
Toluene	Not reported	Not reported	Decrease for PAn
H_2O	Typically decreases	Decreases	Decrease for PAn Small increase for PPy

Different materials have been chosen for investigation in this research because of their sensitivity to the gases of interest (e.g. CO, NO_2 and VOCs). The type and composition of materials employed with my designs are listed in Table 2.3.

The properties of the gas-sensitive materials have been shown to be dependent on the morphology, which is determined by the deposition techniques employed, as is described in greater detail in Chapter 4.

Table 2.3 Details of different materials employed by my chemoresistor designs.

Material class	Type of material	Dopants	Nature of film
MOS	SnO_2	Pure[†]	Thick film
	SnO_2	Pt	Thick film
	SnO_2	Pd	Thick film
	SnO_2	Pure	Thin film
	SnO_2	Pt	Thin film
	SnO_2	Pd	Thin film
XPc	PbPc	As-deposited	~ 1 μm thick evaporated film
	CuPc	As-deposited	
	MgPc	As-deposited	
CP	PPy	Numerous counter-ions [2.37]	Thick polymeric film
	PAn		

2.6 References

2.1 T.T. Tan, J.W. Gardner, J. Farrington and P.N. Bartlett, Electronic Properties of Metal-Poly(Pyrrole) Junctions, *Int. J. Electronics*, **77** (1994) No. 2, 173-184.

2.2 S.M. Sze, *Semiconductor Devices, Physics and Technology*, Wiley, New York, 1985.

2.3 U. Hoefer, K. Steiner and E. Wagner, Contact and Sheet Resistances of SnO_2 Thin Films from Transmission-Line Model Measurements, *Sensors and Actuators B*, **26-27** (1995) 59-63.

[†] Purity is governed by the material source and the deposition technique.

2.4 W. Göpel, J. Hesse and J.N. Zemel (eds.), *Sensors - A Comprehensive Survey, Chemical and Biochemical Sensors*, Vol. 2, Parts I and II, VCH, Weinheim, 1991.

2.5 P.T. Moseley, Materials Selection for Semiconductor Gas Sensors, *Sensors and Actuators B*, **6** (1992) 149-156.

2.6 G. Heiland, Homogeneous Semiconducting Gas Sensors, *Sensors and Actuators*, **2** (1982) 343-361.

2.7 S.R. Morrison, Mechanism of Semiconductor Gas Sensor Operation, *Sensors and Actuators*, **11** (1987) 283-287.

2.8 D. Kohl, Surface Processes in the Detection of Reducing Gases with SnO_2 - Based Devices, *Sensors and Actuators*, **18** (1989) 71-113.

2.9 K. Ihokura and J. Watson, *The Stannic Oxide Gas Sensor*, CRC Press, London, 1994.

2.10 G.B. Barbi and J.S. Blanco, Structure of Tin Oxide Layers and Operating Temperature as Factors Determining the Sensitivity Performances to NO_x, *Sensors and Actuators B*, **15-16** (1993) 372-378.

2.11 I. Sayago, J. Gutiérrez, L. Arés, J.I. Robla, M.C. Horrillo, J. Getino and J.A. Agapito, The Interaction of Different Oxidizing Agents on Doped Tin Oxide, *Sensors and Actuators B*, **24-25** (1995) 512-515.

2.12 P.T. Moseley and B.C. Tofield, *Solid State Gas Sensors*, Adam Hilger, Bristol, 1987.

2.13 S.R. Morrison, Semiconductor Gas Sensors, *Sensors and Actuators*, **2** (1982) 329-341.

2.14 M.J. Madou and S.R. Morrison, *Chemical Sensing with Solid State Devices*, Academic Press, San Diego (1989) p. 424-426.

2.15 G. Sberveglieri, Classical and Novel Techniques for the Preparation of SnO_2 Thin-Film Gas Sensors, *Sensors and Actuators B*, **6** (1992) 239-247.

2.16 R. Sanjines, F. Lévy, V. Demarne and A. Grisel, Some Aspects of the Interaction of Oxygen with Polycrystalline SnO_x Thin Films, *Sensors and Actuators B*, **1** (1990) 176-182.

2.17 S. Chang, Thin-Film Semiconductor NO_x Sensor, *IEEE Trans. Electron Devices*, **ED26** (1979) 1875-1880.

2.18 M.C. Horrillo, J. Gutiérrez, L. Arés, J.I. Robla, I. Sayago, J. Getino and J.A. Agapito, The Influence of the Tin-Oxide Deposition Technique on the Sensitivity to CO, *Sensors and Actuators B*, **24-25** (1995) 507-511.

2.19 G. Williams and G.S.V. Coles, NO_x Response of Tin Dioxide Based Gas Sensors, *Sensors and Actuators B*, **15-16** (1993) 349-353.

2.20 K.D. Schierbaum, U. Weimar, W. Göpel and R. Kowalkowski, Conductance, Work Function and Catalytic Activity of SnO_2 - Based Gas Sensors, *Sensors and Actuators B*, **3** (1991) 205-214.

2.21 J. Watson, K. Ihokura and G.S. Coles, Thin Tin Oxide Gas Sensor, *Meas. Sci. Technol.*, **4** (1993) 711-719.

2.22 N. Yamazoe, Y. Kurokawa and T. Seiyama, Effects of Additives on Semiconductor Gas Sensors, *Sensors and Actuators*, **4** (1983) 283-289.

2.23 F. Gutmann and L.E. Lyons, *Organic Semiconductors*, Wiley, New York, 1967.

2.24 Y. Sadaoka, T.A. Jones and W. Göpel, Fast NO_2 Detection at Room Temperature with Optimized Lead Phthalocyanine Thin-film Structures, *Sensors and Actuators B*, **1** (1990) 148-153.

2.25 P.B.M. Archer, A.V. Chadwick, J.J. Miasik, M. Tamizi and J.D. Wright, Kinetic Factors in the Response of Organometallic Semiconductor Gas Sensors, *Sensors and Actuators*, **16** (1989) 379-392.

2.26 J.D. Wright, *Molecular Crystals*, Cambridge University Press, Cambridge, 1987.

2.27 H. Mockert, D. Schmeisser and W. Göpel, Lead Phthalocyanine (PbPc) as a Prototype Organic Material for Gas Sensors: Comparative Electrical and Spectroscopic Studies to Optimize O_2 and NO_2 Sensing, *Sensors and Actuators*, **19** (1989) 159-176.

2.28 C. Maleysson, M. Passard, J.P. Blanc, V. Battut, J.P. Germain, A. Pauly, V. Demarne, A. Grisel, C. Tiret and R. Planade, Elaboration and Tests of Microelectronically Designed Gas Sensors with Phthalocyanine Sensitive Layers, *Sensors and Actuators B*, **26-27** (1995)144-149.

2.29 B. Bott and T.A. Jones, A Highly Sensitive NO_2 Sensor Based on Electrical Conductivity Changes in Phthalocyanine Films, *Sensors and Actuators*, **5** (1984) 43-53.

2.30 T.A. Jones and B. Bott, Gas-Induced Electrical Conductivity Changes in Metal Phthalocyanines, *Sensors and Actuators*, **9** (1986) 27-37.

2.31 A. Mrwa, M. Friedrich, A. Hofmann and D.R.T. Zahn, Response of Lead Phthalocyanine to High NO_2 Concentrations, *Sensors and Actuators B*, **24-25** (1995) 596-599.

2.32 T.A. Jones, B. Bott and S.C. Thorpe, Fast Response Metal Phthalocyanine-Based Gas Sensors, *Sensors and Actuators*, **17** (1989) 467-474.

2.33 J.J. Miasik, A. Hooper and B.C. Tofield, Conducting Polymer Gas Sensors, *J. Chem. Soc., Faraday Trans. 1*, **82** (1986) 1117-1126.

2.34 P.N. Bartlett, J.W. Gardner and R.G. Whitaker, Electrochemical Deposition of Conducting Polymers onto Electronic Substrates for Sensor Applications, *Sensors and Actuators A*, **21-23** (1990) 911-914

2.35 P.N. Bartlett and S.K. Ling-Chung, Conducting Polymer Gas Sensors Part II: Response of Polypyrrole to Methanol Vapour, *Sensors and Actuators*, **19** (1989) 141-150.

2.36 P.N. Bartlett and S.K. Ling-Chung, Conducting Polymer Gas Sensors Part III: Results for Four Different Polymers and Five Different Vapours, *Sensors and Actuators*, **20** (1989) 287-292.

2.37 N. Blair, The Development and Characterisation of Conducting Polymer Based Sensors For Use in an Electronic Nose, *Ph.D. Thesis*, 1994.

2.38 P.N. Bartlett and J.W. Gardner, *Odour Sensors for an Electronic Nose, In Sensors and Sensory Systems for an Electronic Nose*, J.W. Gardner and P.N. Bartlett (eds.), Kluwer Academic Publishers, Dordrecht, 1992.

2.39 J.W. Gardner, *Microsensors: Principles and Applications*, John Wiley and Sons, Chichester, 1994.

Chapter 3

3. Design of Silicon Chemoresistive Devices

3.1 Introduction

The objective of this Chapter is to describe the design of the different silicon chemoresistive gas sensors produced during my research. A summary of the different chemoresistors produced is shown in Table 3.1. The sensors listed in Table 3.1 have been classified into three types; namely sensor array, discrete or resistive bridge devices. To identify each design described, a Sensor Research Laboratory (SRL) reference code has been applied.

The gases of interest (e.g. NO_2, CO and VOCs) led to the design of chemoresistors incorporating films of MOS, XPc and CP materials (see Chapter 2). The performance of such gas-sensitive materials can be improved by control of the composition and morphology. Moreover, fundamental to the operation of MOS and XPc films is the need to elevate operating temperatures. Resistance heaters have therefore been incorporated in some designs to control the operating temperature. Note that temperature control for CP chemoresistors is not so necessary because their sensing mechanisms are completely different and operate close to RT.

Each gas-sensitive material and corresponding deposition technique places specific requirements on the chemoresistor design; in particular the structure, geometry and composition of the electrodes, substrate and resistance heater. The design methodology for these integral microsensor parts is described for each type of sensor device.

Silicon technology has been employed because it allows miniaturisation, reduced fabrication unit costs and better reproducibility. It also makes possible the integration of the microsensor with its associated signal conditioning circuitry. However, at this stage of study only the sensor element and resistance heater have been integrated into

the design to minimise cost and complexity. Sensor structures based on silicon technology also gave the opportunity of exploiting micromachining techniques to produce MHPs with a very low power consumption. Different three-dimensional structures and thermally insulating materials have been employed here to improve the thermal properties of the microsensor. Although different SADs were produced to investigate different gas-sensitive materials, a common feature is the incorporation of three microheaters per SAD.

Apart from the purpose of material characterisation a SAD was developed to improve the frequently encountered problem of poor long-term stability. The approach to overcoming this problem has been to develop an intelligent dual sensor (SRL125/dual), which self-diagnoses drift caused by poisoning. The theory of the intelligent dual sensor is described in Chapter 5.

To minimise the number of SADs used for general characterisation of different CP films, a large number of discrete sensor designs were produced (as shown in Table 3.1).

The resistive bridge designs are for collaborative work being carried out between Warwick University and Southampton University, to develop the next generation of intelligent sensor systems. This instrument incorporates an Application Specific Integrated Circuit (ASIC) to interface the temperature compensated bridge structure with a microprocessor IC. A brief description of this design is also given.

Silicon microsensor structures described in this Chapter are produced by the sequential deposition and patterning of thin films on the silicon substrate. The sensor design was therefore concerned with generating the lithographic masks used during fabrication to pattern the particular films. Within this Chapter the designs are presented in terms of the layout of the mask subcells (see Appendix A). The masks were designed on the layout editor CAD tool L-Edit™ (Tanner Tools Ltd).

Table 3.1 Details of silicon chemoresistive sensors produced.

SRL Device No.	Quantity Produced	Electrode gap (μm)	Design Details
108/CP	72	10	Hex SAD for characterising CP films
108/var	72	2.5 to 15, in steps of 2.5	Hex SAD with variable inter-electrode gaps to investigate the effect of geometry on sensor performance
108/MOS	96	10	Hex SAD with an aspect ratio of ≈ 200, suitable for characterising MOS films. Also suitable with XPc films with low resistivities
123	720	10	Discrete devices for characterising CP films
125/CP	72	10	Hex SAD compatible with a CP microdeposition technique
125/MOS	90	10	Hex SAD for characterising MOS films with the same design as SRL108/MOS
125/XPc	66	5	Triple element SAD employing an electrode aspect ratio of 10,000 to characterise XPc films
125/Dual	36	-	SAD with three dual sensors to investigate long-term drift properties
127/s10	660	10	Discrete device for characterising CP, 4 × 4 mm^2 with co-planar integrated heater
127/s50	564	50	
127/l10	396	10	Discrete device for characterising CP, 4 × 10 mm^2 with co-planar integrated heater
127/l50	132	50	
127/b10	180	10	Bridge arrangement for thermal compensation
127/b50	60	50	

3.2 Design of Sensor Array Devices

A low power consumption is a key requirement of any sensor design intended for portable instruments. The critical feature that governs the device power consumption is the operating temperature of the gas-sensitive materials. Hence, to minimise thermal losses the SAD designs utilise a membrane microstructure with a cross-section depicted in Figure 3.1.

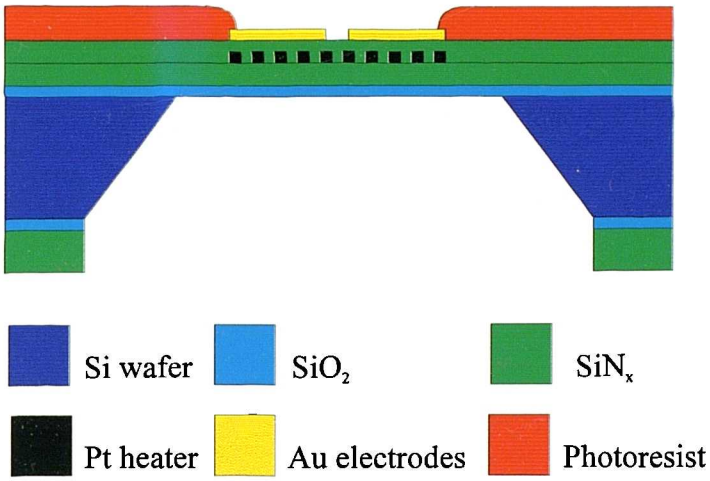

Figure 3.1 Cross-sectional schematic of cell structure in a SAD before gas-sensitive material deposition (10 nm adhesion layers of Ta for Pt and Ti for Au are omitted for the sake of clarity).

The device structure shown in Figure 3.1 can be considered as the integration of two distinct components: Firstly, a MHP structure with a resistance heater embedded in a thermally insulating ultra-thin Si_3N_4 membrane. Secondly, the chemoresistor structure defined by the arrangement of the Au electrodes and gas-sensitive material located on the membrane surface. The gas sensing performance of the chemoresistor is dependent on the operating temperature controlled by the MHP. The MHP is composed of a Pt thin film resistance heater which is sandwiched between two 0.25 μm thick layers of low-stress silicon nitride[†] (SiN_x). Bulk micromachining is employed to realise a membrane structure supported by a silicon substrate frame.

[†] The stoichiometry of the low-stress silicon nitride is propriety, but is normally less than 3:4 as for Si_3N_4.

Note that the thermal performance (e.g. power consumption and response time) of the MHP can be considered as a separate system, as is described in Chapter 6.

The integrated Pt microheaters are situated under each of the sensor elements. This arrangement of superimposing the heater and the electrode area separated by an electrically insulating layer of SiN_x provides a very efficient structure for heating the chemoresistor. A low-power consumption is a result of the combined effect of reducing the heat lost to the substrate and employing a material (e.g. SiN_x) with a low thermal conductivity. Thermal insulation can also be improved by maximising the thermal resistance of the membrane, by either increasing the membrane area, or minimising the membrane thickness. However, the realisable geometry of the membrane is limited by physical restraints, which include the residual stress and the thermally induced stress in the membrane. These properties have been minimised by employing low-residual stress SiN_x layer deposited on an 80 nm thin layer of thermal SiO_2. In order to achieve adequate thermal insulation, the membranes used here have an area of approximately three times larger than the active area of the heated chemoresistor.

It is essential that the whole microsensor system is mechanically stable even during thermal cycling. This is achieved by minimising internal stresses and maximising adhesion between layers. The adhesion of the Au and Pt metallisation is improved by initially depositing a 10 nm adhesion layer of titanium (Ti) and tantalum (Ta), respectively.

The general chemoresistor structure is composed of a 300 nm thin film of Au, which is patterned to form the electrode geometry. The electrode material is primarily selected to have a minimised contribution to the sensors resistance and provide an ohmic contact with the gas-sensitive material. The layout of the Au tracks is determined by the package used and compatibility with the gas-sensitive material deposition. The chemoresistor substrate is the SiN_x MHP surface which provides the necessary electrical insulation. It is also important that the gas-sensitive material has good adhesion with the SiN_x MHP surface. A photoresist layer is used to protect the device, except in areas which require further processing after the wafer fabrication. Photoresist windows expose the electrode areas for gas-sensitive material deposition,

and the Au contact pads, which are required for ultrasonic wedge bonding (Kulicke and Soffa 4126) during device packaging.

Different SADs have been designed for the investigation of the different gas-sensitive materials and the intelligent dual sensor. For the MOS, CP and intelligent dual sensor designs there are arrays of six chemoresistive elements (i.e. hex devices). The SAD designed for investigating XPc films has three chemoresistor elements, due to the higher aspect ratio requiring a larger area. The SADs (except the SRL125/CP SAD) have three MHP structures which heat two chemoresistor elements simultaneously. The SRL125/CP SAD has individual MHPs per sensor element. Details of the geometric designs are now given.

3.2.1 Gold Electrode Design for Sensor Array Devices

3.2.1.1 Electrode Design Suitable for MOS Films

The Au pattern for the SAD primarily intended to characterise MOS films is shown in Figure 3.2. This layout was used for the SRL108/MOS and the SRL125/MOS.

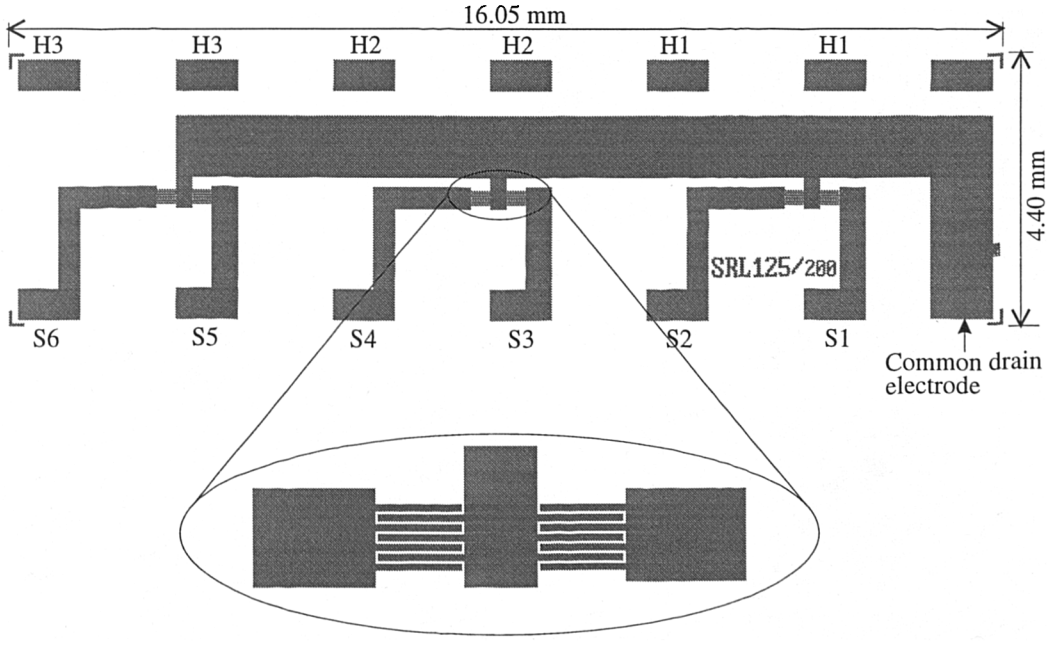

Figure 3.2 Au electrode layout design intended for MOS characterisation. S1-6 are the source electrodes for each sensor element, H1-3 are the contact pads for the three microheaters. The expanded insert shows an interdigitated electrode structure which has an aspect ratio of ≈ 200.

There are six chemoresistors arranged in pairs centred on a membrane with an underlying microheater. One electrode (common) is connected to all six sensors as seen by the wide track across the device. This common connection reduces the number of contact pads and consequently minimises the device size. The chemoresistive active area is further minimised by arranging the adjacent sensors in pairs to share the same common electrode and underlying heater. Each track, from either an electrode or an underlying microheater, terminates at the device edge to a 1.0 $\times$ 0.5 mm^2 Au contact pad. Seven contact pads are arranged either side of the device with a 0.1" pitch, which is compatible with a 14-pin d.i.l. package. To reduce track resistance the connections to the electrodes are as wide as possible.

An electrode aspect ratio of approximately 200 is achieved by using an interdigitated structure, with a finger length of 305 μm and an inter-electrode gap of 10 μm, as shown in the insert of Figure 3.2. An actual SRL125/MOS SAD mounted on a custom PCB d.i.l. header, is shown in Figure 3.3.

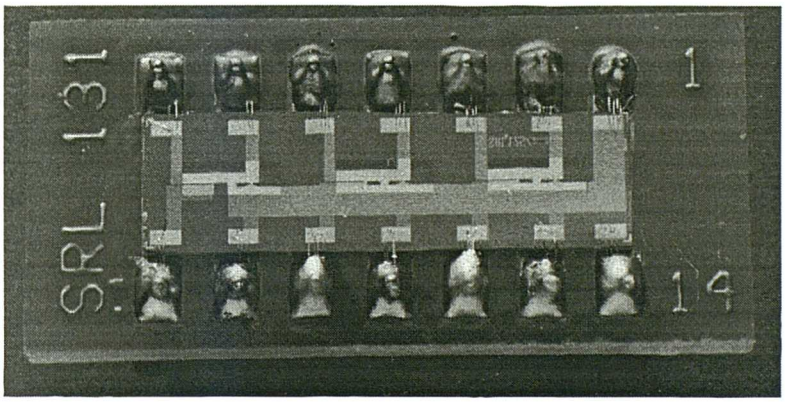

Figure 3.3 Packaged SRL125/MOS hex SAD.

3.2.1.2 Electrode Design Suitable for XPc Films (SRL125/XPc)

The Au electrode structure intended for characterising XPcs is shown in Figure 3.4. The extremely high resistivity of XPc films, typically in the range of 10^6 to 10^9 Ωm [3.1, 3.2], means that a correspondingly high electrode aspect ratio (1×10^4) is required to obtain a sensor resistance which is compatible with the intended interface circuitry. An electrode aspect ratio of 1×10^4 is achieved by using 41 interdigitated fingers, with an electrode finger length of 1245 μm and width of 5 μm, and an inter-

electrode gap of 5 μm. The solid appearance of the active area shown in Figure 3.4 is an illusion due to the printing resolution of this text, but the actual structure is shown in the inserted close-up.

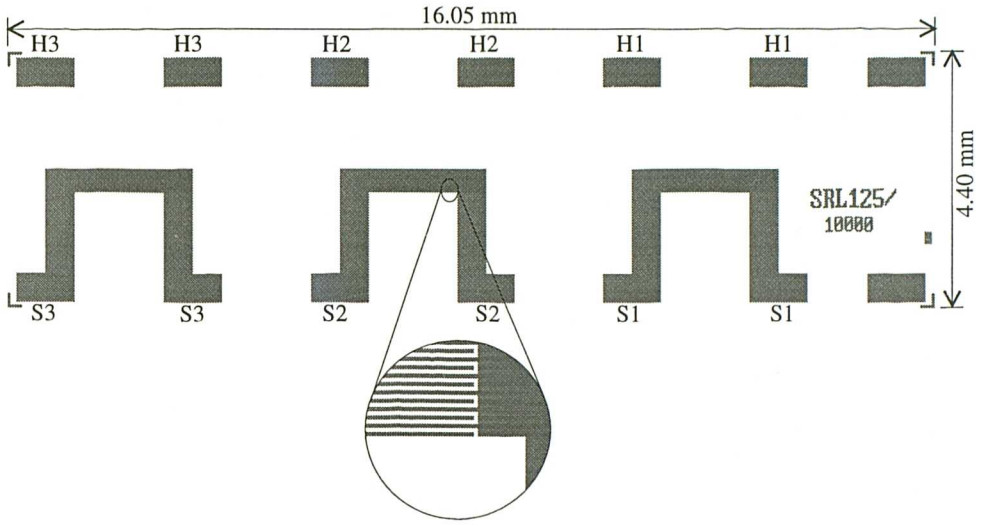

Figure 3.4 Au electrode layout design intended for XPc film characterisation. S1-3 are the source electrodes for each sensor element, H1-3 are the contact pads for the three microheaters. The expanded insert shows the interdigitated electrode structure.

The location of the contact pads are identical to the SRL125/MOS, except that as only three sensors are defined, a common drain is not required. The final packaged SRL125/XPc SAD is shown in Figure 3.5.

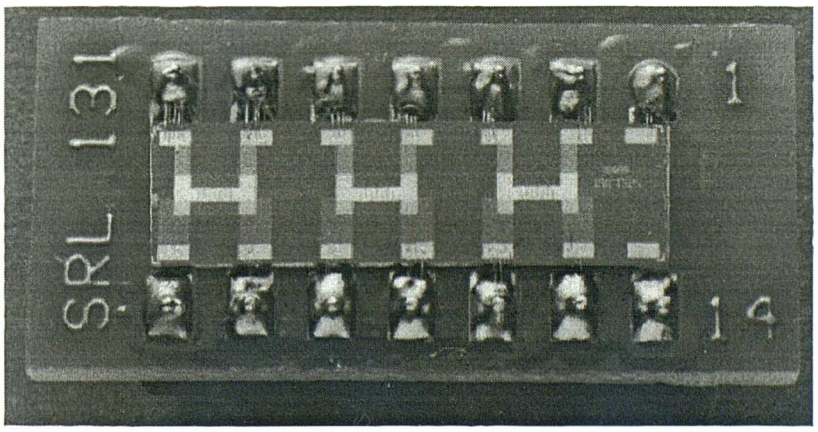

Figure 3.5 Packaged SRL125/XPc triple SAD intended for XPc film characterisation.

3.2.1.3 Electrode Design Suitable for CP Films

The design of the Au electrode pattern for the CP SAD is greatly influenced by the polymer deposition technique. CPs are electrochemically deposited from aqueous or organic solutions, in a divided cell using a conventional three-electrode system, where the device electrodes to be coated (source and common drain) are used as the cell's working electrode [3.3], as described in the next Chapter. The polymer is grown on the electrodes either potentiostatically or by cyclic voltammetry. The two electrodes have the same potential applied during growth and so the film will thicken equally and cross the inter-electrode gap from both sides. To achieve a uniform growth an equal track resistance is required from each contact pad to the corresponding electrode. This feature is incorporated into the Au electrode pattern as shown in Figure 3.6. The SRL108/CP SAD corresponds to an array of three pairs. This layout is also compatible with a 14-pin d.i.l. package. A low aspect ratio of 25 is used (obtained with a 10 μm inter-electrode gap and 250 μm electrode length), since CPs have a low resistivity compared to MOS and XPc films.

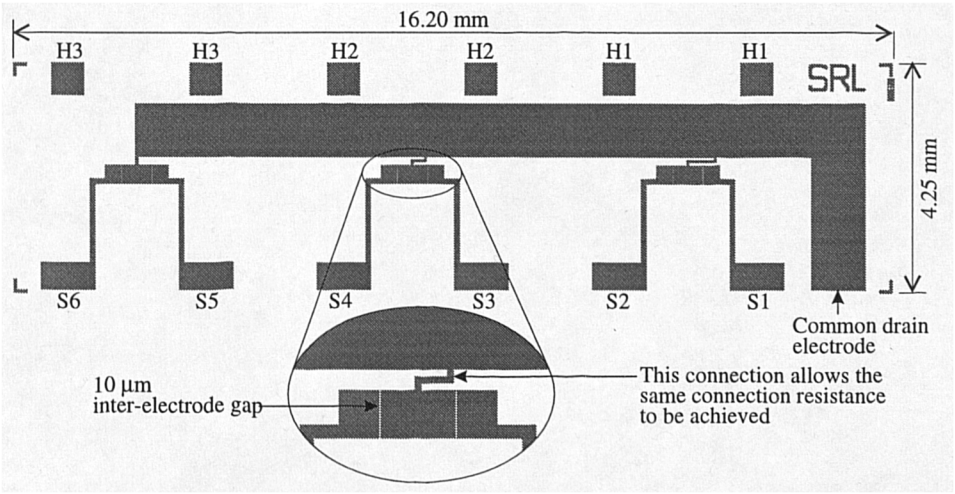

Figure 3.6 Au electrode design for SRL108/CP device intended for CP characterisation.

The limitation of the SRL108/CP design is that different polymer materials cannot be deposited on the adjacent sensors in the pair. To overcome this problem an electrochemical microdeposition technique has been developed which localises the

electrochemistry to a drop extruded on the device surface, described in Chapter 4. An appropriate SAD referred to as the SRL125/CP device has been designed to suit this technique, as shown in Figure 3.7. The common connection is now split into two, hence adjacent sensors have different commons (common electrode A and B). This permits the neighbouring electrodes to be held at a negative potential and thus stop unwanted film deposition. Also, the separation between sensor elements has been extended so that the drop of solution does not spread over two active areas with the same electrode common. Resistance matching of the tracks between contact pad and active electrode area was not as critical as for the SRL108/CP design, because the polymers are grown and characterised independently. This device has allowed a multi-type CP SAD to be achieved.

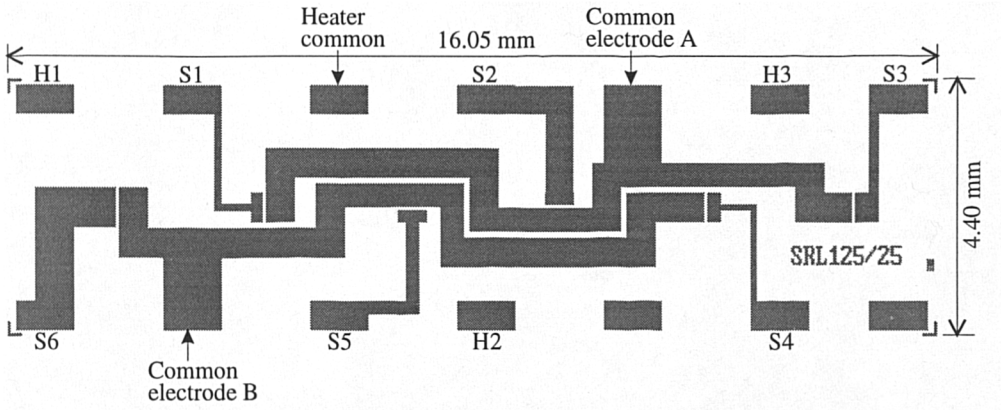

Figure 3.7 Au electrode design for the SRL125/CP device, has two electrode commons (A and B) which allows different CP films to be deposited on the device.

3.2.1.4 Intelligent Dual Sensor Electrode Design

The Au electrode pattern for the intelligent dual SAD (SRL125/dual) is shown in Figure 3.8. The design has three pairs of sensors with a single common electrode for all six sensors. The detailed theoretical operation of this dual sensor is described in detail in Chapter 5. However, at this point it is sufficient to note that the dual device exploits the response of two structurally different chemoresistors. One chemoresistor has an inter-electrode gap much less than the thickness of the gas-sensitive film, while the other chemoresistor has an inter-electrode gap which is much greater than the gas-sensitive film thickness. With an assumed gas-sensitive film thickness of ~ 2 μm, the sensor pair's wide inter-electrode gap is chosen to be 10 μm. The narrow inter-

electrode gap should ideally have a sub-micron dimension. However, because the lithographic processes used here can at best resolve a feature width of ~ 2 μm, a narrow inter-electrode gap is micromachined after the silicon wafer fabrication *via* focused ion beam milling (FIBM), as is described in Chapter 4. Hence, the narrow gap sensor has undefined electrodes until this micromachining technique occurs, as shown in the insert of Figure 3.8.

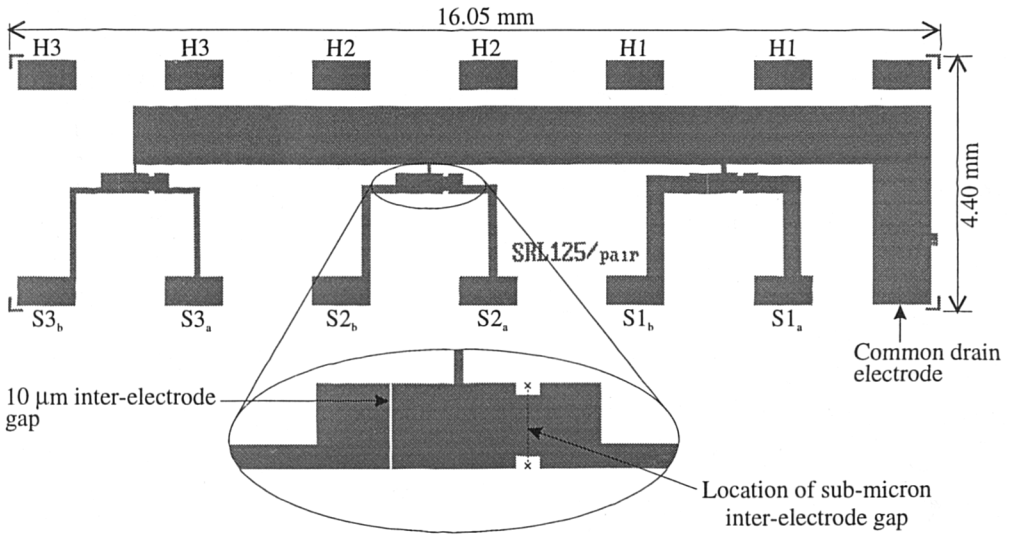

Figure 3.8 Au electrode design (SRL125/dual) for the triple dual SAD. S1-3 are the source electrodes for the three dual sensors, each dual sensor is composed of a pair of sensor elements with, (a) a narrow inter-electrode gap (sub-micron), and (b) a wide (10 μm) inter-electrode gap.

The pair of sensors are situated close together, so the same gas-sensitive material can be simultaneously deposited across both electrode gaps to minimise the variability between sensors. Only MOS and CP films were employed with this device, because the relatively low aspect ratio is ill-suited to XPc films (10 μm inter-electrode gap defines an aspect ratio of 25, while a 500 nm inter-electrode gap defines an aspect ratio of 500).

3.2.2 Photoresist Layout Design

The photoresist layer is patterned to open the windows which define the active areas and contact pads. For the SRL125/MOS and SRL125/XPc design, this layer serves as a passivation layer. However, it is essential for CP devices that the Au tracks are covered, otherwise they would be coated with CP during the

electrochemical deposition technique. Thus, making control of the film growth difficult. A Shipley Microposit 1813[†] photoresist was used, since after hardbaking (as described in more detail in the following Chapter) it is electrochemically inactive.

For the SnO_2 and XPc chemoresistive SADs a photoresist window uncovers the entire membrane area to minimise thermal losses through the structure, and permit operating temperatures above the sinter point of the resist (~ 200°C).

For the CP devices a 250 × 250 μm^2 photoresist window is opened over the 10 μm inter-electrode gap, defining an active area with an aspect ratio of 25. The active area for the intelligent dual sensor device is shown in Figure 3.9, where the electrode area opened for micromachining also exposes the SiN_x substrate, so the FIBM can cut through the Au electrode edge, which reduces the chance of an electrical short after the process.

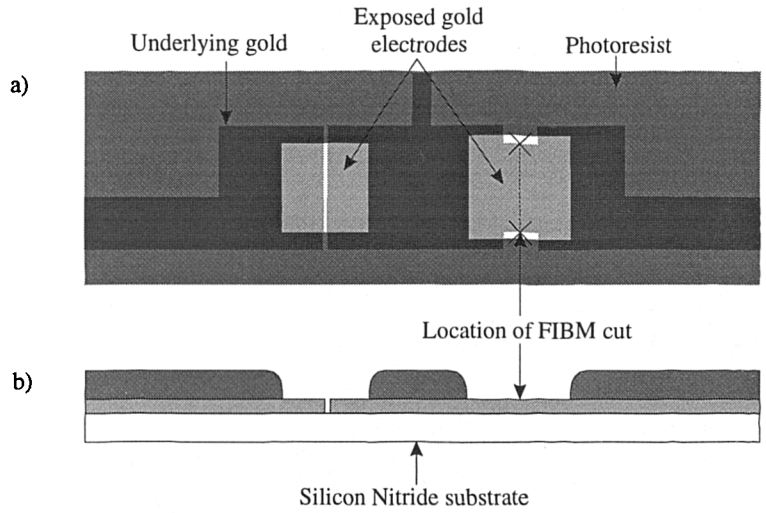

Figure 3.9 Photoresist layout design for sensor pair in a SRL125/dual SAD: a) Windows opened in the photoresist reveal active areas, b) cross-section through photoresist and Au layers. The location of the dotted line indicates where the FIBM cuts the sub-micron inter-electrode gap.

3.2.3 Design of Micro-Hotplate

The specification of the MHP is to isothermally heat the chemoresistor to its operating temperature with the lowest power consumption possible. The structure of the MHP was described earlier, in which a Pt resistance heater was located in the

[†] Microposit 1816 is now used as 1813 is no longer made.

centre of the SiN_x membrane, supported by a Si substrate frame. The MHP design methodology is described in this Section, whereas the actual MHP performance which was characterised and modelled is described in Chapter 6.

3.2.3.1 Pt Heater Element

The integrated microheater layout designs presented in this Section form the photolithographic mask which patterns the Pt thin film during fabrication. The resistance microheater dissipates heat according to i^2R (i.e. Joule heating), where i is the current passed through the element with resistance R. Therefore, a resistance value is required to maintain the heater drive voltage (V) in a range suitable for interface electronics (e.g. < 10 V). A meandering Pt thin film track over the area to be heated was used to provide an adequate resistance, as shown in Figure 3.10.

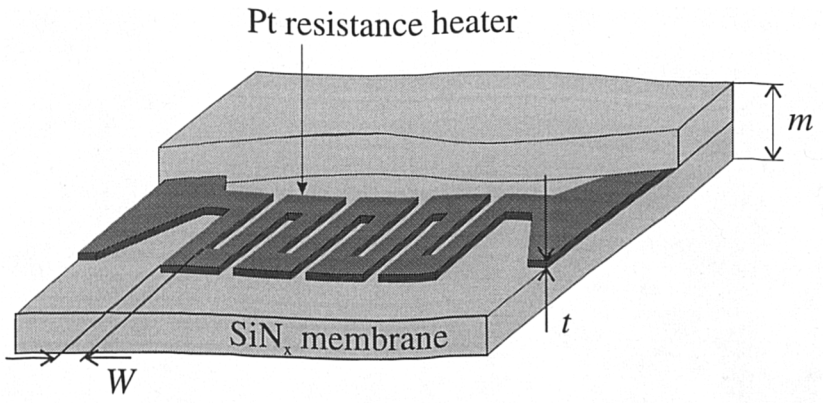

Figure 3.10 Schematic of a cut-away membrane to expose the microheater layout. The layers are not drawn to scale.

In Figure 3.10, W is the track width and t is the Pt film thickness which is 200 nm for SADs. The microheater is sandwiched between two 250 nm layers of low stress SiN_x, which encapsulates the heater within the membrane of thickness m. A 10 nm Ta adhesion layer is used for Pt. The Pt element is also used as a resistance thermometer, because its temperature coefficient of resistivity (α) is relatively high and linear to 0.1 % over the operating temperature range (RT to 700°C). The relationship between resistance and temperature is expressed as,

$$R_T = R_0[1+(\alpha \times \Delta T)] \qquad (3.1)$$

where R_T is the element resistance at temperature T, R_0 is the resistance at RT, and ΔT is the temperature above RT (i.e. ΔT=T-RT). The α for Pt is taken as 38×10^{-4} /°C.

The element resistance is directly proportional to the electrical resistivity, ρ, and inversely proportional to the film thickness, t. A meandering layout with effective track length, L , and width, W, has a resistance of

$$R = \left(\frac{\rho}{t}\right)\left(\frac{L}{W}\right) = R_S\left(\frac{L}{W}\right) \qquad (3.2)$$

The quantity R_S is called the sheet resistance and may be thought of as a two-dimensional material property. The bulk resistivity of Pt at RT is taken to be 11×10^{-8} Ω m. Hence, the sheet resistance for the Pt heater is 0.55 Ω, since a film thickness of 200 nm is used.

3.2.3.2 Thin Film Considerations

Variations in the resistivity of a metal correspond to changes in the mean free path of the conduction electrons. When considering bulk Pt at high temperatures (20 to 2000 K) the mean free path is predominantly effected by electron-phonon and impurity scattering. However, surface scattering of the electrons results in the resistivity increasing whenever the material becomes thin enough for the mean free path to be a significant fraction of the film thickness.

The Sondheimer theory [3.4] describes the thin film effects on resistivity. The expression has been approximated for both large and small thicknesses. The thick film approximation is,

$$\frac{\rho}{\rho_\infty} \approx 1+\frac{3\lambda_\infty}{8t} \qquad \text{for } \frac{t}{\lambda_\infty} > 0.1 \qquad (3.3)$$

and the thin film approximation is

$$\frac{\rho}{\rho_\infty} \approx \frac{4\lambda_\infty}{3t\left[\ln\left(\frac{\lambda_\infty}{t}\right)+0.4228\right]} \quad \text{for } \frac{t}{\lambda_\infty} < 0.1 \qquad (3.4)$$

where t is the film thickness, λ_∞ and ρ_∞ are the mean free path and resistivity of a theoretically infinite thickness, respectively. The mean free path of Pt at 0°C and 100°C is taken to be 11 nm and 7.9 nm, respectively [3.5].

For increasing temperatures, the trend of the mean free path is to decrease which reduces the effect, so considering the mean free path value at 0°C with at Pt film thickness of 200 nm, gives

$$\frac{t}{\lambda_\infty} \approx 18$$

This can be considered as a thick film approximation. Therefore,

$$\frac{\rho}{\rho_\infty} = 1+\frac{3\times11\times10^{-9}}{8\times200\times10^{-9}} \approx 1.02 \qquad (3.5)$$

which corresponds to a resistivity contribution by thin film effects in the order of 2 %. It must be noted that impurities will increase the actual resistivity above that of the pure material ρ_∞. This theory considered here does not take into account grain boundary effects in the metal.

3.2.3.3 MHP Heating

The electrical power applied to the microheater element is dissipated thermally through the structure according to Joule heating. Hence, the temperature of the active area is dependent upon the electrical power required to compensate for the heat lost through the structure. There are three main mechanisms by which heat is lost through the membrane; conduction through the membrane P_m, conduction and convection to the surrounding air P_a, and finally radiation loss P_r. The total heat loss through the structure P_T, can be expressed by,

$$P_T = P_m + P_a + P_r \tag{3.6}$$

To reduce the trial and error method for designing the MHP geometry, models have been generated to describe the power consumption of a MHP in terms of its geometry and the operating temperature required, as reviewed in Chapter 6. A model developed by Dibbern [3.6] was applied during the sensor design to give an indication of the MHP power requirements.

Using Dibbern's model the total thermal power loss, as described by equation 3.6, is expressed by

$$P_T = P_m + (0.33\Delta T + 10)A \tag{3.7}$$

The contributions by P_a and P_r have been assumed directly proportional to the heater area A (expressed in mm^2). The individual contribution by convection was evaluated by

$$P_a \approx 0.33\Delta T \times A \tag{3.8}$$

where P_a is expressed in mW, and ΔT is the temperature difference between the heater area and the ambient. The radiation losses are small and assumed by Dibbern's model to be

$$P_r \approx 10 \times A \tag{3.9}$$

where P_r is also expressed in mW.

The contribution of conduction has been evaluated according to,

$$P_m \approx \frac{2\pi\kappa m\Delta T}{\ln\left(\frac{u}{a}\right)} \tag{3.10}$$

where m is the thickness of the membrane, κ is the membrane thermal conductivity, ΔT is the temperature difference between the active area and the silicon substrate, u the distance across the membrane and a is the distance across the active area. This relationship corresponds to a circular membrane, but losses in a square membrane are only a few percent higher [3.6].

Even though Dibbern's model has made many assumptions, equation 3.7 to 3.10 provides a means of estimating the electrical power required to obtain a predetermined active area operating temperature. This information improves judgement on the heater element resistance and layout geometry.

3.2.3.4 Pt Heater Layout Design for SRL108/CP and MOS, SRL125/MOS and SRL125/dual SADs

The same Pt heater layout design is used for each of the SRL108/CP, SRL125/MOS and SRL125/dual SADs, because the active areas and the operating temperature range (RT to 600°C) are approximately the same. The SRL108/CP SADs were fabricated in the first batch, where the initial layout was slightly different from the other two designs, as shown in Appendix A.

The layout design, as shown in Figure 3.11, consists of three heater elements, which are located as to align with the sensor element active areas. The 0.37 × 1.30 mm^2 heater area is slightly larger than the sensor element active area to reduce the effect of thermal gradients at the edge of the sensing part of the active film.

Without knowing the thermal properties of the multi-layer membrane, an effective 10 μm thick Si_3N_4 membrane was assumed, with a thermal conductivity of 2.5 W/m.K, and u/a was set to 3. Using equations 3.7 to 3.10, an operating temperature of 550°C will theoretically equilibriate with a thermal power loss of approximately 163 mW. The d.c. electrical power across the heater element can be expressed as,

$$P_E = \frac{V^2}{R_H} \tag{3.11}$$

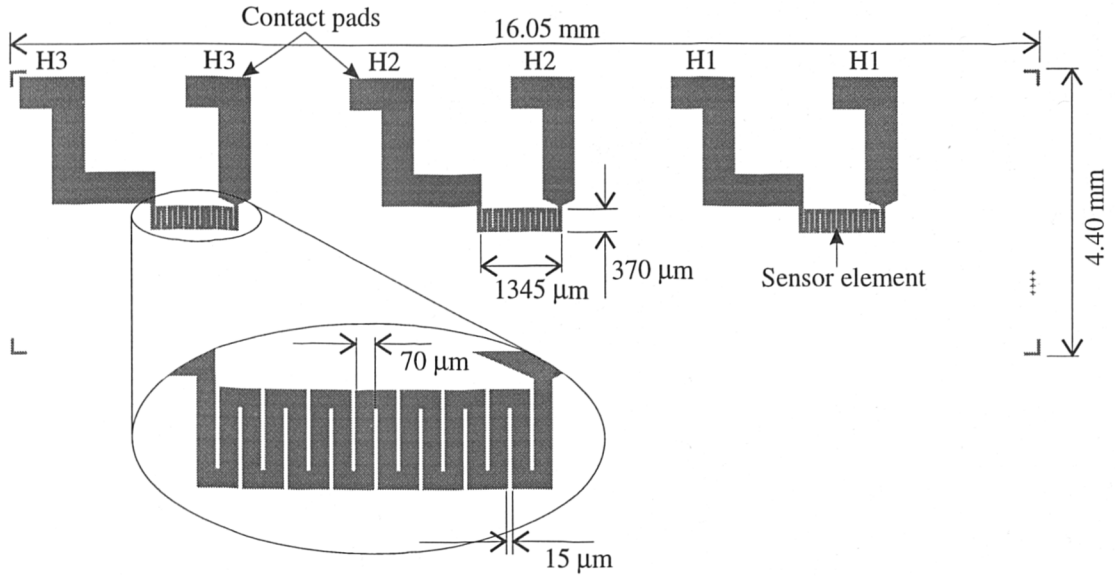

Figure 3.11 Pt heater layout design for SRL125/MOS and the SRL125/dual SADs. A modified layout with the same heater element is used for the SRL108/CP SAD.

where P_E is the d.c. electrical power supplied to compensate for the thermal power losses, V is the d.c. voltage supply and R_H is the heater element resistance. An electrical power supply of 170 mW was assumed to compensate for the thermal power loss, and a standard 5 volt power supply. Thus, according to equation 3.11, a heater element with a resistance of ~ 147 Ω is required. The resistance of the connecting tracks to the contact pad areas has been minimised by maximising track width and so have been assumed to have a negligible resistance. Using equation 3.1 a Pt resistance of 147 Ω at 550°C reduces to a resistance of 49 Ω at RT. Using equation 3.2, with a sheet resistance of 0.55 Ω, the meandering structures length to width ratio should be approximately 90.

Another requirement of the heater element design is that the surface coverage of the meandering structure is maximised to improve the temperature uniformity over the active area. A suitable layout was defined with a 70 µm wide track turning 15 times, with a 15 µm gap between parallel strips, as shown in the insert of Figure 3.11.

3.2.3.5 Pt Layout Design for SRL125/XPc SAD

The Pt layout for the SRL125/XPc SAD, also has three individual microheater elements, as shown in Appendix A. The geometry of each heater element is shown in Figure 3.12.

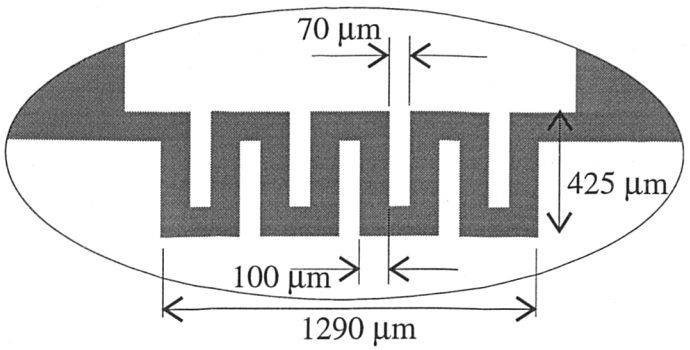

Figure 3.12 Pt heater element design for SRL125/XPc SAD.

This geometry was calculated using the same method as the previous design. A relatively large heater area of 0.425 × 1.290 mm^2 is required. At an operating temperature of 300°C the theoretical thermal power loss is 94 mW. Assuming a 2 volt supply produces the electrical power to compensate for this thermal loss, the resultant heater element resistance is approximately 43 Ω. This resistance decreases to 20.8 Ω at RT. To produce this resistance with the sheet resistance of 0.55 Ω requires a heater element length to width ratio of 37.8. With the geometry shown in Figure 3.12 a ratio of 38.7 is achieved.

3.2.3.6 Pt Layout Design for SRL125/CP SAD

The Pt layout for the SRL125/CP SAD is shown in Figure 3.13. The heater layout is determined by the electrode design layout, as shown in Figure 3.7. The limitation of available contact pads, requires that the three heaters have a common connection. Also, as adjacent active areas are spread too far for it to be practical to have a meandering heater structure under both active areas, a low resistance track connects two meandering structures. Each heater is equivalent to two heater elements in series.

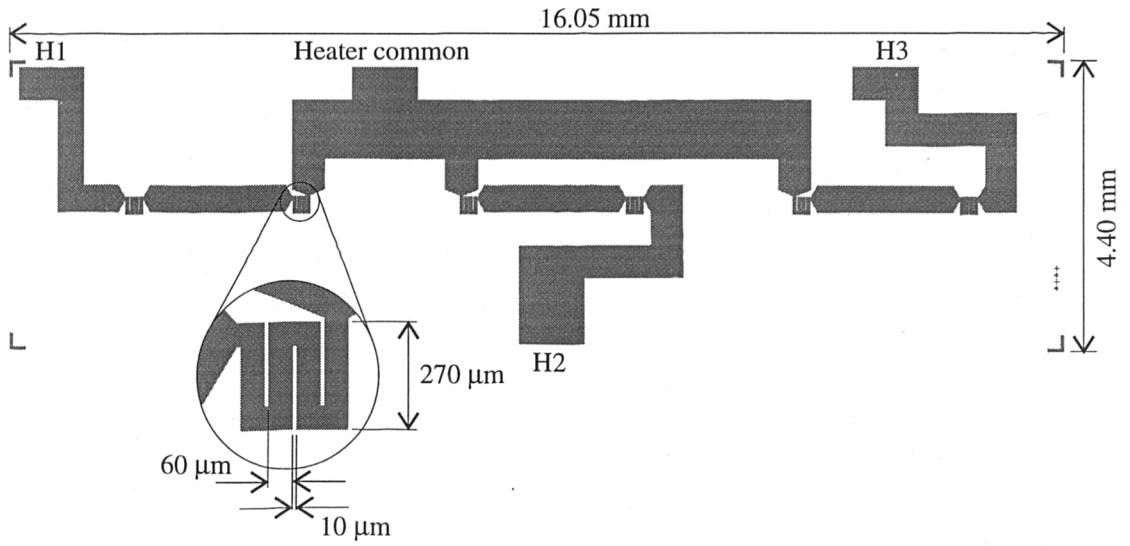

Figure 3.13 Pt layout design defining the heater elements for the SRL125/CP SAD.

Again the heater element geometry was determined by estimating the electrical power required for thermal equilibrium at the required operating temperature. The maximum operating temperature is assumed to be 125°C, as this device is principally for characterising CPs. The heater element area is 0.27×0.27 mm^2. Using equations 3.7 to 3.10 the theoretical thermal power loss of one element is 17.4 mW at 125°C. An electrical power supply of 40 mW is assumed to compensate for two heater elements and the connections. With a 1 volt heater excitation signal the resistance for two elements is approximately 25 Ω. This resistance decreases to approximately 9 Ω at RT. The length to width ratio for the meandering heater structure was determined using equation 3.3 to be approximately 16.5. Using the geometry shown in the insert of Figure 3.13, an aspect ratio of 18.5 is achieved.

3.2.4 Layout Design for Silicon Nitride

Each of the SADs employ a low-residual stress SiN_x film to electrically insulate the Pt heater and sensor electrodes. To allow electrical contact to the Pt heaters requires that windows are opened up in the SiN_x to expose the underlying Pt contact pads. The SiN_x window layout for all the designs correspond to alignment with the Pt contact pads as shown in Appendix A.

3.2.5 Layout Design for KOH Back-Etch

Alkaline chemicals such as potassium hydroxide (KOH) can be used to anisotropically etch single crystal silicon (SCS). The etch-rate is dependent upon the crystallographic orientation within the bulk silicon, so the final shape of the etched membrane structure is nearly completely composed of crystal planes that have a low etch rate. This phenomenon of anisotropic etching for crystalline silicon [3.7] has been well understood for a long time. Increasing attention has been paid to this technology, after recognising its unique capabilities for micromachining three-dimensional structures [3.8]. The strong dependence of the etch-rate on preferred crystal directions and on dopant concentration allows silicon structures to be fabricated in a well controlled and reproducible manner. The resultant shape from a mask layout has even been simulated to a relatively high degree of accuracy using modelling tools [3.9]. KOH etching was used during SAD fabrication to form the membrane structure and V-grooves which were necessary to snap the wafer into discrete devices.

The etch-rate in the <100> direction of the SCS is at least one hundred times faster than in the <111> direction. The wafer used had a (100) plane surface with which the (111) planes intersect at 54.74°. Furthermore, the (111) planes are 90° to each other. If a mask image is formed on the wafer surface with the image edges parallel and/or perpendicular to the <110> directions, the etching will proceed in the <100> direction until the etch front reaches the (111) planes, forming structures as shown in Figure 3.14.

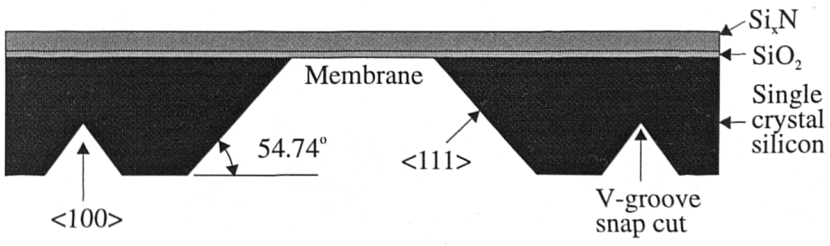

Figure 3.14 Cross-sectional schematic of the KOH anisotropic etched structures.

The etch depth to mask feature width ratio is 0.707. When the full mask design was produced (as shown in Appendix B) the individual design cells butt together to

form a snap cut image with a feature width of 200 μm, which produced a 141 μm deep V-groove around the device. This V-groove depth was adequate to snap the 280 μm thick silicon wafer. A design consideration was that the snap cut mask features must not join to form 'crosses', because this opens up other crystallographic planes which are not restricted by the (111) planes, so leading to etch holes penetrating through the wafer. The design layout for the KOH mask suitable for the SRL125/CP SAD is shown in Figure 3.15. The remaining KOH back etch design layouts are shown in Appendix A.

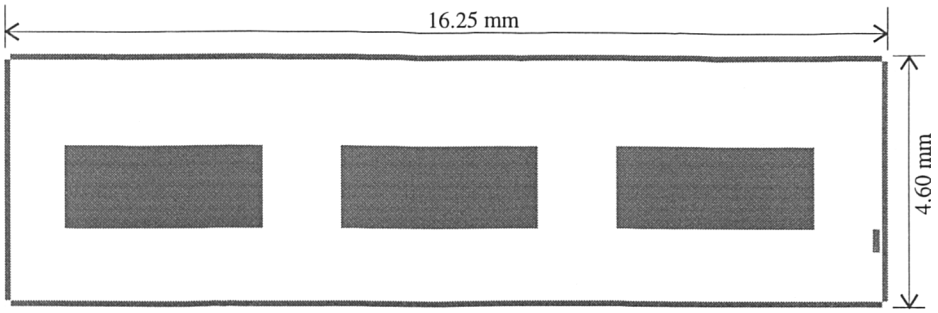

Figure 3.15 Design layout for the KOH mask used for the SRL108/CP SAD.

As mentioned earlier, the area of the membranes were designed to be approximately three times that of the heater area. However, to achieve a membrane with the correct area required the corresponding mask feature to be larger, to account for the 54.74° slope of the wafer sides. The SiO_2 thin layer on the wafer top-side acts as an etch stop as it only etches at a rate of ~ 0.28 nm/minute.

To obtain the required structures, it is essential that the edges of the mask features are parallel or perpendicular to the <110> direction. The silicon wafers are supplied with a primary flat edge with a (110) surface to indicate the orientation of these planes, to which the whole mask can be aligned, as shown at the bottom of the mask designs included in Appendix B.

3.3 Design of Discrete Sensor Devices

There has been a great deal of interest in electrochemically-deposited CPs derived from aromatic or heterocyclic compounds for gas sensing applications. The electrical and physical properties of these materials can be varied considerably by

using different growth conditions, electrolyte or doping ions. The gas sensing performance of certain polymeric chemoresistors can be improved by exploiting the control of these particular properties. However, this approach to improving sensor performance requires the characterisation of a large number of generic CPs. This has generated the requirement for a large number of basic discrete chemoresistive devices. The ease at which the properties of a CP chemoresistor can be modified by changing the deposition conditions, also makes this technology suitable for developing a multi-type CP or hybrid SAD. On-going collaborative research carried out at Warwick University and Southampton University, is characterising the properties of PPy and PAn chemoresistors. These polymers are electrochemically grown at Southampton University under well controlled conditions.

The thermal requirements of CP chemoresistors are not very demanding, because CPs are sensitive to VOCs at low temperatures (e.g. 20°C to 40°C). A MHP structure was therefore employed with a planar heater and chemoresistor arrangement as shown in Figure 3.16. The thermal performance of such a structure is not as good as that for the SADs, but the design still enables rapid temperature control. The device electrodes and integrated heater were fabricated from the same metallisation film to reduce fabrication costs.

The thermal performance and uniformity of this planar structure are increased by using a membrane structure composed of a silicon oxynitride ($Si_xO_yN_z$) and silicon multi-layer. The thermal properties of this structure are adequate for low temperature operation, as described in Chapter 6. Minimising the structures internal stress was again a vital material consideration for mechanical stability. Even though $Si_xO_yN_z$ has a suitably high thermal resistance and a low mechanical stress, the membrane structure was strengthened with a thin layer of silicon, see Figure 3.16.

To fabricate these structures required a set of three masks to photo-lithographically pattern the Au metallisation, the protective photoresist and a back-etch mask, as described in Chapter 4. Four discrete devices were designed as shown by the Au metallisation layouts in Figure 3.17.

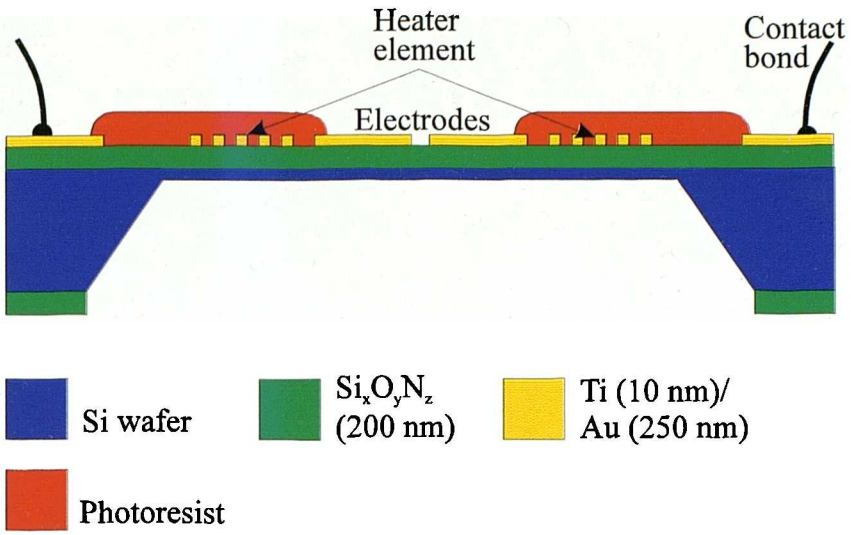

Figure 3.16 Schematic of discrete sensors structure.

It was essential that the designs were compatible with the electrochemical deposition techniques developed at Southampton University, as described in greater detail in Chapter 4. The devices are packaged onto 4-pin metal TO-8 or PCB headers and normally dipped into a standard three electrode cell, where the exposed Au is coated with CP. It is therefore necessary to cover up any metallisation that is to remain uncoated. For all four designs the majority of the metallisation is coated with a protective photoresist layer which is patterned to reveal the contact pads and the electrode region. When these devices are bonded onto the headers it is then only the contact pad areas and bonding wires which need potting. The SRL127/s10 and SRL127/s50 require all four pad areas and associated bonding to be potted before electrochemical deposition of the active film. However, the two longer designs (SRL127/l10 and SRL127/l50) can be dipped into solution held by crocodile clips (without using a PCB header), provided the heater pads are potted and the solution level does not reach the electrode contact pads. There are two designs for both the square and the long devices; one has a 10 μm inter-electrode gap and the other a 50 μm gap. The 50 μm inter-electrode gap is to produce chemoresistors with a higher resistance (> 100 Ω), because the PPy films studied have rather high conductivities. Chemoresistors with a low resistance increase concern about track resistance and connector resistance, as well as a need to pass large currents to measure the device resistance.

a) Discrete device (SRL127/s10) with a 10 µm inter-electrode gap, 4 mm × 4 mm.

b) Discrete device (SRL127/s50) with a 50 µm inter-electrode gap, 4 mm × 4 mm.

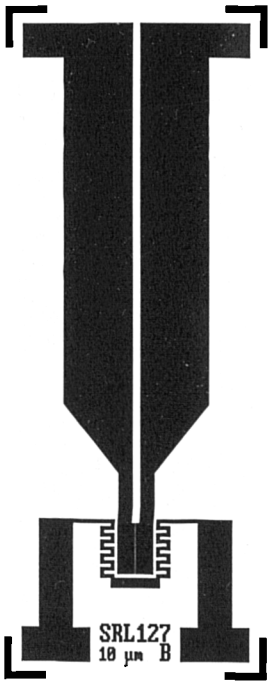

c) Discrete device (SRL127/l10) with a 10 µm inter-elctrode gap, 4 mm × 10 mm.

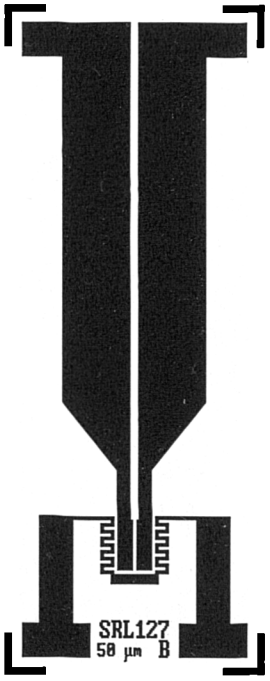

d) Discrete device (SRL127/l50) with a 50 µm inter-electrode gap, 4 mm × 10 mm.

Figure 3.17a) to d) Au layout for discrete designs.

The geometry of the integrated heater is split into two heating regions of meandering track on both sides of the electrodes. This arrangement is intended to increase the thermal uniformity along the inter-electrode gap. Using equation 3.2, where ρ for gold at 100°C is taken as 2.88×10^{-8} Ωm [3.10], the film thickness t is 250 nm, and the heater geometry (l/w) is approximately 100, results in a resistance of 11.5 Ω. Putting this value into equation 3.11, assuming a d.c. supply voltage of 3 volts gives an electrical power supply of 78 mW.

A contact pad pitch of 0.1" is used for compatibility with commercial Au-plated 0.1" pin through PCB headers.

As for the previous SAD designs, a KOH back etch process was used to fabricate the membrane structure and V-grooves. The wafer crystallographic orientation was again <100>, so the same design considerations were made as described in Section 3.2.5. The membrane area is designed to encompass the heater element, as shown in the design cells in Appendix A.

3.4 Design of Bridge Devices

The term 'intelligent sensor' refers to a system where a proportion of signal processing is combined with the sensor to improve the quality of the information presented to an instrument [3.11]. The information quality from the sensor can be improved by either removing or minimising undesirable sensor characteristics; like noise, non-linearity, frequency (time) response, cross-sensitivity and drift. Current collaborative research is being carried out with the Electronics Department at Southampton University is investigating using Application Specific Integrated Circuit (ASIC) technology with gas sensor arrays to produce an intelligent sensor system. The design approach has been to maintain signal quality at all stages in the measurement system, including the sensor design. This design consideration has led to a sensor design with structural compensation to temperature by employing a Wheatstone bridge arrangement [3.11, 3.12].

The intention is to investigate the properties of CPs in a resistance bridge. As these materials operate at RT and the base-line temperature dependence is removed in a bridge (at balance), an integrated heater was not incorporated in the initial design. This simplified the design to the layout of just the Au electrode metallisation and the protective photoresist, as shown in Figure 3.18.

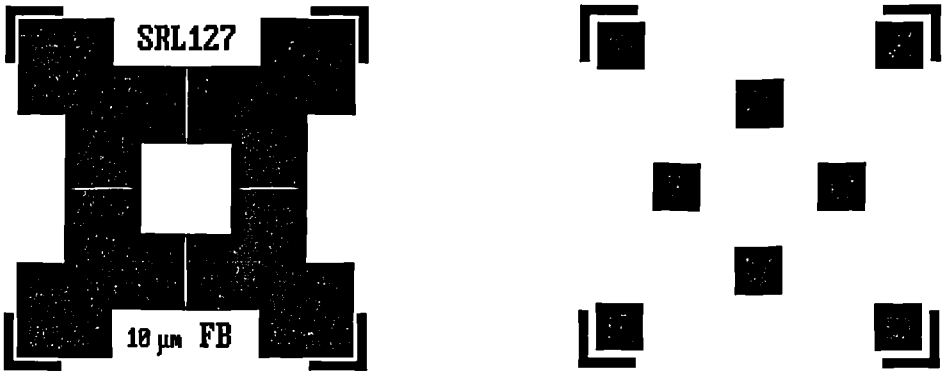

a) SRL127/b10 Au electrode layout of four 10 µm elements

b) Photoresist windows revealing contact pads and electrode areas used for both SRL127/b10 and SRL127/b50

Figure 3.18 Design cells for a) Au metallisation, and b) photoresist windows for the bridge device.

The performance of the bridge depends upon the values of the four resistors, which should be equal for maximum bridge sensitivity. This requires that there is as little geometric error as possible and that the track resistance are all equal and low. Each bridge element has an inter-electrode gap of 10 µm (or 50 µm). To reduce the variability in the resistance of the polymeric elements, the location and size of the active areas are again defined by the photoresist windows. There are also photoresist windows to define the gold contact pads, which have a 0.1" pitch for compatibility with commercial PCB pin connectors. Again to reduce physical variabilities in the design the CPs were electrochemically grown on all four electrode regions simultaneously using the dipping technique described in the following Chapter. This required packaging the devices onto long PCB headers and potting the contact pads and wire-bonds, as shown in Figure 3.19.

For useful operation of the bridge, an active region on opposite sides must be encapsulated in order to remove their chemical sensitivity (but retain their thermal sensitivity). The dummy arms were coated with Teflon™ or Nafion™ by spraying the material through a mechanical mask.

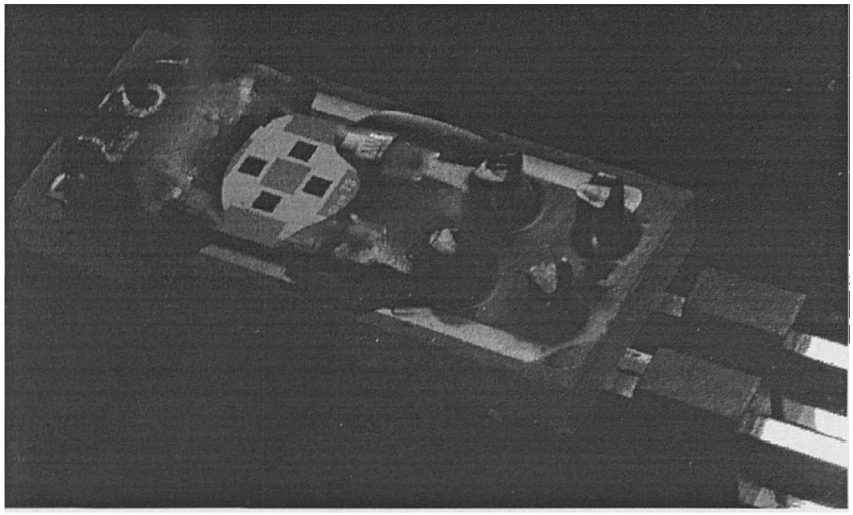

Figure 3.19 Packaged SRL127/b10 device with CPs grown over electrodes, to form the resistive arms (black areas).

3.5 Conclusions

This Chapter has described the design of three types of silicon chemoresistors, namely SADs (triplet and hex), discrete and bridge devices. The key target gases of interest (NO_2, CO and VOCs) have led to the investigation of SnO_2, XPc and CP films, which required the design of specialised chemoresistors. My design approach to the SADs has been discussed in detail because the gas-sensitivity of these devices have been fully characterised with results given in Chapter 8. For suitability in a battery-operated device, the SADs must have an ultra-low power consumption and this characteristic is investigated in Chapter 6.

Many of my design considerations resulted from obtaining compatibility with a standard fabrication procedure. An understanding of the fabrication techniques, which are fully described in the next Chapter, was a vital part in the gas sensor design.

3.6 References

3.1 B.Bott and T.A. Jones, A Highly Sensitive NO_2 Sensor Based on Conductivity Changes in Phthalocyanine Films, *Sensors and Actuators*, **4** (1984) 43-53.

3.2 T.A. Jones and B. Bott, Gas-Induced Electrical Conductivity Changes in Metal Phthalocyanines, *Sensors and Actuators*, **9** (1986) 27-37.

3.3 P.N. Bartlett, J.W. Gardner and R.G. Whitaker, Electrochemical Deposition of Conducting Polymers onto Electronic Substrates for Sensor Applications, *Sensors and Actuators A*, **21-23** (1990) 911-914.

3.4 R.W. Berry, P.M. Hall and M.T.Harris, In *Thin Film Technology,* D.Van Nostrand, New York, 1968.

3.5 L.I. Maissel and R. Glang, In *Handbook of Thin Film Technology,* McGraw-Hill, New York, 1970.

3.6 U. Dibbern, A Substrate for Thin-Film Gas Sensors in Microelectronic Technology, *Sensors and Actuators B,* **2** (1990) 63-70.

3.7 H. Seidel, L. Csepregi, A. Heuberger and H. Baumgärtel, Anisotropic Etching of Crystalline Silicon in Alkaline Solutions, *J. Electrochem. Soc.,* **137** (1990) 3612-3626.

3.8 K.E. Bean, Anisotropic Etching of Silicon, *IEEE Trans. Electron Devices,* **ED-25** (1978) 1185-1193.

3.9 R.A. Buser and N.F. de Rooij, ASEP: a CAD Program for Silicon Anisotropic Etching, *Sensors and Actuators A,* **28** (1991) 71-78.

3.10 A.M. James and M.P. Lord, *Macmillan's Chemical and Physical Data,* The Macmillan Press Ltd., London, 1992.

3.11 J.E. Brignell and N.M. White, *Intelligent Sensor Systems,* IOP Publishing, Bristol, 1994.

3.12 P. Ciureanu and S. Middelhoek, *Thin Film Resistive Sensors,* IOP Publishing, Bristol, 1992.

Chapter 4

4. Fabrication Details

4.1 Introduction

The objective of this Chapter is to describe the fabrication of the sensor designs outlined in the previous Chapter. Their structures require both conventional planar technology and bulk micromachining techniques to be employed during wafer processing. Two wafer fabrication processes are described; one for the SADs and another for the discrete and bridge devices. The SRL125/dual design required an additional FIBM technique to define a sub-micron inter-electrode gap before deposition of the gas-sensitive material. Both the FIBM technique and the gas-sensitive material deposition are described in this Chapter. Finally, a fabrication procedure is then proposed for a hybrid SAD.

4.2 Silicon Wafer Processing

There are two stages involved with photolithographic processing; firstly, the design mask production and secondly, the image transfer from the mask to the wafer.

The artwork design for each mask was produced on the layout editor package, L-Edit™ (Tanner Tools Ltd) on a 486-PC at Warwick University. The output file format (GDSII) from this package is compatible with the mask production at the Central Microstructure Facility, Rutherford Appleton Laboratory, UK. At this facility, each mask file controls the movement of an electron beam process, which lithographically patterns a thin chrome layer on, for example, a 4" square antireflective glass plate. These masks are then used for contact photolithography during wafer fabrication.

There are several methods for transferring the mask image to the wafer [4.1]. The most common method uses a photoresist which is spin-coated onto the wafer over

the thin film to be patterned and selectively exposed to an Ultra-Violet (UV) light source through the mask. The photoresist contains radiation-sensitive groups which chemically respond to UV light, forming a latent mask image which is subsequently developed to pattern the relief image in the photoresist. The areas of photoresist remaining after development protect the underlying thin film, while the exposed film areas can be chemically etched through the openings in the photoresist. Removing the photoresist reveals the required thin film image geometry. There are variations to this procedure depending on the photoresist material used and the subsequent processes. Another method known as the lift-off technique is also used to pattern thin films. Applying this method requires the deposition and patterning of the photoresist prior to the thin film deposition. Providing there is no step coverage by the thin film, the exposed photoresist sidewall permits removal of the photoresist with acetone leaving the thin film pattern. Both these techniques have been employed during the silicon wafer processing of my designs. The SADs were fabricated by the Institute of Microtechnology, Neuchâtel University, Switzerland and the discrete and bridge devices were produced by the Central Research Laboratories (CRL) Ltd, UK. The XPc films were deposited at the HSE, whereas the SnO_2 was deposited at the Institute of Physical and Theoretical Chemistry, Tübingen University, Germany and the Institute of Physics and Technology of Materials, Bucharest, Romania. The CPs films were grown at the University of Southampton. Detailed information relating to some of the fabrication procedures is deemed proprietary and therefore restricted.

4.2.1 Array Device Wafer Processing

A five mask process is required for the fabrication of the SAD structure. Two batches of wafers were fabricated, each requiring a set of masks, as shown in Appendix B. The first batch fabricated the SRL108 SADs, while the second batch produced the SRL125 SADs. Each mask consists of an array of the appropriate cell designs, as described in Chapter 3. The fabrication procedure, which is shown in Figure 4.1, was the same for both batches.

The initial substrate was a 3", 280 μm thick, single-sided polished, <100> oriented, SCS wafer. Prior to processing, the wafers were given an identity mark with a diamond scribe and then subjected to a standard multi-stage cleaning process, which

removed any organic contaminants, adsorbed layers, and particulates. A standard cleaning process was used prior to each thin film deposition to ensure adequate adhesion.

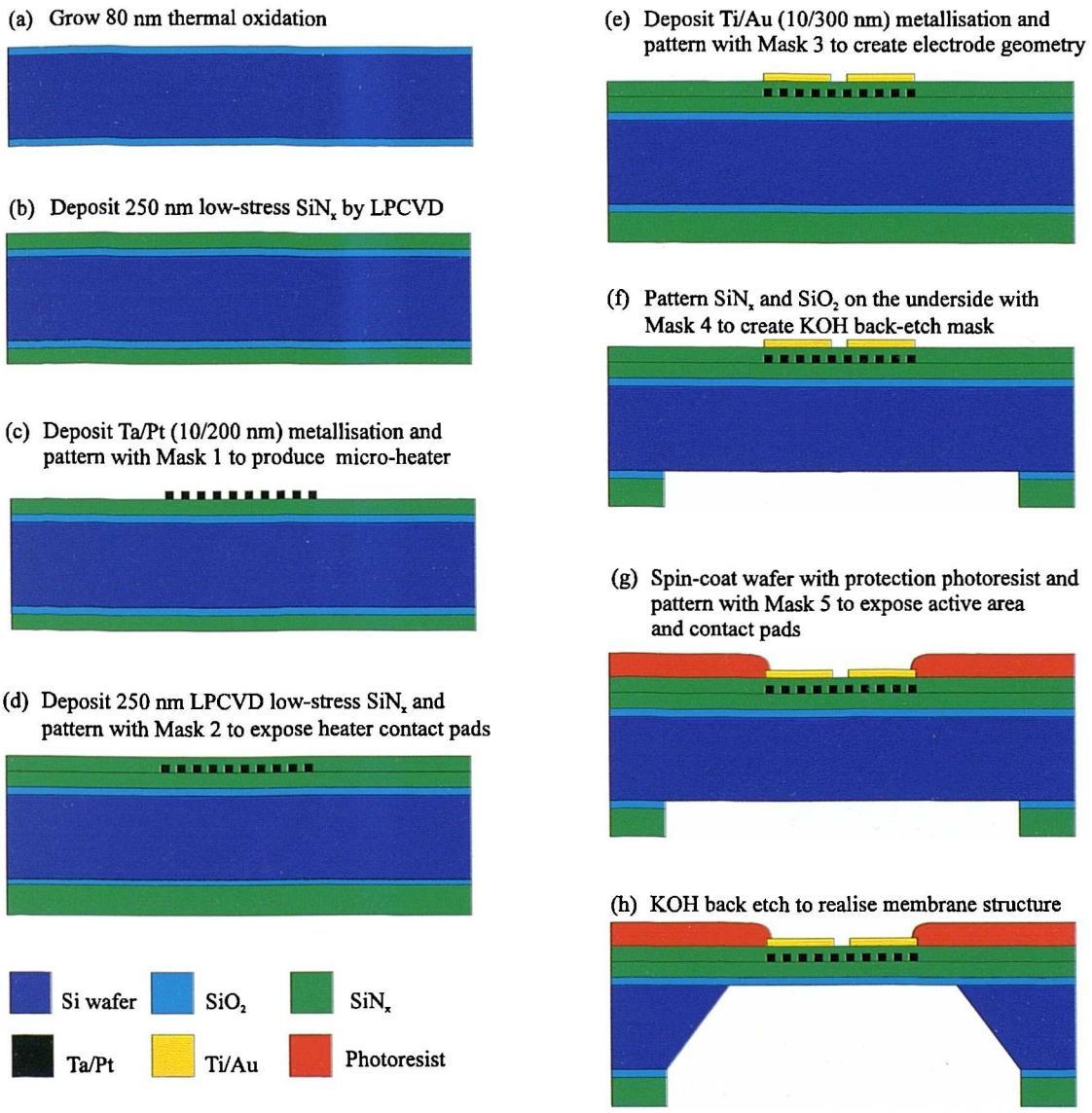

Figure 4.1 Schematic of the wafer processing steps required to fabricate both batches of SADs. These views only indicate the processing steps and do not relate to a specific cross-section and are not drawn in proportion.

Two factors which minimise thermal losses from the microheater, are the choice of membrane material and membrane geometry. Both these considerations have been discussed in Chapter 3, resulting in the design of an ultra-thin SiN_x membrane. However, there are physical limitations on the multi-layer membrane geometry, due to

thin film stress. To ensure a stable membrane during testing requires that both the residual stress and the induced thermal stresses are minimised. Also adequate adhesion between adjacent layers is required to prevent chemical attack on the thin film, which can result in peeling and cracking. These properties are mainly controlled by the thin film deposition conditions.

An 80 nm dry SiO_2 film was thermally grown at 1100°C. The intrinsic stress in thermally grown SiO_2 films has been shown to be negligible at 1100°C [4.2, 4.3], which is essential for mechanical stability of the membrane structure. 250 nm of low-stress SiN_x was then deposited by low-pressure chemical vapour deposition (LPCVD).

The microheaters were realised by patterning a Pt thin film with the first mask using a lift-off technique. The photoresist was first spin-coated onto the wafer and exposed to UV light through the aligned mask. Before the photoresist was developed, it was exposed to chlorobenzene to harden the photoresist surface. Hence, during developing, the photoresist was undercut slightly due to the surface modification. This profile ensures that no side coverage occurs during metallisation deposition, so that when the photoresist was removed it did not interfere with the metallisation which had bonded to the substrate. The photoresist layer acted as a sacrificial layer which was removed with acetone, revealing the mask image patterned into the metallisation.

To improve metal adhesion to the substrate, it is common to use a thin adhesion layer of a more reactive metal. Therefore, before deposition of the 200 nm of Pt a 10 nm tantalum (Ta) adhesion layer was deposited. Both films were deposited by sputtering.

A standard cleaning process prepared the substrate for a second 250 nm LPCVD low-stress SiN_x, which insulates electrically the microheater from the electrodes deposited in a later stage.

The second photolithographic mask process was then carried out to open up windows in the SiN_x. This required plasma etching of the SiN_x to reveal the Pt heater contact pads. The patterned photoresist layer used was then stripped off before another cleaning stage.

The next step involved the deposition of the Au thin film which was patterned with the third mask to define the electrodes. A lift-off technique was again used, so a

10 nm titanium (Ti) adhesion layer followed by 300 nm Au film was sputtered over the patterned photoresist. The photoresist was then removed with acetone to produce the sensor array electrode geometry.

To create the ultra-thin membrane structure required an anisotropic KOH back-etch through the SCS [4.4, 4.5]. Most photoresists are inappropriate for defining features any deeper than 20 μm in KOH etch conditions, so the SiN_x and SiO_2 on the wafer underside were patterned with the fourth mask using plasma etching to form a suitable KOH mask.

Before KOH anisotropic etching, the top-side protection resist had to be processed. The wafers were held onto a spinner with a vacuum and a layer of Shipley Microposit 1813[†] was spun coated over the wafers. This protecting layer was then photolithographically patterned with the last mask to expose the active areas and the contact pads. If this step was attempted after membrane fabrication the spinner vacuum could have fractured the membranes. The photoresist was hardbaked for 1 hour at 180°C after developing, which made it more resistant to chemical attack. This is essential to ensure that the photoresist does not affect the electrochemistry during the CP deposition technique.

The final processing stage was a KOH anisotropic etch, which realises the membrane structure using the top-side thermal SiO_2 as an etch stop. To prevent the wafer top-side being exposed to the etchants, the wafer was mounted in a suitable holder during etching. This stage also produced the V-grooves which allowed the wafers to be easily snapped up to obtain the individual devices.

4.2.2 Discrete and Bridge Device Processing

The discrete and bridge sensor designs were combined onto the same mask set, since the fabrication procedure was identical for both designs. The fabrication procedure, as shown in Figure 4.2, requires three photolithographic masks, as shown in Appendix B.

The initial substrate was a 3", 350 μm thick, double-sided polished, <100> oriented SCS. Some of these designs incorporate a membrane structure, which must

[†] Shipley Microposit 1816 is now used.

be mechanically stable (i.e. low stress) and have the appropriate thermal properties to minimise thermal power loss. The membrane structure realised during fabrication is composed of a thin silicon oxynitride ($Si_xO_yN_z$, where x, y, z refer to an unspecified material stoichiometry) layer on a thin layer of SCS. The physical properties of $Si_xO_yN_z$ [4.6] are suitable for the application, but a thin SCS layer was used to strengthen the structure. As before, to improve adhesion and reduce stress a standard cleaning procedure was carried out between processing steps.

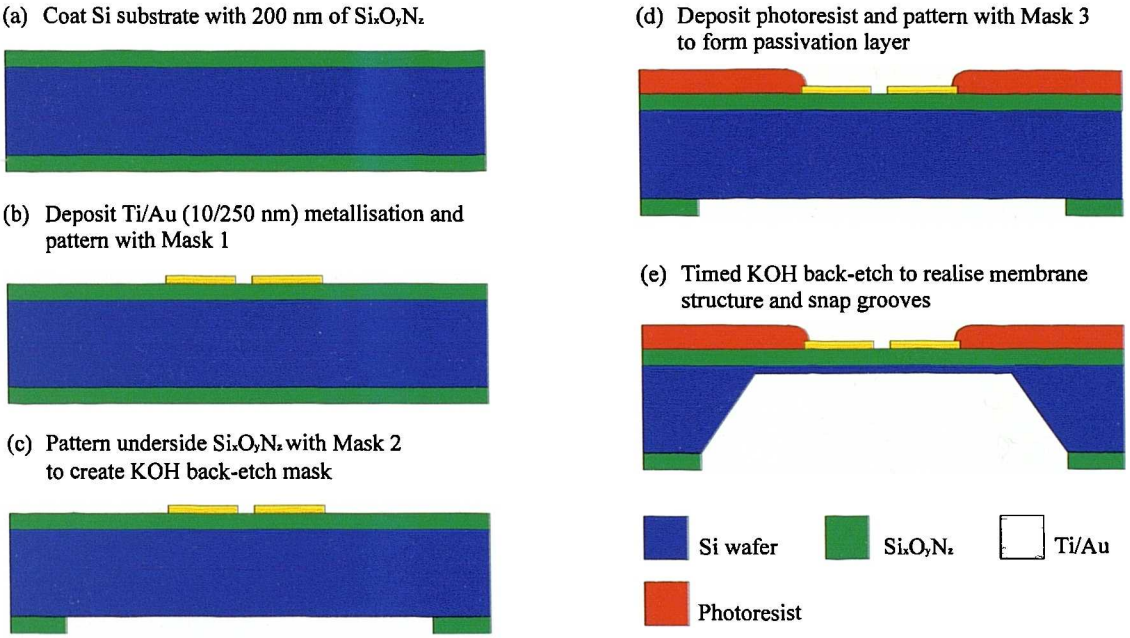

Figure 4.2 Schematic of the wafer processing steps required for the SRL127 batch to fabricate the discrete and bridge devices. These views only indicate processing steps and do not relate to a specific cross-section and are not drawn in proportion.

The $Si_xO_yN_z$ was deposited by LPCVD using controlled flow-rates of dichlorosilane, NH_3 and N_2O.

A 250 nm layer of Au was sputtered onto the substrate with a 10 nm Ti adhesion layer, and patterned photolithographically with the first mask plate. The appropriate wet etchants used during this stage included a Au etch of one part "Gold Etch, Isoclean" (Micro Image Technology Ltd) diluted with two parts deionised water, and a Ti etchant composed of 2 parts ammonium fluoride, 8 parts nitric acid (70 %) and 90 parts deionised water. Both etching procedures were carried out at RT.

A KOH anisotropic silicon etch was again used to produce the membrane and snap grooves. For this procedure the back-side $Si_xO_yN_z$ layer was patterned with the second mask using plasma etching to form a KOH resistant mask. However, prior to the KOH process step, the wafer top-side was protected with a Shipley Microposit 1813 photoresist coating, which was spun on and patterned with the third mask. The photoresist was hardbaked for 1 hour at 180°C after developing.

For the final KOH processing step the wafer was mounted in a jig which protected the wafer top-side from KOH attack. The etching speed of different crystallograhic planes in the SCS is accurately documented [4.5]. This information permitted a timed etch to leave the required thickness of SCS to increase the membrane strength. The thickness of SCS remaining after the etch varies from approximately 1 to 20 μm across the wafer, due to uneven solution agitation across the wafer and a ±5 μm wafer thickness tolerance.

4.3 Focused Ion Beam Milling

For optimum theoretical performance of an intelligent dual sensor device (SRL125/dual), the narrow inter-electrode gap must be much smaller than the gas-sensitive material thickness, as described in greater detail in Chapter 5. Ideally, the electrode gap feature size should be sub-micron. However, conventional photolithographic techniques become impractical when sub-micron resolution is required. The typical resolution of the photolithographic techniques used to fabricate my designs were ~ 1-2 μm. This processing technique is therefore inadequate for defining dimensions of nanometre order. Overcoming this technological limitation has led to a rapid growth in energy beam techniques for nanotechnology [4.7]. A FIBM technique was used [4.8] to cut directly through the Au thin film with a sub-micron resolution. This micromachining technology uses an incident beam of ions to remove material from the substrate surface by sputtering.

This processing was carried out at the Rutherford Appleton Laboratory by Mr John Watson. The FIBM system was composed of three stages: an ion source, ion focusing and beam displacement, as shown in Figure 4.3.

To obtain a very small ion beam spot on the sample surface for nanomachining requires an extremely localised ion source. A liquid metal field ionization source was

used, where a reservoir of liquid gallium (Ga) metal is maintained at the end of a tungsten needle, with a tip radius ~ 2 μm. The tip of the needle faces an extraction aperture, which is like a round washer-like electrode. By applying a voltage between the tip and the aperture produces an electric field that exerts a stress on the liquid Ga, forming a sharp cone. Ions are emitted from the cone tip, which has a radius of ~ 10 nm.

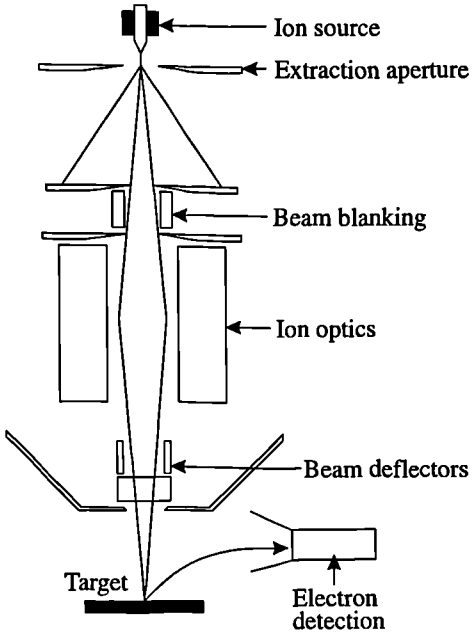

Figure 4.3 Schematic of the FIBM system hardware, which is operated under vacuum.

The column which focuses the ions from the source onto the sample is very much analogous to a series of optical lenses for focusing light. Ion lenses are for the most part electrostatic and consist of very precisely machined washer-like electrodes at some high potentials. The beam passes through the centre of these concentric electrodes, allowing a minimum of ~ 50 nm diameter ion beam to be focused on the substrate surface.

For FIBM writing over selected areas requires a means of turning the ion beam off (beam blanking). This is done by having a pair of electrodes on opposite sides of the beam and applying a voltage, so that the beam is deflected sideways and so is not capable of passing through the aperture. The beam can also be moved around in the Cartesian plane by beam deflectors at the bottom of the column.

Imaging the sample is achieved by detecting secondary electrons during a raster scan of the sample. Two or three frames are taken and processed to form the display. The area to be milled is selected on the display monitor by dragging a rectangular frame over the image. The pixel co-ordinates from this area allow a combined vector/raster scan approach. A blanked-off beam is first deflected to a corner coordinate, where it is turned on for a specific dwell time. It is then blanked-off and shifted to the adjacent coordinate, where it is again pulsed on. This is continued by raster scan until the entire area selected has been "filled in". An adhanced etch rate at the edges, due to glancing incident ions, results in straightening of any curves along the cut edge. The shape of a milled feature is also dependent on whether it is obtained with a single scan or repeated scans. To obtain a more regular feature a repetitive scanning method was used, which reduces such effects like material redeposition.

It was apparent that the feature size of the inter-electrode gap was not limited by the focused ion beam diameter inherent at the sample surface but by the pixel resolution on the display monitor. In order to get a very narrow gap, required the rectangular pattern was drawn out to have a very high aspect ratio. However, when the whole Au area to be cut was in view, and a rectangular pattern was superimposed on the image, the pixel limited narrow edge of the rectangle did not produce a sub-micron feature. To reduce this dimension required that the sample image was magnified to an extent where the whole length to be milled was not shown. Multiple cuts were therefore required to traverse the Au track, as shown in Figure 4.4.

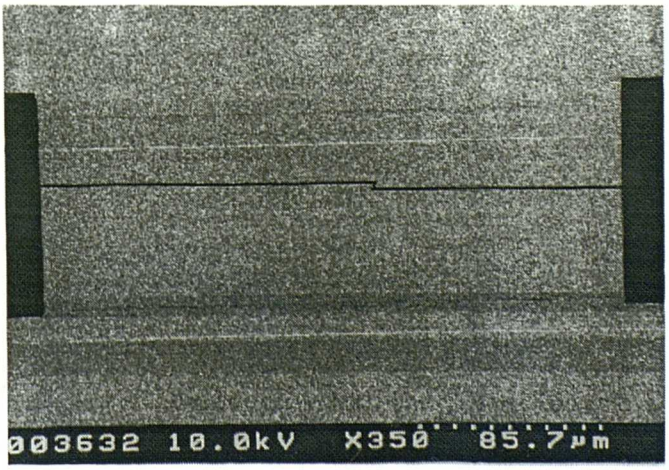

Figure 4.4 FIBM 1 µm inter-electrode gap, which traverses the Au in two main cuts joined with a smaller cut.

To overcome the problem of cut misalignment, the two cuts were offset and overlapped which allowed them to be joined with a third cut as shown in Figure 4.5.

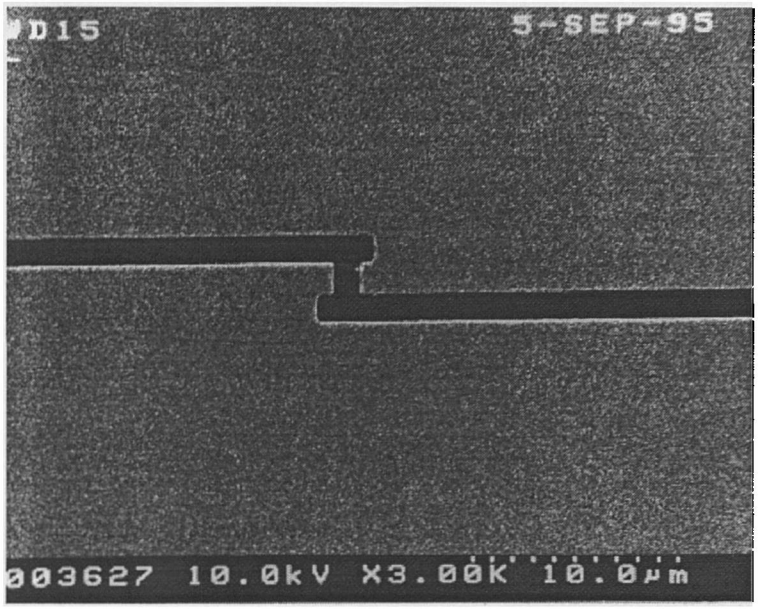

Figure 4.5 Two milled cuts joined by a smaller perpendicular cut to ensure that misalignment is eradicated.

Inter-electrode gaps as small as 500 nm have been milled, as shown in Figure 4.6. Unfortunately, it became impractical to go much below this, because a 100 nm inter-electrode gap required at least 20 cuts plus the joining cuts.

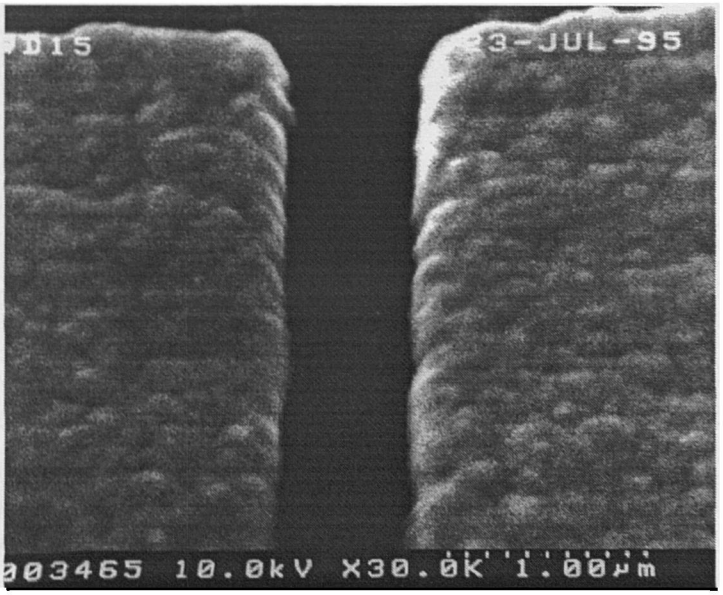

Figure 4.6 500 nm focused ion beam milled inter-electrode gap.

4.4 Deposition of Gas-Sensitive Films

4.4.1 Metal-Substituted Phthalocyanine Deposition

It is well understood that the characteristic properties of XPc films are strongly influenced by the nature of the central metal species [4.9], purity, and also by the film morphology [4.10]. Three XPcs have been investigated; PbPc, MgPc and CuPc. The morphology of these materials is dependent on the deposition conditions, which must be carefully controlled to improve reproducibility. The different techniques that have been used to deposit XPc films, are Langmuir-Blodgett [4.11], thick-film screen-printing [4.12] and evaporation. Films were deposited by evaporation at the HSE, Sheffield, since this technique allowed batch deposition of different XPcs onto the SADs with good control over deposition conditions. Langmuir-Blodgett techniques can deposit monolayers of XPc material, which allows precise control over the deposition rate, but the process was too time consuming for this study. The screen-printing technique allows a thick film (~ 25 μm) of XPc to be deposited. However, screen-printing was not considered due to the possibility of membrane fracture during deposition.

Before evaporation the commercial-grade XPcs were purified by entrainer sublimation [4.13]. The apparatus consisted of a glass tube mounted inside a silica tube, heated at one end by a wound Nichrome element. The impure XPc powder sublimed in the heated zone that was held at 520°C and condensed further down the glass tube due to the temperature gradient and a low flow-rate of N_2. In this way, high purity XPc crystals were formed which were then ready for deposition.

Evaporation of these cyrstals were carried out in an Edwards E306A evaporator at a pressure of 10^{-6} mbar, at a deposition rate of 0.1 nm/s. During deposition of the XPc, the SADs were held in a brass holder, which also acted as a mechanical mask as there were aperatures located over the electrode regions. All three XPc materials were deposited on the same SAD, as shown in Figure 4.7, as a sliding shutter on the brass holder could select which set of holes were open.

The thickness of the materials were measured during and after deposition, with an Edwards FTM5 thickness monitor and a Form Talysurf (Taylor-Hobson), respectively. The thickness results are summarised in Table 4.1.

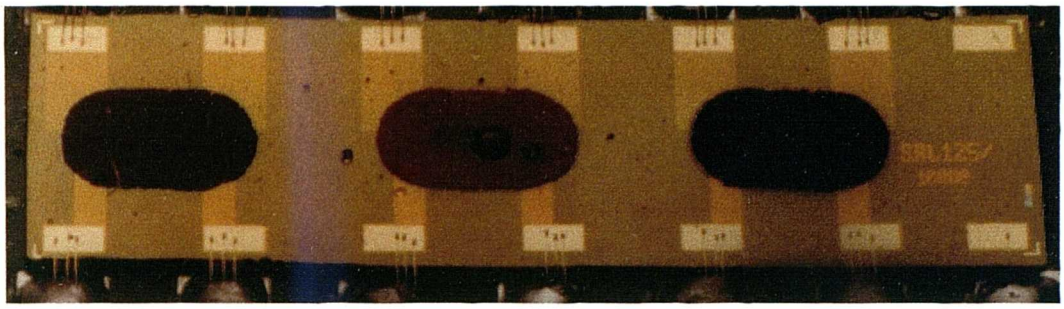

Figure 4.7 SRL125/XPc SAD with PbPc (right), MgPc (centre), and CuPc (left) evaporated over the electrode structure.

Table 4.1 XPc thickness measurements.

	1st. batch thickness (nm)		2nd. batch thickness (nm)	
	Edwards FTM5	Form Talysurf	Edwards FTM5	Form Talysurf
PbPc	430	-	463	2278
MgPc	126	685	298	1734
CuPc	155	1136	410	2261

The FTM5 thin film deposition monitor measures film thickness and deposition rate by the well established crystal microbalance technique. These parameters were calculated using a film density of 7.2 g/cm^3 and an acoustic impedance of 28.9×10^5 $g/cm^2.s$ (data supplied by the HSE). The suggested causes of the scaling error (5.8 ± 2.0) between the two measurements may be due to either aging of the quartz crystal sensor in the Edwards FTM5 thickness monitor or the material properties used were inaccurate. The results obtained by the Edwards FTM5 thickness monitor are dismissed, because the thickness accuracy of the Form Talysurf is reliable to $\pm$ 10 %.

Studies have shown that the electrical characteristics of XPc chemoresistors are greatly dependent on film morphology. As-deposited XPc films prepared by vacuum sublimation were found to consist of fine particles separated by amorphous regions.

By annealing these materials at elevated temperatures it is found that the morphology changes by induced crystallisation of amorphous regions [4.10, 4.14]. This thermal treatment has been found to optimise some of the sensor characteristics, like response time and repeatability. To investigate these effects some of the XPc coated SADs were annealed on-chip at 200°C for 60 minutes.

4.4.2 Electrochemical Deposition of Conducting Polymers

A large number of CP materials have been investigated for use in chemoresistive gas-sensing applications. Resent research carried out at Warwick University has centred around CPs based on PPy and PAn for vapour [4.15, 4.16] and odour [4.17] monitoring applications. The CP chemoresistors described in Chapter 3 had to be suitable for the electrochemical deposition techniques used by Southampton University.

To electrochemically produce a CP the monomer is dissolved in an appropriate solvent contained in an electrochemical cell. A large excess of a species that dissociates to form ions, called a background electrolyte, is added to the solution to ensure that the solution is sufficiently ionically conducting, and to supply a counter-ion which is used to dope the growing polymer. The chemical kinetics within the cell that lead to the CP growth is determined by the voltage applied to the electrochemical cell apparatus.

The electrochemistry was controlled in a cell containing the solution and a standard three-electrode arrangement, as shown in Figure 4.8.

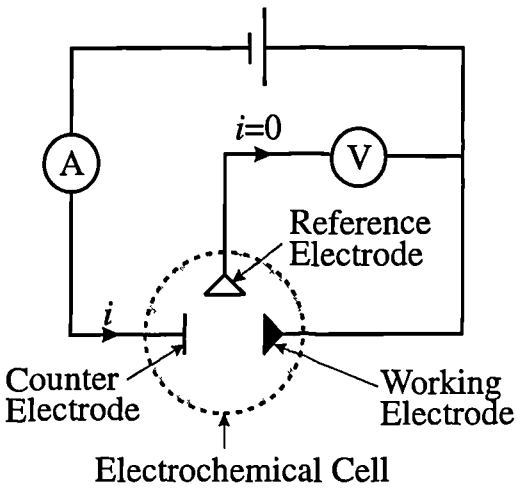

Figure 4.8 Schematic arrangement for a three-electrode measurement.

The working electrodes are the Au regions on the SAD which are to be coated with CP. The reference electrode was a saturated calomel electrode (SCE), while the counter electrode consisted of a Pt gauze. The device is submersed in the electrochemical cell on a suitable PCB header, which allows electrical contact to the working electrode. All metallisation other than the working electrode was encapsulated from the solution. Different headers have been designed for the different CP designs, as explained in more detail later in this Section. The potential between the working electrode and the reference electrode is controlled, while the current flowing from the working electrode to the counter electrode is measured. The reference electrode therefore provides a fixed reference potential from which to measure the potential applied across the working electrode/solution interface. The voltage was measured with a potentiostat.

It is found that most of the applied potential is dropped at the electrode/solution interface, creating a very high field at the electrode surface ($\sim 4 \times 10^8$ V/m) [4.18]. These high fields can control the addition or removal of electrons to molecules in the solution near the electrode surface. It is this oxidation or reduction of the monomer molecule in solution by which electropolymerisation can proceed by a complex mechanism to grow the CP on the working electrode. For example, Gardner *et al.* [4.18] describes the general mechanisms involved in electrochemical growth of PPy. The structure and gas sensing properties of electrochemically synthesized films depend upon the monomer, the choice of counter-ion used to dope the polymer, the solvent used and the conditions during deposition. Electrochemistry allows a high degree of control over all these growth conditions.

Two different methods have been employed to deposit CPs on my sensor designs; namely cyclic voltammetry and potentiostatically. Cyclic voltammetry consists of ramping the potential of the working electrode in a cyclic manner between preset limits, and recording the corresponding current as a function of the applied potential with respect to the reference electrode. The I/V characteristics are an indication of the surface reactions leading to CP growth. Using this method, the amount of CP can be controlled by the number of deposition cycles employed.

The alternative potentiostatic method involves stepping the potential of the working electrode (e.g. from 0 to 0.85 V for PPy). The thickness of the film can be estimated from the total charge passed [4.19].

The growth across an inter-electrode gap on the chemoresistor designs is achieved by applying the same potential to both electrodes. Hence, the CP films grow at equal rates on each electrode and cross the inter-electrode gap from both sides.

In order to ensure consistant, uniform polymer growth on the devices it is essential that the Au electrodes are cleaned electrochemically prior to polymer deposition. This process involves cycling the electrode potential three times between -0.3 V to 1.8 V at a sweep rate of 100 mV/s in 2 mol/dm^3 sulphuric acid. A voltammogram obtained for a clean device under these circumstances is shown in Figure 4.9.

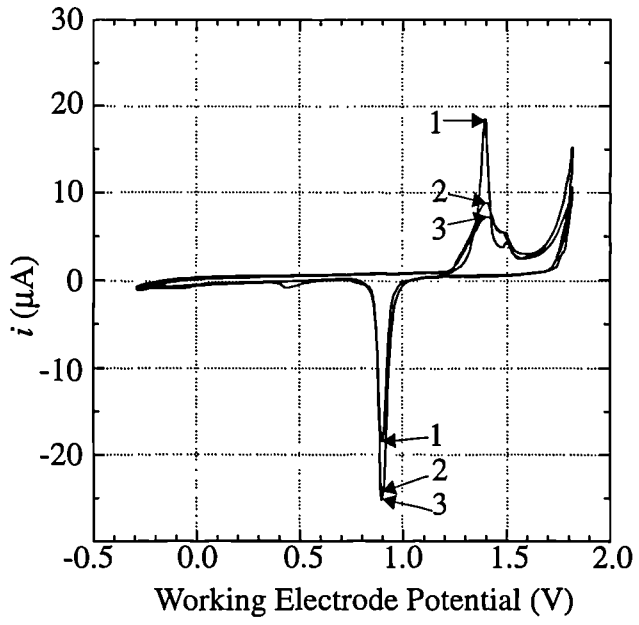

Figure 4.9 Typical cyclic voltammogram for a clean, uncontaminated Au electrode surface, showing the first three scans.

The anodic current peak at the positive potential of ~ 1.2 V with respect to the SCE, corresponds to the formation of a oxide monolayer on the Au surface. The peak at 0.9 V on the cathodic scan corresponds to the removal of the oxide layer. The formation and removal of this oxide layer has the effect of cleaning the Au electrodes.

The area under the oxide stripping peak (+ 0.9 V) on the cathodic sweep is an indication of the electrode area. The sensor substrates were then rinsed with reagent grade water and immersed in water until required for use.

As mentioned previously, during CP deposition the sensor devices were mounted on a PCB, which allowed the devices to be dipped into the electrochemical cell while having non-shorting electrical contact with the electrodes. Any metal exposed to the mixture is coated with CP, so all metal areas which are not to be covered with polymer must be potted.

The discrete and bridge devices were mounted on packages specifically designed at Warwick University to be a suitable PCB for the electrochemical dipping technique. Any device contact pads wire bonded to the package are permanently covered with electrochemically inactive glue. A square discrete device packaged on a PCB header is shown in Figure 4.10.

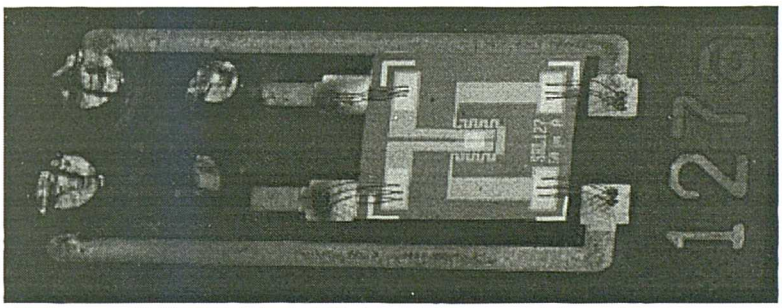

Figure 4.10 Square discrete device packaged on header. The Au pads and wire bonds still need to be covered with epoxy sealant, before CP growth.

The SRL108/CP design requires rebonding and packaging after polymerisation if the dipping technique of CP deposition is used. Therefore, a temporary wax seal was used to cover up the Au pads during processing, which was removed by melting. The same wax material was used to hold the device to the PCB during the deposition technique.

A number of different CPs based on PPy and PAn have been deposited with a variety of different counter-ions. The majority of CPs grown on my devices have been formed by potentiostatically stepping the voltage. A typical current time growth transient for the deposition of PPy, with different alkylsulfonate counter-ions in aqueous solution, is shown in Figure 4.11. The potential of the pair of Au electrodes

was stepped from 0 to +0.85 V and held constant for two minutes. At the end of this time the potential was stepped back to 0 V and the current allowed to decay for two minutes. The potential held during CP growth is important, because it determines the final oxidation state of the polymer and hence its conductivity. The current at any point in the deposition is a measure of the rate of polymer growth and the total charge passed is related to the total amount of polymer deposited onto the device (~ 10 to 100 μm). Following deposition of the polymer films the devices were washed with water and allowed to dry at RT before use.

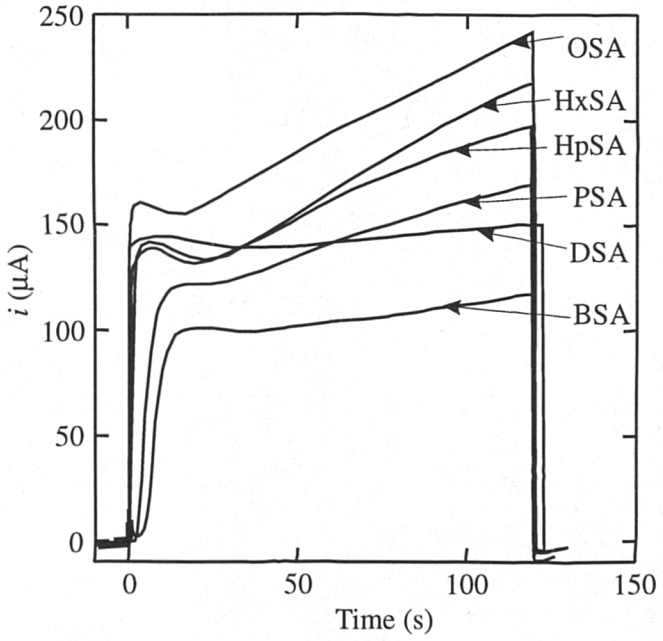

Figure 4.11 Potential step growth transients for PPy films grown with six different alkylsufonate counter-ions in aqueous solution ; which include butanesulfonate (BSA), pentanesulfonate (PSA), hexanesulfonate (HxSA), heptanesulfonate (HpSA), octanesulfonate (OSA), and decanesulfonate (DSA).

The dipping technique is adequate if the same CP is to be deposited on all sensor array elements. However, in an effort to have different CPs on the same SAD, a microdeposition technique was designed by Bartlett and Gardner [4.20] and built at Southampton University. The microdeposition apparatus is shown in Figure 4.12.

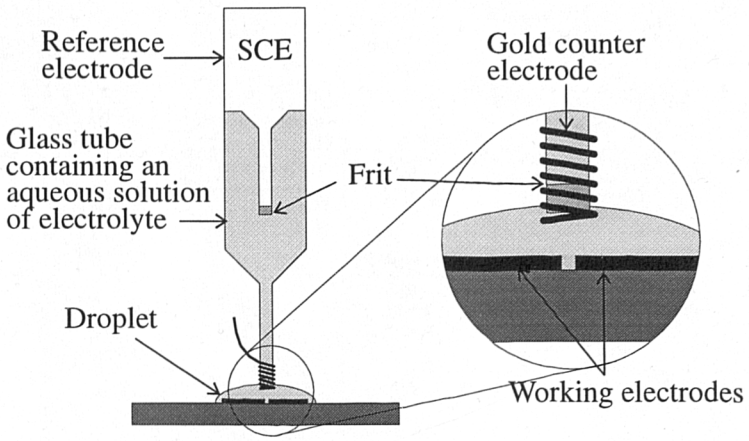

Figure 4.12 Microdeposition apparatus patented by Warwick University [4.20].

This technique localises the electrochemistry to a single drop of growth solution which is extruded over the growth region. The three-electrode configuration is established by dipping the apparatus into the drop. The end of the apparatus is a 3 mm diameter glass tube which leads to the larger glass body containing the same aqueous solution of electrolyte as in the drop. The counter electrode is a Au wire wound around the end of the apparatus tip, which slightly protrudes into the droplet without touching the working electrode. The reference electrode is a purpose built SCE which extends into the electrolyte inside the glass apparatus. A frit separates both the SCE from the electrolyte and the electrolyte from the droplet, which only allows ion transport between the regions.

The microdeposition technique has produced a hybrid CP SADs with minimal substrate preparation using the SRL125/CP SAD.

4.4.3 SnO_2 Deposition

Since the discovery that the electrical properties of SnO_2 can be used to detect gases, a great deal of research has been carried out to optimise the sensor performance for gas monitoring applications. This research has generated a wide variety of different fabrication techniques, because the sensor performance was discovered to depend greatly on the morphology, thickness and material composition [4.21]. The various SnO_2 structures developed have been classified as either ceramic, thick-film or thin-film [4.22]. Both thick and thin film based SnO_2 chemoresistors have been investigated with the SADs described in Chapter 3. The thin film deposition was

carried out at the Institute of Physical and Theoretcial Chemistry, Tübingen University, Germany, while the thick films were prepared and deposited at both Tübingen University and The Institute of Physics and Technology of Materials, Bucharest, Romania.

Investigations into the effect of morphology has established that polycrystalline SnO_2 is more sensitive than single crystal SnO_2 for gas sensing applications. Moreover, the grain and nanocrystallite size have been identified as being the most influential morphological property on thick and thin SnO_2 sensor performance. The grain size is determined by the SnO_2 deposition conditions and any thermal post-processing [4.23].

The composition of a SnO_2 film is also known to play an important role in the sensors characteristics. Additives have been used as catalysts to enhance the chemical kinetics that lead to gas sensitivity [4.24, 4.25]. Some of the thick and thin film SnO_2 sensors deposited on my designs have been doped with Pd and Pt to investigate their effect.

4.4.3.1 Thin Film SnO_2 Deposition

A wide variety of chemical vapour deposition (CVD) [4.26] and physical vapour deposition (PVD) [4.27] techniques have been used by researchers to deposit thin film SnO_2 [4.28]. In this study, a 50 nm amorphous SnO_2 was deposited onto the sensor substrate by electron beam deposition from a SnO_2 target in a high vacuum (Edwards 306 A). Usually the SnO_2 grain size is adjusted by a controlled annealing procedure, based upon the annealing temperature and the annealing time. For example, an average grain size of 20 nm can be produced in a furnace at 700°C for 12 hours. However, at 700°C the Au electrodes on the sensor array substrates degrade. To overcome this problem the SnO_2 was annealed on-chip using the integrated microheater up to a temperature of approximately 600°C. A monolayer of Pt and Pd dopants was deposited prior to annealing, by a sputtering process (Balzer SCD 050).

4.4.3.2 Thick Film SnO_2 Deposition

The method used for thick film SnO_2 deposition involved the preparation of a SnO_2 paste, which was manually 'painted' or dropped onto the sensor array substrate (a process used by Figaro Inc. (Japan) to manufacture millions of units). A heat-

treatment finally fixes and dries the material forming the active area. However, there are a number of steps during the preparation which determine the materials morphology, which are explained as follows:

Firstly, ammonia is added to pure tin chloride to precipitate out tin hydroxide. This is then heat-dried to give a very pure powder. Secondly, the tin hydroxide is calcined by heating to obtain pure SnO_2 powder. The temperature and time of calcination defines the crystallite size, which is closely related to the eventual sensor properties. Three calcination procedures have been invesigated at 450°C, 800°C and 1000°C giving an average grain size of 17, 80 and 110 nm, respectively (these results were obtained from Transmission Electron Microscopy (TEM) and X-ray analysis of the samples). The powders are doped by impregnation with Pd and Pt chlorides, which are then thermally treated to create metal clusters at the surface of the oxide crystallites. Thirdly, the powder is mixed with propandiol to form a paste suitable for application to the sensor substrate, which is then allowed to dry. The final stage in the deposition involves on-chip annealing the SnO_2 at 600°C. This thermal treatment increases the strength of the material due to sintering, but the dimensions of the resultant grains are the same as the initially formed crystallites.

4.5 Fabrication of a Hybrid SAD

To fabricate a hybrid SAD incorporating any combination of the sensor technologies investigated here, it is essential that the different fabrication processes are compatible. Fortunately, this is the case providing that a general fabrication sequence is followed, as shown in Figure 4.13.

Steps (1) and (2) would define the MHP structures and inactive sensor regions. The devices could be snapped after either step (1) or (2). The CP has to be deposited first, if a dipping technique is to be employed, to prevent the growth solution becoming contaminated. If the localised microdeposition technique is to be used then steps (3), (4) and (5) can be done in any order. It is essential that any heat-treatment steps do not expose the CP to a temperature above ~ 150°C, likewise, XPc to a temperature above ~ 250°C. The performance of the MHP designs allow both the SnO_2 and the XPc films to be individually annealed on-chip.

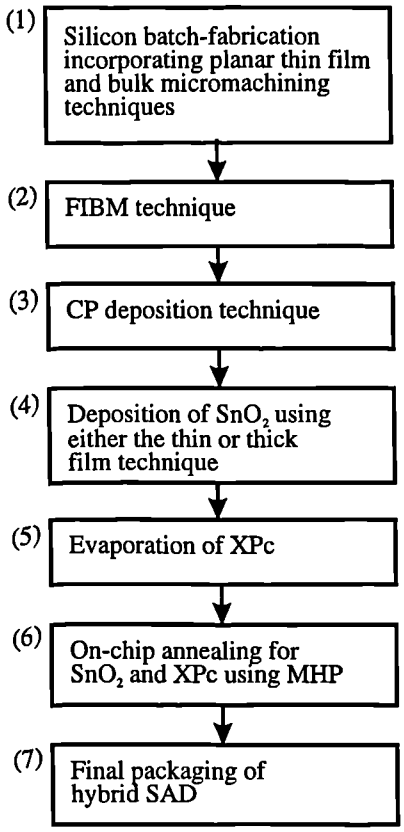

Figure 4.13 Fabrication sequence to produce a hybrid with the different sensor technologies investigated.

4.6 Conclusions

This Chapter has given an overview of the wide variety of techniques used to fabricate the different sensor designs described in Chapter 3.

Firstly, the silicon wafer processing procedure was described for the SADs and for the discrete and bridge devices. This involved conventional silicon planar technology and micromachining techniques.

The SRL125/dual device required a sub-micron inter-electrode gap feature which used a FIBM micromaching technique.

After the silicon wafer processing and FIBM process, all the chemoresistor substrate designs are completed and ready for gas-sensitive material deposition. The deposition techniques and the deposition conditions used that may affect the sensors performance are discussed for XPc, CP and SnO_2 films. The physical properties of these chemoresistive elements are known to influence a gas sensors response, and as a result play an important role in the gas sensor modelling, as described in the next

Chapter. With the experience gained from the different techniques, the fabrication procedure for a hybrid SAD was finally proposed.

4.7 References

4.1 S.J. Moss and A. Ledwith, *The Chemistry of the Semiconductor Industry*, Chapman and Hall, New York, 1987.

4.2 D. Kouvatsos, J.G. Huang, V. Saikumar, P.J. Macfarlane and R.J. Jaccodine, SiO_2 Film Stress, Thickness Dependence, Non-Planar Oxidation, and Fluorine-Related Effects, *J. Electrochem. Soc.*, **139**, No. 8, (1992) 2322-2326.

4.3 L.M. Mack, A. Reisman and P.K. Bhattacharya, Stress Measurements of Thermally Grown Thin Oxides on (100) Si Substrates, *J. Electrochem. Soc.*, **136**, No. 11, (1989) 3433-3437.

4.4 K.E. Bean, Anisotropic Etching of Silicon, *IEEE Trans. Electron. Devices*, **ED-25** (1978) 1185-1193.

4.5 H. Seidel, L. Csepregi, A. Heuberger and H. Baumgärtel, Anisotropic Etching of Crystalline Silicon in Alkaline Solutions, *J. Electrochem. Soc.*, **137**, No. 11 (1990) 3612-3626.

4.6 V.S. Nguyen, S. Burton and P. Pan, The Variation of Physical Properties of Plasma-Deposited Silicon Nitride and Oxynitride with Their Compositions, *J. Electrochem. Soc.*, **131**, No. 10, (1984) 2348-2353.

4.7 S. T. Davies, Use of Energy Beams for Ultra-high Precision Processing of Materials. In *From Instrumentation to Nanotechnology*, J.W. Gardner and H.T. Hingle (eds.), Gordon and Breach Science Publishers, Reading,1990, 159-179.

4.8 J. Melngailis, Critical Review: Focussed Ion Beam Technology and Applications, *J. Vac. Sci. Technology B*, **5**(2), (1987), 469-495.

4.9 T.A. Jones and B. Bott, Gas-Induced Electrical Conductivity Changes in Metal Phthalocyanine, *Sensors and Actuators*, **9** (1986) 27-37.

4.10 Y. Sadaoka, T.A. Jones and W. Göpel, Fast NO_2 Detection at Room Temperature with Optimized Lead Phthalocyanine Thin-film Structures, *Sensors and Actuators B*, **1** (1990) 148-153.

4.11 H. Wohltjen, W.R. Barger, A.W. Snow and N. Lynn Jarvis, A Vapour-Sensitive Chemoresistor Fabricated with Planar Microelectrodes and a Langmuir-Blodgett

Organic Semiconductor Film, *IEEE Trans. Electron. Devices,* **ED-32**, No. 7, (1985) 1170-1174.

4.12 A.W.J. Cranny, J.K. Atkinson, P.M. Burr and D. Mack, A Comparison of Thick- and Thin-Film Gas-Sensitive Organic Semiconductor Compounds, *Sensors and Actuators B*, **4** (1991) 169-174.

4.13 J.D. Wright, *Molecular Crystals*, Cambridge University Press, Cambridge, 1987.

4.14 T.A. Jones, B. Bott and S.C. Thorpe, Fast Response Metal Phthalocyanine-Based Gas Sensors, *Sensors and Actuators,* **17** (1989) 467-474.

4.15 P.N. Bartlett and S.K. Ling-Chung, Conducting Polymer Gas Sensors Part II: Response of Polypyrrole to Methanol Vapour, *Sensors and Actuators,* **19** (1989) 141-150.

4.16 P.N. Bartlett and S.K. Ling-Chung, Conducting Polymer Gas Sensors Part III: Results for Four Different Polymers and Five Different Vapours, *Sensors and Actuators,* **20** (1989) 287-292.

4.17 T.C. Pearce, J.W. Gardner, S. Friel, P.N. Bartlett and N. Blair, Electronic Nose for Monitoring the Flavour of Beers, *Analyst*, **118** (1993) 371-377.

4.18 J.W. Gardner and P.N. Bartlett, Potential Applications of Electropolymerized Thin Organic Films in Nanotechnology, *Nanotechnology*, **2** (1991) 19-32.

4.19 P.N. Bartlett, J.W. Gardner and R.G. Whitaker, Electrochemical Deposition of Conducting Polymers onto Electronic Substrates, *Sensors and Actuators A*, **21-23** (1990) 911-914.

4.20 J.W. Gardner and P.N. Bartlett, "Microsensor Deposition Device", British Patent Application No. 9400855.4.

4.21 W. Göpel and K.D. Schierbaum, SnO_2 Sensors: Current Status and Future Prospects, *Sensors and Actuators B,* **26-27** (1995 1-12.

4.22 K.D. Schierbaum, U. Weimar and W. Göpel, Comparison of Ceramic, Thick-Film and Thin-Film Chemical Sensors Based Upon SnO_2, *Sensors and Actuators B,* **7** (1992) 709-716.

4.23 M.S. Dutraive, R. Lalauze and C. Pijolat, Sintering, Catalytic Effects and Defect Chemistry in Polycrystalline Tin Dioxide, *Sensors and Actuators B,* **26-27** (1995) 38-44.

4.24 N. Yamazoe, Y. Kurokawa and T. Seiyama, Effects of Additives on Semiconductor Gas Sensors, *Sensors and Actuators,* **4** (1983) 283-289.

4.25 G. Martinelli and M.C. Carotta, Influence of Additives on the Sensing Properties of Screen-Printed SnO_2 Gas Sensors, *Sensors and Actuators B,* **15-16** (1993) 363-366.

4.26 G. Sberveglieri, P. Nelli, G.P. Benussi, L.E. Depero, M. Zocchi, G. Rossetto and P. Zanella, Enhanced Response to Methane for SnO_2 Thin Films Prepared with the CVD Technique, *Sensors and Actuators B,* **15-16** (1993) 334-337.

4.27 G. Williams and G.S.V. Coles, The Influence of Deposition Parameters on the Performance of Tin Dioxide NO_2 Sensors Prepared by Radio-Frequency Magnetron Sputtering, *Sensors and Actuators B,* **24-25** (1995) 469-473.

4.28 G. Sberveglieri, Classical and Novel Techniques for the Preparation of SnO_2 Thin-Film Gas Sensors, *Sensors and Actuators B,* **6** (1992) 239-247.

Chapter 5

5. Modelling of Chemoresistive Gas Sensors

5.1 Introduction

In general, a gas-monitoring instrument determines the target gas concentration by processing the sensor output according to a mathematical function or look-up table (LUT) derived during calibration. This often leads to an empirical model being developed that relates the gas sensor output to the gas concentration under specific operating conditions. In this Chapter I discuss the basic models that describe the characteristics of MOS, XPc and CP chemoresistors, against which my designs can be compared and assessed.

Common problems associated with the gas-sensitive materials investigated in this thesis are poor selectivity and poor long-term stability, as described in Chapter 2. These problems have in the past limited the accuracy of gas-monitoring instruments. In an attempt to identify the gas sensor mechanisms that govern performance, researchers have proposed physicochemical mechanisms which have led to the development of theoretical models. Validated theoretical models may assist in the selection of an appropriate pre-processing algorithm [5.1] and improve the accuracy of the gas sensing instrument. The main physicochemical mechanisms identified as determining the characteristics of the chemoresistors investigated here are discussed.

From theoretical models developed by Gardner [5.2] the response from a pair of canonical chemoresistors that exploit the geometry to provide a poisoning diagnostic, has been studied for potential application in an intelligent sensor. The principle relies on one sensor having a very narrow inter-electrode gap (e.g. submicron) with respect to the film thickness (e.g. 2 microns), while the second sensor has a very wide (e.g. 10 μm) inter-electrode gap with respect to the film thickness. This Chapter describes

both this theoretical principle (which has been implemented in the SRL125/dual SAD) and its expected behaviour.

The gas sensing mechanisms for chemoresistors employing MOS, XPc and CP films are dominated by the interactions of molecules with surface sites (which include the internal surface for porous films), as outlined in Chapter 2. Although these mechanisms differ between materials and target gas, the sensor system can be described by a generalised block diagram, as shown in Figure 5.1.

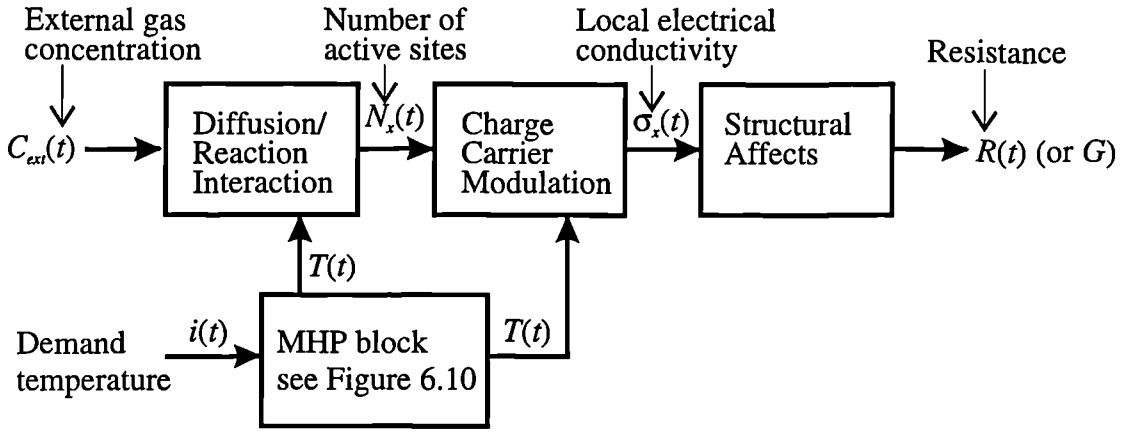

Figure 5.1 Block diagram of general chemoresistor system, where C_{ext} is the external gas concentration, N_x is the local number of activated internal sites that lead to a change in electrical charge carrier, σ_x is the local electrical conductivity, R and G are the measured sensor resistance or conductance, respectively, T is the operating temperature, and t is a time variable indicating a dynamic system.

The physicochemical mechanisms that determine the theoretical models are described for each sub-system. The first sub-system describes the diffusion-reaction process that defines the interaction between the internal bound and the external gas concentrations. The materials considered here are porous, allowing gas to diffuse into the material, whereupon, it may react with an internal surface to produce an activated site. The local[†] number of active sites, N_x, will vary through the gas-sensitive film according to the diffusion-reaction sub-system (the subscript x indicates the position through the film perpendicular to the substrate plane).

[†] Local refers to a small volume within the film.

The transfer function for the MHP sub-system is determined by the thermal characteristics described and modelled in Chapter 6. The MHP sub-system functions provide control of the chemoresistor operating temperature.

For each activated surface site formed, there is a corresponding change in the localised charge concentration and/or carrier mobility, that leads to a change in σ_x.

The final sub-system describes the chemoresistors output signal (e.g. conductance, G, or resistance, R,) which is related to the integration of σ_x through the gas-sensitive film and the geometry of the chemoresistor.

It has been assumed in order to simplify the chemoresistor system (as shown in Figure 5.1) that there is only one target gas (with concentration, C_{ext}), in clean air at a known humidity. In the absence of the target gas (C_{ext}=0), the G in clean air conditions at a constant humidity and temperature is known as the base-line conductance, G_o (under similar conditions the measured R is referred to as the base-line resistance, R_o).

The geometrical notation used during this Chapter is described in Figure 5.2.

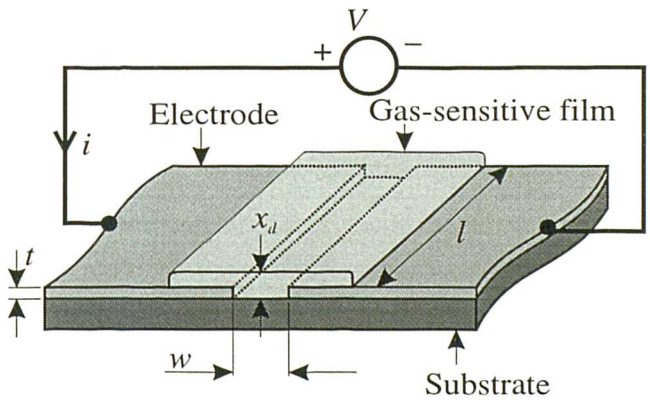

Figure 5.2 Schematic of chemoresistor showing the geometrical notation used during modelling, where V is the applied voltage, i is the current, t is the electrode thickness, l is the electrode length, w is the inter-electrode gap and x_d is the gas-sensitive film thickness.

5.2 Empirical Expressions for Steady-State Characteristics

Empirical expressions which give a good fit to steady-state characteristics can be found, against which the theoretical models can be validated.

It is well known that a power law expression may be used to describe the steady-state response of MOS and XPc films to changes in concentration for particular gases.

Clifford *et al.* [5.3] derived a quantitative model to describe the response of Taguchi gas sensors (SnO_2 chemoresistors with a porous sintered pellet structure) to reducing gases. It was demonstrated that the significant features of the responses to CH_4 or water are an asymptotic approach to constant resistances at very low concentrations and an asymptotic approach to a power law relationship at high concentrations. According to Clifford *et al.* [5.3] the simple mathematical expression used to describe the response curve to CH_4 is,

$$R \approx R_o\left(1 + K_{CH_4} C_{CH_4}\right)^{-\beta} \tag{5.1}$$

where C_{CH_4} is the methane concentration, and K_{CH_4} is a sensitivity coefficient. If R is plotted against the logarithm of C then β is the gradient of the asymptotic slope at high concentrations. Similarly, the response to CO is also found to follow a power law, where

$$R \approx R_o\left(K_{CO} C_{CO}\right)^{-\beta} \tag{5.2}$$

Power law expressions have also been characterised for oxidising gases (e.g. NO_2). Hence the increase in resistance with an increasing gas concentration generates a positive power coefficient [5.4]. Clifford *et al.* [5.3] also characterised the effect of operating temperature, where a straight line was observed between the logarithm of the gas sensitivity coefficients against the inverse temperature.

It is also widely known that the conductance of XPc films increase upon exposure to an oxidising gas. Plotting the resistance-concentration characteristics for a XPc chemoresistor on a logarithmic axis has been shown to generate a linear relationship [5.5, 5.6]. A power law expression can therefore also be used to describe the XPc characteristics. A XPc temperature response has been measured [5.7] with the same form as the MOS films.

Finally, Bartlett *et al.* [5.8] have obtained the steady-state response of a CP (PPy) chemoresistor to different concentrations of methanol, which demonstrate typical

characteristics. The response (R) increases linearly with concentration at low concentrations and approaches a constant at high concentrations. A plot of the inverse change in resistance against inverse gas concentration defines the characteristics in a form which can be expressed by a straight line at high concentrations. The base-line conductance has also been shown to depend on temperature, which can generally be described by a variable range hopping of the Mott type [5.8].

5.3 Diffusion and Reaction Models

Investigations into gas sorption in MOS, XPc and CP films have led to the material surface to be considered as a number of immobile sites at which the target gas can react. At equilibrium, after exposure to a target gas, a certain portion of the total number of sites, N_m, will be activated by the gas, described by the site occupancy θ, according to

$$\theta = \frac{N}{N_m} \tag{5.3}$$

where N is the number of activated sites. For homogeneous films the distribution of sites is assumed to be uniform throughout the film. Furthermore, any microscopic structural inhomogenity in MOS, XPc and CP films can be ignored because of macroscopic homogeneity. The macroscopic mechanisms can be modelled using effective medium theory. The relationship between the external gas concentration, C_{ext}, and the number of active sites, N, through the film is considered as a device sub-system, as shown in Figure 5.1. The steady-state relationship between the site occupancy θ and C_{ext} at a constant temperature is called the sorption isotherm. The form of this isotherm is determined by the reaction steps that proceed to produce the activated sites, while the kinetic rates govern the amount of adsorbate N. The reactions require a steady mass transport, in order to reach equilibrium through the film. The rate of gas diffusion in porous materials is therefore a key property in defining the profile of activated sites. A non-uniform gas concentration profile arises when the rate of gas diffusion cannot maintain the rate of gas consumption in an irreversible reaction mechanism (e.g. combustion of reducing gases in MOS films).

The transient characteristics of this sub-system are dependent on the rate of mass transport (i.e. diffusion) and the sorption reaction rates.

The theoretical models which describe this sub-system have been referred to as diffusion-reaction models. The fundamental elements of this model are the reaction process models, adsorption isotherms and diffusion considerations. Each are therefore outlined in this Section.

5.3.1 Adsorption Isotherms

A knowledge of the quantity of gas adsorbed together with its associated equilibrium concentration enables an adsorption isotherm to be specified. The isotherm models encountered with MOS, XPc and CP films are limited to adsorption of up to a monolayer of species (where the species being adsorbed is the target gas for XPc and CP films and O_2 with MOS films) onto immobile sites [5.9].

The simplest isotherm is the Langmuir isotherm which is based on the assumption that every adsorption site, '< >', is identical and that the ability of a gas species, A, to bind there is independent of whether or not nearby sites are occupied.

The dynamic interaction is,

$$A + < site > \underset{k_b}{\overset{k_f}{\Leftrightarrow}} < A > \tag{5.4}$$

where $< A >$ is the adsorbed gas species formed, with k_f and k_b as the forward and backward reaction rates, respectively. For a chemoresistor with an active volume ,V, the rate of change of site occupancy ($d\theta/dt$) due to adsorption is proportional to the concentration of A and the number density of vacant sites $N_m(1-\theta)/V$, so

$$\frac{d\theta}{dt} = k_f C N_m (1-\theta)/V \tag{5.5}$$

Whereas, the $d\theta/dt$ due to desorption is proportional to the number density of adsorbed species, $N_m\theta/V$, hence

$$\frac{d\theta}{dt} = k_b N_m \theta / V \tag{5.6}$$

At equilibrium the two rates are equal, and solving for θ gives the Langmuir isotherm,

$$\theta = \frac{N}{N_m} = \frac{KC}{1+KC} \tag{5.7}$$

where the reaction-rate coefficient, $K=k_f/k_b$.

If adsorption occurs *via* a mobile dissociative process, then two surface sites are required for both adsorption and desorption. The Langmuir isotherm then becomes [5.10],

$$\theta = \frac{N}{N_m} = \frac{(KC)^{1/2}}{1+(KC)^{1/2}} \tag{5.8}$$

This modified form of the Langmuir isotherm demonstrates the importance of the chemical reactions occurring to form the activated site. The dynamic interaction (equation 5.4) typical of the direct reaction between the gas and surface sites (Eley-Rideal mechanism) may be a simplification of the actual adsorption kinetics. For example, Windischmann *et al.* [5.11] has developed a microscopic model describing the interaction of CO with a MOS film, which incorporates an intermediate physisorption process. The existence of such physical states may not change the reaction energetics but the kinetics might be affected. The product of K with a partition coefficient may be included to account for the additional energy state.

In some cases, the heat of adsorption decreases as θ increases, which suggests that the energetically most favourable sites are occupied first, e.g. adsorbed surface ions may apply an additional electrostatic repulsion to which subsequent adsorbants have to overcome. By making the assumption that the heat of adsorption falls

logarithmically with coverage, the Freundlich isotherm has been defined [5.9], according to

$$\theta = AC^{\beta} \tag{5.9}$$

where A is a constant of proportionality and β is the power coefficient.

The adsorption isotherm can be compared to the chemoresistors empirical characteristics, assuming the conductance is directly proportional to the site occupancy. These comparisons have been widely carried out by researchers to identify the dominant gas sensing mechanisms in a film. It is widely accepted that the power law form of a Freundlich adsorption isotherm can be used to model MOS [5.12] and XPc [5.7] films.

Williams *et al.* [5.13] has reviewed the literature which describes the reaction kinetics of gas adsorption of MOS films. By applying the mass action law to the proposed reaction kinetics an equation relating N to the gas concentration can be derived [5.14, 5.15]. Both the adsorption kinetics of reducing gases (e.g. CO) and oxidising gases (e.g. NO_2), have been shown to have the same form as the Freundlich isotherm.

The chemisorption of a gas on XPc films proceeds *via* physisorption to the surface, whereupon, charge is transferred at the reaction site. The adsorption of the target gas has to compete with oxygen adsorption for the surface sites. Although, the exact reaction kinetics are not well understood, a Freundlich isotherm fits XPc characteristics very well.

The exact gas sensing mechanisms associated with CP are still unknown, as outlined in Chapter 2. However, the close fit of the Langmuir isotherm to CP characteristics suggests that the corresponding adsorption mechanism can be used for CP modelling [5.8].

5.3.2 Diffusion-Reaction Considerations

The previous Section on sorption isotherms assumed that the gas concentration was constant within the porous film, so that the number of activated sites, N, was a function of the gas concentration $F(C)$. In this case, any change in gas mixture will

result in a perturbation of N for a finite period. The time to reach a new equilibrium will depend on the reaction rates of the processes leading to the activated site and the rate of mass transport between the surface and the gas bulk. The response time associated with a porous film is therefore dependent on the diffusion-reaction model. To maintain a uniform gas concentration in the film at equilibrium (i.e. steady-state) requires that no gas is consumed, i.e. a reversible chemisorptive process. However, for an irreversible process (e.g. a combustion process) the local gas concentration, C_x, may vary through the film, where x is the depth through the film[†]. The theoretical gas concentration profiles are considered for the different gas-sensitive materials as follows:

In general, the gas sensing mechanisms assumed to be operating in CP and XPc films are based on the equilibrium between the target gas in the external gas phase and that adsorbed onto the sites. At equilibrium, the target gas will penetrate the entire film, to form a uniform gas concentration profile, because these interactions do not involve the irreversible combustion of molecules which must be replenished by mass transport. However, the reaction mechanism for a MOS film with reducing gases is generally accepted to proceed *via* an irreversible reaction [5.16]. Hence, thick porous MOS films will contain a non-uniform gas concentration and consequently a local site occupancy θ_x profile.

Williams *et al.* [5.13] have derived an expression for the gas concentration profile $C_x(x)$ relating to the consumption of gas species, A, as depicted in Figure 5.3.

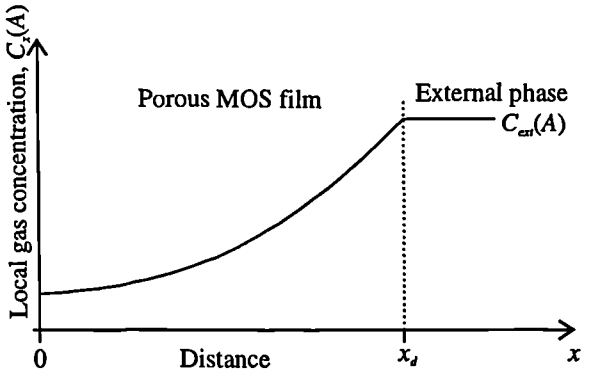

Figure 5.3 Schematic of a reducing gas concentration profile through a MOS film as a result of a constant external gas concentration of $C_{ext}(A)$.

[†] It is assumed that the variations are limited to the direction perpendicular to the substrate plane.

If the diffusing substance is irreversibly converted to another product by a first-order reaction [5.10], so that the rate of removal of diffusing substance is $k_r C_x(A)$, where k_r is the reaction rate of removal, then the diffusion equation perpendicular to the substrate plane becomes [5.17]

$$\frac{\partial C_x(A)}{\partial t} = D_A \frac{\partial^2 C_x(A)}{\partial x^2} - k_r C_x(A) \tag{5.10}$$

where D_A is the diffusion coefficient of gas A inside the film and assumed independent of C_x. In the steady-state, $\partial C_x(A)/\partial t = 0$, so the concentration profile shown in Figure 5.3 is given by the solution of,

$$\frac{\partial^2 C_x(A)}{\partial x^2} - \frac{k_r}{D_A} C_x(A) = 0 \tag{5.11}$$

which is

$$C_x(A) = \frac{C_{ext}(A)\cosh\left[(x/x_d)(k_r\tau)^{1/2}\right]}{\cosh(k_r\tau)^{1/2}} \tag{5.12}$$

where the diffusion time constant $\tau = x_d^2/D_A$.

A simple way to model this hyperbolic gas concentration profile is to define an effective reaction depth (x_b) which separates the regions of reactive and unreactive sites. This simple binary model has been referred to by Gardner [5.2] as a moving-boundary gas concentration profile, where the reaction depth is a function of the external gas concentration $C_{ext}(A)$ rather than time. From the form of equation 5.12, if the gas is very reactive or there is a high concentration of sites (e.g. strong catalyst) leading to a high k_r, then only a thin surface layer of the homogeneous film contains activated sites which can contribute to the sensor response.

Diffusion-reaction models have also been developed to describe the transient response of the gas sensor, in which the time constant associated with charge transfer is negligible compared to the time constants associated with diffusion-reaction processes. The approach to generating the models have been to substitute the adsorption isotherm into the modified equation for diffusion in a reversible reaction process between the gas and the gas-sensitive material [5.17], according to

$$\frac{\partial C}{\partial t} = D\frac{\partial^2 C}{\partial x^2} - \frac{1}{V}\frac{\partial N}{\partial t} \tag{5.13}$$

where V is the volume of the active material. This has been carried out for the Langmuir isotherm [5.18] to describe the transient response of CP chemoresistors [5.19, 5.20]. Equation 5.13 has also been solved for a Freundlich isotherm that can be used to describe the transient response of both XPc [5.7] and MOS [5.12] chemoresistors.

5.4 Modelling of Film Conduction

This Section describes the relationship between the activated reaction sites and the film conductivity. The electrical conductivity, σ, of a semiconducting material is related to the electron and hole concentrations (n and p, respectively) and their mobilities (μ_e and μ_h, respectively) by the standard equation

$$\sigma = e(n\mu_e + p\mu_h) \tag{5.14}$$

where e is the charge on electron and hole charge carriers. SnO_2 is an n-type semiconducting material in air, i.e. in which the majority carriers are electrons and $n>>p$, so equation 5.14 can be simplified to,

$$\sigma_{SnO_2} \approx en\mu_e \tag{5.15}$$

Conversely, holes are the majority charge carrier in *p*-type XPc films, so

$$\sigma_{XPc} \approx ep\mu_h \tag{5.16}$$

The concentration and proportion of *n* and *p* carriers in CP films is determined by the deposition conditions and the materials used (e.g. monomer and counter-ion). However, the majority of stable CP systems are *p*-type materials (e.g. PPy and PAn).

A macroscopically electrically homogeneous material is assumed with a uniform density of sites and charges. For this study it is also assumed that the adsorbed gas changes the carrier concentration, although a similar argument for changing the carrier mobility is possible. If a diffusion-reaction process produces a local gas concentration profile, then a local charge carrier profile is also expected. Thus, this situation would create a local conductivity (σ_x) profile which would be a function of the gas concentration profile $F(C_x)$.

The precise mechanisms by which charge is transferred at the surface and conduction takes place depends on the gas-sensitive material.

5.4.1 Conduction in MOS Films

As introduced in Section 2.2 of Chapter 2, the base-line conductivity, σ_0, of a SnO_2 film in pure air is determined by charge generation from bulk defects in the SnO_2 films and the depletion of this charge by adsorbed oxygen at internal surfaces and grain boundaries. The depth of the depletion layer, i.e. Debyé length (L_D) is [5.21],

$$L_D = \left(\frac{\varepsilon_r \varepsilon_o kT}{e^2 n_b} \right)^{1/2} \tag{5.17}$$

where ε_r denotes the relative dielectric permittivity, ε_o the vacuum permittivity, k Boltzmann's constant, e is the electron charge and n_b is the bulk concentration of electrons. Typical values of L_D can range from approximately 1 to 100 nm [5.13]. It has been recognised that reducing gases react with bound oxygen sites (e.g. O^-, O^{2-})

and release electrons, so leading to a reduction in L_D [5.16]. Conversely, in general, oxidising gases create more oxidised sites, which leads to a greater depletion layer [5.4]. However, some SnO_2 films doped with Bi_2O_3 have shown the opposite of the expected sensitivity to the oxidising gas NO_x [5.22].

Williams *et al.* [5.13] have described different cases of a microscopic model which are determined by the grain structure and the depletion layer. If the grains touch but are not sintered, the electrons must flow over a surface barrier to transfer from one grain to the next. A change in the charge on the surface states increases the surface barrier V_s, according to the Schottky relation [5.13],

$$V_s = eN_s^2/2\varepsilon_r\varepsilon_o n_b \tag{5.18}$$

where N_s is the charge on the surface. Morrison [5.14] has modelled the conductance of a porous SnO_2 film dominated by Schottky barriers, according to an activated process where,

$$\sigma = \sigma_o \exp[-eV_s/kT] \tag{5.19}$$

and eV_s is the surface barrier potential energy at temperature T. This equation is consistent with the characteristic temperature dependence of thick MOS films. The conductance, σ_o, in Schottky barrier limited conduction is related to the intra-granular conductance [5.23]. Equation 5.18 can be related to the fraction of sites occupied because $N_s=N_m\theta$.

If the material is sintered, then inter-granular necking becomes a more significant feature in controlling the resistance, as outlined in Section 2.2 of Chapter 2. The adsorption of a gas then changes L_D and so modulates the channel width through which the current flows. If L_D increases to a point where the neck is depleted, then again the carriers must overcome a potential barrier to traverse the neck. However, the barrier height is not as high as in the Schottky barrier case [5.21].

Schierbaum *et al.* [5.21] have also derived the conductance of a film composed of nanocrystals with an average grain diameter smaller than L_D. This model assumes that

the entire nanocrystal is depleted at the surface, so that on a macroscropic level the material can be considered as a homogeneous film, in which the conduction band is modulated by the interaction with sorbing species. An exponential dependence of a nanocrystalline sensor conductance (G) on the temperature (T) has been proposed by Schierbaum *et al.* [5.21] according to,

$$G = P\sigma_0 \exp\left(-\left[E_C - E_F\right]_b / kT\right) \tag{5.20}$$

where E_F and E_C is the Fermi energy level and conduction band energy level, respectively, in the bulk upon gas exposure, σ_0 denotes the bulk conductivity and P is a constant of proportionality, which is determined by the sensors geometry.

Many researchers have obtained a good fit between a microscopic potential barrier limited conductance model and the characteristics of porous SnO_2 sensors [5.24, 5.25].

5.4.2 Conduction in Organic Materials

The precise conduction mechanisms associated with XPc and CP films are not well understood. Gutmann *et al.* [5.26] have reviewed the different types of charge transfer possible in XPc films.

XPc films are p-type semiconductors and follow equation 5.16. In clean air at the operating temperature of interest the bulk conductivity is defined by the amount of chemisorbed O_2. Reaction with O_2 abstracts an electron from the film which increases p. Further electron immobilisation occurs due to sorption of a gas with a higher electron affinity than O_2, e.g. NO_2. These effects have been observed experimentally [5.7] where the change in the number of holes δp is equal to the number of electrons immobilised at the surface δn (i.e. $\delta p = \delta n$), where

$$\delta n \propto N = \theta N_m = KC^{\beta} \tag{5.21}$$

The conductivity therefore becomes

$$\sigma = e\mu_n(p_o + \delta p)/V \tag{5.22}$$

where p_o is the number of holes in the bulk when the film is exposed to air. However, in many cases equation 5.22 can be simplified because $\delta p >> p_o$.

The conductivity of CPs can be modelled simplistically in terms of mechanisms involving the hopping of charge carriers between localised states of adjacent chain segments or different chains [5.27]. It is generally accepted that the temperature dependence of the film conductance is described by a variable range-hopping model of the Mott type.

Gardner *et al.* [5.20] have considered this general conduction process as a three-dimensional randomly distributed array of identical resistive links. The macroscopic conductance of such a system is determined by the way in which the links are connected. Due to the complex nature of this problem and the fact that the gas effects are small, models of CP films have assumed that the film conductivity is linearly related to site occupancy, according to

$$\sigma_x = \sigma_o[1 - S\theta(C_x)] \tag{5.23}$$

where S is a gas-sensitivity coefficient. However, this linear model does in fact agree with experimental data taken on CPs by Bartlett *et al.* [5.8].

5.5 Modelling Chemoresistor Geometry

To investigate the geometrical affects on chemoresistor conductance, an *n*-type material is considered (e.g. SnO_2) as an example. The geometrical parameters governing the electrical properties, can be introduced to the model by integrating the current density, J, over a surface bisecting the electrodes to define the device current, i,

$$i = \int_0^1 J.l\,dx' = \int_0^1 \sigma_x E.l\,dx' \tag{5.24}$$

where x' is x/x_d, and E is the electric field across the electrodes. Gardner [5.28] has modelled the effect of chemoresistor geometry on the gas sensor characteristics for different configurations, in order to define a chemoresistor geometry with an optimal performance. It was apparent that two of the configurations investigated by Gardner [5.28], which included thick parallel electrodes and thin coplanar electrodes, describe the two limits of the structures produced here (described in Chapters 3 and 4), as represented in Figure 5.4.

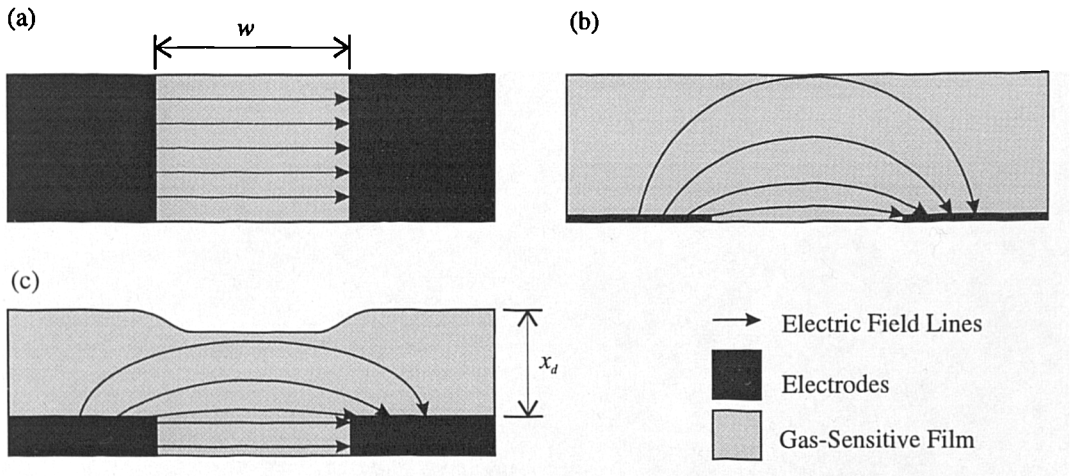

Figure 5.4 Schematic of electrode configuration and associated electric field lines for: (a) thick parallel electrodes, (b) thin coplanar surface electrodes and (c) expected device electrode configuration, combining characteristics from both (a) and (b).

The simplest electrode configuration consists of the homogeneous layer sandwiched between two metal electrodes in a parallel-plate configuration, as shown in Figure 5.4 (a). In this structure, the electric field equals the applied voltage, V, divided by the inter-electrode gap, w (i.e. $E=V/w$) and the edge effects are ignored. This can be substituted in equation 5.24 to derive the device conductance G, according to

$$G = \frac{i}{V} = \frac{\sigma_x x_d l}{w} \tag{5.25}$$

where *l/w* is referred to as the aspect ratio of the electrode structure.

The electric field bisecting the thin semi-infinite coplanar electrode, $E(x_d)$, as shown in Figure 5.4 (b) is more complicated, but an analytical solution has been derived using conformal mapping,

$$E(x_d) = \frac{V}{\pi}\left[x_d^{\,2} - \frac{w^2}{4} \right]^{-\frac{1}{2}} \tag{5.26}$$

The electric field equipotential and flux lines defined by equation 5.26 are hyperbolae and ellipses, respectively [5.28]. If equation 5.26 is substituted into equation 5.24 then the steady-state conductance (*i/V*) in air becomes,

$$G_o = \frac{\sigma_o l}{\pi} \ln\left[1 + \left(1 + \frac{w^2}{4x_d^{\,2}} \right)^{\frac{1}{2}} \Big/ \frac{w}{2x_d} \right] \tag{5.27}$$

Now consider the designs described in Chapter 3 with electrode thicknesses of $t \approx$ 300 nm for SADs, and $t \approx$ 250 nm for the SRL127/device. When a macroscopically homogeneous layer of thickness x_d is deposited on the device then if $x_d < t$ the electrode arrangement must be considered as having the thick parallel electrode configuration shown in Figure 5.4 (a). Conversely, if $x_d > t$ the electric field would comprise of both configurations, as shown in Figure 5.4 (c). The electric field solution to this case is a Jacobean elliptical integral of the third kind with a finite electrode thickness *t* entering equation 5.26. Note that for CP and thick MOS films, which are typically 10 to 100 μm thick, the field solution can be approximated to that of the thin co-planar electrodes.

5.6 Theoretical Response of an Intelligent Dual Sensor

Analysing theoretical models helps to identify fundamental parameters or mechanisms that determine the basic characteristics of a chemoresistor. Control of

such parameters should lead to the design of a superior chemoresistor e.g. one that is more selective to the target gas. Alternatively the model may provide information with which to design a new type of more "intelligent" sensor. Gardner [5.2] has developed a theory to describe the theoretical response of a pair of sensors and has shown in particular cases how it may be used to diagnose sensor stability (e.g. effects due to poisoning). This Section outlines the theory which has been implemented in the SRL125/dual SAD.

The theory assumes that the chemoresistor has thin coplanar electrodes coated with a homogeneous gas-sensitive film. When a gas of concentration C is introduced it can diffuse into the porous film and react at sites dispersed uniformly throughout the film. These reaction sites modify the local conductivity σ_x of the film according to a function $F(C_x)$ that depends upon the local gas concentration C_x. Assuming that the conductivity is proportional to the site occupancy, then the local conductivity may be related to a function of the local gas concentration according to,

$$\sigma_x(C_x) = \sigma_0\left[1 + S.F(C_x)\right] \tag{5.28}$$

where S is a gas-sensitivity coefficient, σ_o is the gas-free conductivity, and $F(C_x)$ is related to the diffusion-reaction properties and the adsorption isotherm associated with the material. If equation 5.28 is substituted in the expression for conductance (equation 5.24) and integrated for x through the film (with thickness x_d) an expression can be derived for the gas-dependence conductance, $G(C_x)$. This can then be used with equation 5.27 to give a steady-state response, $\Re$, in terms of the fractional change in conductance [5.2],

$$\Re = \frac{G(C_x) - G_0}{G_0} = \frac{\sigma(C_x) - \sigma_0}{\sigma_0}$$

$$= \frac{\int_0^1 F(C_x)/\left[(x')^2 + (w/2x_d)^2\right]^{1/2} dx'}{\ln\left\{\left[1+\left(1+w^2/4x_d{}^2\right)^{1/2}\right]/(x/2x_d)\right\}} \tag{5.29}$$

The operation of a dual sensor device requires that one device has a inter-electrode gap, w_n, which is much less than the gas-sensitive film thickness (i.e. $w_n << x_d$) and the other has an inter-electrode gap, w_w, which is much greater than film thickness (i.e. $w_w >> x_d$). These two limiting cases can be considered as follows: In the case of the narrow-gap device, the electric field effectively probes the inner most part of the film. However, in the case of the wide-gap device, the sensing electrodes probe the entire film. These conditions are represented in Figure 5.5.

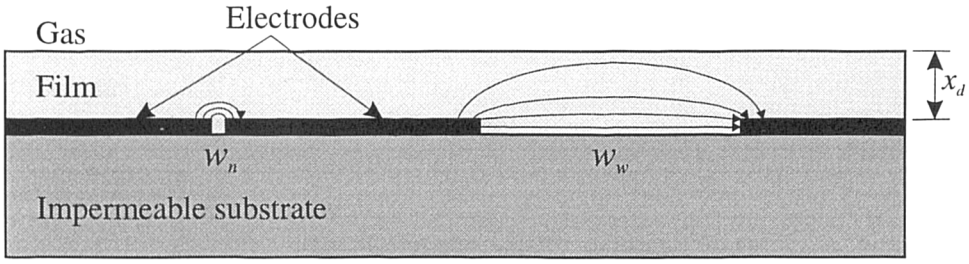

Figure 5.5 Schematic of a dual device structure with two integrated coplanar sensors, one with a narrow inter-electrode gap (i.e. $w_w << x_d$) and the other with a wide inter-electrode gap (i.e. $w_w >> x_d$) compared with film thickness x_d.

The response $\Re_n$ of the narrow-gap sensor becomes,

$$\Re_n \approx \frac{\int_0^1 F(C_x)/\left[(x')^2 + (w_n/2x_d)^2\right]^{1/2} dx'}{\ln(4x_d/w_n)} \tag{5.30}$$

Whereas the electric field inside the wide-gap sensor is nearly independent of x' and so equation 5.29 simplifies to,

$$\Re_w \approx \int_0^1 F(C_x)\,dx' \tag{5.31}$$

Lithographic techniques make possible the fabrication of both electrodes types under the same gas-sensitive film. The theoretical response of such a dual sensor device is described by

$$\frac{\Re_n}{\Re_w} \approx \frac{\int_0^1 F(C_x)\Big/\left[(x')^2 + (w_n/2x_d)^2\right]^{1/2} dx'}{\ln(4x_d/w_n)\int_0^1 F(C_x)\,dx'} \tag{5.32}$$

The model assumes that $\sigma_x \propto \theta_x$, and $F(C_x)$ has the functional form of the adsorption isotherm θ_x (see Section 5.3.1) which depends upon the local gas concentration profile (see Section 5.3.2). Gardner [5.2] considered two profiles that illustrate the limiting cases of steady-state diffusion-reaction considerations; namely, a uniform gas profile (type I) and a moving-boundary gas profile (type II).

A uniform gas concentration profile is expected for MOS films with a low concentration of reaction sites and CP and XPc films. For a type I case the concentration profile is independent of distance x and so the geometric factors cancel out, resulting in an equal change in conductance response for the narrow-gap and wide-gap chemoresistors. A plot of $\Re_n$ against $\Re_w$ becomes a straight line, as shown in Figure 5.6.

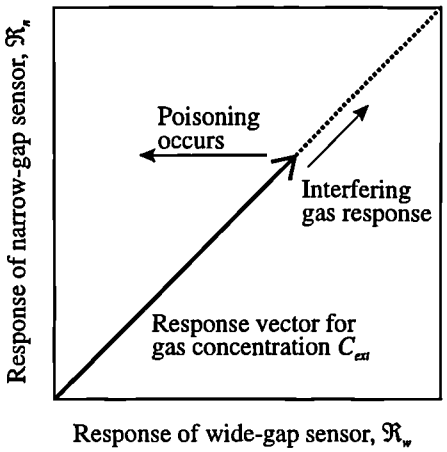

Figure 5.6 Theoretical response of the dual sensor device to a gas with a type I concentration profile with arbitrary units. The effect of poisoning is diagnosed by a shift in the operating vector.

As the concentration increases, so the length of the sensor pair response vector increases. The response vector will always lie upon the straight line at equilibrium. The presence of an interfering gas will not move the response vector off the characteristic operating line, because it will affect both sensors equally (unless its concentration profile is not uniform). If poisoning de-sensitises the outside part of the film first, this would cause the response of the wide-gap sensor to fall, while the response of the narrow-gap sensor will remain unchanged. Consequently, the dual sensor response parameter would rise off the characteristic line as the film poisons, which could be used as a diagnostic tool (see Figure 5.6). If a poisoning gas persisted it may penetrate far enough into the film to affect the narrow-gap response. However, if the poisoning effect is evenly distributed throughout the film then the response vector will not move off the characteristic operating line, but simply reduce its length.

The second limiting case (type II) considered by Gardner [5.2] is referred to as the moving-boundary gas concentration profile, as described in Section 5.3.2. When a MOS film has a high catalytic activity, it is probable that the gas entering the film is rapidly consumed and so does not penetrate all the way into the film. As the external gas concentration increases so the moving-boundary penetrates further through the film until it eventually reaches the impermeable substrate. At this concentration, and at higher concentrations, the gas concentration within the film becomes approximately uniform. The corresponding function of the local gas concentration is equal to the adsorption isotherm (e.g. Freundlich for MOS) from the surface to the depth of

boundary penetration, x_b (i.e. $x_d \leq x \leq x_b$). However, between the boundary and substrate (i.e. $0 \leq x \leq x_b$) the local gas concentration drops to zero.

The response of the dual sensor is now a function of the position of the boundary, according to,

$$\frac{\Re_n}{\Re_w} \approx \frac{\ln\left\{2\Big/\left[\left(x_b/x_d\right)+\left(x_b^{\,2}/x_d^{\,2}+w_n^{\,2}/4x_d^{\,2}\right)^{1/2}\right]\right\}}{\ln\left(4x_d/w_n\right)\left(1-x_b/x_d\right)} \tag{5.33}$$

As stated above, at a certain gas concentration the boundary meets the substrate and the profile becomes uniform again (i.e. type I). Equation 5.33 has been solved under certain conditions that give typical operating characteristics as shown in Figure 5.7.

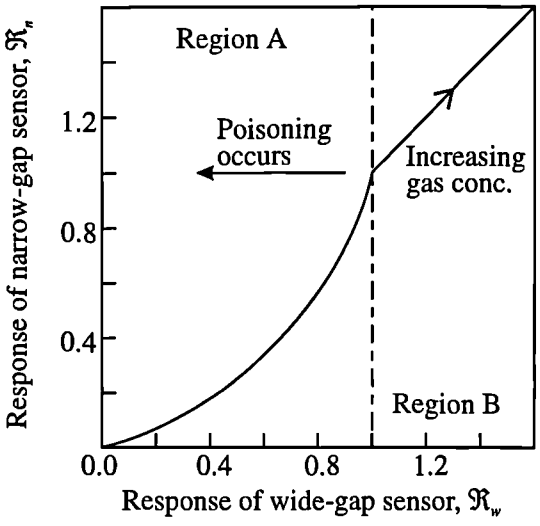

Figure 5.7 Theoretical response of the dual sensor device to a gas with a type II concentration profile (moving-boundary) with arbitrary units. The effect of poisoning is diagnosed by a shift in the operating vector. Region A is where the boundary is contained within the film, while region B is the point where the gas penetrates the film thickness forming a uniform gas concentration profile.

In region A the gas does not penetrate far enough into the film to affect all the material probed by the field lines defined by the narrow-gap electrodes and so the sensor provides a reduced response. The amount of deviation from the type I operating curve (see Figure 5.6) depends on the value of the narrow inter-electrode

gap. Once again, poisoning of the film would cause a shift in the operating line. In region B the dual sensor behaves exactly as in the case of type I profile and the characteristic operating line has a unit slope.

As mentioned above, films doped with highly active catalysts, have a small penetration depth and so the operating curve stays in region A. In this region the dual sensor response can still be used but with a different functionality than before. A careful choice of the electrode separation could ensure that the narrow-gap sensor is activated at a particular target gas concentration and thus provide an alarm level that is less prone to drift.

To investigate these theoretical properties a dual sensor device was designed (i.e. SRL125/dual) with a wide inter-electrode gap of 10 μm and a narrow inter-electrode gap of either 0.5 μm or 1.0 μm. The actual characteristics obtained for the SRL125/dual SAD are described in Chapter 8.

5.7 Conclusions

In this Chapter I have given an overview of the three sub-systems that describe a chemoresistive microsensor, namely; diffusion-reaction process, local carrier modulation and chemoresistor geometry. The underlying mechanisms for the operation of each sub-system and the associated models have been described.

The theoretical operation of a dual sensor device has been described for possible application in an intelligent sensor system for diagnosing long-term stability. The structure of this sensor has been implemented in the SRL125/dual SAD, in order to investigate its theoretical validity. The results obtained are discussed in Chapter 8.

The theoretical models outlined are highly dependent on operating temperature. This quantity is controlled by the MHP designs, which are characterised in the next Chapter.

5.8 References

5.1 J.W. Gardner, Detection of Vapours and Odours from a Multisensor Array Using Pattern Recognition Part 1. Principle Component and Cluster Analysis, *Sensors and Actuators B*, **4** (1991) 109-115.

5.2 J.W. Gardner, Intelligent Gas Sensing Using an Integrated Sensor Pair, *Sensors and Actuators B*, **26-27** (1995) 261-266.

5.3 P.K. Clifford and D.T. Tuma, Characteristics of Semiconductor Gas Sensors I. Steady State Gas Response, *Sensors and Actuators*, **3** (1982/83) 233-254.

5.4 S. Chang, Thin-Film Semiconductor NO_x Sensor, *IEEE Trans. Elec. Devices*, **ED-26** (1979) 1875-1880.

5.5 B. Bott and T.A. Jones, A Highly Sensitive NO_2 Sensor Based on Electrical Conductivity Changes in Phthalocyanine Films, *Sensors and Actuators*, **5** (1984) 43-53.

5.6 T.A. Jones and B. Bott, Gas-Induced Electrical Conductivity Changes in Metal Phthalocyanines, *Sensors and Actuators*, **9** (1986) 27-37.

5.7 J.W. Gardner, M.Z. Iskandarani and B. Bott, Effect of Electrode Geometry on Gas Sensitivity of Lead Phthalocyanine Thin Films, *Sensors and Actuators B*, **9** (1992) 133-142.

5.8 P.N. Bartlett and S.K. Ling-Chung, Conducting Polymer Gas Sensors Part II: Response of Polypyrrole to Methanol Vapour, *Sensors and Actuators*, **19** (1989) 141-150.

5.9 G. Wedler and D.F. Klemperer, *Chemisorption: An Experimental Approach*, Butterworths, London, 1976.

5.10 P.W. Atkins, *Physical Chemistry, 5 th Edition*, Oxford University Press, Oxford, 1994.

5.11 H. Windischmann and P. Mark, A Model for the Operation of a Thin-Film SnO_x Conductance-Modulation Carbon Monoxide Sensor, *J. Electrochem. Soc.*, **126** (1979) 627-633.

5.12 J.W. Gardner, A Non-Linear Diffusion-Reaction Model of Electrical Conductance in Semiconductor Gas Sensors, *Sensors and Actuators B*, **1** (1990) 166-170.

5.13 D.E. Williams, Conduction and Gas Response of Semiconductor Gas Sensors, In *Solid State Gas Sensors*, P.T. Moseley and B.C. Tofield (eds.), Adam Hilger, Bristol, 1987.

5.14 S.R. Morrison, Mechanisms of Semiconductor Gas Sensor Operation, *Sensors and Actuators*, **11** (1987) 283-287.

5.15 S. Strässler and A. Reis, Simple Models for N-type Metal Oxide Gas Sensors, *Sensors and Actuators*, **4** (1983) 465-472.

5.16 D. Kohl, Surface Processes in the Detection of Reducing Gases with SnO_2-Based Devices, *Sensors and Actuators*, **18** (1989) 71-113.

5.17 J. Crank, *The Mathematics of Diffusion*, Oxford University Press, Oxford, 1975, p. 326.

5.18 P.N. Bartlett and J.W. Gardner, Diffusion and Binding of Molecules to Sites within Homogeneous Thin Films, *Phil. Trans. R. Soc. Lond.* A (1996) 354, 35-57.

5.19 J.W. Gardner and P.N. Bartlett, Design of Conducting Polymer Gas Sensors: Modelling and Experiment, *Synthetic Metals*, **55-57** (1993) 3665-3670.

5.20 J.W. Gardner, P.N. Bartlett and K.F.E. Pratt, Modelling of Gas-Sensitive Conducting Polymer Devices, *IEE Proc.- Circuits Devices Syst.*, Vol. **142**, No. 5, (1995) 321-333.

5.21 K.D. Schierbaum, U. Weimar, W. Göpel and R. Kowalkowski, Conductance, Work Function and Catalytic Activity of SnO_2-Based Gas Sensors, *Sensors and Actuators B*, **3** (1991) 205-214.

5.22 G. Williams and G.S.V. Coles, NO_x Response of Tin Dioxide Base Gas Sensors, *Sensors and Actuators B*, **15-16** (1993) 349-353.

5.23 P.K. Clifford and D.T. Tuma, Characteristics of Semiconductor Gas Sensors II. Transient Response to Temperature Change, *Sensors and Actuators*, **3** (1982/83) 255-281.

5.24 R.K. Srivastava, P. Lal, R. Dwivedi and S.K. Srivastava, Sensing Mechanism in Tin Oxide-Based Thick-Film Gas Sensors, *Sensors and Actuators B,* **21** (1994) 213-218.

5.25 H. Geistlinger, Electron Theory of Thin-Film Gas Sensors, *Sensors and Actuators B*, **17** (1993) 47-60.

5.26 F. Gutmann and L.E. Lyons, *Organic Semiconductors*, Wiley, New York, 1967.

5.27 G. Wegner and J. Rühe, The Structural Background of Charge-Carrier Motion in Conducting Polymers, *Faraday Discuss. Chem. Soc.*, **88** (1989) 1-17.

5.28 J.W. Gardner, Electrical Conduction in Solid-State Gas Sensors, *Sensors and Actuators*, **18** (1989) 373-387.

Chapter 6

6. Characterisation and Modelling of Micro-Hotplates

6.1 Introduction

The sensor array (SRL108 and SRL125) and the discrete (SRL127) designs incorporate integrated heaters to elevate the chemoresistors to the desired operating temperature. The operating temperature is determined by the electrical power dissipated thermally to the environment. For a gas-monitoring instrument employing an array of commercial MOS gas sensors, the power consumed by the sensor heaters would be an appreciable fraction of the overall system power consumption (e.g. each Figaro gas sensors require ~ 1 W). Reducing the power consumption is vital for applications involving battery-powered portable instruments, as is the case for a mining environment e.g. personal monitors for miners. MHP structures have been employed where the heating elements are either embedded (e.g. SADs) or in a planar arrangement (e.g. discrete) in a thin thermally-resistive membrane to reduce thermal power losses. There are three different mechanisms by which thermal power can be lost; namely thermal conduction, convection and radiation, each are considered [6.1].

In this Chapter I characterise both the steady-state and transient thermal properties of the MHP structures. For open-loop control of the operating temperature it is essential that the steady-state characteristics relating the temperature to the applied electrical power are specified for each sensor. The steady-state calibration of the microheater resistance versus temperature is described first. From which the temperature coefficient of resistance (TCR) and base-line resistance of the heater are computed, so that the element can be used as a resistive temperature sensor. The steady-state I/V characteristics of the heater define both the power dissipated (i.e. $P_H=VI$) and the resistance (i.e. $R_H=V/I$). The known TCR and base-line resistance allow the measured heater resistance to be accurately converted to temperature.

Hence, the heater temperature also provides the opportunity for closed-loop temperature control, although it was not employed during the microsensor characterisation. The MHP performance was primarily assessed by measuring the heater power consumption against temperature statically and dynamically.

Another very important MHP parameter is its thermal time constant, which describes the rate at which the MHP reaches a desired steady-state value after a step change in electrical power. The time constant and corresponding frequency response have been measured for each MHP design, and the effect of various conditions on these parameters have also been investigated. These thermally insulated MHP structures inherently have a fast response time, because of their small thermal capacitance and thermal conductance. Work is currently underway to investigate the advantages of pulsed mode heating which requires a fraction of the power consumed for continuous heating on these devices. The results will be reported elsewhere.

In Chapter 3 a model proposed by U. Dibbern [6.2] was used to calculate the theoretical power consumption of the MHP designs. The comparison with the actual characteristics provides an assessment of the limitations of the model. However, modelling was a fundamental part of optimising the design of our microsensors. This minimised development costs by reducing the number of silicon runs needed to produce a microsensor with the desired specification. Characterisation of the MHPs then provides the information necessary to evaluate the accuracy of the models. Two different modelling approaches have been investigated; these were a finite element method (FEM) and a lumped element method. These models are used to define the steady-state and transient characteristics of a MHP. The uses and limitations of each method are described in this Chapter.

6.2 Steady-State Characterisation of MHP

6.2.1 Characterisation of Microheater Resistance and Temperature

The resistance heaters were calibrated over a temperature range of RT to approximately 130°C. The resistance was measured by a Maplin M-4510 Digital Multimeter (DMM), while the devices were housed in a temperature controlled (±1°C) oven. A typical response of three microheaters on a SAD is shown in Figure 6.1.

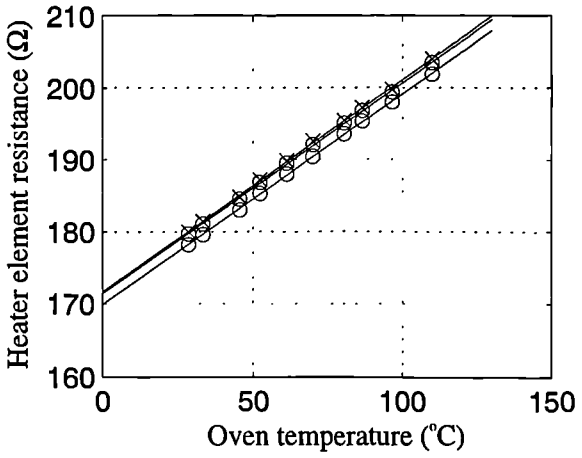

Figure 6.1 Plot of resistance versus temperature for 3 heater elements of a SRL125/MOS SAD.

These characteristics are of the form described in Section 3.2.3 by equation 3.1. The microheaters have been calibrated by calculating the TCR and base-line resistance from this data. The TCR was calculated using a least squares fit to the data. It can be seen that the lines are parallel and so differences in the temperature sensitivity are small, whereas the larger differences in resistance can be attributed to slight variations in the heater geometry and material composition. The properties measured for each microheater design are summarised in Table 6.1 and compared to the theoretical values used during the design.

Each design with the same heater composition should have the same TCR, because this property is independent of heater geometry. From Table 6.1 the TCR is $2.0 \times 10^{-3} \pm 0.3 \times 10^{-3}$ /°C for Pt elements. It was found that the TCR errors were small for microheaters on the same device, however, the errors increase between devices fabricated on different parts of the wafer or different wafer runs. Likewise, the heater resistance at RT was expected to be the same for similar designs, apart from a small error due to geometrical variability. Although the average resistance difference between Pt elements on the same chip is only 0.3 Ω, the resistance error between different devices can be ± 10 Ω. The error is even more pronounced between microheaters fabricated in different batches, as is the case for SRL108/CP and SRL125/MOS devices.

Table 6.1 Experimental and theoretical values of microheater parameters for different designs.

Sensor design	Experimental Resistance Ω, at 22.0 ± 1°C	Experimental TCR × 10^{-3} /°C (theory 3.8 × 10^{-3} /°C)	Theoretical heater resistance Ω, at RT
SRL108/CP	189.6 ± 20	1.71 ± 0.05	49.5
SRL125/CP	60.6 ± 10	2.14 ± 0.05	20.4
SRL125/MOS	109.0 ± 10	2.03 ± 0.05	49.5
SRL125/XPc	45.9 ± 10	2.24 ± 0.05	21.3
SRL125/dual	90.7 ± 10	1.94 ± 0.05	49.5
SRL127 Discussed later	16.2 ± 2	2.11[†]	

The difference between the theoretical and the measured resistances is likely to be due to increased bulk scattering from a more polycrystalline structure and higher impurity level. A high impurity concentration may be expected for sputtered films, because of the presence of the reactor gas in the thin film [6.3]. Furthermore, the influence of the 10 nm Ta adhesion layer [6.4] may also increase the experimental resistivity from the bulk value used (11 × 10^{-8} at RT). Variations in the metal microstructure and impurity concentration across the wafer would explain the localised improvement in reproducibility.

The same properties have been characterised for the Au heater employed in the SRL127 designs, as shown in Figure 6.2. A TCR of 2.108 × 10^{-3} /°C was calculated from a least squares fit. The heater was designed to have a theoretical value of 11.5 Ω at 100°C, compared with a measured value of 20.3 Ω.

[†] It must be noted that not enough SRL127 devices were calibrated to allow an accurate TCR tolerance to be stated.

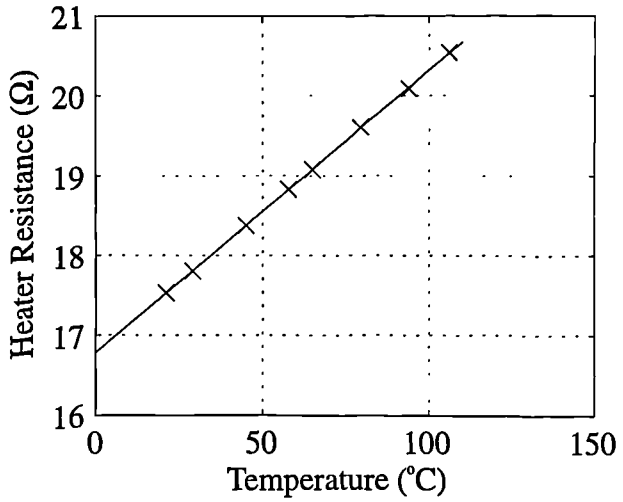

Figure 6.2 Plot of temperature against heater resistance for a SRL127 device heater.

6.2.2 Steady-State Power Consumption of Micro-Hotplates

Electrical power applied to the microheater is dissipated thermally from the MHP. When the MHP reaches its steady-state operating temperature, the electrical power consumption must be in equilibrium with the thermal losses. The steady-state power consumption was measured by applying a constant current (with a Knick Current Calibrator, Model J152) through the heater element, and recording the voltage developed across it (with a DMM). The I/V characteristic allows the calculation of the electrical power and the heater resistance. Whereupon, the resistance was then converted to the operating temperature using the temperature/resistance calibration described in Section 6.2.1. These measurements were carried out for each of the different MHPs. For the sake of convenience the heater resistance/temperature calibration function was assumed to have only a small extrapolation error (~ ±1 % up to 700°C) because the TCR for Pt is known to be extremely linear. Plotting the heater power against operating temperature, allows the heater performance to be determined. A comparison of the power consumption for each MHP geometry is shown in Figure 6.3 and Figure 6.4, for the sensor array and discrete devices, respectively.

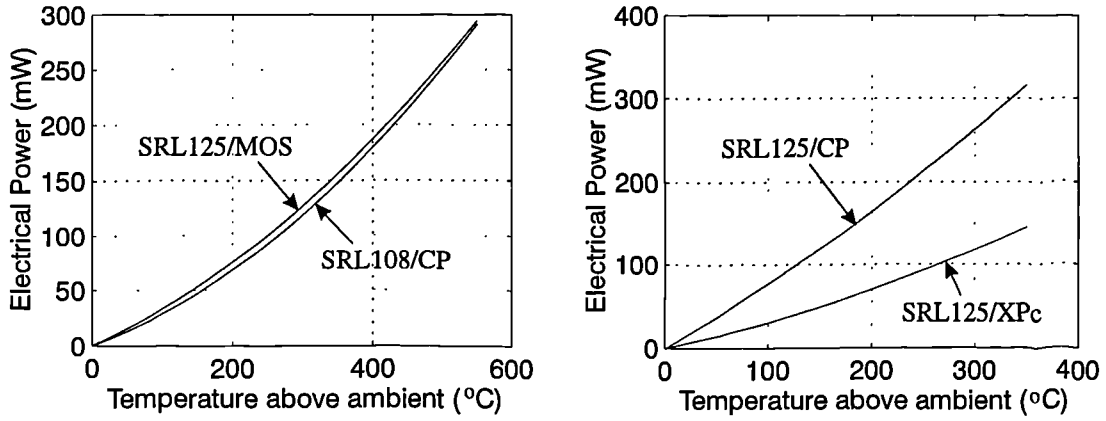

Figure 6.3 Power consumption characteristics for SRL108/CP, SRL125/MOS, CP and XPc devices represented by second-order polynomials fitted by least squares method to data. The MHPs were uncoated.

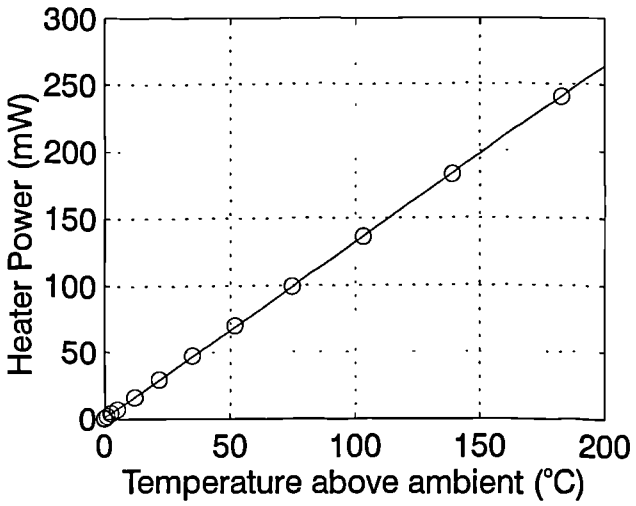

Figure 6.4 Power consumption characteristics for a SRL127 MHP with a first-order least squares fit. The MHP was uncoated.

As expected the power consumption of the SRL127 MHP is considerably higher than that of the SAD MHPs, although the power consumption is still less than 100 mW over the temperature range of interest (0 to 100°C). The power consumption of the SADs is extremely low, especially the SRL108/CP, SRL125/CP and SRL125/MOS MHPs which heat two chemoresistors.

For the SADs at temperatures less than 150°C the power curves are approximately linear. As shown by Figure 6.3, the power loss becomes non-linear at temperatures higher than 150°C.

An empirical model has been used to describe the data, according to a second-order equation

$$P_H = \alpha_P(T_H - T_a) + \beta_P(T_H - T_a)^2 \qquad (6.1)$$

where P_H is the heater power, T_H-T_a represents the difference between the operating temperature (T_H) and the ambient temperature (T_a), and α_P and β_P are the thermal loss-coefficients [6.5]. The values of the coefficients experimentally determined for the SADs are shown in Table 6.2.

Table 6.2 Thermal loss-coefficients for MHPs.

Device	α_P (mW/°C)	β_P (μW/°C^2)
SRL108/CP	0.233	0.537
SRL125/MOS	0.229	0.535
SRL125/XPc	0.260	0.438
SRL125/CP	0.721	0.517
SRL127	1.315	Second-order term neglected

It must be noted, that the standard deviations on α_P and β_P are ± 0.02 mW/°C and ± 0.02 μW/°C^2, respectively, for heaters on the same device. Each heater must be calibrated individually to ensure an accurate operating temperature (< ±2°C).

6.2.3 Contributions from Different Thermal Loss Mechanisms

To produce accurate models of the steady-state behaviour of MHPs, the contributions to thermal loss by the different mechanisms were investigated for a SRL125/MOS device. In general the various heat transfer processes are categorised into three basic mechanisms; namely conduction, convection and radiation [6.1].

Heat conduction is the term applied to the mechanism of internal energy exchange within a body or from one body to another, by the exchange of the kinetic energy of motion of the molecules by direct communication, or by the drift of free electrons in the case of heat conduction in metals. The distinguishing feature of conduction is that it takes place within the boundaries of a body, or across the

boundary between bodies in contact, without an appreciable displacement of the matter comprising the body.

Convection is the term applied to the heat transfer mechanism which occurs in a fluid by the mixing of one portion of the fluid with another portion. The actual process of energy transfer from one fluid molecule to another is still one of conduction, but the energy may be transported from one point in space to another by the displacement of the fluid itself. In some cases, the fluid motion may be caused by external means (e.g. fan, pump), which is known as "forced convection". While, if the fluid motion is caused by density variations which are created by the temperature differences existing in the fluid mass, the process is called "free convection". Also by varying the fluid flow velocity, a mixed phase of both free and forced convection characteristics occurs between the transition from purely free convection to purely forced convection.

Thermal radiation is the term used to describe the electromagnetic radiation which has been observed to be emitted at the surface of a body at an elevated temperature. This electromagnetic radiation is emitted in all directions and may pass from one body to another without the need of a medium of transport between them.

The magnitude of contributions to thermal power loss by each of the mechanisms described above (e.g. conduction, convection and radiation) are investigated. It must be noted that the quantity of heat loss by convection through the air, must first be transferred at the boundary between the MHP and air by a conduction process.

The power loss characteristics described in the previous Section were measured in still air at RT. To remove the convective heat transfer component the power consumption was also measured under vacuum (10^{-5} Torr) by mounting the MHP in a thin film evaporator unit (Bir-Vac Ltd.). The results allowed a comparison of thermal power losses for a MHP in still air and in vacuum, as is shown in Figure 6.5.

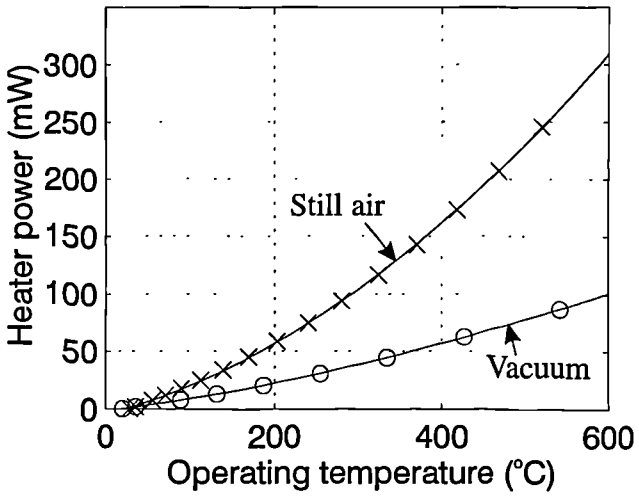

Figure 6.5 Comparison of a SRL125/MOS MHP power consumption in still air at 30°C (conduction, convection and radiation losses) and in a vacuum at 10^{-5} Torr (conduction and radiation).

Assuming that heat loss in the vacuum does not contain any convective heat losses (due to the absence of air) the MHP power consumption under vacuum is due to conduction and radiation heat loss only. Moreover, the magnitude of convective power lost in still air can be derived from the difference of the two characteristics.

The radiation power loss is expected to be small over the temperature range used during characterisation. However, the theoretical magnitude can be derived using the well known Stefan-Boltzmann law [6.1, 6.6],

$$P_r(T) = \varepsilon\sigma A\left(T_H^{\,4} - T_a^{\,4}\right) \tag{6.2}$$

where P_r is the net power radiated out of the body, A is the heated area, ε is the effective emissivity of the surface and σ is the Stefan-Boltzmann constant (56.7×10^{-9} W/m^2K^4). Assuming the MHP surface is a black body ($\varepsilon = 1$) and emits radiation from a heater area of 4.977×10^{-7} m^2. Note that this area is doubled to define A, because radiation is emitted from both sides of the SRL125/MOS MHP. This theoretical P_r can be subtracted from the heater power characterised in a vacuum to obtain a theoretical conduction power loss (P_m). The calculated thermal power contributed by convection (P_a), conduction and radiation losses are shown in Figure 6.6.

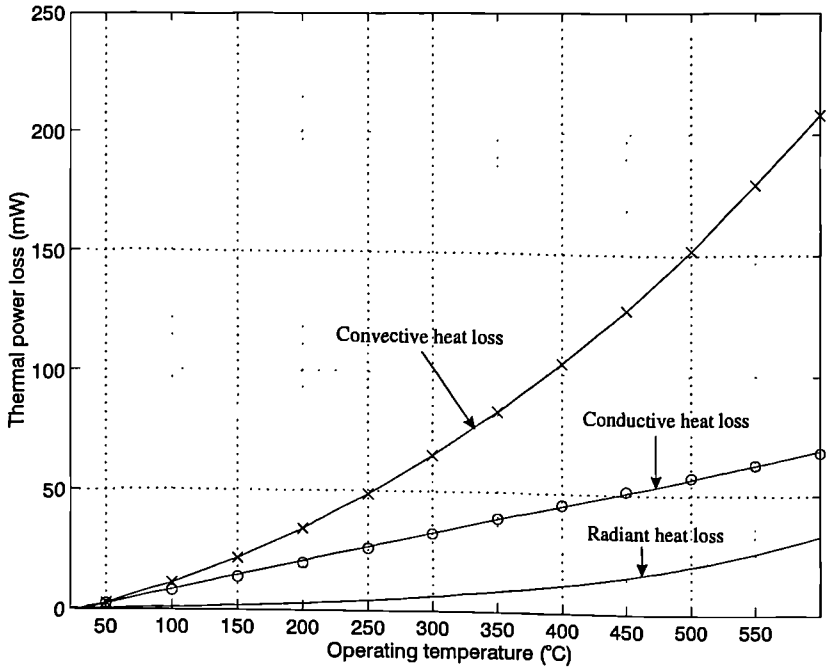

Figure 6.6 Thermal power loss of various heat-transfer mechanisms for a SRL125/MOS device.

From Figure 6.6 it is apparent that the conductive power loss can be expressed by a first-order expression, where

$$P_m(T_H) = (0.123 \times T_H) - 3.295 \tag{6.3}$$

and the convection power loss can be expressed by a second-order expression, where

$$P_a(T_H) = (4.129 \times 10^{-4} T_H^{\,2}) + (0.104 \times T_H) - 3.332 \tag{6.4}$$

It has been shown that the heat loss contribution from convection is a significant portion of the total heat loss above approximately 50°C.

If the MHP was placed in a gas flow, additional heat would be transferred to the flow by forced convection. The effects of forced convection are normally not considered because gas sensors usually have protective mesh surrounds and operate in low flows (e.g. Figaro recommend an average flow velocity of ≤ 50 cm/s). However, the significance of this effect is investigated.

A SRL125/MOS device was mounted in a chamber in the microcomputer controlled mass flow system, which makes up part of the gas sensor test system

described in Chapter 7. The flow can be controlled from 0 to 500 ml/min, which relates to an average flow velocity (U) of 0 to 2.78 cm/s, at the point in the sensor chamber with a cross-sectional area of 3 cm^2. The MHP structure was then heated to 472°C with a power consumption of 207.6 mW. The effect of U on operating temperature and power consumption were determined from the microheaters I/V characteristics, as shown in Figure 6.7.

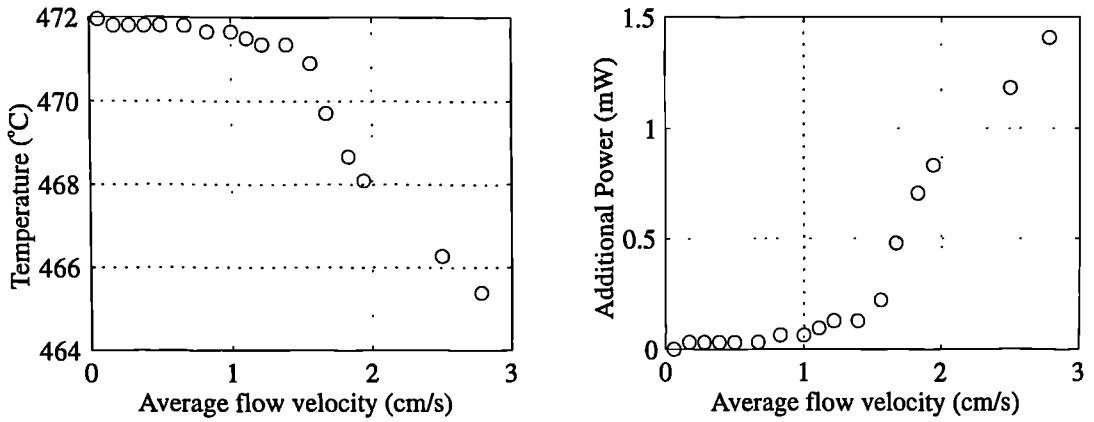

Figure 6.7 The effect of average flow velocity on; (a) operating temperature, and (b) power consumption for constant-temperature operation.

The operating temperature reduces when $U > \sim 1.5$ cm/s due to the additional forced convection losses. However, below this value, the MHPs thermal properties appear almost independent of U. The additional power required to maintain the MHP at a constant temperature is shown in Figure 6.7(b). However, the gas flow can be neglected as a sub-system input variable, because the operating temperature only changes by approximately 1.5 %, at the maximum U possible in the test system.

6.2.4 Assessment of Model Used to Design Micro-Hotplate

To recapitulate from Chapter 3, Dibbern's heat loss model [6.2] was used to estimate the thermal losses for the MHPs, in order to design a suitable heater geometry. A comparison of the theoretical and actual power losses at specific operating temperatures are shown in Table 6.3.

Table 6.3 Theoretical and actual MHP power consumption for SADs.

Sensor array device	Operating temperature (°C)	Theoretical power consumption (mW)	Actual power consumption (mW)
SRL108/CP	550	170	270
SRL125/MOS	550	170	274.3
SRL125/XPc	300	94	104.3
SRL125/CP	125	17	76.1

It is apparent that the present model parameters used during the MHP design, did not give a particularly good prediction. The model described in Chapter 3 is the contribution of the three heat-transfer mechanisms,

$$P_H = P_m + P_a + P_r \tag{6.5}$$

where P_H is the total thermal power loss.

The theoretical power loss calculated for each heat-transfer mechanism derived by Dibbern's [6.2] model, can be compared with the power losses derived in Section 6.2.3, as shown in Figure 6.8.

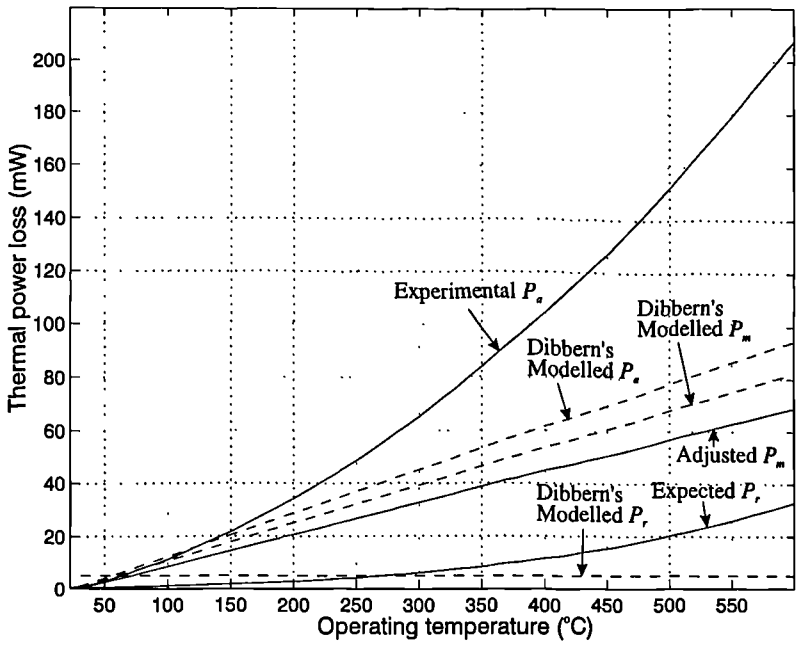

Figure 6.8 Comparison of the heat loss mechanisms derived from the model (dashed lines) and the measured and theoretical values (solid lines) for a SRL125/MOS device described in Section 6.2.3.

Comparing Dibbern's model and adjusted conduction power loss, it is apparent that the first-order P_m model is reasonable. Equation 3.10 describes Dibbern's model for P_m which is dependent on the membrane geometry, the specific heat conductivity (κ) of the membrane material, and on the temperature difference between the MHP and ambient temperature. The modelled P_m was achieved by using a membrane thickness of 10 μm and κ = 2.5 W/m.K. Effective medium theory can be used to model a multi-layer structure that contains different materials with different thermal properties. If κ remains the same, then the accuracy of P_m can be improved by using an effective membrane thickness of 8.5 μm.

The main difference between the measured and modelled convection losses is that the P_a model assumes a first-order expression, while the measured data shows a good second-order polynomial fit. The model is therefore limited to a temperature range of 25°C to 150°C. To obtain better accuracy at higher temperatures the gradient of the P_a model can be increased by increasing the effective hotplate area. However, once this is implemented the model only becomes accurate at a temperature where the P_a model intersects the actual convection characteristics.

The model simplification to assume a constant radiation loss for P_r is fundamentally different from the Stefan-Boltzmann law, as seen in Figure 6.8. This limits the P_r model accuracy to a small temperature range either side of the intersection with the plot of the Stefan-Boltzmann assumption (at approximately 270°C).

The accuracy of the model can be improved by using the Stefan-Boltzmann law to account for radiation losses. Also the effective geometry of the MHP can be adjusted to improve accuracy, which would be limited to a small temperature range.

Using the results obtained with the SRL125/MOS device the accuracy of the model can be improved by deriving better model coefficients. However, each of the MHP designs must be characterised by the same procedure, to derive the actual thermal properties.

6.2.5 Review of the Micro-Hotplate Physical Properties that Determine Thermal Power Loss

The main geometrical properties of the MHP structure are shown in Figure 6.9.

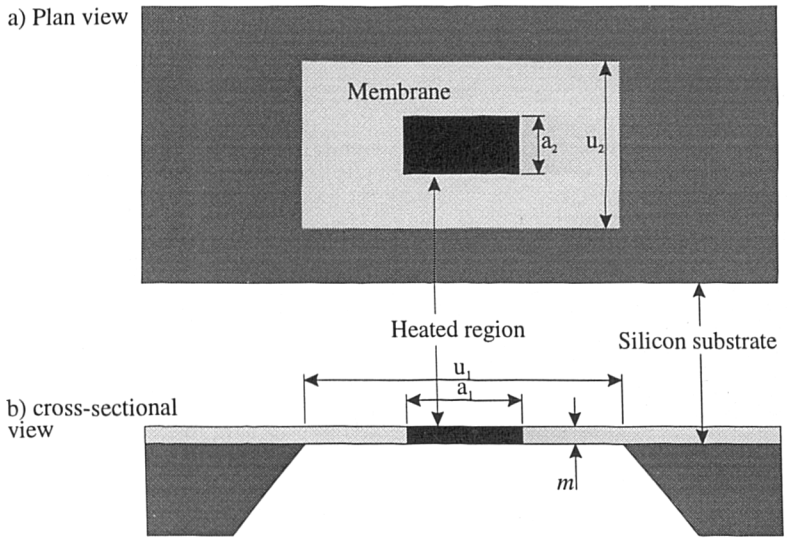

Figure 6.9 Schematic of the main geometrical properties of the SAD MHP: (a) plan view and (b) cross-sectional view.

The heated volume $a_1 \times a_2 \times m$ mm^3 is assumed to be isothermal. The dimensions of each SAD design thermally characterised are shown in Table 6.4

Table 6.4 MHP design dimensions.

Devices	a_1 mm	a_2 mm	u_1 mm	u_2 mm	Membrane details
SRL108/CP	1.345	0.370	3.465	1.110	SiO_2 + Si_3N_4, m = 0.08 + 0.50 μm, respectively
SRL125/MOS	1.345	0.370	3.235	1.110	
SRL125/XPc	1.290	0.425	2.541	1.275	
SRL125/CP	0.270	0.270	0.810	0.810	
SRL127	-	-	1.800	1.250	Si + $Si_xO_yN_z$, m = 5.0 + 0.2 μm, respectively

The SRL127 designs are heated in two regions because of the planar structure used, this makes it difficult to calculate the effective geometry.

Each membrane is comprised of different materials. Where the κ of the different materials are the physical property that determines the amount of conduction power loss. The values of κ for some of the materials employed are shown in Table 6.5.

Table 6.5 Thermal conductivity of membrane materials.

Material	$\kappa(T)$ (W/m.K)	T (K)	Reference
Au	318	300	[6.6]
Si	168	273	[6.7]
SiO_2	1.4	300	[6.6]
Si_3N_4	9-30	300	[6.6]
$SiN_{1.1}$	3.2 ± 0.5	300	[6.8]

For modelling applications, the membrane is simplified as a homogeneous layer. For this assumption to provide accurate results suitable values for κ and membrane effective thickness (m) must be selected.

Comparing the power consumption of the SRL127 device to the SRL108 and SRL125 devices, the higher power consumption for the SRL127 device can be explained by the higher thermal conduction through the thicker membrane (which is partly composed of a Si layer). Also the higher than expected power consumption of the SRL125/CP device, could be explained by the high surface-area coverage of the Au electrodes over each membrane.

6.3 Transient Micro-Hotplate Characteristics

Investigations into thermal power loss have identified the mechanisms by which the heat generated is transferred to the environment. The results were obtained at steady-state i.e. when the heat generated is in equilibrium with the heat loss. This Section describes the MHPs characteristics when the thermal system is not in equilibrium. The transient response of the MHP can be modelled as having an MHP surface temperature output variable and a heater power input variable, as shown in Figure 6.10.

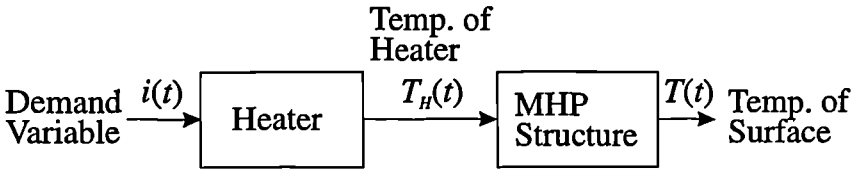

Figure 6.10 Control block diagram of the operating temperature.

The thermal system of the MHP is no different from any other physical system, in that the output variables do not reach their steady-state value instantaneously, due to energy storage in the MHP, known as the thermal capacity (C). In general, $C=c_p \times m$, where c_p is the specific heat property of a material and m the mass of the body. Hence, for microstructures with a very small m, the thermal capacity is corresponding small. When considering the MHP, this property produces a very rapid change of heat storage to an input transient, and consequently the MHP obtains its steady-state temperature in a very short time (< 15 ms).

A rapid thermal time constant allows the operating temperature of the chemoresistors to be pulsed rapidly. A pulsed-mode of operation alters the reaction kinetics on the sensing film surface, producing a time-varying response signature that is characteristic of the gas being sensed [6.9], which may improve selectivity of a gas sensor system. Also the power consumption for a pulsed-mode may be significantly less than for a chemoresistor operating at a constant temperature.

The transient response of the MHPs also provides information that can be used to produce a dynamic model of the microstructures.

6.3.1 Measured Transient Response

The transient response of the MHP was investigated indirectly by placing the microheater resistance (R_H) in a potential divider network with a commercial resistor (R) with a value of 100.26 Ω, as shown in Figure 6.11.

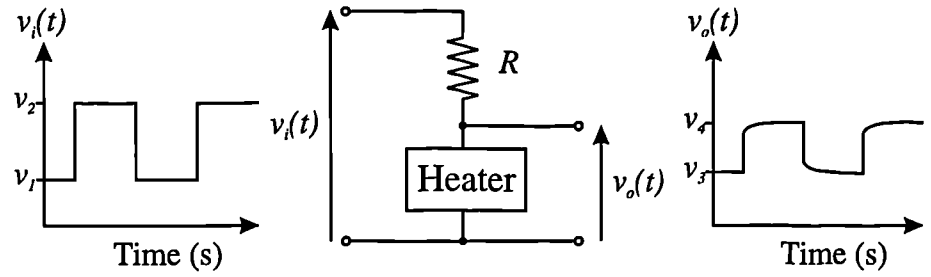

Figure 6.11 Schematic of potential divider network (centre) used to measure MHP transient characteristics, and a transient response (right) to a square wave input signal (left).

A square wave with a variable d.c. offset ($v_i(t)$) was applied to the potential divider with a function generator (Thandor, TG501, supplied by R.S. Ltd.). The indirect measurement of the MHP thermal time response to a square wave assumes that the temperature of the resistance heater element (T_H) responds instantaneously to an applied voltage, and the voltage across R reaches steady-state instantly. These assumptions are valid if the actual time response of these actions are much less than the time it takes the MHP to reach thermal equilibrium. The output voltage $v_o(t)$ shown in Figure 6.11 is a typical response of the network, which is explained as follows:

Assuming that $v_i(t)$ starts at the lower voltage level v_1, this voltage gets attenuated through the circuit by the ratio $R_H/(R+R_H)$ to give the voltage v_3. At this point R_H is at a base-line resistance (R_B). At the instant $v_i(t)$ steps up to the higher voltage level of v_2, $v_o(t)$ is initially attenuated by the ratio $R_B/(R+R_B)$. However, at this higher voltage level more heat is generated, which increases the operating temperature of the sensor. An increase in temperature corresponds to an increase in R_H, hence more of $v_i(t)$ appears across the microheater. This is reflected by an increase in $v_o(t)$, that continues to increase as R_H increases, until the MHP is in thermal equilibrium. At this steady-state region, R_H has increased by a characteristic resistance ΔR_S, so $R_H = R_B+\Delta R_S$. The input voltage v_2 is now attenuated by $(R_B+\Delta R_S)/(R+R_B+\Delta R_S)$ to produce the steady-state output voltage v_4.

The opposite happens during a step fall in $v_i(t)$, where the transient $v_o(t)$ relates to MHP cooling. Even though the temperature is not being measured directly, the time constant of the transient voltage signal can be assumed to be the same as the thermal time constant.

The $v_o(t)$ transient response information was captured in the time domain of a frequency analyser (Hewlett Packard, 3563A), as shown in Figure 6.12, for a SRL125/MOS device.

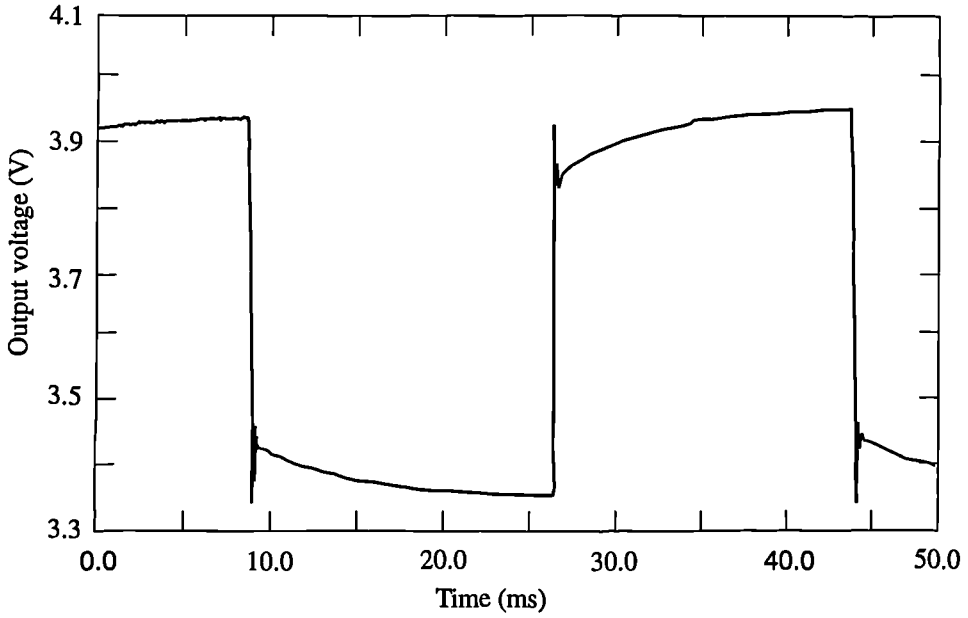

Figure 6.12 Transient heater response of a SRL125/MOS device, to a square wave drive voltage.

The transient data can be analysed to obtain the time constant (the time taken for a transient signal to reach 63 % of the final steady-state value). With respect to Figure 6.11, the output voltage values for v_3 and v_4 are 3.355 and 3.940 volts, respectively. These steady-state values correspond to operating temperatures of 228.7°C and 275.8°C, respectively. From the form of the MHP characteristics shown in Figure 6.12 the thermal system can be described by a first-order model, with a time constant (τ) calculated as 4.336 ms. Similar results were obtained for the SRL108 and SRL125 devices, as described in Table 6.6.

The relationship between τ and the device operating temperature was investigated. The operating temperature was varied by applying a larger square-wave voltage (pk-pk). The characteristics for a SRL125/MOS device is shown in Figure 6.13.

Table 6.6 Transient details of different SADs.

Device	v_3 (Volts)	v_4 (Volts)	Operating temp. at v_3 (°C)	Operating temp. at v_4 (°C)	τ (ms)
SRL108/CP	3.353	6.261	184.8	367.6	4.843
SRL125/MOS	3.355	3.940	228.7	275.8	4.336
SRL125/CP	2.980	4.250	168.8	293.4	2.775
SRL125/XPc	2.255	3.900	242.0	504.3	4.766

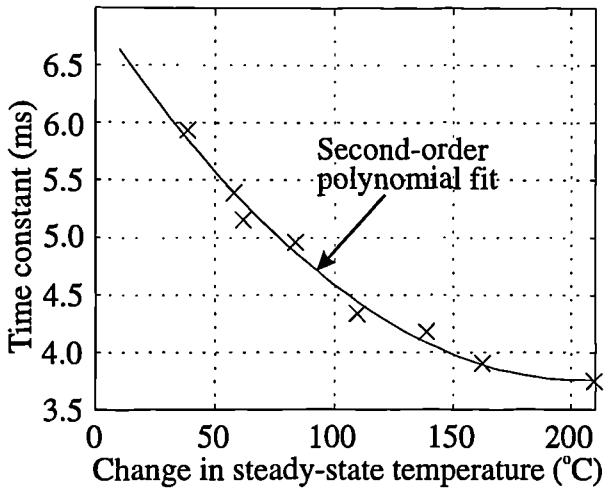

Figure 6.13 Relationship between the time constant and the change in steady-state operating temperature for a SRL125/MOS device.

There are temperature dependent thermal properties (e.g. κ and c_p) throughout the MHP that govern the time constant. It is therefore difficult to quantitatively determine the contribution of particular properties. However, some properties may be dominant, e.g. the thermal conductivity of Si_3N_4 decreases by ~ 20 % over the temperature range 0 to 300°C [6.7].

The frequency response of the MHP system was also investigated to obtain the time constant in the frequency domain. The frequency analyser applied a sinusoidal signal (2 $V_{pk\text{-}pk}$), offset by + 2 $V_{d.c.}$ signal to the potential divider network, while $v_o(t)$ was measured on a separate channel. The attenuation ($v_o(t)/v_i(t)$) was then scanned over a frequency range of 0.5 to 250 Hz, as shown in Figure 6.14, for a SRL125/MOS device.

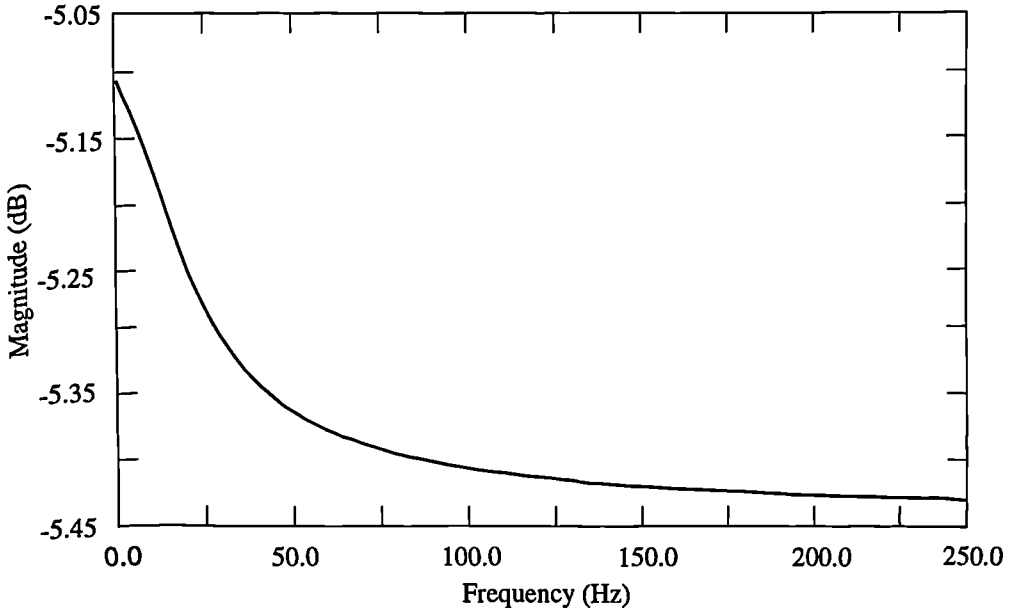

Figure 6.14 Frequency response of a SRL125/MOS MHP.

The frequency at which the attenuation is "cut off" is an indication of the time constant. At very low frequencies (where the frequency is much less than $1/\tau$) the MHPs operating temperature varies sinusoidally with time, between the temperatures according to the maximum and minimum voltages. However, as the frequency of $v_i(t)$ increases (when the frequency is comparable or greater than $1/\tau$) the MHP cannot reach thermal equilibrium and therefore does not reach the maximum and minimum temperatures achievable at low frequencies. Consequently, the pk-pk voltage across the microheater decreases, resulting in a drop in the attenuation. This effect increases to an asymptotic value (when the frequency is much greater than $1/\tau$) where the change in temperature is negligible. Higher MHP thermal time constants, have a lower cut-off frequency, as shown later in Section 6.3.2. This is illustrated in Figure 6.15, where three SRL125/XPc MHPs are compared; one device is uncoated, one has 0.685 μm of MgPc and another device has a ~ 2.20μm of PbPc. The layers of XPc are expected to increase the thermal conduction loss and thermal capacity of the structure, which consequently increases the thermal time constant. By comparing the frequency responses of the different structures its is apparent that this is the case.

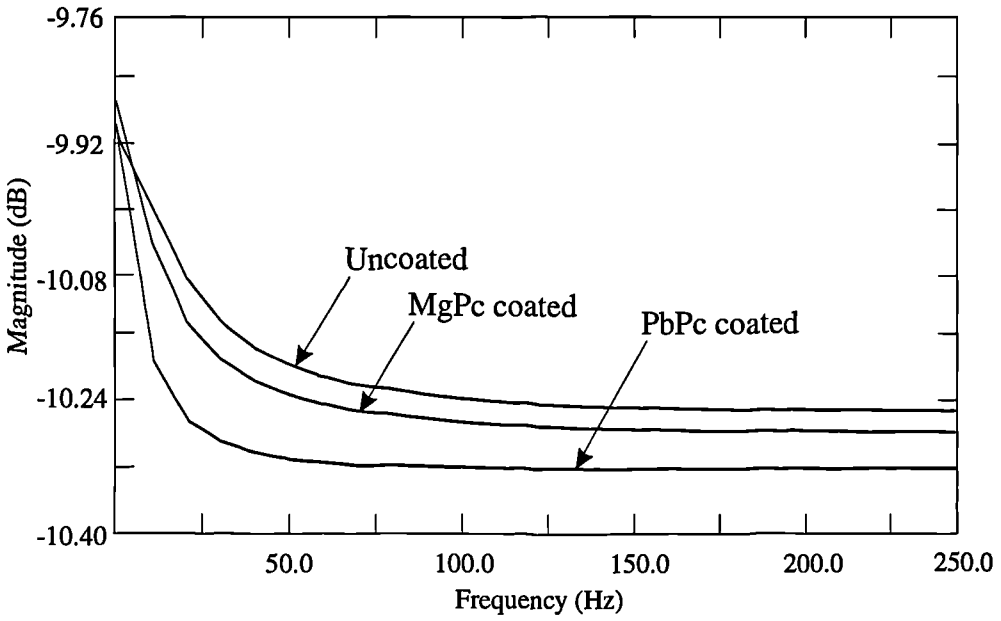

Figure 6.15 Comparison of the frequency response of SRL125/XPc MHPs uncoated and coated with MgPc (0.685 μm) and PbPc (2.20 μm).

6.3.2 Analysis of Transient Characteristics

If the microheater is considered as an unidentified system, the characteristics obtained allow an equivalent electrical circuit to be proposed, which is physically non-representative of the thermal loss mechanisms. As seen from the measured data the transient response is recognised as a first-order system [6.10].

At the steady-state limits the system can be modelled by resistive elements. If the system is initially at a low voltage, this corresponds to a characteristic microheater resistance value (R_B). The response to a voltage step results in the resistance increasing to a steady-state value ($R_B+\Delta R_S$) depending on the voltage change by a characteristic amount. The transient response between these two steady-state limits is introduced by placing a capacitance (C) in parallel with R_S, as shown in Figure 6.16. The resistor values are dependent on $v_i(t)$ according to the characteristics obtained during steady-state calibration.

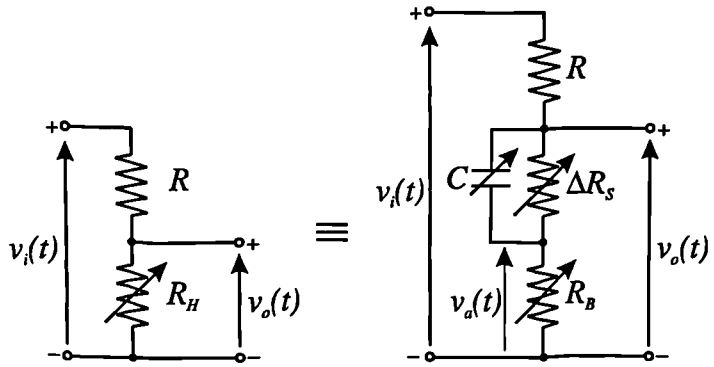

Figure 6.16 MHP transient response equivalent circuit.

An electrical input-output model can be generated by applying the node-equation method [6.10] to the circuit. The two current-law equations for the nodes whose voltages are unknown, are

$$\frac{(v_o - v_i)}{R} + \frac{(v_o - v_a)}{\Delta R_S} + C\left(\dot{v}_o - \dot{v}_a\right) = 0 \tag{6.6}$$

$$\frac{v_a}{R_B} + \frac{(v_a - v_o)}{\Delta R_S} + C\left(\dot{v}_a - \dot{v}_o\right) = 0 \tag{6.7}$$

By combining equations 6.6 and 6.7 to eliminate v_a, the input-output differential equation relating v_i and v_o is derived,

$$\dot{v}_o + \left[\frac{\left(\frac{\Delta R_S + R_B + R}{\Delta R_S}\right)}{C(R + R_B)}\right] v_o = \left(\frac{R_B}{R + R_B}\right)\dot{v}_i + \left[\frac{\left(\frac{R_B + \Delta R_S}{\Delta R_S}\right)}{C(R + R_B)}\right] v_i \tag{6.8}$$

The transfer function $H(s)$ of this system can be expressed in Laplace transforms, where $H(s)$ is defined as the ratio of the Laplace transform of the output $V_o(s)$ to the Laplace transform of the input signal $V_i(s)$. $H(s)$ describes the properties of the system alone; that is, the system is assumed to be in its quiescent state, hence the initial conditions at $t = 0$ are assumed to be zero. Therefore,

$$H(s)=\frac{V_o(s)}{V_i(s)}=\frac{\left(\frac{R_B}{R+R_B}\right)s+\left[\frac{\left(\frac{R_B+\Delta R_S}{\Delta R_S}\right)}{C(R+R_B)}\right]}{s+\left[\frac{\left(\frac{\Delta R_S+R_B+R}{\Delta R_S}\right)}{C(R+R_B)}\right]} \tag{6.9}$$

The response to a unit step function input can be described in the Laplace domain by multiplying the transfer function by the unit step Laplace transform (*1/s*). Thus

$$V_o(s)=\frac{1}{s}\times H(s) \tag{6.10}$$

This can now be solved to describe the transient response to the unit step input in the time domain, hence

$$\frac{v_o(t)}{v_i(t)}=\left(\frac{R_B+\Delta R_S}{\Delta R_S+R_B+R}\right)+\left[\left(\frac{R_B}{R_B+R}\right)-\left(\frac{R_B+\Delta R_S}{\Delta R_S+R_B+R}\right)\right]\exp^{-\left[\frac{R_B+\Delta R_S+R}{\Delta R_S C(R_B+R)}\right]t} \tag{6.11}$$

This can be compared to the general first-order system response to a constant input,

$$v_o(t)=v_{SS}+[v_o(0)-v_{SS}]\exp^{-\frac{t}{\tau}} \tag{6.12}$$

where $v_o(0)$ is the initial output voltage at $t=0$, v_{SS} is the output voltage reached at steady-state and τ is the characteristic time constant. Therefore, considering equation 6.11,

$$v_o(0)=\left(\frac{R_B}{R_B+R}\right)v_2,\ v_{SS}=\left(\frac{R_B+\Delta R_S}{R_B+\Delta R_S+R}\right)v_2,\ \text{and}\ \tau=\frac{C\Delta R_S(R_B+R)}{R_B+\Delta R_S+R}$$

To use this model for analysis the equivalent component values have to be established. From the data shown in Figure 6.12 and the steady-state characteristics, R_B = 151.1 Ω, ΔR_S = 9.55 Ω and R = 100.26 Ω. Substituting these resistances and τ = 4.336 ms into the time constant expression, a capacitance of $C = 4.713 \times 10^{-4}$ F is derived. The expression is only valid for a particular voltage, because R_B and ΔR_S are voltage dependent. These component values relate to a step voltage to a steady-state value of 3.934 V. The solution to a unit step function is multiplied by this constant voltage to give the analytical response of the system, as shown in Figure 6.17.

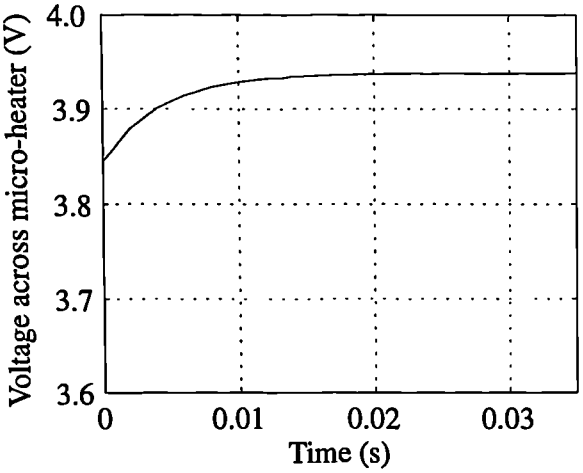

Figure 6.17 Theoretical transient response of the equivalent circuit to step input to 3.934 volts.

This shows a good fit to the measured data shown in Figure 6.12.

The frequency response of the system transfer function $H(s)$ can be derived by replacing s by $j\omega$, where ω is frequency (rad/s). To find the magnitude $M(\omega)$ of $H(j\omega)$, the magnitude of the numerator is divided by the magnitude of the denominator, obtaining

$$M(\omega) = \frac{\left[C(R+R_B)\right]^2\left(\frac{R_B}{R+R_B}\right)^2\omega^2 + \left(\frac{R_B+\Delta R_S}{\Delta R_S}\right)^2}{\left[C(R+R_B)\right]^2\omega^2 + \left(\frac{\Delta R_S+R_B+R}{\Delta R_S}\right)^2} \qquad (6.13)$$

Using R = 100 Ω, R_B = 150 Ω, ΔR_S = 10 Ω and $C = 4.7 \times 10^{-4}$ F, the theoretical frequency response is shown in Figure 6.18.

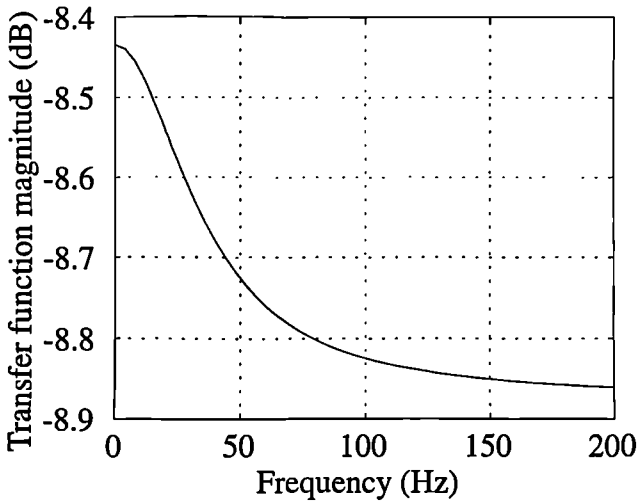

Figure 6.18 Theoretical frequency response.

This has the same form as the data obtained as shown in Figure 6.14. The frequency value that corresponds to the characteristic time constant (τ) can be evaluated by substituting $\omega = 1/\tau$ into the expression for $M(\omega)$. This gives a theoretical value of

$$H\left(\frac{1}{\tau}\right) = \frac{\left(\frac{R_B}{R+R_B}\right)^2 + \left(\frac{R_B+\Delta R_S}{R_B+\Delta R_S+R}\right)^2}{2} \qquad (6.14)$$

Using the component values specified above, $M(1/\tau)$ = -8.65 dB, at this magnitude the frequency is ≈ 35 Hz, which gives $\tau = 4.5 \times 10^{-3}$ ms.

This system analysis allows an equivalent circuit to be generated, which could be employed in circuit modelling (e.g. PSPICE), although the model is limited because the component values depend upon the voltage magnitude and are thus non-linear.

6.4 Modelling of Micro-Hotplate

For future MHP designs it would be desirable if there were accurate models which would allow prediction and simulation of the MHP thermal properties. This would allow design optimisation before commitment to sensor fabrication. The basic problem of thermal modelling is to provide a means of calculating the spatial and temporal distribution of temperature through a membrane structure in which heat is generated, under certain initial and boundary conditions. There are different approaches to thermal modelling available, which include analytical [6.11, 6.12], numerical e.g. using a finite element method (FEM) [6.11], or circuit simulation [6.13].

Both analytical and numerical methods are based on the solution of the heat-transport equation (Fourier's equation) under appropriate boundary conditions. The general heat-transport equation is based on energy conservation principles on an element, whereby, the heat conducted in to and out of the element, plus the heat generated inside the element (q^*) is equal to the heat stored within the element. Selecting the Cartesian co-ordinate directions to be x, y and z, the equation is

$$c_p \rho \left(\frac{\partial T}{\partial t} \right) = \kappa \left(\frac{\partial^2 T}{\partial x^2} + \frac{\partial^2 T}{\partial y^2} + \frac{\partial^2 T}{\partial z^2} \right) + q^* \qquad (6.15)$$

where T is the temperature of the element, ρ is the elements material density, c_p is the elements specific heat, t is time, κ is the thermal conductivity and q^* is the heat generated [6.1]. This equation represents a volumetric heat balance which must be satisfied at each point in the membrane structure, but it assumes that each volumetric element has a constant temperature throughout and κ is the same in all directions.

An analytical solution of the heat-transport equation is reviewed as a modelling technique, however, the initial approach to thermal modelling of my MHP designs employed approximate numerical methods; which include both FEM and lumped element methods.

6.4.1 Analytical Modelling

Analytical solutions of the general heat-transport equation exist for special cases, where the derivations can be simplified due to reduction of the dimensions investigated and choice of boundary conditions. Temperature gradients within the membrane perpendicular to the surface plane can be neglected due to conductive heat loss dominating through the membrane structure, resulting in a two-dimensional problem. A further reduction to a one-dimensional thermal model is possible if structural symmetry enables a description of the in-plane heat conduction by only one co-ordinate [6.11, 6.12, 6.14].

The rectangular membranes can be approximated to a circular geometry, which allows the heat-transport equation to be further reduced to one-dimension, using cylindrical co-ordinates,

$$c_p \rho \left(\frac{\partial T}{\partial t} \right) \approx \kappa \left(\frac{\partial^2 T}{\partial r^2} + \frac{1}{r} \frac{\partial T}{\partial r} \right) + q^* \qquad (6.16)$$

where r is the radius of the circular membrane. In the case of steady-state heat generation, equation 6.16 simplifies to

$$\kappa \left(\frac{\partial^2 T}{\partial r^2} + \frac{1}{r} \frac{\partial T}{\partial r} \right) + q^* = 0 \qquad (6.17)$$

This equation has been solved elsewhere to optimise the performance for a thermoelectric microsensor employing a microheater [6.12]. The parameters which are optimised are dependent on the temperature distribution from the centre of the membrane to the Si substrate. However, the minimisation of thermal power loss which is of greatest concern here is not dependent on the exact knowledge of the temperature field. Therefore, the initial models investigated to optimise MHP designs employ numerical methods. Also numerical methods provide a simple method to model the transient response.

6.4.2 Numerical Modelling

Exact analytical solutions only exist for a few simple geometries. However approximate numerical techniques exist which are able to solve in principle any problem of any structural complexity. Numerical (finite difference) methods produce temperature values at selected discrete points and at discrete time intervals. Thus, the accuracy of the numerical analysis depends on the choice and number of discrete points (nodes), discrete time intervals and type of difference parameter. However, assumptions can be made to simplify the number of discrete points with only a slight decrease in model accuracy.

One numerical method is based on the representation of the derivatives in the heat-transport equation by a finite difference approximation (*via* the use of Taylor's expansion). The MHP structure can be sub-divided by a set of lumped volumes with a constant temperature each represented by a node, where a finite difference equation can be specified at each node to describe the heat balance between adjacent nodes. These finite difference equations may be interpreted in a physical way that permits convenient generalisations [6.1].

Firstly, the total heat flow between two nodes (q) can be expressed by

$$q = \frac{T_1 - T_2}{R_{th}} \tag{6.18}$$

where T_1 - T_2 is the temperature difference between two nodes and R_{th} is the thermal resistance. Assuming thermal conduction between adjacent volumes the thermal resistance can be expressed by

$$R_{th} = \frac{\delta x}{\kappa A_k} \tag{6.19}$$

where δx is the distance between the two nodes, κ is the thermal conductivity and A_k is the cross-sectional area of contact between the two volumes (normal to the one-dimensional co-ordinate x).

This expression suggests that an electrical analogy can be used. The MHP can be represented by a network of these isothermal lumps which are identified by nodal points, and the thermal resistances can be symbolised by electrical resistors between each node. The existence of convective losses from the structure surface exposed to an ambient fluid may be accounted for by adding to the network another node representing the fluid. The thermal connection between these nodes can again be represented by a thermal resistance according to

$$R_{th} = \frac{1}{hA_c} \tag{6.20}$$

where h is the heat-transfer coefficient and A_c represents the surface area exposed to the convecting fluid.

For situations involving transient modelling, finite difference equations can be generated for the partial derivative of temperature with respect to time. These take into account the heat storage of each lumped nodal element. Continuing with the electrical analogy, the heat storage is represented by an electrical capacitance connected between the node and the ambient temperature node. This capacitance is recognised as the thermal (heat) capacity of the lumped volume surrounding the node, according to

$$C = V\rho\, c_p \tag{6.21}$$

where V is the volume of the lumped element, ρ is the material density and c_p has the same definition as described in Section 6.3.

The result of applying these concepts to a thermal situation is that the differential equations are replaced by an algebraic expression for each nodal subdivision of the object. Thus, for a case in which the structure is investigated with N nodes of unknown temperature, N algebraic equations are obtained which involve these unknowns. There are several methods available for the solution of a system described by simultaneous equations. For a system involving a high N the sequence of operations involved to solve the equations can take a significant length of time. Hence, computer programs exist which reduce the processing time and increase the

models accuracy by considering many more lumped elements. The packages used for this operation are referred to as finite element methods (FEM). Such a FEM analysis has been investigated for a SRL125/MOS device using the software package TMA MEDICI. The development and limitations of this method are described.

As in the same way as simplifying an analytical model, assumptions about the temperature distribution through the MHP can be applied to simplify the numerical analysis, which reduces the number of nodes considered. A highly simplified equivalent circuit model is also described to compare its application.

6.4.2.1 FEM Modelling of a SRL125/MOS Micro-Hotplate

There are a wide variety of FEM packages available for thermal modelling, several have been successfully employed to analyse the thermal characteristics of MHPs [6.11, 6.15, 6.16]. A two-dimensional (2-D) numerical simulation using the package TMA MEDICI [6.17] was used to analyse a SRL125/MOS MHP (The FEM investigation was undertaken by Dr Florin Udrea, at the Department of Engineering, Cambridge University).

In order to perform a thermal FEM analysis, the geometrical and physical model of the MHP was established. The package only considers a 2-D cross-section through the structure. When the 2-D dimensions are specified the program generates a finite element mesh of the cross-section. The size of the lumped elements can be reduced around the areas of interest to improve accuracy.

To obtain an accurate operating temperature in the centre of the membrane, it is essential that the equivalent 2-D heat generation and heat loss is independent of the third dimension. To obtain heat generation the meandering Pt heater had to be converted to an equivalent solid polysilicon heater with the equivalent electrical power dissipation. The change of heater material is necessary because MEDICI does not contain the thermal properties for Pt. Also, assuming the temperature profile through the membrane (normal to the surface plane) is constant, it is possible to convert the MHP geometry to an equivalent structure with the heater on the membrane underside. This simplifies the geometry of the 2-D structure to be entered into the program, without loosing too much accuracy. The membrane was initially assumed to be composed of a 0.5 μm homogeneous layer of Si_3N_4 with $\kappa = 18.5$ W/m.K.

To obtain an accurate heat-transfer through the 2-D structure an equivalent geometry must be described to allow heat loss in the third dimension to be neglected. To simplify this procedure the rectangular SRL125/MOS MHP layout was converted to a square layout, as shown in Figure 6.19, with the membrane and heater area the same in both cases.

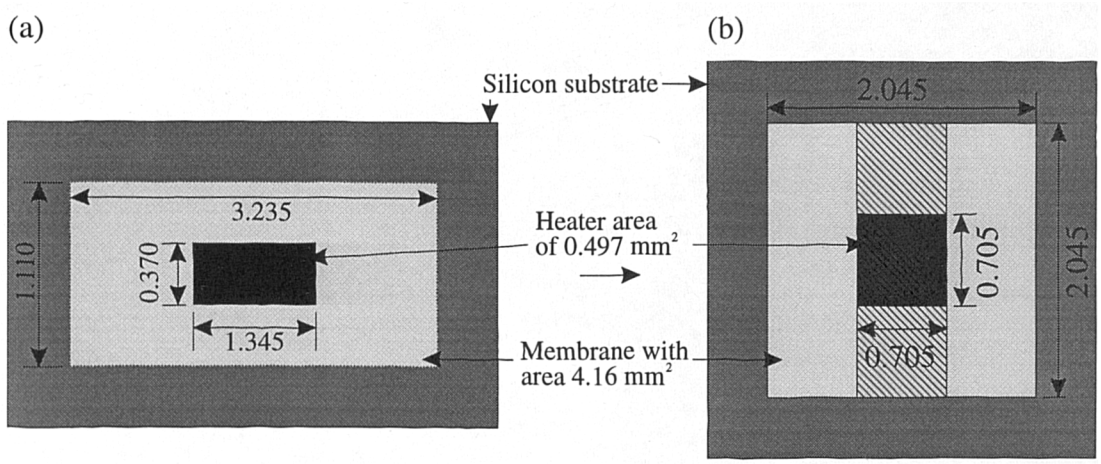

Figure 6.19 Plan view of the SRL125/MOS membrane (a) actual, and (b) equivalent dimensions used. (All dimensions are in mm).

To neglect heat loss in the third dimension the area to be heated must extend across the entire membrane length in the third dimension, as indicated by the *hatched* region. With this geometry in mind, an equivalent heat generation must exist in the modified heater area. From the steady-state power versus operating temperature characteristics, for a SRL125/MOS MHP operating at 300°C the current is 26 mA and the applied voltage is 4.36 V. If this current is to heat the equivalent area then the same current density ($J = 26 \times 10^{-3}/2045 = 1.27 \times 10^{-5}$ A/μm) is required from the polysilicon heater. The doping level of the modelled polysilicon heater was varied until the same J was achieved. Initially the steady-state characteristics of the power loss versus maximum operating temperature indicated that the power loss was too low. This was expected, since MEDICI only models conduction losses. To improve the thermal power loss accuracy an additional layer of polysilicon was included over the heater area on the membrane top-side. The additional conduction loss through this structure is intended to compensate for the lack of convective heat loss. The modelled power loss characteristics is as shown in Figure 6.20.

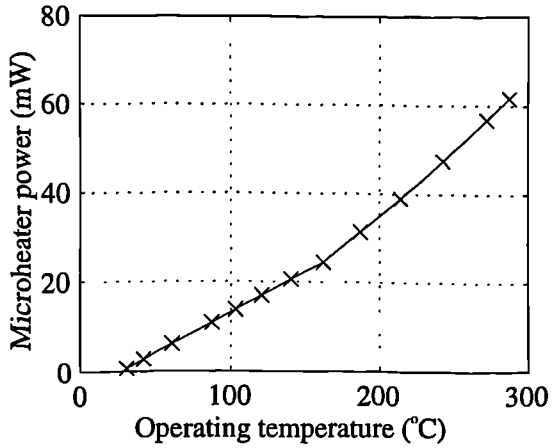

Figure 6.20 Power consumption derived from FEM analysis.

The preprocessing stage of the FEM analysis was completed by entering the equivalent geometry of the 2-D cross-section. The model was then used to investigate the transient response of the structure. The temperature response to an applied heater voltage step is shown in Figure 6.21. The voltage step was represented by a change from 0 to 4.36 V over a period of 1 μs.

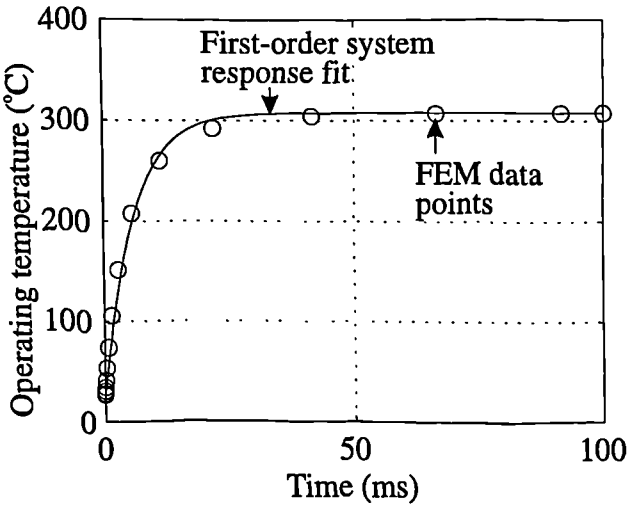

Figure 6.21 Transient response generated by FEM analysis.

To measure the time constant of this model, the solid line superimposed over the data points in Figure 6.21 is generated from equation 6.12. A time constant of ~ 6 ms gives the nearest fit. Comparing this to a measured time constant of 4.3 ms, it suggests the model provides a high transient accuracy. However, because the model

only considers conduction losses, the measured second and fourth order characteristics of convection and radiation losses, respectively, cannot be easily modelled. This limits the accuracy of the steady-state power loss analysis.

It has been shown that a high degree of accuracy is obtainable for the transient response. However, to use this method as a tool to simulate the thermal performance of future MHP designs, the thermal properties assumed for the equivalent structure need further validation to ensure model accuracy.

6.4.2.2 Lumped-Element Model

An alternative approach to FEM modelling was the generation of a much simpler lumped-element model. Instead of sub-dividing the structure into a high-density of nodal points forming a mesh, which can only be numerically solved *via* FEM analysis, the structure is divided into only a few critical points, as shown in Figure 6.22(a).

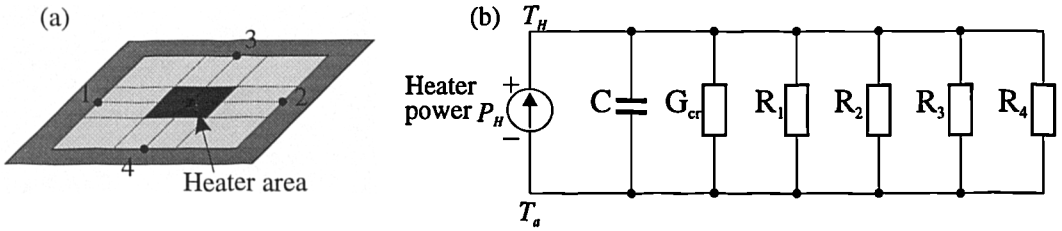

Figure 6.22 Schematic of the nodal subdivision of (a) the membrane, used to generate (b) an equivalent circuit.

This simplification assumes that; the temperature profile is constant through the membrane thickness, the silicon frame and the gas above and below the membrane are at ambient temperature, and convection and radiation losses are restricted to the heater area above and below the membrane. These assumptions define the boundary conditions which allow a heat flow model of the MHP to be described by lumped elements (represented by an equivalent electrical circuit), as shown in Figure 6.22 (b). Where T_H and T_a are the heater and ambient temperature, respectively, C is the thermal capacitance of the heater region, G_{cr} is a thermal conductor associated with convection and radiation losses from the heated area, and $R_{1\text{-}4}$ are the resistances through the membrane due to thermal conduction from the heater node to the four nodes on the edge of the silicon substrate frame. In order to arrive at this simplified equivalent circuit a number of equivalent circuit components had to be either

neglected or combined with other heat flow/storage mechanisms. For example, heat conduction is neglected through the corners of the membrane and thermal convection is neglected outside the heated area. These simplifications create errors between the characteristics derived using the model and the measured characteristics. The components used in the thermal model are dependent on the geometry and the thermal properties of the lumped membrane. The accuracy of the model components are improved by using the information determined from the measured characteristics, since the geometry parameters have been simplified.

The model can be expressed by the heat flow at the membrane node, according to

$$C\frac{dT_H}{dt} = P_H - \Delta T\left(\frac{1}{R_1}+\frac{1}{R_2}+\frac{1}{R_3}+\frac{1}{R_4}+G_{cr}\right) \tag{6.22}$$

where $\Delta T=(T_H - T_a)$.

Equation 6.19 defines the thermal resistance R_{th}, which can be expressed in terms of the lumped element geometry as

$$R_{th} = \frac{1}{\kappa m}\left(\frac{\delta x}{a}\right) \tag{6.23}$$

symbols have the same definition as described in equation 6.19, but the term A_k is expanded to define a the width of the lumped element and m the lumped membrane thickness. Using the membrane geometry notation described in Figure 6.9 the total conductive thermal loss can be expressed as the parallel combination of the individual conductive resistances, according to

$$R_{cond} = \frac{1}{\kappa m}\left(\frac{u_1 u_2}{4(u_1 a_1 + u_2 a_2)}\right) \tag{6.24}$$

where R_{cond} (K/mW) is the thermal resistance associated with the total conductive heat loss.

The characterised measured conductive losses described in equation 6.3, generates a presumed thermal conductance for a SRL125/MOS MHP of G_{cond} = $1/R_{cond}$ = 0.123 mW/K. Using the SRL125/MOS membrane dimensions shown in Table 6.4, $\kappa m = 22.74 \times 10^{-3}$ mW/K. This can be compared to the theoretical lump-value which is the sum of κm for the individual membrane layers [6.12]. The SRL108 and SRL125 membranes are composed of 80/500 nm of $SiO_2/SiN_{1.1}$, which have the thermal conductivities described in Table 6.5. Using these values only accounts for 1.7×10^{-3} mW/K of the total κm measured. However, the partial coverage of Au (300 nm) electrodes on the membrane top-side requires that an equivalent additional Au layer is considered. An equivalent 66 nm Au layer compensates for the previous shortfall in κm.

The convection (G_c) and radiation (G_r) losses have been combined and expressed in the model as a thermal conductance (G_{cr}), where

$$G_{cr} = G_c + G_r = 2A\left(h\Delta T + \varepsilon\,\sigma\left(T_H{}^4 + 298^4\right)\right) \tag{6.25}$$

where A is the heater area, h is the convective heat transfer coefficient, ε and σ have the same definition used in equation 6.2 and T_H is the MHP temperature (in Kelvins). The area is multiplied by 2 to account for losses from both the top and under-side of the membrane (assuming they are equal). However, it was suggested in Section 6.2.3 that h is not constant. Therefore, to improve the accuracy of the model, the coefficient, h, is replaced by a first-order function of ΔT according to

$$h = 414.8\Delta T + 1.04 \times 10^5 \tag{6.26}$$

Similar compensation was required for the MHPs thermal capacitance, which is theoretically described by equation 6.21. The lumped value of C is theoretically the sum of the individual layer capacitances. However, since the c_p of SiO_2 and $SiN_{1.1}$ are approximately the same at RT, ~ 700 (J/kg.K), this value was initially used assuming a lumped $SiN_{1.1}$ membrane (580 nm thick) with ρ = 3 g/m^3. Substituting these values into equation 6.21 for the SRL125/MOS MHP geometry, gives $C = 6.06 \times 10^{-7}$ J/K.

The values validity can be assessed by considering the measured transient response, since $\tau = RC$, as described in Section 6.3.2. The value of R is calculated by the application of the parallel combination of the thermal resistance components G_{cr} and G_{cond}. Using equations 6.21, 6.24 to 6.26, at an operating temperature of 276°C gives a theoretical time constant of 1.65 ms, compared to the measured value of 4.336 ms. The inaccuracy between the modelled and measured value of τ requires that an equivalent value of C is derived from the measured data. The theoretical value of R_{th} corresponding to the measured data ($\tau = 4.336$ ms) is 2.87×10^3 (K/W), which defines $C = 1.5 \times 10^{-6}$ J/K. Dividing this value by the heater area A, derives a capacitance per unit area of ≈ 3.0 J/K.m. This can now be used as a model coefficient, replacing C by $3A$. The lumped element model for SRL125/MOS design can now be represented in terms of MHP geometry and temperature, according to

$$3a_1a_2\frac{dT}{dt} = \begin{bmatrix} 2a_1a_2\left(412.9\Delta T^2 + 1.04\times10^5 + \sigma\left(T_H{}^4 + 298^4\right)\right) \\ + \left[\frac{9.1\times10^2\left(u_1a_1 + u_2a_2\right)}{u_1u_2}\right] \end{bmatrix} - P_H \qquad (6.27)$$

The steady-state accuracy of this model was investigated by setting the left hand side of equation 6.27 to zero. The theoretical thermal power loss compared to the measured characteristics is shown in Figure 6.23.

Likewise the accuracy of the model to calculate the time constant was investigated as shown in Figure 6.24.

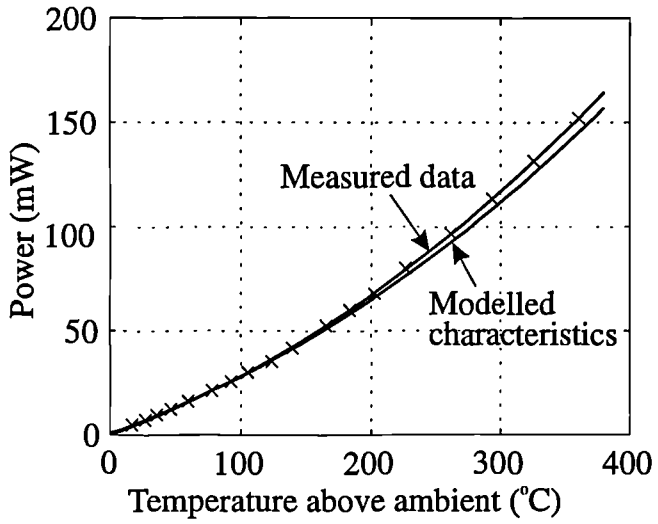

Figure 6.23 Comparison of measured data and a lumped element model for thermal power loss for a SRL125/MOS device.

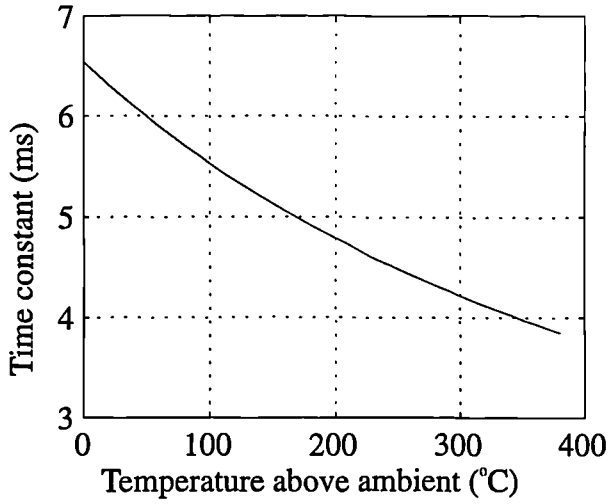

Figure 6.24 Lumped element model simulation of time constant versus temperature for SRL125/MOS MHP.

Figure 6.24 shows a very close fit to Figure 6.13, which suggests the relationship between τ and temperature is primarily determined by the temperature dependent G_{cr}. A close fit between the model and the data is expected for this design, since the model parameters are derived from the measured characteristics. However, the model accuracy was assessed by applying the model to other membrane geometries. The application of the model with a SRL125/XPc MHP geometry is compared to the measured characteristics, as shown in Figure 6.25.

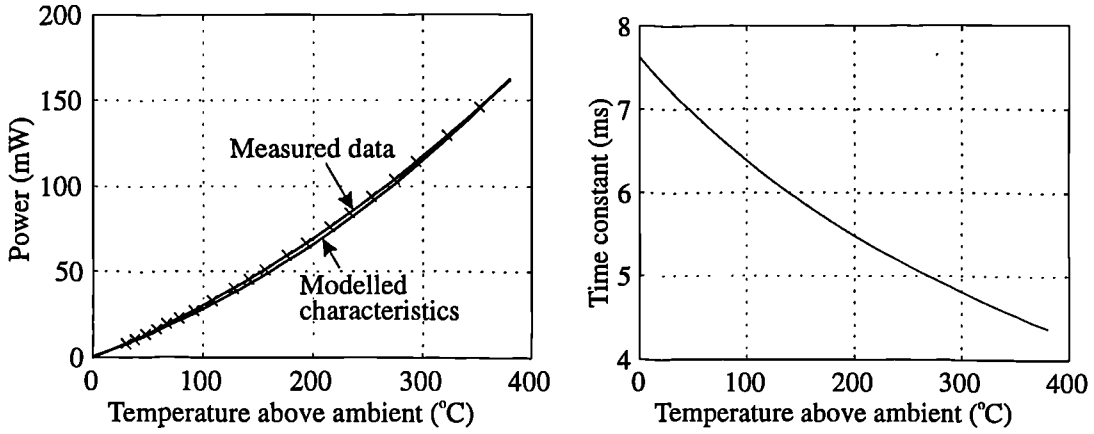

Figure 6.25 Modelled characteristics of SRL125/XPc MHP.

It is apparent that the model fits extremely well with the measured data for the power loss and the time constant datum shown in Table 6.6. The same characteristics were determined for SRL125/CP using the model. However, the initial steady-state SRL125/CP characteristics obtained by the model for thermal power loss were inaccurate using the calculated model coefficients. To improve the accuracy to that shown in Figure 6.26 required that a value of κm was increased to 265×10^{-3} mW/K.

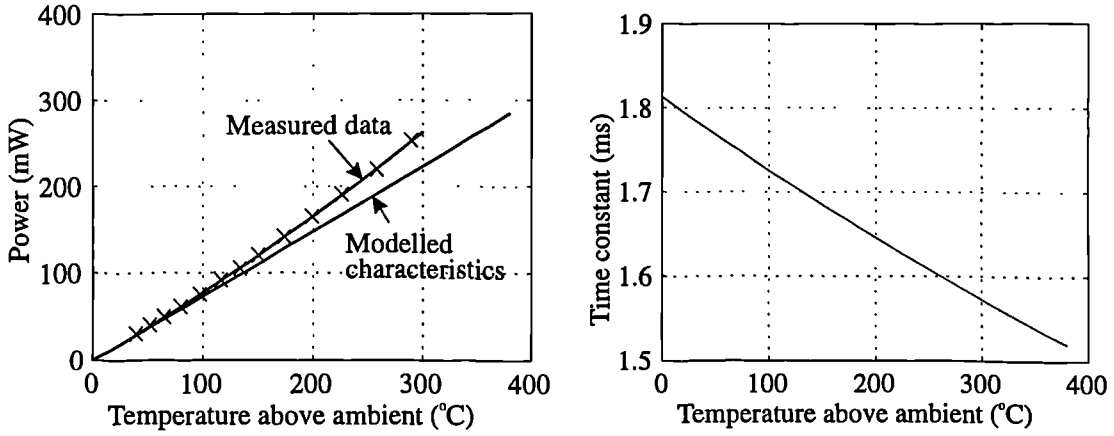

Figure 6.26 Modelled characteristics for the SRL125/CP MHP.

This significant difference may be attributed to the high surface coverage by the metallisation layers over the membrane, as well as the split membrane structure. However, the time constant characteristics shown in Figure 6.26 were obtained using

the original value for κm, which provides a close theoretical value to the actual datum measured, as described in Table 6.6.

The lumped-element model is limited to simulating MHPs with a similar structure to the SRL125/MOS device. It has been shown that as the MHP geometry diverts from the SRL125/MOS device used to generate the model parameters, the model predictions become more inaccurate as in the case with the SRL125/CP MHP. A possible reason for the model errors is the difference in equivalent thickness of metallisation between designs. Therefore, more designs require characterisation with the model to provide a more quantitative definition of the metallisation layers contribution to the thermal performance of the MHP.

6.5 Conclusions

In this Chapter I have described the characterisation and modelling of the MHPs incorporated in the chemoresistor designs. Both the steady-state and transient characteristics have been investigated.

Typical characteristics taken for a SRL125/MOS MHP show that a d.c. power consumption of 185 mW is required to heat two chemoresistors to ~ 400°C, and for a pulsed signal the operating temperature transient has a time constant of ~ 4 ms. These properties have demonstrated the designs suitability for ultra-low power applications. The mechanical stability of the MHP were also noted to be very good, even during high thermal stress.

Work is being carried out at Warwick to exploit the rapid thermal time response by investigating heating the microsensor with a pulsed electrical signal, which will considerably reduce the average power consumption.

By comparison of the power consumption in still air and a vacuum (10^{-5} Torr) the contribution to the heat loss by different mechanisms were described. In the temperature range of RT to 350°C the largest contribution to heat loss is conduction, whereas above 350°C the largest contribution to heat loss is by convection. Investigations also suggest that the heat loss by forced convection can be neglected in the test flow system.

Both transient and frequency responses of the MHPs were characterised. These responses compare closely with a first-order system, which allows the MHP to be

represented in terms of electrical components. This is ideal for future interface circuit modelling (e.g. using PSPICE).

An overview of different thermal modelling techniques has been given, that introduce the numerical modelling methods employed. One approach was FEM analysis using the package TMA MEDICI, that has the potential for good prediction of the time constant, but the temperature distribution was not representative of the actual MHP and the steady-state power consumption accuracy is limited. It was concluded that further comparisons were required to improve the accuracy of the FEM model. An alternative approach led to the development of a lumped-element model, which was described. The corresponding model coefficients were calculated from the measured characteristics of the SRL125/MOS MHP. This model gave a close prediction of characteristics for structures similar to that of the SRL125/MOS. However, coefficient modifications were required to describe the SRL125/CP design. The initial results obtained with this model are very encouraging, but further model validation is required from the characterisation of the other designs.

6.6 References

6.1 A.J. Chapman, *Heat Transfer 4th Edition*, (1984), Macmillan Publishing Company, New York.

6.2 U. Dibbern, Miniaturisation of Gas Sensor Substrate. Problems and Benefits of Microelectronic Technology, *Sensors and Actuators B,* **2** (1990) 63-70.

6.3 R.W. Berry, P.M. Hall and M.T. Harris, *Thin Film Technology*, D. Van Nostrand Company, Inc., London, 1968.

6.4 P. Krebs and A. Grisel, A Low Power Integrated Catalytic Gas Sensor, *Sensors and Actuators B,* **13-14** (1993), 155-158.

6.5 J.W. Gardner, A.C. Pike, N.F. de Rooij, M. Kouldelka-Hep, P.A. Clerc, A. Hierlemann and W. Göpel, Integrated Array Sensor for Detecting Organic Solvents, *Sensors and Actuators B,* **26-27** (1995) 135-139.

6.6 G.C.M. Meijer and A.W. van Herwaarden, *Thermal Sensors,* IOP Publishing Ltd., Bristol, 1994.

6.7 A.M. James and M.P. Lord, *Macmillan's Chemical and Physical Data*, The Macmillan Press Ltd., London, 1992.

6.8 C.H. Mastrangelo, Y.C. Tai and R.S. Muller, Thermophysical Properties of Low-Residual Stress, Silicon-Rich, LPCVD Silicon Nitride Films, *Sensors and Actuators A,* **21-23** (1990), 856-860.

6.9 R.E. Cavicchi, J.S. Suehle, K.G. Kreider, M. Gaitan and P. Chaparala, Optimized Temperature Pulse Sequences for the Enhancement of Chemically-Specific Response Patterns from MHP Gas Sensors, *Technical Digest of Transducers'95, The 8th International Conf. on Solid-State Sens. Actuators, (1995), Stockholm,* 209-D5, 823-826.

6.10 C.M. Close and D.K. Frederick, *Modeling and Analysis of Dynamic Systems,* Second Edition, Houghton Mifflin Company Ltd., London, 1993.

6.11 U. Dillner, Thermal Modeling of Multilayer Membranes for Sensor Applications, *Sensors and Actuators A,* **41-42** (1994), 260-267.

6.12 F. Völkein and H. Baltes, Optimisation Tool for the Performance Parameters of Thermoelectric Microsensors, *Sensors and Actuators A,* **36** (1993), 65-71.

6.13 F.J. Auerbach, G. Meiendres, R. Müller and G.J.E. Scheller, Simulation of the Thermal Behaviour of Thermal Flow Sensors by Equivalent Electrical Circuits, *Sensors and Actuators A,* **41-42** (1994), 275-278.

6.14 T. Elbel, R. Lenggenhager and H. Baltes, Model of Thermoelectric Radiation Sensors Made by CMOS and Micromachining, *Sensors and Actuators A,* **35** (1992), 101-106.

6.15 S.K.H. Fung, Z. Tang, P.C.H. Chan, J.K.O. Sin and P.W. Cheung, Thermal Analysis and Design of a Micro-Hotplate for Integrated Gas Sensor Applications, *Technical Digest of Transducers'95, The 8th Int. Conf. on Solid-State Sens. Actuators,* (1995), 207-D5, 818-821.

6.16 F. Udrea and J.W. Gardner, Design of a Silicon Sensor Array for Gas Analysis, *Int. J. Microelectronics,* Vol. 27, No. 6 (1996) 449-457.

6.17 Technology Modeling Associates, Inc., *MEDICI Manual, Version 2.0,* September, 1994.

Chapter 7

7. Gas Sensor Test System

7.1 Introduction

When designing a sensor test system, it is necessary to consider what information is required, such as a particular sensor attribute, or to establish a sensor's suitability for a particular application. In order to assess the suitability of a sensor in a particular application, its response to changes in gas concentration under various conditions needs to be fully characterised. Ideally, to ensure suitable operation in the field, a gas sensor test system should be capable of characterising a sensors response to any changes in its environment. However, in practice this is limited to a few key physical variables of interest. It is necessary to characterise chemoresistive gas sensors under closely controlled environmental conditions, because their performance is strongly influenced by changes in ambient conditions. Therefore, the physical variables selected for control in the system are the gas concentration, temperature and humidity. For sensor characterisation, the effect of these physical variables should be studied over their expected ranges.

A variety of automated test systems have been reported that characterise gas sensors. Many share common features such as microcomputer control, flow injection *via* pressurised bottles, and control of gas temperature and humidity. The main differences between test systems arise from the sensor technology being investigated (e.g. MOS chemoresistors [7.1-7.3], SAW devices [7.4, 7.5]) and analyte of interest (e.g. vapours [7.2, 7.3, 7.5], gases [7.1, 7.4, 7.6] and odours [7.7]). CP coated chemoresistors can be characterised at Warwick University in an existing test system for VOCs and odour delivery. However, a new sensor test system was required to characterise the response of MOS and XPc SADs to low concentrations of CO and NO_2, at various temperatures and humidities.

The test system must provide accurate, reliable and repeatable parameters. An automated test system is required to improve data accuracy and repeatability by removing manual errors, and provide the high amount of data necessary for characterisation. It is essential that the physical variables are accurately known during testing, to ensure confidence in the results obtained and any model validation. Ideally, the physical variables which are controlled and measured by the test system, should be equal to the physical values set on the system user interface and stored in the data. In practice, the errors are minimised by adequate calibration of the test system. The techniques used to calibrate flow-rate, temperature and humidity are discussed.

7.2 Test System Design

The gas sensor test system that I have developed is shown in Figure 7.1, which combines both chemical and electronic hardware to provide a fully automated computer-controlled system. The test conditions which control the gas concentrations, humidity and MHP operating temperature during the test sequence can be programmed *via* the user interface with the Personal Computer (PC). The real-time system allows data to be simultaneously collected from upto twelve chemoresistive sensors from two SADs, two temperature sensors, a humidity and a flow sensor. The data are stored on the PC to allow further analysis after testing.

The sensor testing system is designed to control the concentration of CO, NO_2 and humidity and sensor operating temperature so the performance of the SADs can be determined.

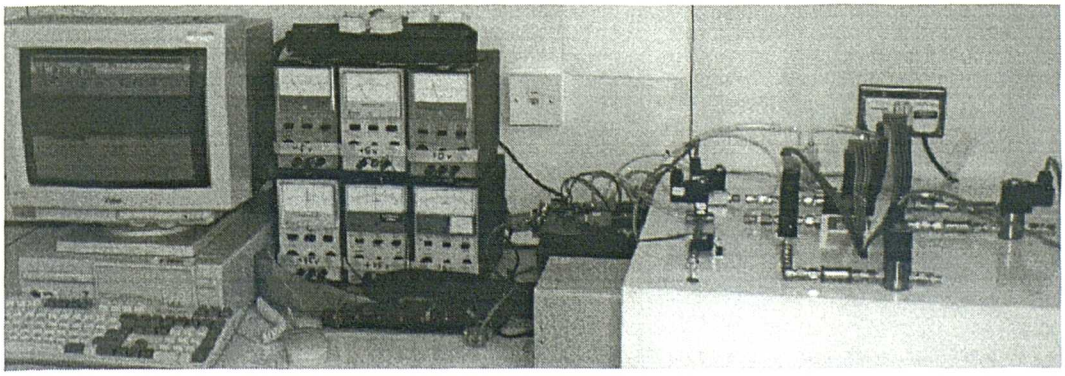

Figure 7.1 Novel gas sensor test system for chemoresistive silicon sensors comprising a 486-based PC (left), temperature-controlled sensor chamber and interface electronics (centre) and gas mixing (right).

A block diagram of the sensor test system is shown in Figure 7.2. The test system involved the development of gas flow hardware, signal conditioning and test sequence software. The hybrid† test system contains both discrete-time and continuous sub-systems. The hardware sub-system requires continuous control signals and generates continuous measurement signals, which are interfaced to the discrete-time PC sub-system by a National Instruments® data acquisition (DAQ) AT-MIO-16 card. The National Instruments® data acquisition package LABVIEW® for Windows, Version 3.1.1 (Labview), is installed on the PC and programmes have been written to control the sequence of physical variable changes during testing and to sample the corresponding sensor response signals. This software package presents the state of the system to the user as though the whole system is continuous.

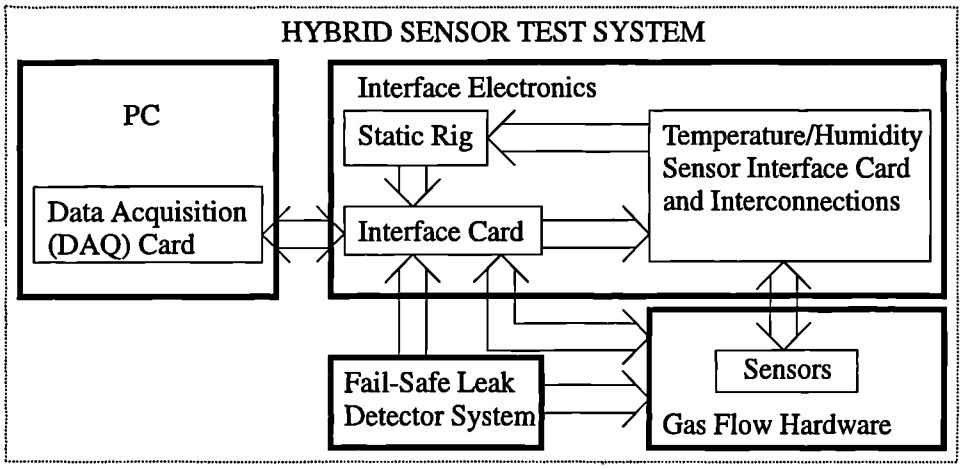

Figure 7.2 Schematic of the sensor test system.

A number of safety features have been incorporated into the system, because of the need to handle hazardous gases. One safety feature involves a fail-safe signal which automatically stops the hazardous gas supply when a leak is detected. The fail-safe signal is activated if either a commercial CO monitor detects a CO leak or if the fume cupboard extractor is not operating. In both cases the fail-safe signal determines the state of operation of the test system, as described in Section 7.2.4.

The design of the sensor chamber has been constructed to accomodate the 14-pin d.i.l. SADs previously described in Chapter 3. However, the sensor chamber can

† This refers to a system containing both continuous and discrete electronic sub-systems.

easily be modified for other sensor designs. Details of the sensor test system are given below:

7.2.1 Gas Flow Hardware

The gas flow hardware, schematically depicted in Figure 7.3, is primarily concerned with the mixing of the target gases and controlling the gas concentrations, gas temperature and humidity. A key to the system components, suppliers and specifications are shown in Table 7.1. The system is capable of controlling the concentration of a binary gas mixture and a vapour. However, the gas flow hardware was designed to operate with low concentrations of NO_2, CO, and water vapour.

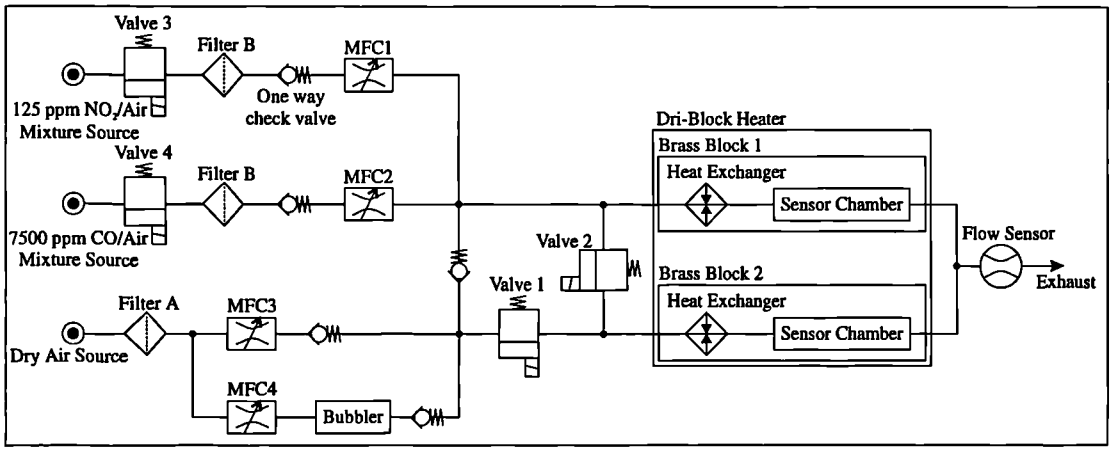

Figure 7.3 Schematic of the gas flow hardware which supplies preconditioned gases to the sensor chambers.

Table 7.1 Gas flow hardware parts key.

Symbol	Part	Supplier	Details
◉	125 ppm NO_2/Air mixture source	BOC Special Gases Ltd.	Gas cylinder containing 125 ppm NO_2 in dry air. Concentration accuracy ± 1.0 % (Spectra Seal, guaranteed accuracy over 5 years). Supply pressure controlled by a stainless steel double stage gas regulator (valve fittings conform to BS 14).

Table 7.1 Gas flow hardware parts key, continued.

◉	7500 ppm CO/Air mixture source	BOC Special Gases Ltd.	Gas cylinder containing 7500 ppm CO in dry air. Concentration accuracy; filling tolerance ± 0.5 - 1.0 %, analysis tolerance ± 1 % (α - Standard). Supply pressure controlled by a brass single stage gas regulator (valve fittings conform to BS 4).
◉	Dry air source	BOC Gases Ltd.	Gas cylinder containing dry air. Pressure controlled by a standard single stage gas regulator.
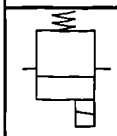	Valves 1,2. Camozzi miniature solenoid valve	Farnell Electronic Components Ltd.	Solenoid 2-way valve with 24 $V_{d.c.}$ switching voltage. Electrical connection is by a 3-pin DIN 40050.
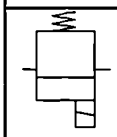	Valve 3,4. Solenoid valves	Hydralectric Appliance Controls Ltd.	Normally closed on/off valve, controlled by a 24 $V_{a.c.}$ signal. Electrical connection is by a 3-pin DIN 40050.
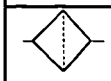	Swagelok filter	Birmingham Valve & Fitting Co. Ltd.	'F' Series inline filter, with a stainless steel sintered element with a mean pore diameter of 0.5 µm. Filter A also includes a carbon filter in series.
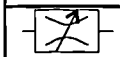	(MFC 1,2) Brooks Instrument B.V.	Fisher-Rosemount Ltd.	Model TR 5850. 0 to 10 ml/min flow range. Flow is controlled by a 0 to 5 V command signal.

Table 7.1 Gas flow hardware parts key, continued.

	(MFC 3) Brooks Instrument B.V.	Fisher-Rosemount Ltd.	Model TR 5850. 0 to 250 ml/min flow range. Flow is controlled by a 0 to 5 V command signal.
	MFC 4	Unit Instruments Ltd.	Model UFC - 1000. 0 to 250 ml/min flow range. 0 to 5 V command signal.
	One way check valve	Birmingham Valve & Fitting Co. Ltd.	Swagelok 'C' Series poppet check valve with a cracking pressure of 0.02 Bar.
	Bubbler	Fisons Scientific Equipment Ltd.	250 ml Drechsel (gas washing) bottle and head with sintered frit to maximise vapour concentration in the air flow.
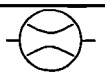	Flow sensor	Farnell Electronic Components Ltd.	Microbridge mass air flow sensor provides a signal conditioned output (1 to 5 V) over flow rate range of 0 to 1000 ml/min.
	Fittings	Birmingham Valve & Fitting Co. Ltd.	Swagelok tube fittings are used between the gas sources and valve 1,2. Corrosion resistant stainless steel fittings are required for sections in the system exposed to NO_2, while brass fittings are used in the remainder of the system.
	Fittings	Hydrafit Ltd.	Compression fittings required to connect tubing to valves 1,2 and the brass blocks.

Table 7.1 Gas flow hardware parts key, continued.

⊢	Tubing	Economatics Ltd.	4 mm OD (2.5 mm ID) Teflon tubing is used to connect between the Swagelok and Hydrafit fittings. Teflon 6 mm OD (4 mm ID) is used to connect the exhaust flow to the fume cupboard.
	Dri-block® heater	Techne Ltd.	A Dri-block® heater, DB-2P allows 3 preset temperatures to be set in the range of room temperature to 110°C, long term stability is within ± 0.1°C.

Four mass flow controllers (MFCs) are used to set the gas concentrations and humidity. MFC 3 controls the flow-rate of dry air into the system in the range of 0 to 250 ml/min, while MFC 1 and MFC 2, control the flow-rate (0 to 10 ml/min) of 125 ppm NO_2/air mixture and 7500 ppm CO/air into the system, respectively. The fourth MFC, which shares the same air source as MFC 3, passes a controlled air flow through a bubbler to create a humidified air supply. The required concentration of NO_2, CO and humidity is regulated by dilution with the dry air source. For testing sensors suitable for hazardous gas monitoring, characterisation in the range of the gas exposure limits stipulated by the Health and Safety Executive [7.8] is required. To achieve this specification, the chemical hardware is capable of controlling NO_2 and CO concentrations in the ranges of 0 to 3 ppm and 0 to 50 ppm, respectively.

The gas supplies are filtered upstream from the MFC to prevent particulate matter accumulating in the MFC aperture. The air supply is also passed through a carbon filter to absorb organic molecules from the compressed air supply. Solenoid valves are located prior to the filters, to close off the NO_2 and CO lines if a hazard is detected.

One way check valves are positioned at various points in the system to direct the gas flow. In the case of a source pressure reduction during operation, the one way check valves located before MFC 1, 2 and after MFC 3 and the bubbler, prevent the subsequent back pressure forcing any hazardous gases into unacceptable parts in the system. A check valve is also positioned between the dry/wet air junction and the

NO_2/CO junction. The directed air flow dilutes the NO_2/CO mixture to the required concentration, without permitting any back flow. This prevents the exposure of non-corrosion resistant fittings to the reactive gases.

The possibility of a hazardous gas leak has been minimised by using compression fittings and corrosion resistant materials in critical regions. The integrity of the system joints were tested with a solution which consequently bubbles at the point of a leak.

Two identical brass blocks have been machined, as shown in Figure 7.4, which each house a SAD, a temperature sensor and a humidity sensor.

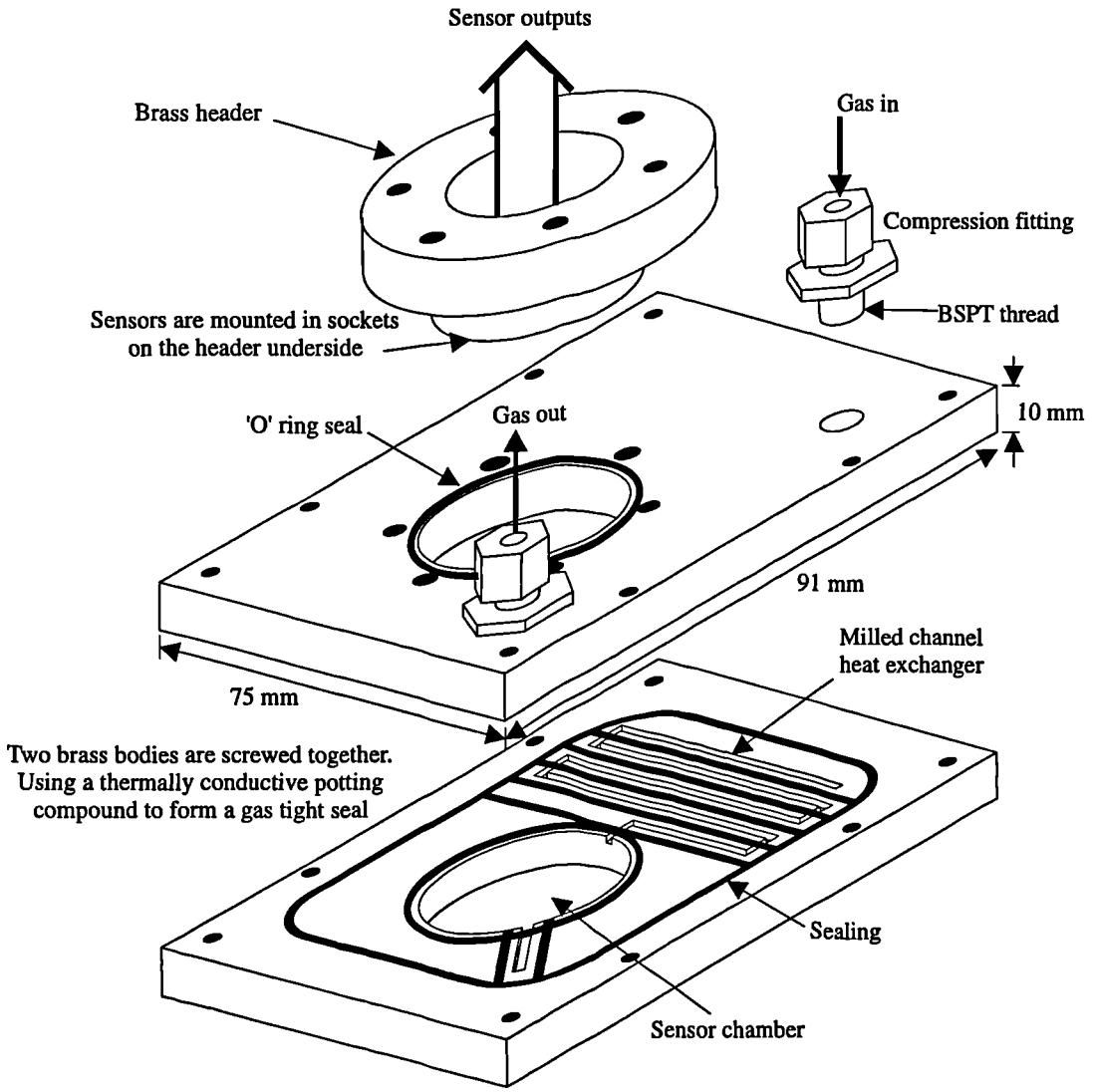

Figure 7.4 A semi-exploded diagram of the brass block sensor housing.

Sensor chamber 1 is directly connected to the sample gases, while the flow composition to the chamber 2 is controlled by the state of solenoid valves 1 and 2. Refering to Figure 7.3, if valve 1 is closed and valve 2 open, then the same sample gas passes through both chambers. However, if valve 1 is open and valve 2 is closed only the humidity controlled air sample flows through the chamber. This provides the option of running two SADs in differential mode to remove common mode errors.

To achieve a constant air flow temperature independent of flow-rate, the brass blocks are mounted in a Dri-block® heater. The gas upon entering the inlet fitting is directed through a heat exchanger, which is a meandering channel machined into the brass block. The gas temperature increases to one of three predetermined Dri-block® temperature settings (RT to ~ 100°C), before passing through the sensor chamber to the gas flow outlet. The heat exchanger dimensions ensure that even for the maximum flow rate the gas temperature still attains the brass block temperature.

The detachable brass header accommodates the sensors. The header is screwed onto the brass block, with an 'O' ring providing an gas tight seal. The output flow from the two brass blocks are then connected, before passing through a flow sensor. The flow sensor monitors the system for leaks by comparing the system output flow rate with the total input flow rate controlled by the MFCs.

The system exhaust is then safely expelled through tubing connected to a fume cupboard extractor.

7.2.2 Virtual Instrument

For the user to control and measure the physical variables during testing, a National Instruments® plug-in DAQ card and software package Labview have been installed on a PC. This combination allows the creation of a virtual instrument (VI). The definition of a VI is, a layer of software and/or hardware added to a general-purpose computer in such a fashion that users can interact with the computer as though it were their own custom-designed traditional electronic instrument.

A traditional electronic instrument consists of three major components; acquisition, analysis and presentation, as shown in Figure 7.5.

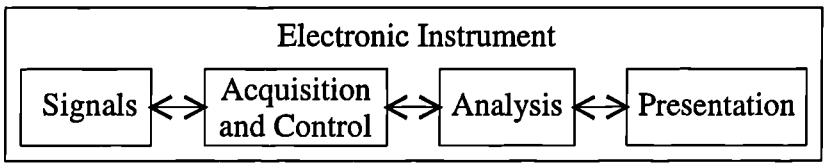

Figure 7.5 Basic components of an electronic instrument.

The VI installed on the PC also has these components, however, their operation is flexible and user configurable. Within the VI the hardware used for the acquisition and control is the DAQ card. The analysis and presentation is carried out by the high-level graphics-orientated application software (Labview). This package provides complete flexibility when defining the instruments functionality and user interface front panel.

The design approach to the VI has been to install the DAQ card directly into a PC expansion slot. These expansion slots are an extension of the processor bus inside the PC itself, and therefore create a real-time data acquisition/control system. The front-end hardware available on the DAQ board, which is required to handle the system control and measurement signals, include an analogue to digital converter (ADC), a digital to analogue converter (DAC) and a digital input/output (DIO) port. The DAQ hardware has no front panel of its own, so it cannot be used as a stand alone instrument. Therefore, the computer and monitor are required components of the instrument, whereby the Labview created front panel set up on the PC's monitor, is the only means to operate the instrument. The development of the VI front panel and test sequence is described later in Section 7.2.5.

The plug-in DAQ board is an AT-MIO-16H-9, which is a high performance multifunction analogue, digital, and timing I/O board, as described in the specification of Appendix C. The AT-MIO-16 contains a 12-bit ADC with 16 analogue inputs, two 12-bit DACs with voltage outputs and eight lines of TTL-compatible digital I/O, with which to monitor and control the sensor test system.

7.2.3 Design of Signal Conditioning Circuitry

Physical quantities in the test system can be classified as either measured or controlled variables. The general system components required in the processing of signals for measurement and control are depicted in the schematic in Figure 7.6.

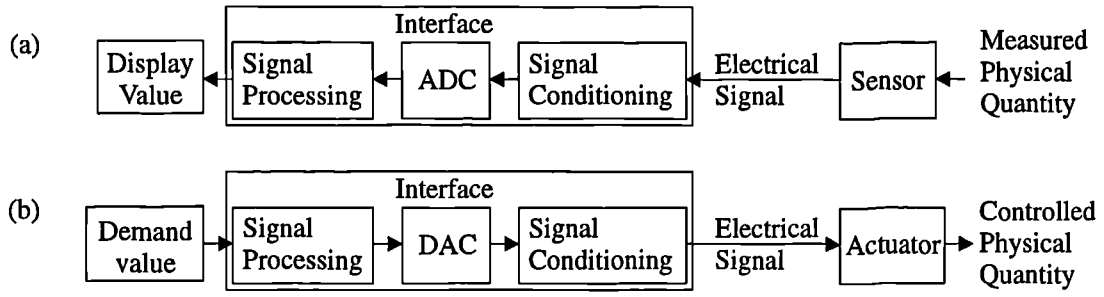

Figure 7.6 Schematic of system components necessary for (a) measurement, (b) open-loop control.

The interface requirement of measurement is to modify the electrical sensor output to a signal suitable for display or recording in the VI. Conversely, the system open-loop control demands need to be modified to a signal suitable for the actuator [7.9]. Considering the test system in terms of these blocks, the software package Labview provides the signal processing stage, while the plug-in AT-MIO-16 board provides part of the interface electronics, as described in Section 7.2.2. To design the signal conditioning circuitry the system signals must be modified for compatibility with the DAQ board. The system signals are summarised in Table 7.2.

Table 7.2 Measurement and control signals required by sensor test system.

System Signals	
Measurement	Open-loop control of
12 Chemoresistive sensor signals	4 MFCs
2 Temperature sensor signals	2 Solenoid valves[†]
1 Humidity sensor signal	6 MHP operating temperatures
1 Flow sensor signal	
1 Hazard signal.	

[†] Refering to Figure 7.3, valves 3 and 4 are controlled soley by the safety override system and so are independent of the system microcomputer.

The measurement and control signal data flow is as shown in Figure 7.7. The various signals are conditioned by three units; the main interface PCB, the static rig and the temperature/humidity interface PCB. The "static rig" is the name given to a standard Eurorack instrument already developed at Warwick University for an electronic nose [7.10].

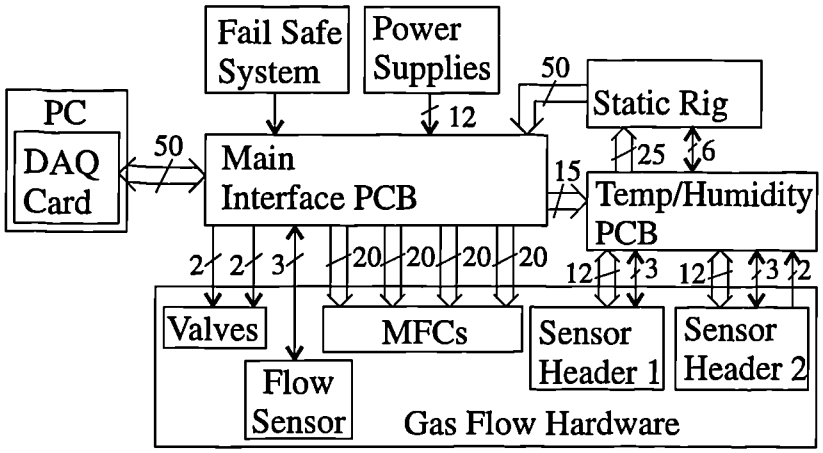

Figure 7.7 Block diagram of system data flow.

The main interface PCB is connected to the plug-in DAQ card with a 50-way ribbon cable. Its functions are to condition all the control signals and the fail-safe leak detector signal, as well as interconnecting the conditioned measurement signals to the DAQ inputs.

The temperature/humidity interface PCB, conditions the signals from the temperature and humidity sensors, drives the device microheaters, and interconnects the gas sensors with the static rig.

7.2.3.1 Design of Main Interface PCB

The main interface PCB conditions the open-loop control signals from the DAQ card, which control the MFCs, the solenoid valves, and the operating temperature of the MHPs. The signal from the fail-safe leak detection system must also be conditioned. The pre-conditioned sensor outputs from the static rig and flow sensor are connected to a suitable DAQ input *via* the interface PCB.

Six analogue control signals are required to operate the chemical hardware. Due to the plug-in DAQ boards limitations of only providing two 12-bit analogue outputs,

an 8-bit digital I/O port is also used to control the hardware. Six digital output signals are conditioned *via* a serial DAC to provide the four MFC analogue command signals, while the remaining two bits control the solenoid valves. The two DAQ board analogue outputs control the operating temperature of the six MHPs on the two SADs. However, independent control of the MHPs is not implemented, since only two analogue supply voltages are available.

The main interface PCB shown was designed using Cadstar as a single-sided board layout and made in the department, as is shown in Figure 7.8. A schematic of the electronics is shown in Figure 7.9.

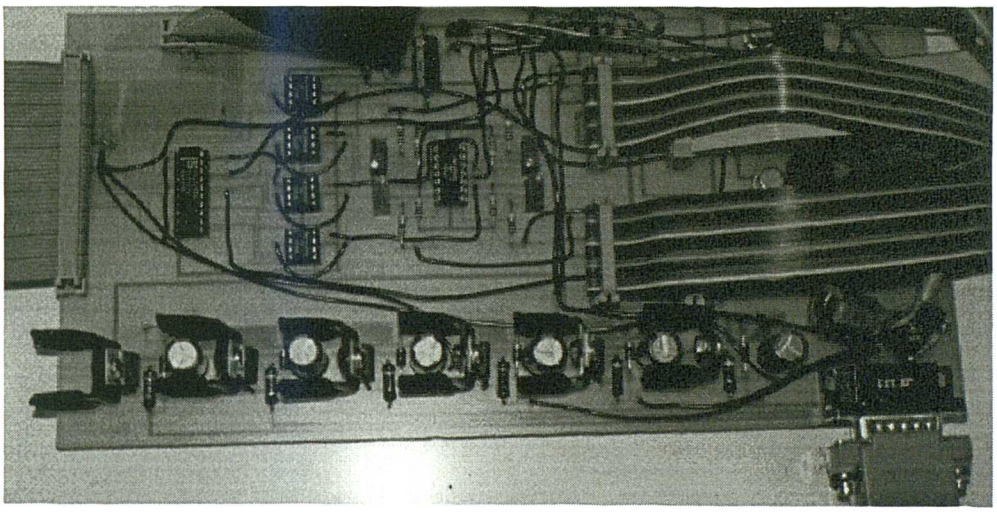

Figure 7.8 Main interface PCB, which includes the six power transistors (bottom) to drive the SAD MHPs.

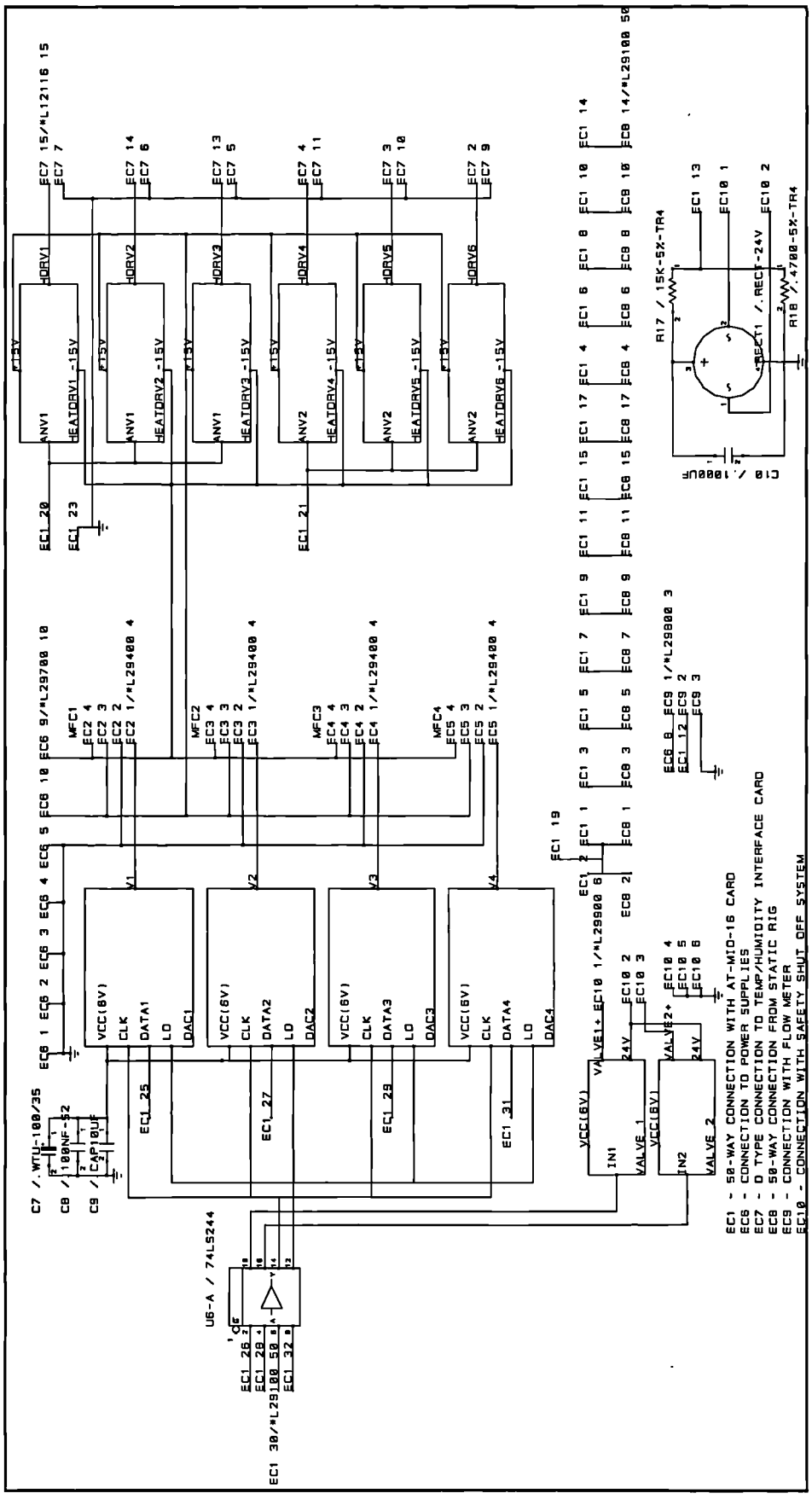

Figure 7.9 Schematic of Main Interface PCB.

MFC Control Signal Circuitry

In order to achieve four additional analogue control signals from the digital outputs, four 12-bit serial input DACs (DAC-8512, Analogue Devices Ltd.) are used, functionally shown in Figure 7.10. The DAC-8512 is a complete serial input, 12-bit, voltage output DAC designed to operate from a single +5 V supply. Coding for the DAC-8512 is binary with the Most Significant Bit (MSB) loaded first. It is capable of providing 0 to + 4.095 V output, for a one millivolt-per-bit accuracy.

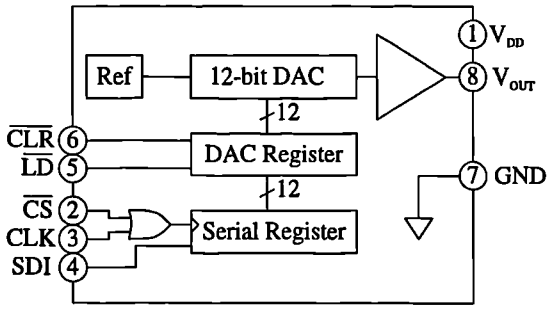

Figure 7.10 Functional block diagram of the DAC-8512.

The Chip Select (CS) and clear (CLR) functions are tied 'low' and 'high', respectively, during operation. The serial logic supplied to Serial Data Input (SDI), Load Data (LD) and clock (CLK) are controlled within Labview. The software user interface allows analogue values to be varied on the VI front panel, which are simultaneously converted to 12-bit binary numbers. Each bit is sequentially clocked out from the DAQ. The input data to the SDI is clocked into an internal serial register on the positive edges of the CLK input. When all 12 bits have been clocked into the serial register, an active low LD input, writes the serial register data into the DAC register, which is then converted to an analogue signal. The analogue output from the DAC register is held until the next 12-bit word is loaded in.

The four DAC-8512 share common CLK and LD inputs, because all four MFCs operate simultaneously as well as having synchronised SDI input signals. These common signals are buffered prior to connection with the DACs. The MFCs themselves have a number of functions available, however, they only require the analogue control signal and power connections (+15 V, -15 V, GND) for basic operation. The flow-rate is linearly controlled over the full flow range with a 0 to 5 V

signal. The 0 to 4.095 V output range of the DAC, is therefore amplified to the required 0 to 5 V range by a non-inverting amplifier with a trimming pot to calibrate the output. A very low-noise quad operational amplifier (OP470) is used for all four control signals. The circuitry schematic of this sub-module is shown in Figure 7.11.

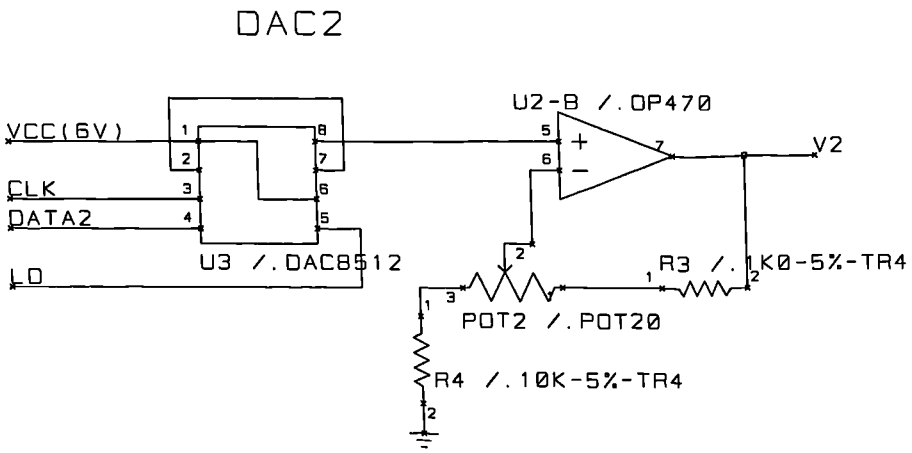

Figure 7.11 Schematic of a DAC sub-module to produce a MFC control signal.

Solenoid Valve Drivers

The solenoid valves 1 and 2 (see Figure 7.3) require a regulated 24 $V_{d.c.}$ supply for operation, and the valve driver circuitry is shown in Figure 7.12. The 24 V supply is switched by a reed relay, which in turn depends upon the biasing of a standard *n-p-n* transistor. The logic level of the digital signal controls the biasing of the transistor.

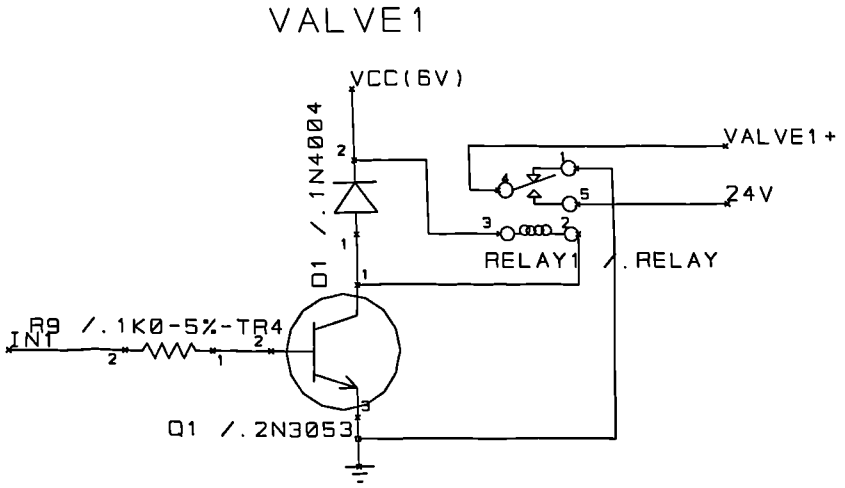

Figure 7.12 Schematic of a valve driver sub-module.

Micro-Hotplate Driver Circuitry

The microheaters are electrically equivalent to a variable resistor. Its operating temperature is set by the electrical power dissipation which is in turn determined by the heat loss from the silicon sensor to its environment. The MHPs have been calibrated and modelled as described in Chapter 6.

The two 12-bit analogue outputs from the plug-in DAQ board are used to provide high-speed open-loop control of the MHP temperatures. Each output drives all three MHPs on a SAD[†], so each microheater must be calibrated in order to obtain an accurate operating temperature (±2°C).

Under voltage control, we have used three temperature drive modules, as shown in Figure 7.13, to satisfy the MHP power requirements for the three heaters. Within each sub-module there is a voltage follower power amplifier, which provides an adequate maximum current supply of 325 mA to each MHP. To minimise the possibility of thermal shock fracture of the MHP membrane, any rapid input voltage transients are suppressed by the 1000 μF capacitor. A voltage limiter is also incorporated to prevent the maximum voltage being exceeded, and so limit the operating temperature of the MHP to a reliable level.

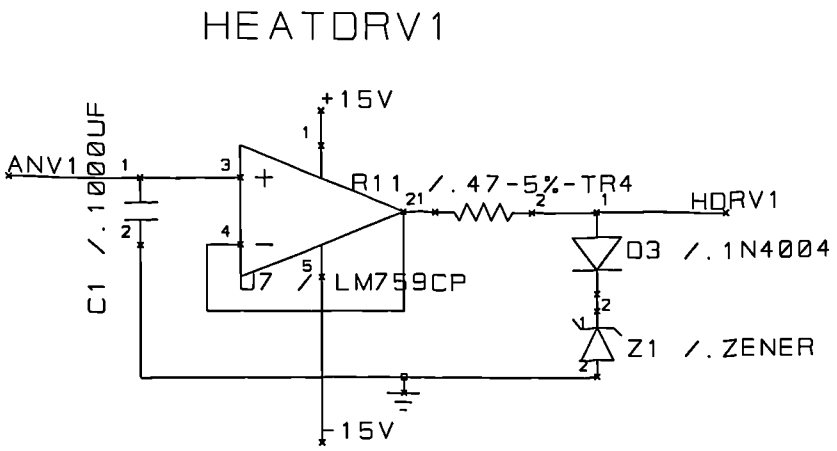

Figure 7.13 Schematic of a MHP driver sub-module.

[†] Microprocessor-based independent control of the heaters is being developed separately at Warwick University.

7.2.3.2 Static Rig Utilisation

The static rig, as shown in Figure 7.14, was developed at Warwick University to condition the signals for up to 12 chemoresistive sensors for an electronic nose [7.10].

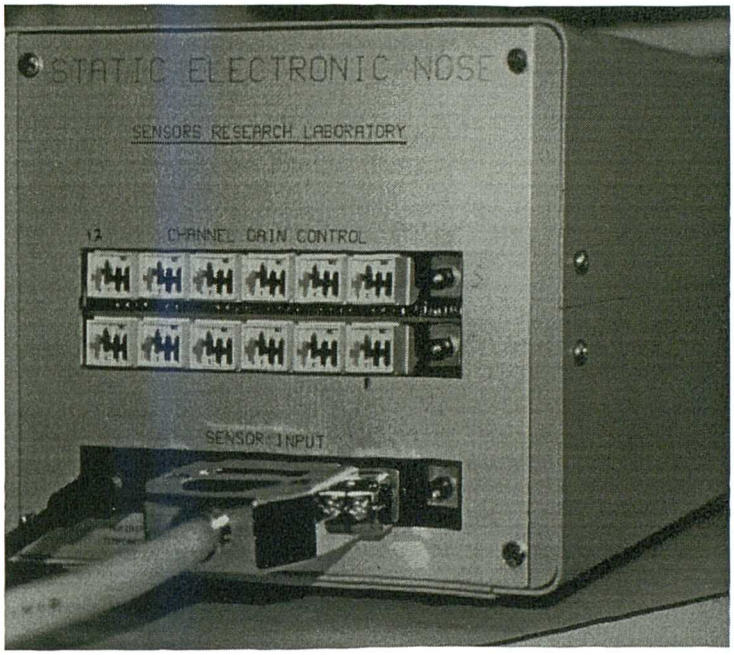

Figure 7.14 Static rig developed at Warwick University to condition the output signals from 12 chemoreistors.

The signal conditioning circuitry lies on standard Eurocards within the static rig and produces an output voltage for each of the twelve sensor channels. The sensor signals are connected to the front panel of the static rig by a 25-way 'D'-type connector, while the output is a 50-way ribbon cable. The 0 to 9.54 V output signal is linear with sensor resistance. The choice of the operating resistance range is selected *via* d.i.l. switches on the front panel, and colour coded as summarised in Table 7.3. In this way it is possible to measure the resistance of the sensors over a wide dynamic range from ohms to kilo-ohms.

Table 7.3 Selection of measurement range of sensor resistance *via* the static rig.

DIP switch setting (colour coded)	Resistance range on each channel (Ω)
Yellow	20 to 880 k
Orange	0.5 to 19 k
Red	50 to 1900
Brown	5 to 190

7.2.3.3 Design of the Temperature/Humidity Interface PCB

The function of the temperature/humidity interface PCB is to condition the sensor signals from two temperature sensors and a humidity sensor, as well as interconnecting the gas sensor outputs to the static rig and the control signals from the main interface PCB to the MHPs. Figure 7.15 shows the PCB connected to the sensor housing.

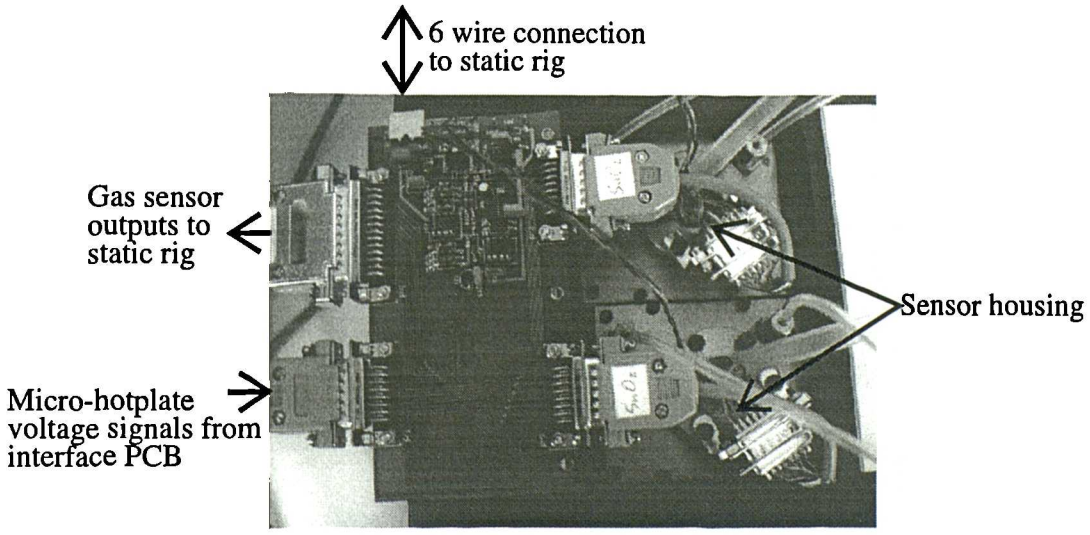

Figure 7.15 PCB to monitor the temperature and humidity of the gas and drive the MHPs.

The sensors are mounted on a detachable brass header, as shown in Figure 7.16. The pins from the 14-pin d.i.l. socket used to hold the SAD are fed through the header and soldered directly to a 15-way 'D'-type connector attached to the other side of the brass header. The connection cables between the headers 'D'-type connector and the

temperature/humidity PCB connectors are not standardised because the pin-out configuration varies between sensor designs. Instead specific connection cables have been produced for sensor designs with different pin-outs. Tracks on the PCB connect the six sensor outputs from each of the two 15-way 'D'-type connectors to a 25-way 'D'-type connector, which is linked to the static rig. Another 15-way 'D'-type connector receives the MHP voltage signals, which are similarly connected *via* the PCB to the two 15-way connectors.

The temperature sensor (LM35DZ, National Semiconductors Ltd.) is a 3-pin IC giving a linear voltage output of 10 mV/°C. Each brass header houses one temperature sensor IC, which is hardwired directly to the temperature/humidity PCB. A switch on the interface PCB provides selection of one temperature sensor. The switch is only used during the calibration phase to check that the two sensor chambers are in thermal equilibrium.

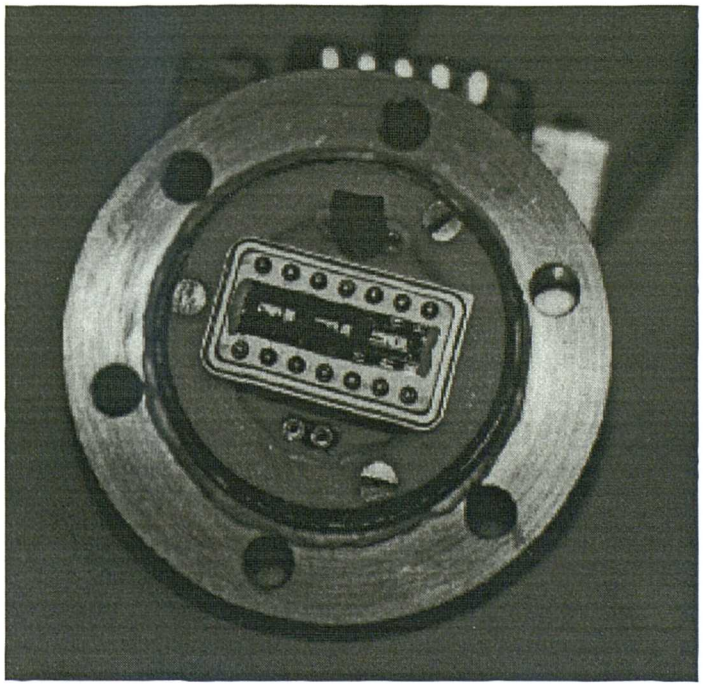

Figure 7.16 Underside of detachable brass header with temperature IC (top), SAD (centre), and humidity sensor (not plugged in).

A polymeric type relative humidity (RH) sensor (Minicap 2, Panametrics Ltd.) is also mounted in one of the sensor headers. The dielectric constant of the polymer and hence its capacitance varies with RH. This sensor is directly connected to the

interface PCB by a short 2-wire low capacitance cable in order to minimise the capacitance of the cable. The humidity sensor output is conditioned on the board to provide a d.c. voltage signal.

Both the interface circuits power supply and conditioned temperature and humidity sensor outputs are connected from/to the static rig by a standard six wire cable.

7.2.4 Fail-Safe Leak Detection System

The safety hazard posed by using toxic sample gases is a major design consideration of our test system. Even though the possibility of a leak has been minimised by the use of high quality hardware, it is still essential that the system is fail-safe. Thus, the flow of hazardous gases into the sensor test system is halted when either the fume cupboard that extracts the exhaust is off, or a leak is detected in the room.

In order to determine whether the fume cupboard is drawing air, an airflow switch (RS Components Ltd.) has been placed in the exhaust duct. When the fume cupboard is on, this sensor controls a 24 $V_{a.c.}$ signal to the fail-safe leak detector system. This signal controls valves 3 and 4 of the gas flow hardware (see Figure 7.3), therefore, ensuring that hazardous gases cannot enter the sensor test system unless the fume cupboard is on.

For leak detection two commercial CO detectors (BRK Brands Europe Ltd.) have been modified to turn the 24 $V_{a.c.}$ signal off when an alarm is sounded, which consequently stops the gas flow.

The 24 $V_{a.c.}$ signal is also connected to the main interface PCB, where it is rectified to a 7 $V_{d.c.}$ signal. This signal is connected to the DAQ card, allowing the testing system to monitor continuously for hazardous gases. If a leak occurs during a test then the Labview testing sequence program can also adopt a fail-safe state.

7.2.5 Test Sequence Program

As described in Section 7.2.2, the VI functions required from the system software are analysis and presentation. The presentation function refers to; the test sequence control parameters to be entered at the VIs front panel, and measured test system quantities to be displayed and stored. The analysis function is responsible for the

conversion of the entered and displayed parameters to a format which is compatible with the DAQ card. This function also deals with the sequence of the DAQ input/output signals to ensure operation of the signal conditioning circuitry and data acquisition.

A flow diagram of the general test sequence is shown in Figure 7.17. Before the automated test sequence can start, the user has to load the gas sensors into the brass housing and load the test sequence parameters. A warm-up period of 45 minutes is recommended by the MFC manufacturers to ensure the required flow-rate, as well as allowing the Dri-block® heater to reach equilibrium. The test sequence parameters are entered *via* the VI front panel, allowing the user to specify the sensors operating temperature, gas flow-rates and time duration for each sequence during the test.

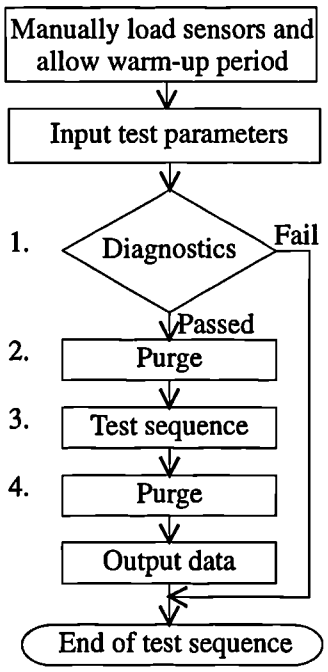

Figure 7.17 Flow-chart of the test sequence.

1. Once the test program has started, a diagnostic sequence ensures that the system is operating correctly before collecting data. Checking the fail-safe system signal indicates that the fume cupboard is working. Also monitoring the flow sensor output during operation of each of the MFCs, checks that the flow supplies are correctly operating and that the gas flow hardware has no leaks. If these signals indicate that

the system is operational, then the test program continues, otherwise the program stops.

2. A purge sequence then passes clean air through the pipework to remove any unwanted sample gases or contaminants. It also allows the sensors base-line resistance to stabilise at a specific operating temperature prior to testing.

3. The test sequence is made up from a sequential change in programmable physical parameters. The period between condition changes is also initially programmed. Data are sampled throughout the test sequence.

4. The gas flow hardware is expurgated again before the data are saved to a text file on the hard disc. To ensure a safe idle state the system is reset before program completion.

7.2.5.1 VI Front Panel

The VI front panel, as shown in Figure 7.18, is the test system user interface on the PCs monitor, which allows the test sequence parameters to be programmed, as well as indicating the progress of the program.

The programmable parameters include the state of valves 1 and 2, the sequence step duration (seconds), the flow-rate of the MFCs (ml/min) and the two MHP drive voltages. An individual valve state is entered initially, since the valve states are not varied during a test run. However, the remainder of the sensor test system parameters have the facility to be changed for each step of the sequence, as can be seen by the tabulated layout of the front panel. At the end of each sequence step row there is an LED indicator and a 'STOP' button. The LED indicates which step the sequence is currently operating and the 'STOP' button allows the test sequence program to be stopped during the test.

The diagnostic section on the front panel indicates the results from the diagnostic tests.

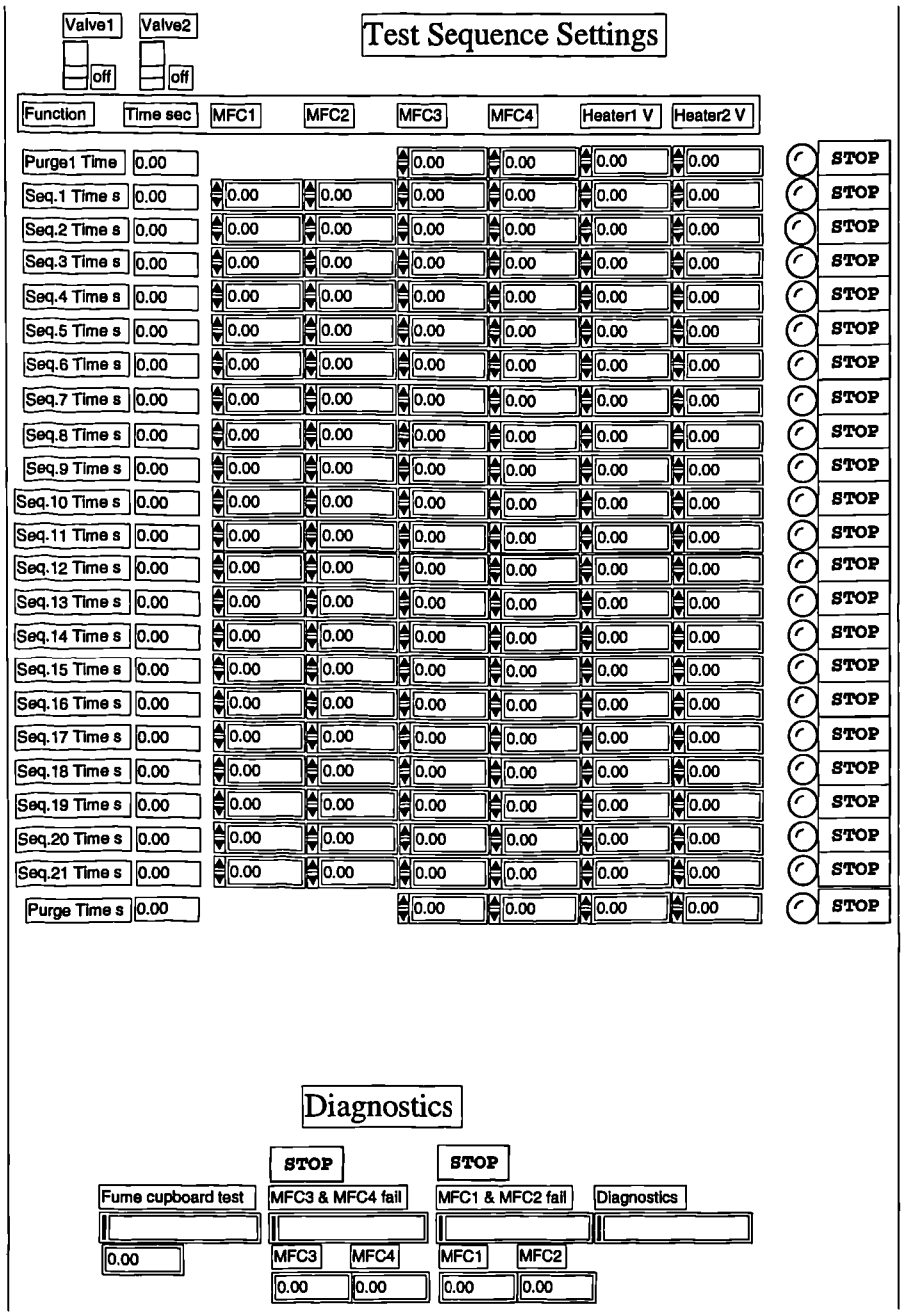

Figure 7.18 Labview front panel graphical user interface.

7.2.5.2 Software Design

Labview is a high-level graphics-orientated application software. The program is created graphically, whereby program commands and functions are seen as graphic symbols and icons. However, Labview is still a high-level language which obeys many rules seen in more conventional high-level languages.

The first sequence in the program controls the diagnostic tests, as shown in the flow-chart of Figure 7.19. The first condition box checks the fail-safe system signal.

If the fume cupboard is off or malfunctioning the program will set all the control signals to zero and indicate a 'fail' message prior to the program ending. However, if the fail-safe signal is greater than 5 V the fume cupboard is working and it is safe to proceed with the program. If this condition has passed then the program sets all the control signals to zero, before testing the MFCs.

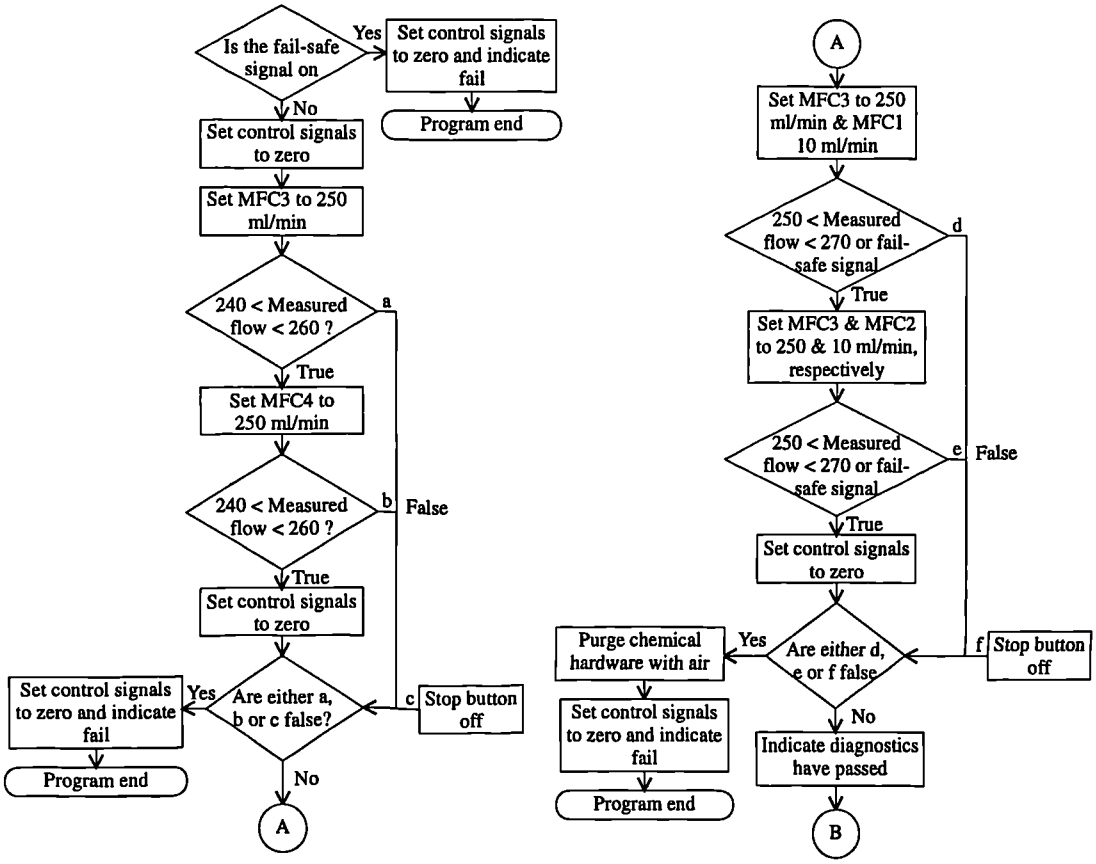

Figure 7.19 Flow-chart of diagnostic section in the test sequence program.

The next diagnostic tests the operation of MFC3 and MFC4 and the integrity of the gas flow hardware. MFC3 is tested by setting a flow-rate of 250 ml/min and validating this flow-rate at the exhaust with the flow sensor. A stabilisation time of approximately 15 seconds during the test ensures the flow-rate reaches a steady-state. The same test is done with MFC 4. During both these tests the fail-safe system signal is again checked. If either of these flow tests are failed or the front panel stop button is active, then the program sets all the control signals to zero and indicates an error before the program ends. If the tests were passed then the program continues.

The same flow diagnostic procedure is then carried out to test MFC1 and 2, respectively. However, the test flow ranges were selected to suite the MFC specification. Once these tests have been completed a 'diagnostics passed' message is displayed on the front panel. The remainder of the test sequence program is shown in Figure 7.20. The first operation reads the state of valves 1 and 2 and the purge1 time from the front panel. The LED is then switched on indicating that the purge1 step has started. At this point, data from the DAQ cards 16 analogue inputs are sampled. All the remaining variables for the purge1 stage are then read from the front panel. Again the condition of the fail-safe system signal and the stage stop button are checked. If these conditions fail, then the program purges with air by setting MFC3 to 250 ml/min. Once the gas flow hardware is decontaminated all the control signals are set to zero before the program end. This fail path ensures the program sets the sensor test system in a fail-safe state.

If the last condition passes then the control signals for the MFCs, the valves and the MHP drive voltages are sent to the gas flow hardware.

A condition stage checks whether the purge time has been completed. If not, the program loops back to the sample data function and proceeds until the purge time is completed.

From this point the program runs to the first of the testing stages. The first variable obtained from the front panel is the sequence 1 (seq.1) time. The associated LED is then turned on and the input data are acquired. Again the fail-safe signal is measured along with the seq.1 'STOP' button. As before, if this condition fails then the program follows the same response until the testing system is in the fail-safe state. If this condition is passed then seq.1 control variables are read from the front panel and used to drive the system hardware. If the seq.1 time has not been completed the program continues to loop back to the collect data function until the time has ellapsed.

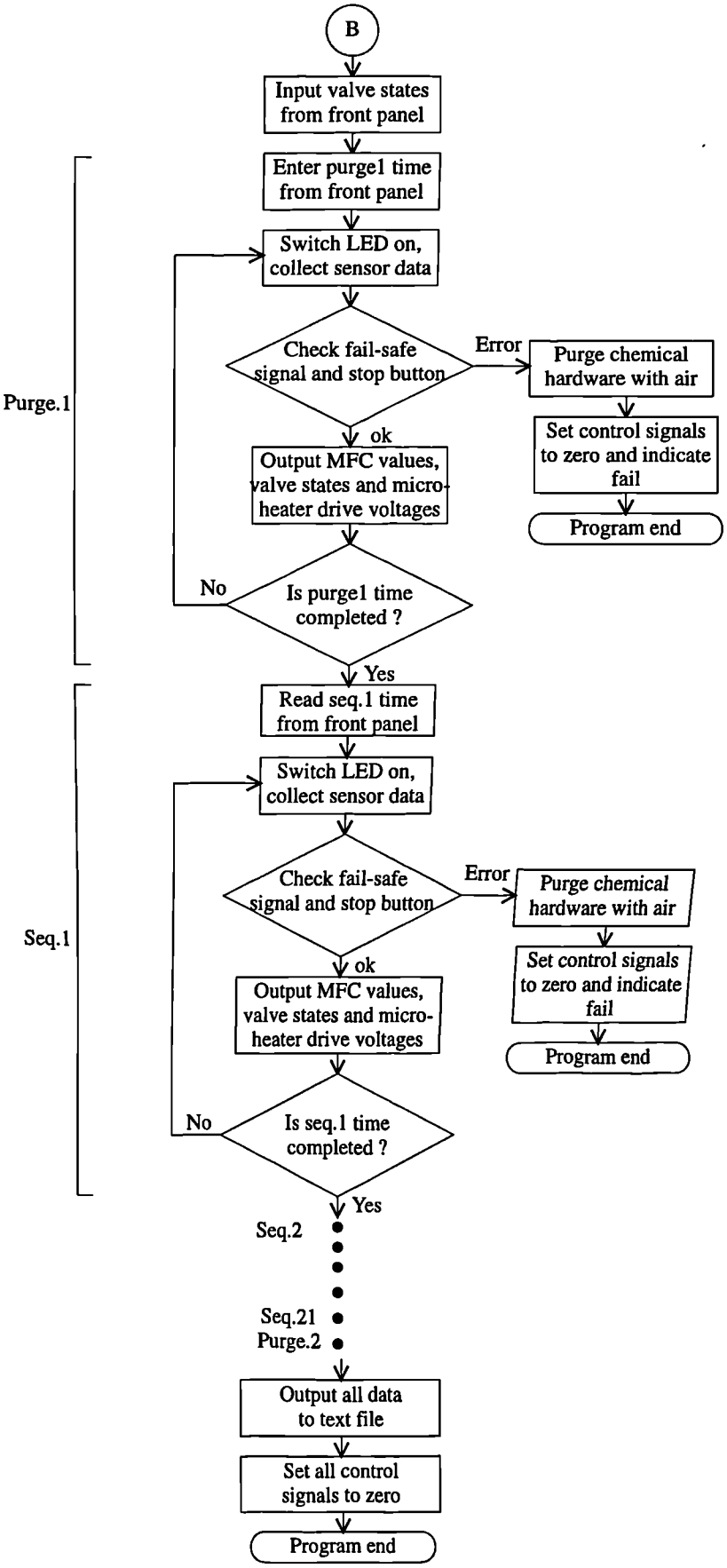

Figure 7.20 Flow-chart of the main test sequence.

The flow-chart structure for seq.1 is then repeated for the remainder of the sequence stages up to seq.21. A second purge cycle is activated with the same program flow-chart as the initial purge cycle. After completion of the second purge, the stored data from each stage are then chronologically ordered and saved in a text file suitable for spreed sheet applications. This data is then ready for data analysis.

The final function in the test sequence program is to set all the control signals to zero, rendering the system in a fail-safe state.

7.2.5.3 Labview Data Processing

Data processing within Labview is straightforward, by implementing 'equation' functions within the software. This is applied to some of the front panel control variables which are converted to voltage levels compatible with the signal conditioning circuitry. Conversely, some measured electrical signals fed into the DAQ card are processed so the information stored is the actual physical quantity being measured rather than the sensors output voltage.

In order to represent the output voltage from the system sensors as the physical measurands, requires the calibration of the sensor sub-systems. Sensor calibration for the testing system is described in Section 7.3, while the method of data analysis governs the data format and is outlined in Section 7.4.

7.3 Test System Commissioning

The test system must be commissioned to ensure that the physical variables controlled by the user are the actual physical quantities exposed to the sensors and that the sensor response data stored by the test system are the actual sensor output quantities.

A systems approach to the test system is considered to relate the data to the physical variables. The PC controlled test system can be represented by a system block diagram, as shown in Figure 7.21.

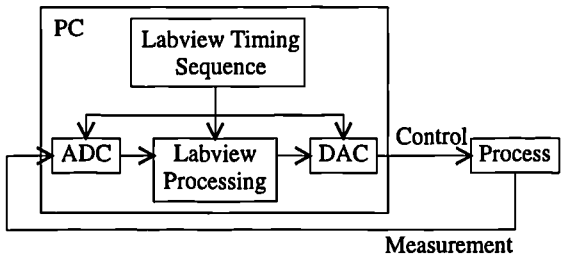

Figure 7.21 Block diagram of PC controlled system.

The electrical and gas flow hardware external to the PC which control and measure the physical variables are represented by the process block.

In order to calculate the physical quantities from the electrical signals being generated and measured by the DAQ, requires calibration of the related sub-systems. The process block is expanded to show the sub-systems involved, as shown in Figure 7.22.

The sub-systems which are concerned with the control of the concentration of the sample gases and MHP operating temperature are the gas flow hardware and microheater driver systems, respectively. Whereas, the sub-systems responsible for measuring the physical variables are the flow sensor, humidity sensor, gas temperature sensor and the gas sensor systems. All of the above sub-systems require calibration.

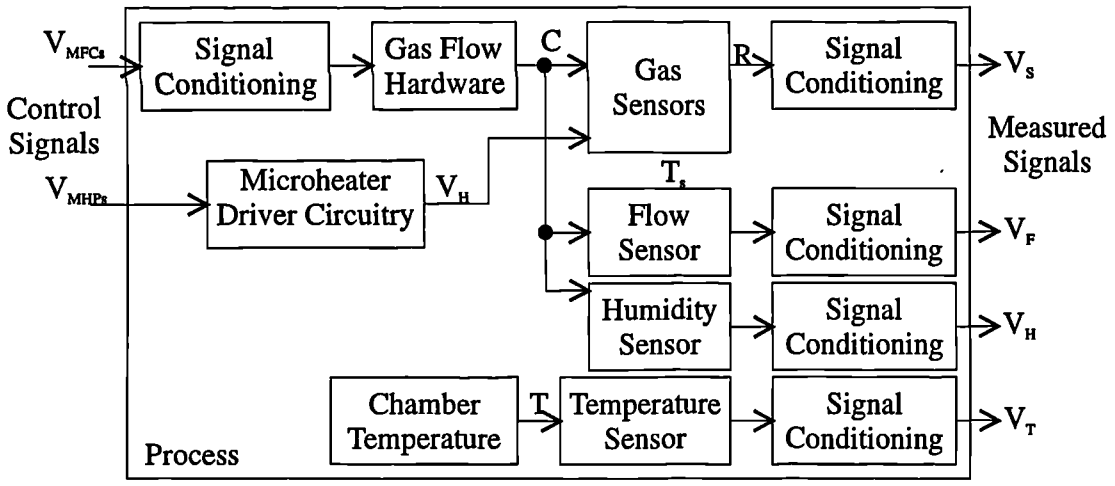

Figure 7.22 Block diagram of test system hardware, where V_{MHPs} and V_{MFCs} are the control signals for setting the MHPs operating temperature and the flow rates, respectively, and V_S, V_F, V_H and V_T are the measured signals from the signal conditioning circuitry associated with the gas sensors, flow sensor, humidity sensor and temperature sensors, respectively.

Due to the physical nature of these sub-systems, a change in control variable does not produce an immediate change in the physical quantity being controlled. Therefore the transient behavior of the sub-systems needs to be determined. The large amount of processing required by Labview during each sample is reflected by a relatively long sampling time of approximately 0.5 s. The transient error can be neglected for the electronic sub-systems because they reach steady-state in far less than 0.5 s. However, the flow system transients have a response time which is greater thant 0.5 s. The effect of gas flow response on concentration of sample gas and humidity are described in Section 7.3.2. The signals presented in Labview are assumed to be the same as the analogue electrical signals to/from the DAQ hardware because of the speed and accuracy (12-bit) of the DAQ card.

Steady-state calibration of each measurement and open-loop control system allows a function to describe the relationship between the actual physical variable and the corresponding electrical signal which is interfaced with the PC. The data can be presented in terms of the corresponding physical variables by applying the calibration function within Labview. The approach to steady-state calibration is described in the next Section.

Once the testing system is calibrated the data accuracy and the data analysis limitations can be determined. Only when these criteria are satisfied can the data be used for sensor characterisation and validation of sensor system models.

7.3.1 Steady-State System Calibration

The approach taken to calibrate the steady-state sensor outputs were to measure the signal conditioning output voltage response with the VI, during exposure to a known physical variable range. Conversely, calibrating control values was achieved by measuring the actual physical quantities with a calibrated instrument, over a range of control voltages from the DAQ. The calibration functions are presented for each sub-system.

7.3.1.1 Gas Concentration and Flow-Rate Calibration

The sample gas concentration and humidity are dependent upon the flow-rate of the MFCs. Ideally, the best way to calibrate this system is to vary the MFC control voltages over a suitable range of values and measure the gas/vapour concentration with a calibrated instrument. Unfortunately, due to lack of availability of a suitable instrument this approach was not possible. However, since the concentration is directly related to the dilution ratio between the flow-rates, an accurate determination of the gas concentration can be achieved by calibrating the flow-rates. The gas cylinder concentration accuracy is ±1 %.

For each MFC, the control signal was varied on the VI front panel, while the flow was measured by a rotameter (Series 1100, MFG. CO. Ltd, which has a typical accuracy of ±2 %) on the exhaust port. A 0 to 5 V command signal to the MFC linearly controls the flow-rate from zero to the maximum flow rate. To achieve this voltage range from the signal conditioning requires a 0 to 4.096 V signal from the DAQ card. Within Labview, the required flow-rate can be set on the front panel and scaled to the corresponding control voltage signal. The MFC command signal then controls the actual flow, which can be compared with the programmed flow. The measured flow output values are plotted against system input values for both MFC 3 and MFC 4, as shown in Figure 7.23.

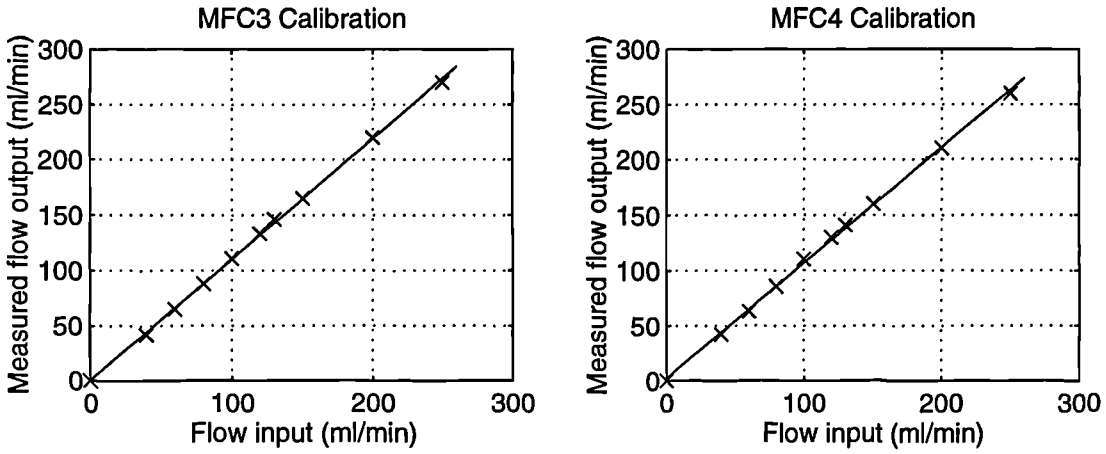

Figure 7.23 Calibration data for MFC3 and MFC4.

A first order least squares fit has been plotted through the data points to obtain a calibration function for MFC3 of,

$$F_m = \frac{(F_{set} - 0.6925)}{1.0912} \tag{7.1}$$

and similarly, for MFC4,

$$F_m = \frac{(F_{set} - 2.1723)}{1.0445} \tag{7.2}$$

where F_{set} is the demanded flow-rate (ml/min) and F_m is the measured flow-rate (ml/min). These functions are utilised within the Labview program to improve the accuracy of the controlled flow rate to ±5 % over the operating range 50 to 250 ml/min.

The 0 to 10 ml/min flow rate range of MFC1 and MFC2 is too small for the rotameter to produce similar calibration data, as for MFC3 and MFC4. However, the flow rate change has been measured separately for both MFCs, when their maximum flow is added to a steady background flow of 100 ml/min. However, extra processing is not required for MFC1 and MFC2, because the full scale change produced a 10 ml/min actual flow increase.

7.3.1.2 Integrated Micro-Heater Calibration

As described in Chapter 6 the integrated microheater can be used as both a thin film Platinum Resistance Thermometer (PRT) and a heater. For each MHP design the resistance is measured over a range of temperatures to define its TCR. The heater is then driven by a constant current source while measuring the voltage across the heater, which defines the relationship between electrical power and resistance. The heater calibration, as described in Chapter 6, allows a function to be defined relating the applied voltage and sensor resistance. However, as described in Section 7.2.3.1, the analogue voltage output from the DAQ card passes through the heater driver signal conditioning circuitry, which is equivalent to having the microheater in a potential divider with a 51 Ω resistor (± 0.5 %). The voltage dropped across the 51 Ω resistor has to be compensated for, by multiplying the required voltage by a factor of,

$$\left(\frac{R_H(T)+51}{R_H(T)}\right)$$

where R_H is the sensor resistance in ohms at an arbitrary temperature, T.

These functions can be applied in Labview, to generate the required voltage to drive the microheaters to a specific temperature. The combined accuracy of the calibration functions and resistor value, allow the heater resistance to be controlled with an accuracy of ±6 %.

7.3.1.3 Flow Sensor Calibration

The flow sensor measures the flow-rate at the gas flow hardware exhaust, to check the MFC operation and system integrity.

Flow sensor calibration was achieved by measuring the flow sensor voltage (V) signal with the VI, over a controlled range of pre-calibrated flow-rates (F), as shown in Figure 7.24. A rotameter was connected to the exhaust to check the flow-rates.

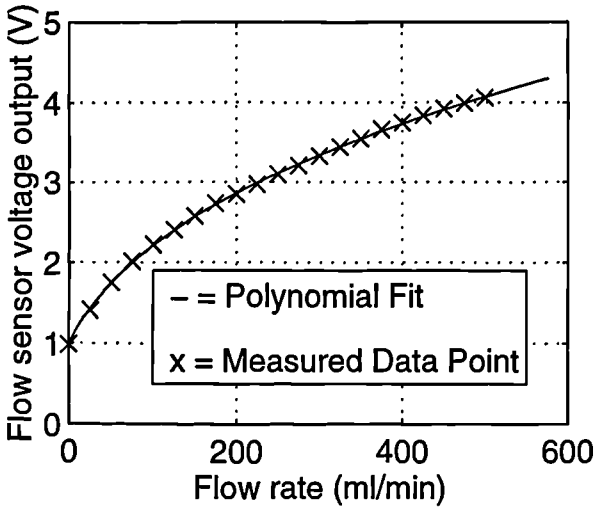

Figure 7.24 Flow sensor calibration.

A third order least squares polynomial was fitted to the data points, defining the calibration function as,

$$F = (3.85 \times V^3) + (15.08 \times V^2) + (2.91 \times V) - 21.4 \qquad (7.3)$$

where the sensor voltage V is in volts, and flow-rate F in ml/min. The high accuracy of the polynomial allows the measurement error to be neglectible when compared to the ±5 % flow-rate accuracy.

7.3.1.4 Temperature Sensor Calibration

The temperature sensor ICs in each of the sensor chambers were calibrated by measuring the sensors output voltage over a range of sensor chamber temperatures. The chamber temperature was manually adjusted on the Dri-block® heater in which the brass blocks are mounted. The temperature sensor ICs were calibrated separately, because the other brass block housed a 'stick' thermometer, with an accuracy of ±1.0°C. The assumption was made that the temperature was the same in both brass blocks.

The characteristic response of the two temperature sensors are shown in Figure 7.25.

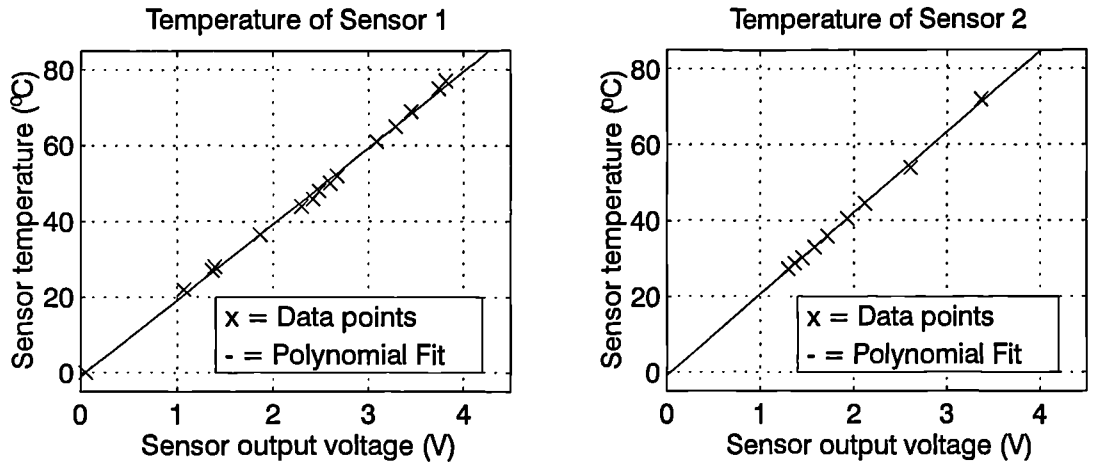

Figure 7.25 Calibration data for the two temperature sensor ICs.

A first order least squares fit is plotted through the data points, from which the temperature (T) is calibrated to the sensors output voltage (V) by the functions,

$$T = (20.083 \times V) - 0.961 \tag{7.4}$$

$$T = (21.383 \times V) - 0.836 \tag{7.5}$$

for the sensors in chambers 1 and 2, respectively. The accuracy of the polynomial fit to the data points is better than ±1 °C, which allows the temperature to be measured with an accuracy of ±2°C from RT to 80°C. It was noted that the temperature sensor output is independent of any gas flow cooling effects.

7.3.1.5 Humidity Sensor Calibration

Calibration of the humidity sensor system, involved monitoring the output voltage from the signal conditioning circuitry with the VI, while controlling the absolute humidity. The response of most chemical sensors are dependent on the ambient temperature, unsurprisingly the Minicap 2 RH sensor is no exception. Therefore, the humidity response is calibrated over the intended gas temperature range of 25°C to 55°C. The sensor utilises thin film polymer materials which are known to be cross-sensitive to a variety of gases and vapours. Fortunately, the response change

to the gases of interest are less than 1 % over the concentration range, hence this effect has been neglected.

The humidity was controlled by varying the dilution ratio between the dry air supply and the humidified air supply. Humidity saturation in the bubbler is maximised by minimising the bubble size by passing the gas through a glass frit and maximising the bubble path length through the bubbler. Therefore, the saturated air supply has an absolute humidity concentration of 31.31×10^3 ppm at a room temperature of 25°C. The inaccuracy caused by this assumption can be neglected compared to the tolerances of the flow-rates, which have already been calibrated in Section 7.3.1.1.

The gas temperature was controlled by the Dri-block® heater and measured with the calibrated temperature sensors.

Output voltage data for changes in absolute humidity at a constant temperature were taken. This test was repeated over the ambient operating temperature range, to form the data set, shown in Figure 7.26.

By using the software package Matlab©, a least squares regression technique was applied to the data to derive a function between absolute humidity, temperature and voltage output. The model developed generates a good fit to the data points as shown in Figure 7.27.

By rearranging the model, the expression,

$$H = \frac{V - \left[\left(7.54 \times 10^{-5} \times T^2\right) - \left(1.09 \times 10^{-2} \times T\right) + 2.37\right]}{\left[\left(8.82 \times 10^{-6} \times T^2\right) - \left(1.17 \times T\right) + 4.26 \times 10^{-2}\right]} \qquad (7.6)$$

has been defined for absolute humidity (H) in ppm in terms of sensor output voltage (V) and temperature (°C). This is implemented within Labview so the humidity data stored corresponds to the measured absolute humidity. This gives a signal accuracy of ±10 % over the humidity range 6,200 to 25,000 ppm.

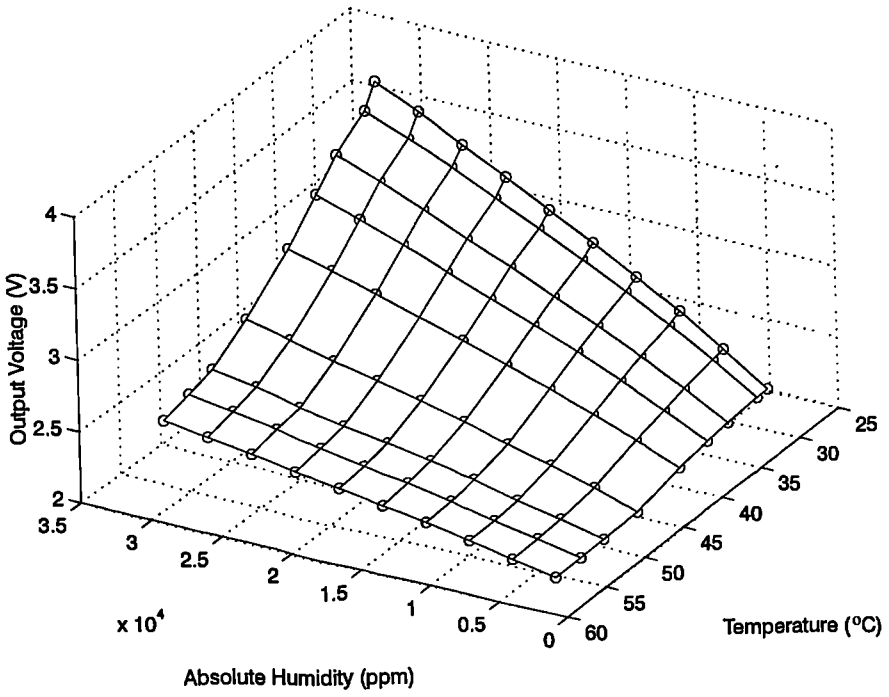

Figure 7.26 Humidity sensor response data.

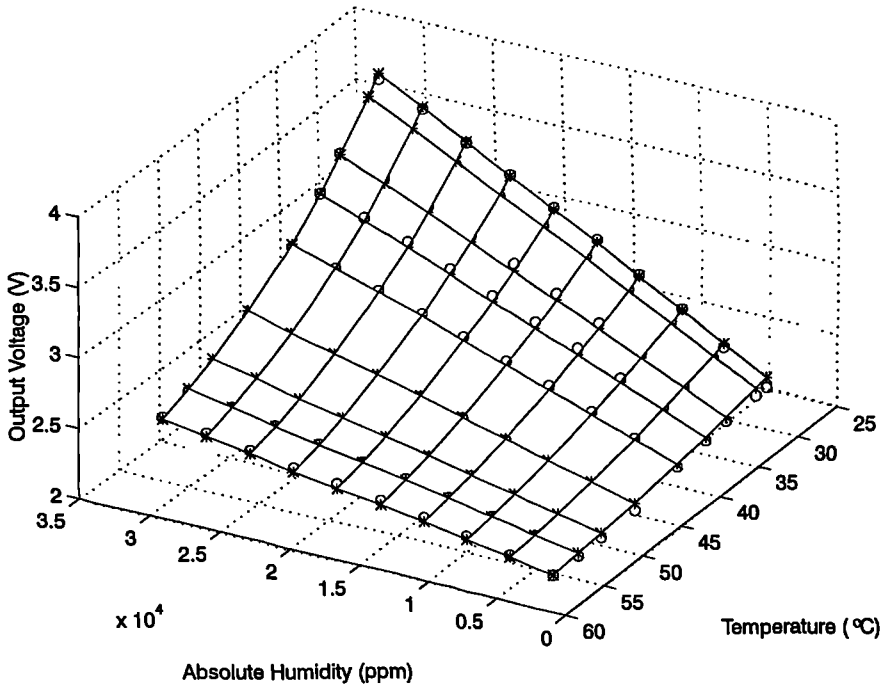

Figure 7.27 Calibration model superimposed as a mesh over the data points.

It must be noted that converting absolute humidity to RH is not straightforward, since RH is itself dependent on temperature [7.6]. The RH inside the sensor chamber can be calculated by dividing the water vapour concentration by the saturated water

vapour concentration at the temperature of interest. The saturated water vapour concentration at various temperatures is established from data books [7.11]. The data collected for absolute humidity was converted to RH, as shown in Figure 7.28.

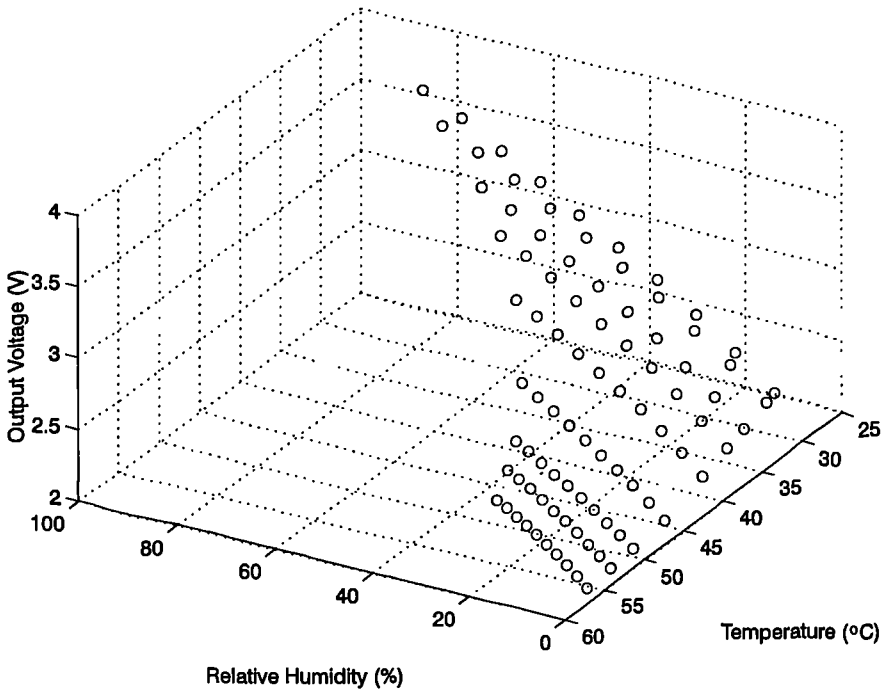

Figure 7.28 Computation of RH from humidity sensor output and gas temperature.

7.3.1.6 Static Rig Calibration

In the gas sensor measurement sub-system, only the signal conditioning is calibrated, because the response of gas sensors to changes in the controlled physical parameters are undefined.

The static rig provides the signal conditioning for testing chemoresistive gas sensors. The natural variability of the different sensor materials and hence base-line resistance and sensitivity, require that the static rig can accomodate a wide range of values. Therefore, a d.i.l. switch on the static rig front panel permits the circuitry to measure resistance values over approximately four orders of magnitude, as described in Section 7.2.3.2. For each range, a resistive input signal is converted to an output voltage signal in the range of 0 to 9.54 V. This output voltage saturates at 9.54 V if the input resistance is greater than the selected input range.

Calibration of this instrument is necessary to evaluate the scaling factor between the static rig output voltages and the input resistances. Before calibrating the static rig, the variable gain and offset for each input channel were set to the same value. A number of standard resistors were used to obtain the calibration data, as summarised in Table 7.4. The data produced a first order relationship between the input resistance and static rig output voltage. These calibration functions allow the resistance to be measured with an accuracy of ±2 % over 10 to 100 % of the resistance range.

Table 7.4 Static rig calibration parameters.

d.i.l. switch setting (colour coded)	Function between input resistance (R) in ohms and output voltage (V) in volts	Maximum resistance value before saturation (Ω)
Yellow	$R = (9.28\times10^{4})V$	880 k
Orange	$R = (2.018\times10^{3})V$	19.15 k
Red	$R = (201.8)V$	1.915 k
Brown	$R = (20.18)V$	191.5

Before running the test sequence program, the base-line resistance of each chemoresistor must be established. This is achieved by loading the sensors into the test system and applying a Labview calibration program, which allows the user to monitor the sensors resistance while controlling the sensors operating temperature. The d.i.l. switches can be manually toggled to obtain the most suitable range for each channel before testing.

7.3.2 Test System Dynamics

The test system dynamics have been simplified because the electronic sub-systems reach steady-state during each data sample. This is not true for the control of the gas concentrations and humidity, which are dependent on the transient response of the MFCs and the flow system dynamics.

The transient response data acquired from the gas sensor and humidity sensor are not representative of the sensor system response, since the flow system response also contributes to the data. This effect is not critical for the humidity, because only steady-state information is required. However, the transient characteristics of the gas

sensors are determined by the physicochemical mechanisms which dictate the transduction property of the sensor system. Consequently, the real dynamic behavior of a sensor system is often compromised, because changes in gas concentration at the sensor surface are erroneously assumed to be ideal step inputs. This assumption may be acceptable if the gas sensors time response is much greater than that of the flow system. However, if the response times are comparable, then the transient sensor information cannot be obtained unless the transient response of the flow system (i.e. transfer function) has been obtained.

Ideally, to calibrate the flow system requires measurement of the sample gas concentration in the sensor chamber, to step changes in the MFC command signal with respect to time. This method would require a gas-monitoring instrument with a very fast response time. Since an appropriate instrument was not available a more approximate method has been adopted.

The approach taken relies on the assumption that the gas concentration is directly related to the ratio between the flow-rate of sample gas and flow-rate of air. The transient response is thus determined from the collective response from the MFCs and fluid dynamics of the pipework.

The flow sensor which has a response time of 5 ms is used to calibrate the response time of the MFCs to a step change in the MFC command voltage, assuming the gas flow into the pipework equals the gas flow out, due to the gas being incompressible. To limit the complexity of the model only one input variable is used, by assuming a constant air flow of 250 ml/min. The input variable is the command voltage to the 0 to 10 ml/min MFC, which controls the flow-rate of the sample gas into the pipework.

The dynamic response of the pipework is assumed to contribute a delay time which is proportional to the volume of pipework divided by the flow-rate. This delay is dominated by the time it takes the sample gas to reach the interconnection with the faster air flow, since the MFC which controls the sample gas flow-rate has a maximum flow rate of only 10 ml/min. The gas velocity profile across the pipework is assumed constant at the point of dilution with air, since the gas flow velocity into the pipework is slow and the pipework length is short. The gas drift distance caused by diffusion is assumed to be negligible compared to the distance covered due to the gas velocity.

There is also a first order time delay associated with the gas mixing with the air in the sensor chamber. The time constant is related to the chamber volume divided by the inlet flow-rate, which is approximately 1.6 s for a flow-rate of 250 ml/min.

The dynamic response of the MFCs were investigated with the flow sensor. Consequently, the empirical response was assumed to be a first order lag system with a time constant of approximately 1 s. Using these assumptions a model was created, relating the input MFC command signal to the output sample gas flow at the sensor chamber. Since the input and output variables can be converted to concentration, the model allows a comparison to be made between the concentration control signal and the expected physical gas concentration with respect to time, as shown in Figure 7.29.

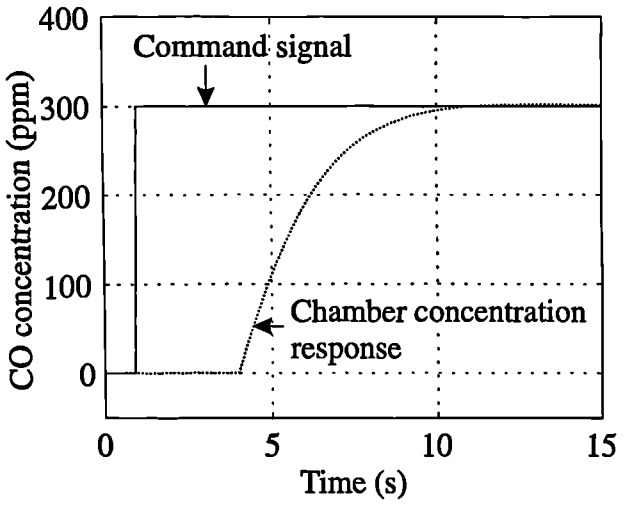

Figure 7.29. Gas concentration response to a step change in command signal.

With these model parameters, the response to a full scale step in the MFC command signal is a pure time delay of ~ 3 s before the gas concentration starts to increase with a time constant of ~ 2.6 s. This model gives an appreciation of the delays expected, although its reliability needs to be validated from real data. It does demonstrate that the system dynamics are determined by the mechanical flow of gas and not by the interface electronics or software programme.

7.4 Data Analysis

The data collected during each test sequence program are saved as a text file, which can subsequently be loaded into a spread-sheet package for initial analysis. The functions derived from the system calibration, modify the sampled data to represent the physical parameters being measured. Therefore, the response information of the sensor resistances, system flow-rate, sensor chamber temperature and RH to physical parameter changes, can be specified at any sample point or visualised in a graph.

The analysis method applied to the data is determined by what information is required. A typical test sequence varies a physical parameter while keeping the other physical state variables constant. Basic gas sensor response characteristics, like sensitivity, response time and long term stability can be established from the data. However, to characterise the gas sensor to all the physical variables, requires carrying out a number of test sequences. The data obtained can be used to characterise the sensor or validate the models described in Chapter 5.

The response of the twelve gas sensors in the data file are suitable for analysis by PARC programs, or they may require pre-processing algorithms [7.12] to fit the models within the PARC method. The PARC performance may also be improved by employing signals from the temperature and humidity. However, the collection of large data-sets over days, weeks or months should permit a better tolerance to sensor drift.

7.5 Conclusions

In this Chapter I have presented the design and construction of a gas sensor test system which characterises the response of chemoresistive gas sensors to ppm changes in CO, NO_2 concentrations in air, at various RHs and operating temperatures. The test station was used to collect the data presented in Chapter 8.

The accuracy of the sensor test system has been determined by various calibration routines and is summarised in Table 7.5. The inverse of the steady-state calibration functions derived for each sub-system are implemented in Labview, in order that the data are displayed and stored in terms of the physical variables (e.g. temperature and humidity).

Table 7.5 Accuracy of gas sensor test system.

Control		Measurement	
Physical variable	Accuracy	Physical variable	Accuracy
Gas flow (50 to 500 ml/min)	± 5 % within 6 s	Sensor resistance (10 to 100 % range)	± 2 %
Operating temperature from RT to 300 °C	± 6 % within 100 ms	10 to 90 % absolute humidity (ppm) @ 30 to 55 °C	± 10 %, response time of ~ 1 min
		Chamber temperature	± 2°C
		Flow sensor	± 5 %

The dynamic response of the test system has been considered, in particular the response of the flow system which controls gas concentration and humidity. By developing a simple model of the flow system dynamics the response of the gas concentration to a step excitation of the MFC is seen to have a delay time of 3 s and a rise time of approximately 3 s. This approximate model gives an appreciation of the limitations of transient analysis of the gas sensor data. However, it should be noted that the typical response time of MOS and XPc sensors are determined by the surface chemical reaction-rates and are ~ 10 to 100 s.

7.6 References

7.1 I. Harvey, G. Coles and J. Watson, The Development of an Environmental Chamber for the Characterization of Gas Sensors, *Sensors and Actuators,* **16** (1989) 393 - 405.

7.2 V. Demarne, A. Grisel, R. Sanjines and F. Lévy, Integrated Semiconductor Gas Sensors Evaluation with an Automatic Test System, *Sensors and Actuators B,* **1** (1990) 87 - 92.

7.3 T. Nakamoto, S. Ustumi, N. Yamashita, T. Moriizumi and Y. Sonoda, Active Gas/Odor Sensing Using Automatically Controlled Gas Blender and Numerical Optimization Technique, *Sensors and Actuators B,* **20** (1994) 131 - 137.

7.4 M. Nieuwenhuizen and J. Harteveld, An Automated SAW Gas Sensor Testing System, *Sensors and Actuators A,* **44** (1994) 219 - 229.

7.5 J. Grate, D. Ballantine and H. Wohltjen, An Automated Vapor-Generation and Data Collection Instrument for the Evaluation of Chemical Microsensors, *Sensors and Actuators,* **11** (1987) 173 - 188.

7.6 H-E. Endres, H. Jander and W. Göttler, A Test System for Gas Sensors, *Sensors and Actuators B,* **23** (1995) 163-172.

7.7 J.W. Gardner, T.C. Pearce, S. Friel, P.N. Bartlett and N. Blair, A Multisensor System for Beer Flavour Monitoring Using an Array of Conducting Polymers and Predictive Classifiers, *Sensor and Actuators B,* **18-19** (1994) 240-243.

7.8 Health and Safety Executive, EH40/95 Occupational Exposure Limits *1996*, HMSO, London, 1996.

7.9 R. Pallás-Areny and J.G. Webster, *Sensors and Signal Conditioning*, John Wiley and Sons, New York, 1991.

7.10 T.C. Pearce, J.W. Gardner, S. Friel, P.N. Bartlett and N. Blair, Electronic Nose for Monitoring the Flavour of Beers, *Analyst,* **118** (1993) 371-377.

7.11 A.M. James and M.P. Lord, Macmillan's Chemical and Physical Data, *The Macmillan Press Ltd,* London, 1992.

7.12 J. W. Gardner, Detection of Vapours and Odours from a Multisensor Array Using Pattern Recognition Part 1. Principal Component and Cluster Analysis, *Sensors and Actuators B,* **4** (1991) 109-115.

Chapter 8

8. Characterisation of Chemoresistors

8.1 Introduction

The objective of this Chapter is to present the results obtained from the testing of the gas-sensitivity of MOS, XPc and dual SADs. The different chemoresistors tested are summarised in Table 8.1.

Table 8.1 Summary of SAD characterisation described in this Chapter.

Sensor Design, SRL Code	Gas-Sensitive Material	Parameters Varied during Characterisation	Section Discussed
125/XPc	PbPc	NO_2, temperature	8.2
	MgPc	NO_2, temperature	8.2
	CuPc	-[†]	8.2
108/MOS	Thin film SnO_2: undoped, Pd and Pt doped	CO, NO_2, temperature, humidity	8.3.1
125/MOS	Thick film SnO_2: undoped, Pd and Pt doped	CO, NO_2, temperature, humidity	8.3.2
125/dual	Thick film SnO_2	CO	8.4
	CP	-	8.4

[†] Reasons for the missing data are described in the appropriate Section.

All the results reported here have been acquired on my gas sensor test system (with a gas temperature of 30°C) that has been described in the previous Chapter. This test system provides a means of testing the SADs to changes in the concentration of CO, NO_2 and a vapour (e.g. usually humidity). The CP coated chemoresistors require alternative test conditions, and are therefore being characterised by other researchers at the Universities of Warwick and Southampton. This work will be reported elsewhere, but an example of a typical response from a CP chemoresistor is also discussed.

The results presented are classified according to the type of chemoresistor investigated; namely, XPc, SnO_2, CP and intelligent dual sensor device. The device characteristics obtained are reported and, where possible, compared with the theoretical models described in Chapter 5.

8.2 Characterisation of XPc Chemoresistors

Tests were carried out on the three different XPcs (e.g. PbPc, MgPc and CuPc) at elevated temperatures to changes in NO_2 concentration. However, two problems became apparent: Firstly, the SRL125/XPc MHPs exhibits a hot spot in the centre of the membrane. Secondly, stresses were induced during testing which led to membrane fracture. The reason for the induced stress is uncertain, but two plausible explanations are; a thermal mismatch between the XPc and the substrate, or thermal gradients caused by the hot spot. The induced membrane stress becomes apparent when the membrane curls up after fracture. The consequence of a MHP suffering from non-uniform heating is shown in Figure 8.1.

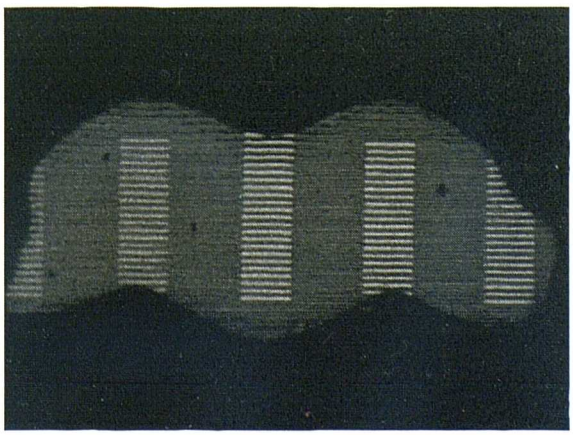

Figure 8.1 A hole formed by evaporation of the XPc caused by a hot spot on the SRL125/XPc MHP.

The hole formed in the XPc film suggests that the temperature at the centre of the MHP was increased above the sublimation temperature of the XPc. Unfortunately, this thermal non-uniformity demonstrates that the MHP calibration carried out in Chapter 6, only allows accurate control of an average temperature. The amount of temperature deviation over the membrane is dependent on the MHP geometry. The temperatures quoted in this Chapter therefore refer to an average operating temperature. However, the geometry of the hole provides important information (i.e. membrane isotherms) for improving the MHP design, as reviewed in the following Chapter.

The only results obtained with the as-deposited XPc films are shown in Figure 8.2. These results compare two runs from the same MgPc chemoresistor at 120°C and 180°C. The sequence of NO_2 exposure after 3½ hours initialisation in air was as follows; 125 ppb (3 hours), air (4 hours), 250 ppb (3 hours), air (4 hours), 500 ppb (3 hours) and a final 4 hour purge in air. Both tests were carried out at 38 % RH.

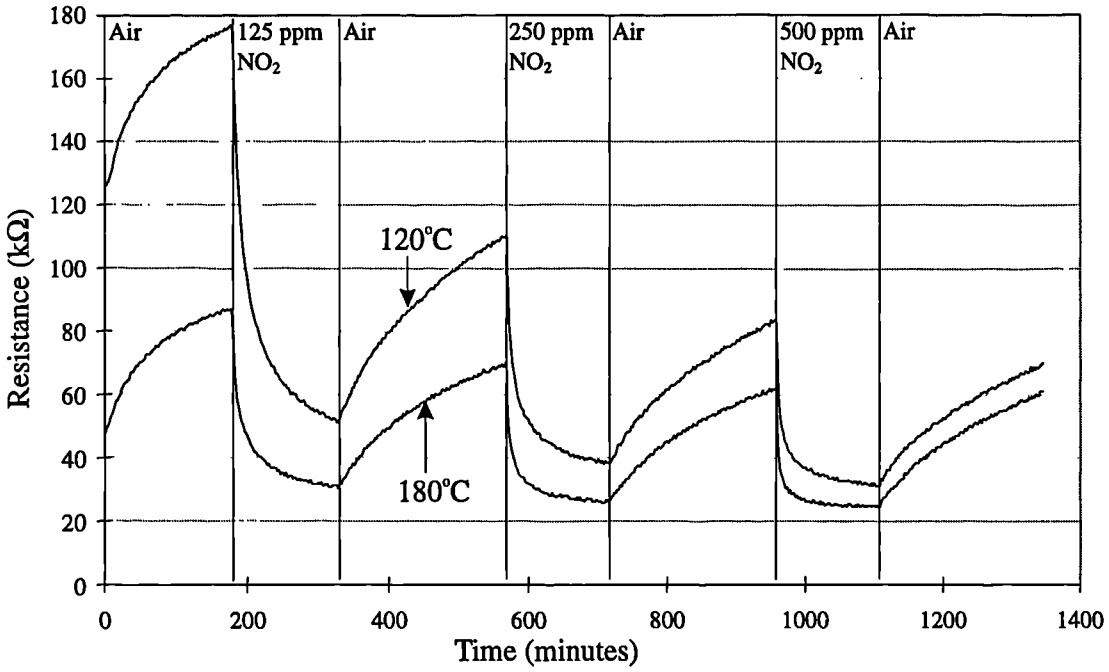

Figure 8.2 Response of as-deposited MgPc at two different operating temperatures (e.g. 120°C and 180°C) to changes in NO_2 concentration in air at 38 % RH.

The changes in resistance obtained during the test are typical of that expected from a XPc chemoresistor exposed to NO_2. Whereby the resistance decreases as the

NO_2 adsorbs on the internal sites, generating more *p*-type carriers. However, it can be seen from the time response in Figure 8.2 that the kinetics of this process are very slow (~ 1 hour), and indeed impractical for an early warning instrument. However, these characteristics do demonstrate that the time response becomes faster, as either the temperature increases from 120°C to 180°C, or when the NO_2 concentration increases. In an attempt to improve the response of XPc films a heat-treatment stage was investigated, since it has been reported elsewhere [8.1] that annealing the as-deposited film reduces the response time with some loss in sensitivity.

On-chip annealing of the chemoresistors was carried out with the temperature control of the MHP. The microheater was powered (72 mW) to give an average temperature of 200°C for 1 hour, after which the power was steadily stepped down over approximately a 30 minute period.

Unfortunately, device characterisation was again hampered by the problem of membrane fracture. However, some results obtained from a PbPc device before failure, are shown in Figure 8.3. An operating temperature of 125°C and a humidity of 43 % was maintained during the test. Alternating 10 minute periods of NO_2 and air were exposure after initialisation in air for 50 minutes, the NO_2 concentrations were; 31 ppb, 63 ppb, 125 ppb, 250 ppb, 500 ppb and 1000 ppb.

The results show that a response time of ~ 1 minute is possible when the PbPc chemoresistor is exposed to 1 ppm of NO_2 at 125°C.

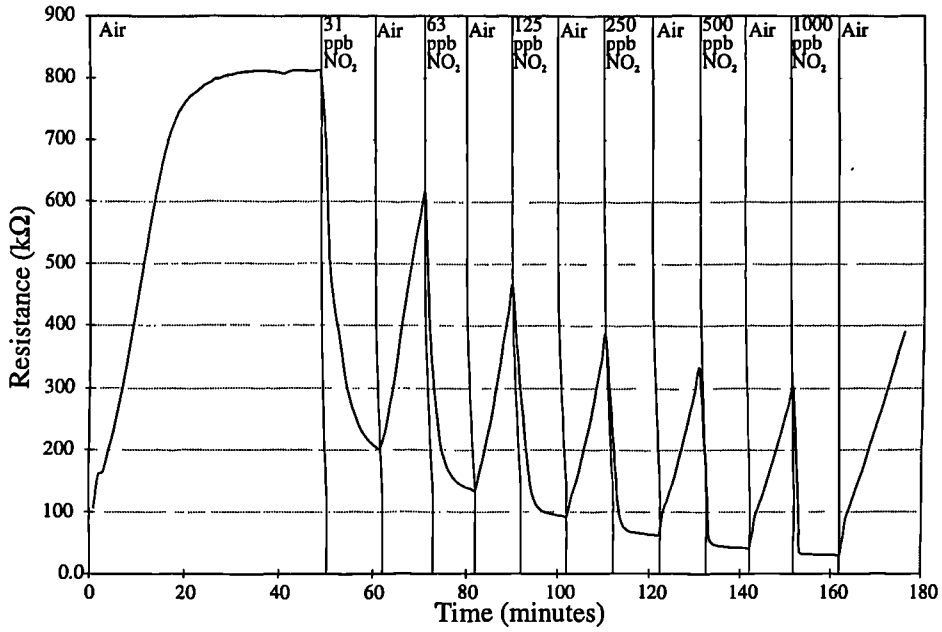

Figure 8.3 Response of an annealed PbPc chemoresistor to changes in NO_2 concentration in air at an operating temperature of 125°C and 43 % RH.

8.3 Characterisation of SnO_2 Chemoresistors

8.3.1 Thin Film SnO_2 Chemoresistors

This Section describes the characterisation of thin film (~ 50 nm) SnO_2 chemoresistors (e.g. SRL108/MOS SAD) to NO_2 and CO. The films were deposited by a thin film technique (see Chapter 4) and were either undoped SnO_2 or doped with Pd or Pt. Although the application of interest is a multicomponent gas mixture, at this stage in the research, the sensors are characterised to one componet at a time.

The response of the three thin films (e.g. undoped, Pd doped and Pt doped) to pulses of low concentrations of NO_2 at 367°C and 38 % RH, are compared as shown in Figure 8.4. NO_2 concentrations of; 0.625 ppm, 1.25 ppm, 2.5 ppm, 5.0 ppm and 6.25 ppm were exposed to the sensors in alternate pulses (10 minute) with air.

The response from each of the chemoresistors exhibits an increase in resistance when exposed to NO_2. The response of the undoped thin film SnO_2 can be described by two distinct phases; firstly, there is an initial rapid mechanism that, secondly, gives way to a slower mechanism which causes a longer response time (~ 5 minutes) before reaching a steady-state resistance. However, the incorporation of the Pd and Pt dopants in the material appears to catalyse the slow mechanism apparent in the

undoped film, to an extent where both the Pd and Pt doped films have a response time (τ_{90}) < 1 minute.

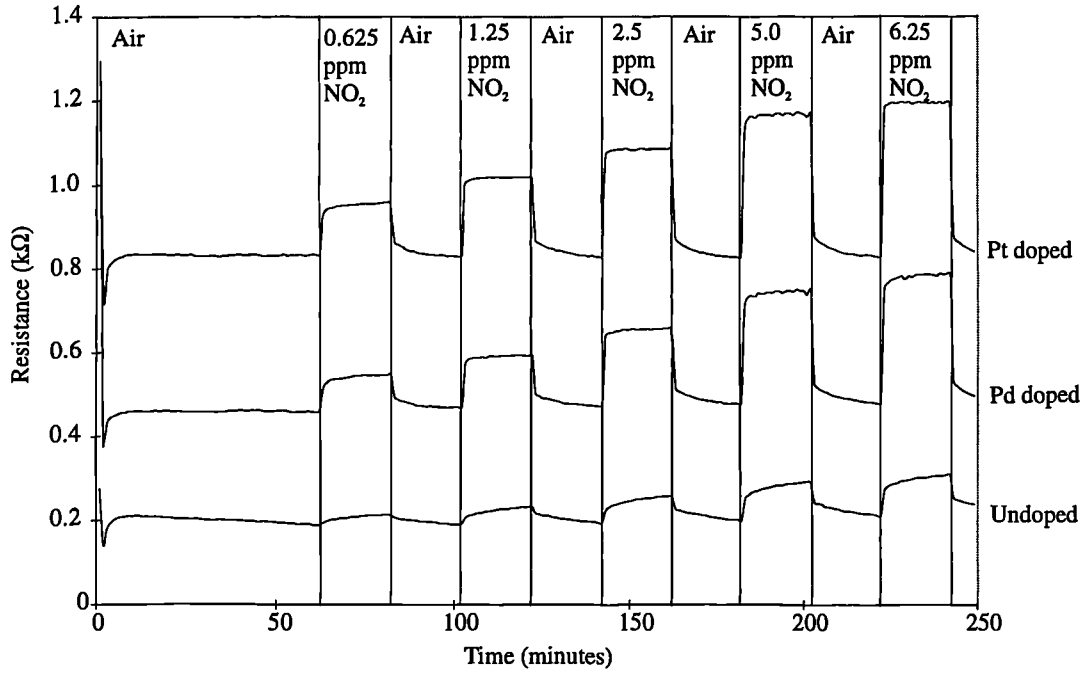

Figure 8.4 Characteristics from undoped, Pd doped and Pt doped thin film SnO_2 chemoresistors at a constant operating temperature of 367°C and 38 % RH.

The adsorption isotherm associated with the response to NO_2 has been investigated by plotting the fractional change in resistance against the NO_2 concentration. A Freundlich isotherm (see Chapter 5, Section 5.3.1) best describes the characteristics, because plotting logarithmically the fractional change in resistance against the logarithm of concentration produces a straight line as shown in Figure 8.5.

The data can be represented by a straight line equation, according to

$$\log\left(\frac{\Delta R}{R_0}\right) = \beta \log C + K \qquad (8.1)$$

where R is the resistance, R_o is the base-line resistance, ΔR is the change in resistance (i.e. $\Delta R=R-R_o$), C is the concentration, β is the gradient of the line (the power term in the Freundlich isotherm expression), and K is a constant. The characteristics of the three chemoresistors are summarised in Table 8.2.

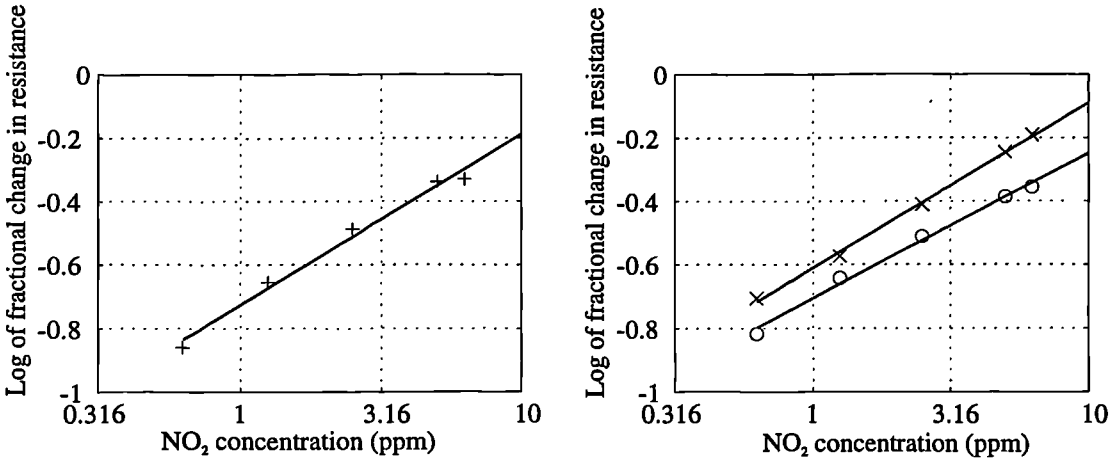

Figure 8.5 Plot of the logarithm of the response (fractional change in resistance) against concentration, for (a) undoped ('+') (b) Pd ('×') and Pt ('o') doped thin SnO_2 film at 367°C and 38 % RH.

Table 8.2 Response coefficients for the NO_2 data shown in Figure 8.5.

Thin film SnO_2 sensor	β (ppm^{-1})	K
Undoped	0.538	-0.726
Pd	0.521	-0.611
Pt	0.457	-0.705

The affect of temperature has been investigated by operating the sensors at 310°C, 367°C, and 418°C and exposing them to the same test conditions. The results for an undoped thin film SnO_2 chemoresistor is shown in Figure 8.6 (at 310°C) and Figure 8.7 (at 367°C and 418°C).

From Figure 8.6 and Figure 8.7 it has been noted that as expected the base-line resistance and the response times decrease as the temperature increases. The same characteristics were also found for Pd doped and Pt doped thin SnO_2 chemoresistors as shown in Figure 8.8 and Figure 8.9, respectively. From these characteristics it is noted that the change in resistance to NO_2 exposure decreases with increasing temperature.

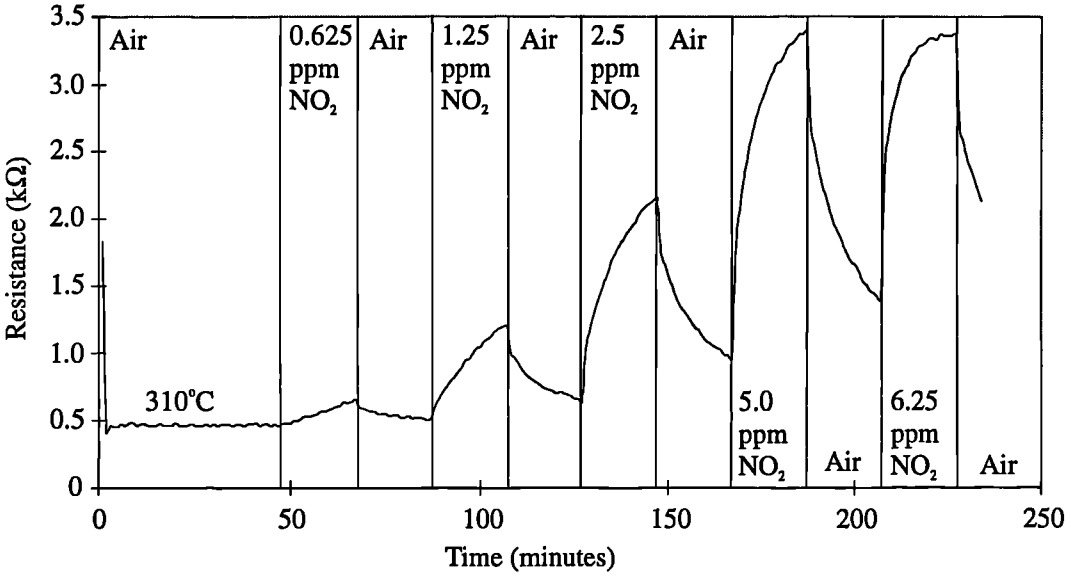

Figure 8.6 Response of undoped thin film SnO_2 chemoresistor to pulses of different NO_2 concentration at a 38 % RH and 310°C.

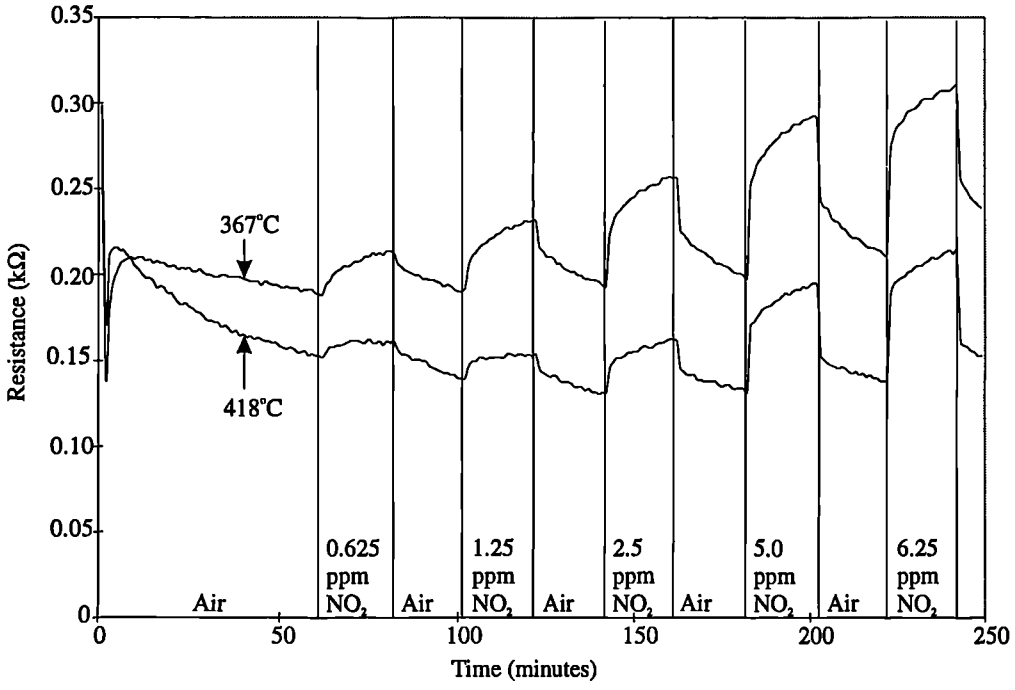

Figure 8.7 Response of undoped thin film SnO_2 chemoresistor to pulses of different NO_2 concentration at a 38 % RH and 367°C and 418°C.

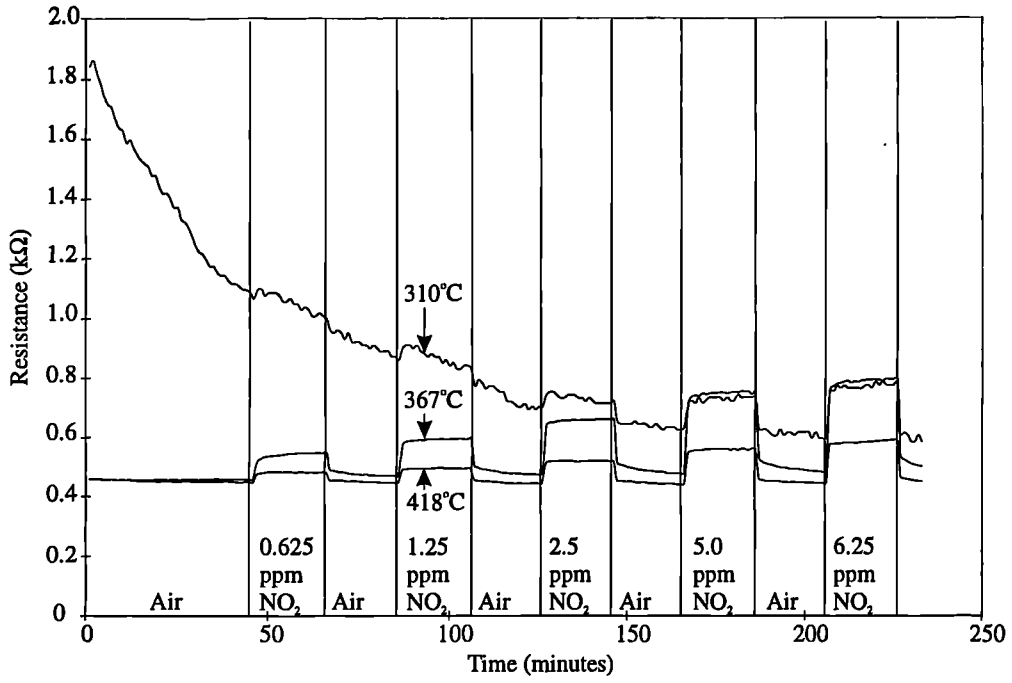

Figure 8.8 Pd doped thin film SnO_2 chemoresistors response to pulses of different NO_2 concentration at a 38 % RH at an operating temperature of 310°C, 367°C and 418°C.

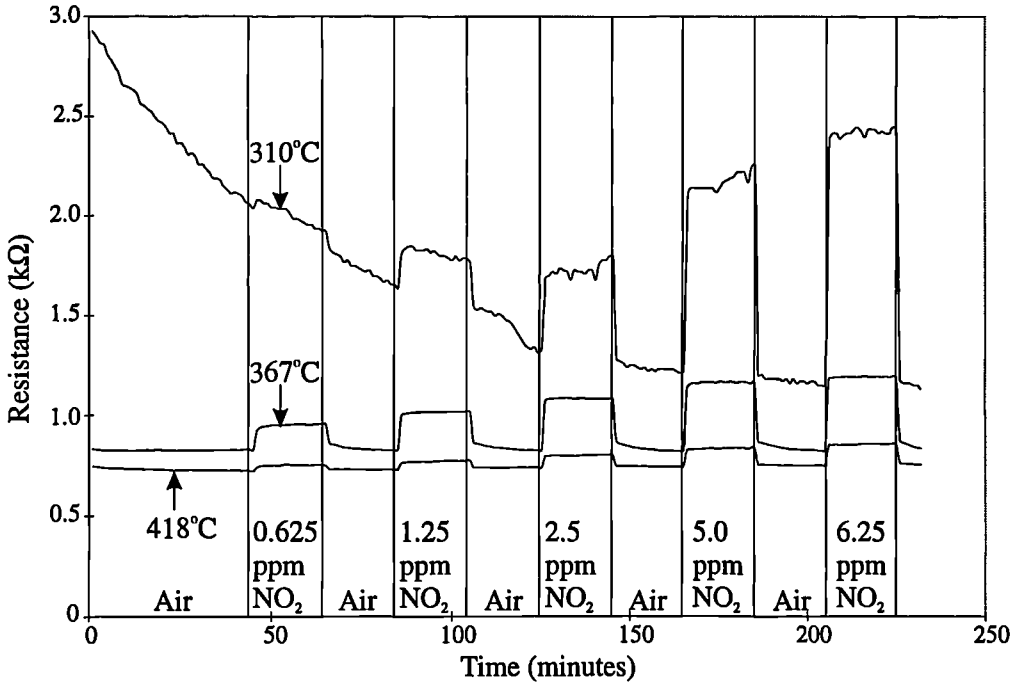

Figure 8.9 Pt doped thin film SnO_2 chemoresistor response to pulses of different NO_2 concentration at a 38 % RH at an operating temperature of 310°C, 367°C and 418°C.

Humidity effects have been investigated by running the same sequence of NO_2 pulses at 367°C at different humidities (e.g. 0 %, 38 %, 55 %, and 70 % RH). The

response for the undoped thin film SnO_2 chemoresistor at these different RHs are shown in Figure 8.10. It can be seen that the base-line resistance and change in resistance to NO_2 concentration both decrease as the RH is increased from dry conditions to 55 %, however, this trend is reversed as the RH is then increased further to 70 %.

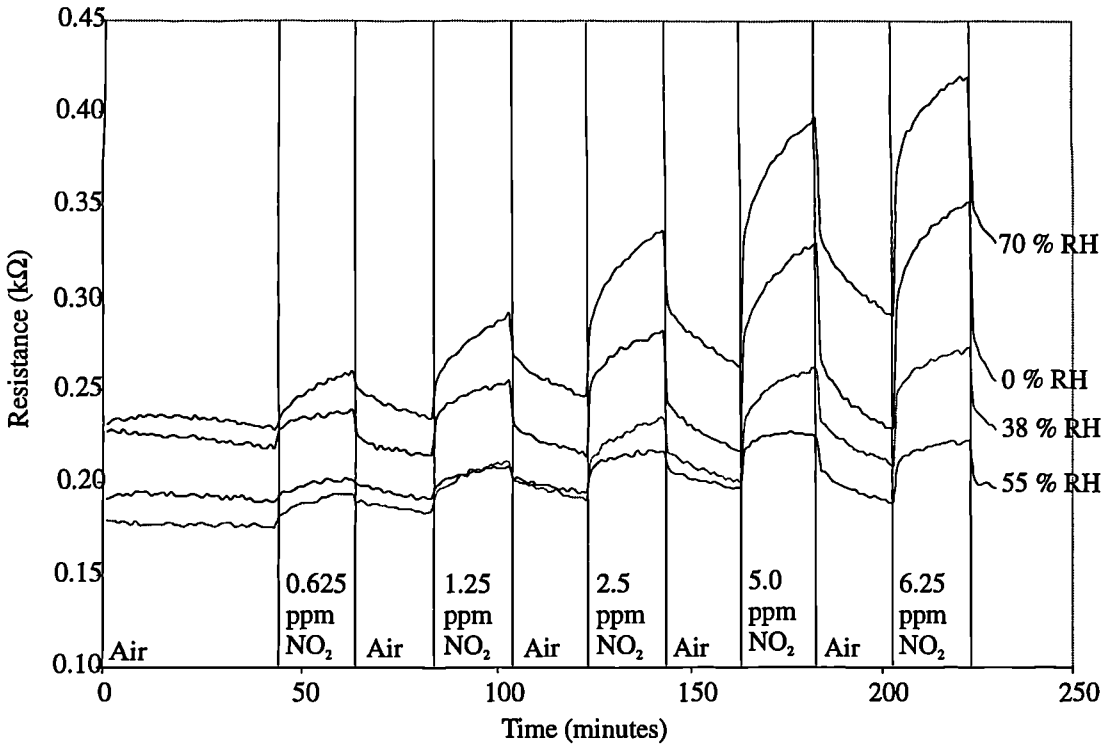

Figure 8.10 Response of undoped thin film SnO_2 chemoresistor to pulses of different NO_2 concentrations at different RH (e.g. 0 %, 38 %, 55 % and 70 %) at 367°C.

Similar trends have been obtained for the Pd and Pt doped thin film SnO_2 chemoresistors. The response for the doped chemoresistors to RH changes was easier to analyse because their faster response time produced steady-state data. The response (i.e. fractional change in resistance) for a Pd and Pt doped thin film SnO_2 chemoresistors to changes in low concentrations of NO_2 and RH are shown in Figure 8.11.

A potentially useful feature to note from Figure 8.11 (a) is that the fractional change in resistance for Pd doped SnO_2 is nearly independent of changes in humidity. Whereas, the fractional change in resistance for Pt doped SnO_2 has a lower response at 70 % RH than at 0 % RH. Between these two limits the characteristics can be

described by a third order expression. For example, the response ($\Re$) at 6.25 ppm NO_2 can be described in terms of humidity (H), according to,

$$\Re = 3.67\times10^{-6}H^3 + 4.50\times10^{-4}H^2 - 1.84\times10^{-2}H + 0.62 \qquad (8.2)$$

However, there was insufficient data available to determine an accurate RH calibration over the NO_2 concentration range.

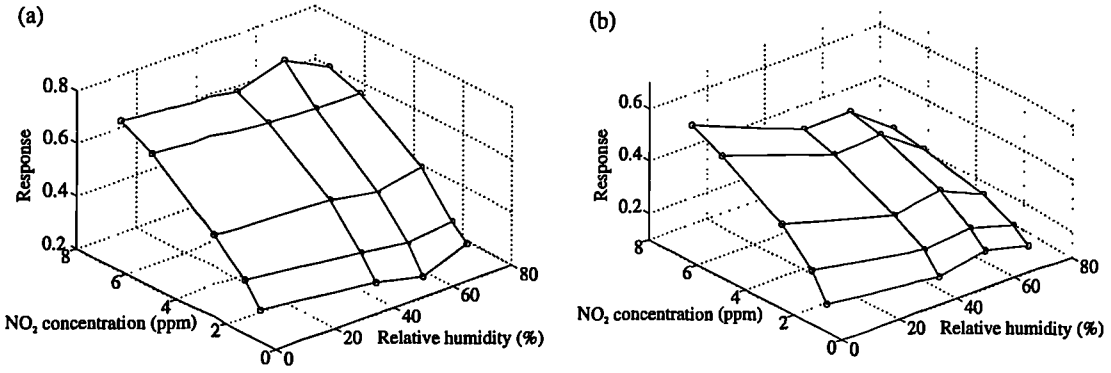

Figure 8.11 Response of (a) Pd doped and (b) Pt doped thin film SnO_2 chemoresistors at various NO_2 concentrations and RHs at an operating temperature of 367°C. The response is defined as the fractional change in resistance.

The tests described previously, were also carried out to investigate the response of the thin film SnO_2 chemoresistors to low concentrations of CO. Alternate pulses (10 minutes) of CO and air were exposed to the sensors, the concentration sequence was 7.8 ppm, 15.6 ppm, 31.3 ppm, 62.5 ppm and 125 ppm. The characteristics of the chemoresistors at an operating temperature of 367°C and 40 % RH are shown in Figure 8.12.

The response of the chemoresistors show a characteristic increase in conductance (i.e. decrease in resistance) when exposed to CO. The response time (τ_{90}) of each of the chemoresistors at higher CO concentrations (e.g. 125 ppm) is approximately 1 minute.

The temperature dependence of the chemoresistors were investigated by applying the same CO concentrations and humidity as for the data shown in Figure 8.12, at 310°C, 338°C, 367°C, 394°C and 418°C. For example, the corresponding responses at these different temperatures for a Pd doped chemoresistor, is shown in Figure 8.13.

The fractional change in conductance was extracted from this data at 125 ppm CO, and likewise, for the responses from undoped and Pt doped chemoresistors, thus allowing the responses to be plotted against temperature, as shown in Figure 8.14. From the data points shown in Figure 8.14 it is seen that the response of the undoped and Pd doped chemoresistors increases to temperatures up to 400°C, whereas the Pt doped chemoresistor exhibits a peak at approximately 370°C.

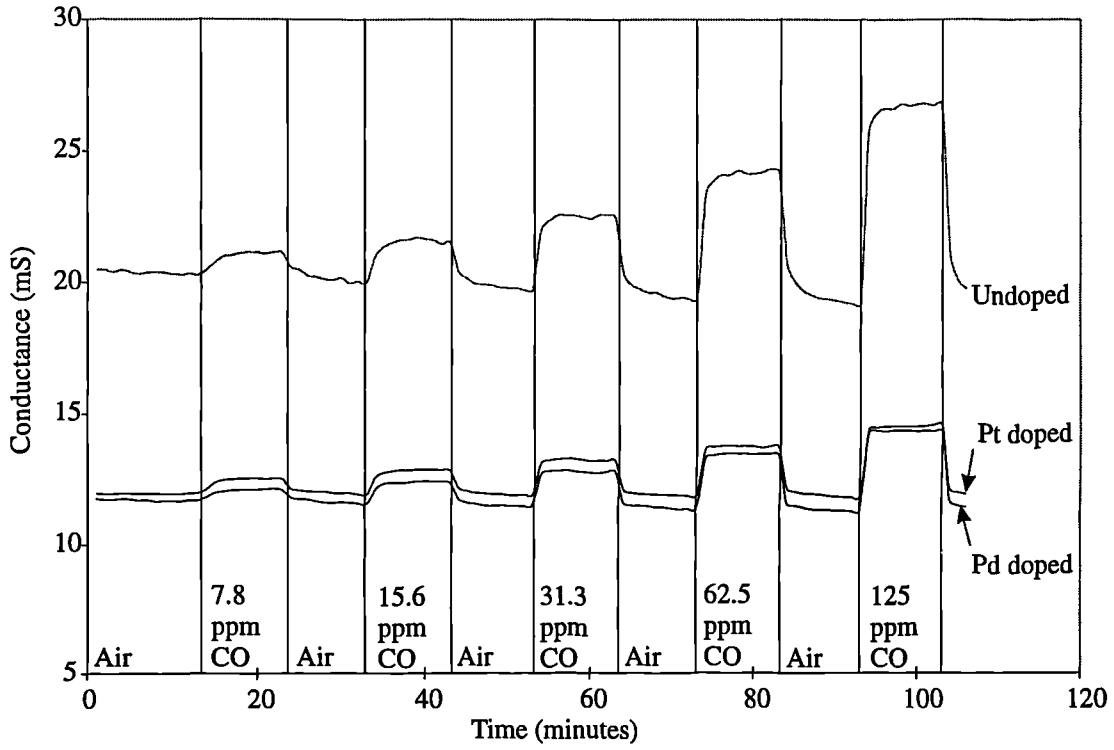

Figure 8.12 Response of undoped, Pd doped and Pt doped thin film SnO_2 chemoresistors to low concentrations of CO (e.g. 7.8 ppm, 15.6 ppm, 31.3 ppm, 62.5 ppm and 125 ppm) at 367°C and 40 % RH.

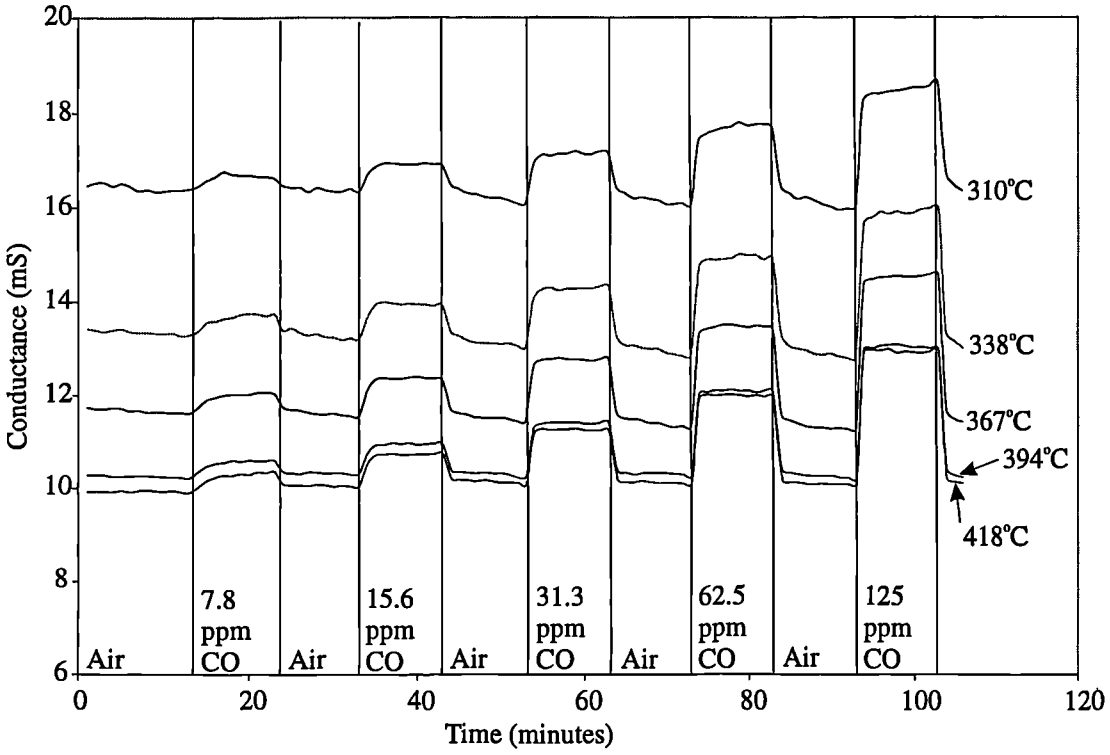

Figure 8.13 Response of a Pd doped thin film SnO_2 chemoresistor to different CO concentrations and operating temperatures at 40 % RH.

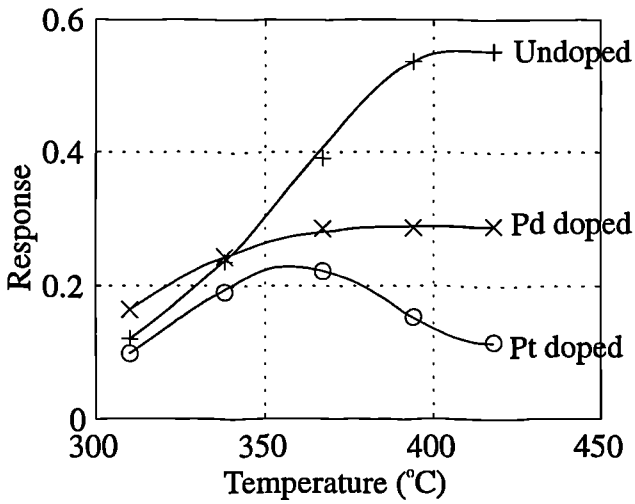

Figure 8.14 Temperature dependence of the response to 125 ppm CO for undoped ('+'), Pd doped ('x') and Pt doped ('o') thin film SnO_2 chemoresistors. The response is defined as the fractional change in conductance.

Maintaining an operating temperature of 367°C the chemoresistors were exposed to a sequence of CO concentrations (7.8 ppm, 15.6 ppm, 31.3 ppm, 62.5 ppm and 125 ppm) at different humidities (e.g. 0 %, 21 %, 40 %, 50 % and 68 %). The change

in sensor response (i.e. fractional change in conductance) to CO concentration and RH is shown in Figure 8.15.

It is apparent from the data shown in Figure 8.15 that the change in response for undoped thin film SnO_2 is small over the RH range. However, the response characteristics ($\Re$) at 125 ppm can be expressed by a third order expression involving RH (H), according to,

$$\Re = 3.39\times10^{-6}H^3 - 3.77\times10^{-4}H^2 + 9.04\times10^{-3}H + 0.424 \qquad (8.3)$$

The response of the Pd doped thin film SnO_2 to RH shows a rapid increase from 0 % to 21 %. At higher humidities the response appears independent from RH. Whereas, the response of the Pt doped thin film SnO_2 appears independent from RH.

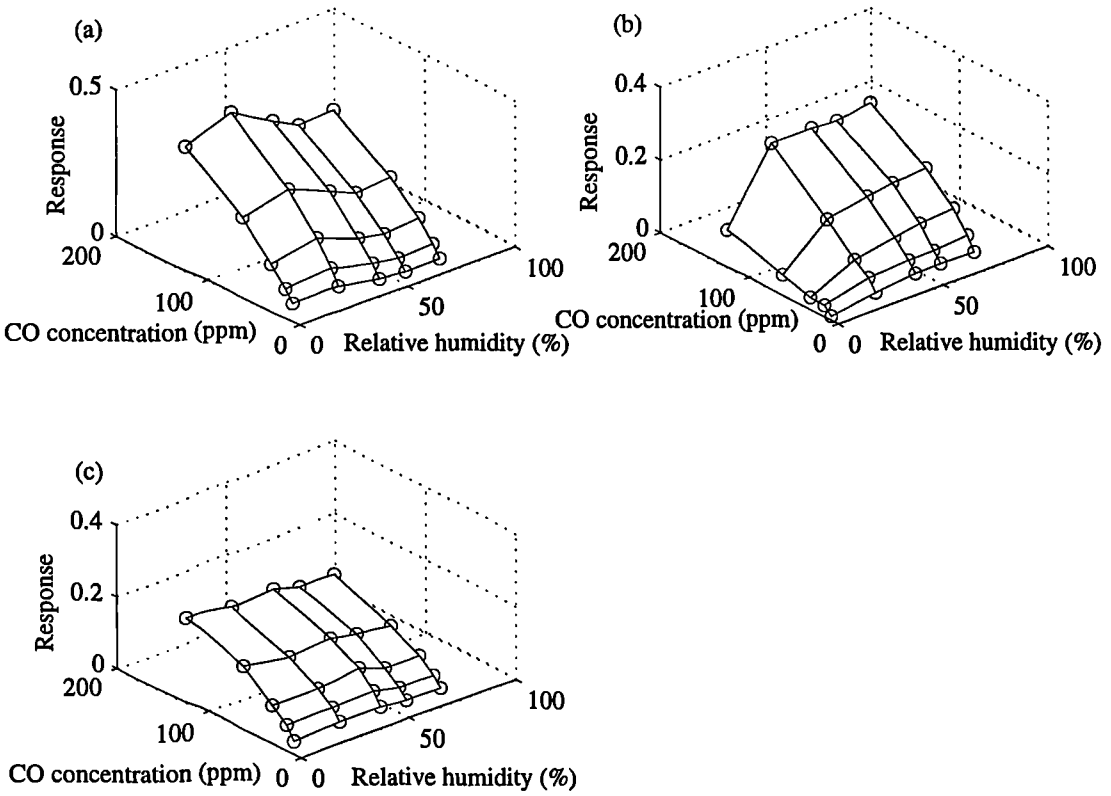

Figure 8.15 Response of (a) undoped, (b) Pd doped and (c) Pt doped thin film SnO_2 chemoresistor to low concentrations of CO (e.g. 7.8 ppm, 15.6 ppm, 31.3 ppm, 62.5 ppm and 125 ppm) and RH (0 %, 21 %, 40 %, 50 % and 68 %) at 367°C. The response is defined as the fractional change in conductance.

It was found that the logarithm of the response against the logarithm of the CO concentration produces linear characteristics, which is consistent with the power expression of the Freundlich isotherm. An example of these characteristics are shown in Figure 8.16, for undoped, Pd doped and Pt doped chemoresistors at 40 % RH and 367°C.

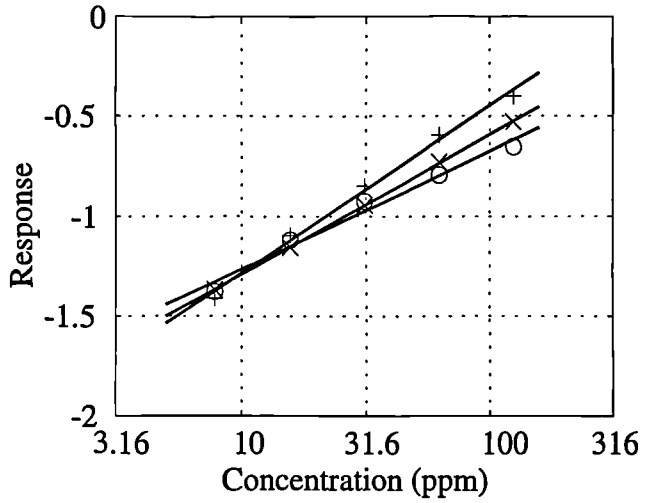

Figure 8.16 Linear characteristics of the logarithm of the sensor response (fractional change in conductance) against the logarithm of CO concentration, at 367°C and 40 % RH. '+' are the data points for an undoped sensor, 'x' are the data points for a Pd doped sensor and 'o' are the data points for a Pt doped thin film SnO_2 chemoresistor.

These characteristics exhibit a reasonable straight line fit (in conductance), described by,

$$\log\left(\frac{\Delta G}{G_o}\right) = \beta \log C + K \qquad (8.4)$$

where G is the conductance, G_o is the base-line conductance, ΔG is the change in conductance (i.e. $\Delta G = G - G_o$), while C, β and K have the same definition as described for equation 8.1. The coefficients of the data shown in Figure 8.16 are summarised in Table 8.3.

Table 8.3 Response coefficients for the CO data shown in Figure 8.16.

Thin film SnO_2 sensor	β (ppm^{-1})	K
Undoped	0.836	-2.12
Pd doped	0.696	-1.99
Pt doped	0.588	-1.85

Tests were carried out on the thin film SnO_2 chemoresistors, in order to exploit the thermal properties of the MHP by pulsing the sensors operating temperature. The effects of rapidly pulsing the sensors operating temperature were investigated, with alternating pulses (10 s) of a base-line 367°C and higher temperatures (e.g. 372°C, 378°C, 383°C, 393°C, 400°C, 405°C and 410°C) as shown in Figure 8.17. A NO_2 concentration of 1.25 ppm and 38 % RH was maintained constant throughout the test.

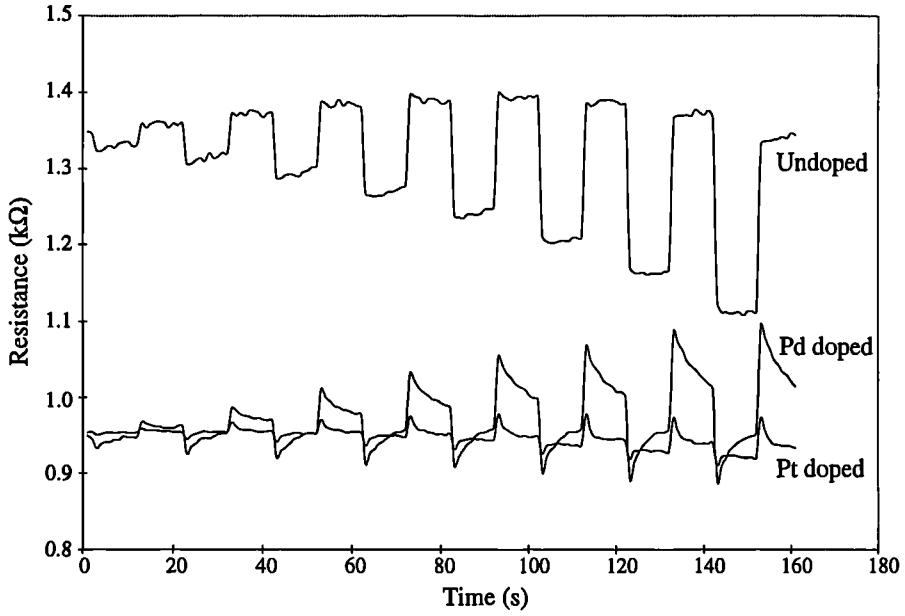

Figure 8.17 Response of thin film SnO_2 chemoresistors to 38 % RH and 1.25 ppm NO_2. 10 s pulses of 372°C, 378°C, 383°C, 394°C, 400°C, 405°C and 410°C were run with a base-line operating temperature of 367°C.

This test demonstrates how the fast thermal time constant of the MHP (~ 5 ms) can be used to control the operating temperature of the material. These thermal properties make possible the rapid control of the reaction kinetics on the gas sensor surface, which in turn controls the sensitivity and specificity of the material.

It is evident that the temperature dependence towards different gases may be a selective feature of the results. By again exploiting the very rapid thermal properties of the sensors the thin film SnO_2 chemoresistors were exposed to 30 s periods of different operating temperatures. The chemoresistors were pulsed at 310°C, 367°C and 418°C in an atmosphere of 31.3 ppm CO at 40 % RH, as is shown in Figure 8.18. The same test was then carried out, except in an atmosphere of 2.5 ppm NO_2 at 40 % RH, as is shown in Figure 8.19.

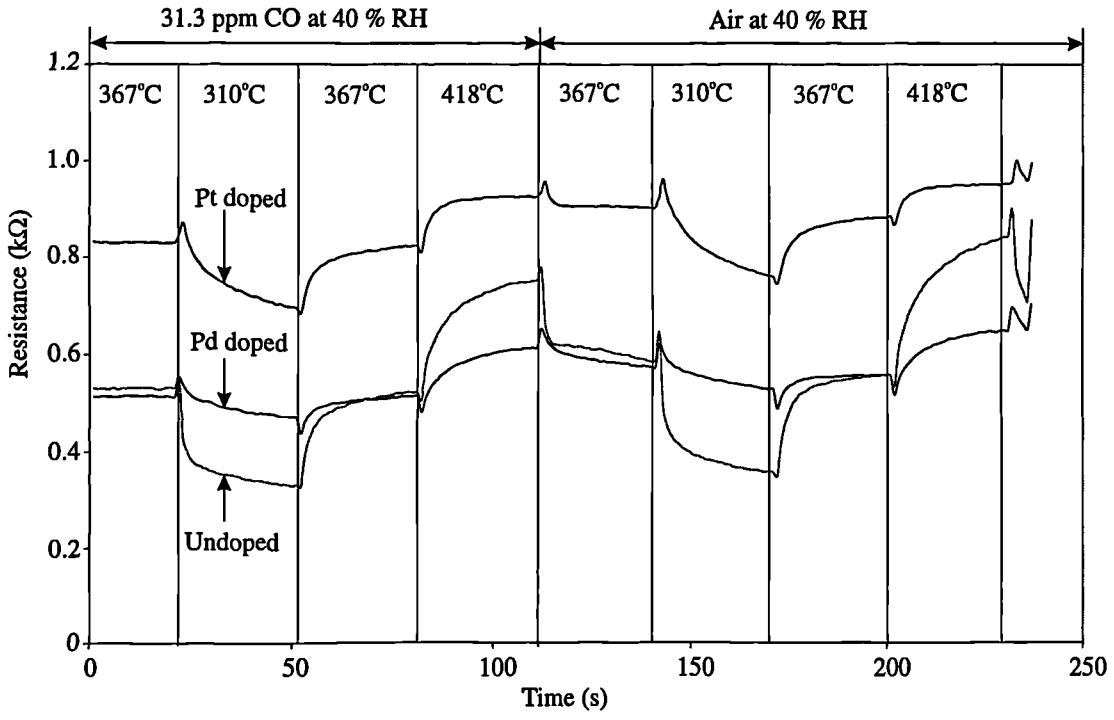

Figure 8.18 Response of thin film SnO_2 chemoresistors (e.g. undoped, Pd doped and Pt doped) to a sequence of 30 s temperature pulses at 367°C, 310°C, 367°C, 418°C, 367°C, 310°C, 367°C and 418°C in 31.3 ppm CO and air at 40 % RH.

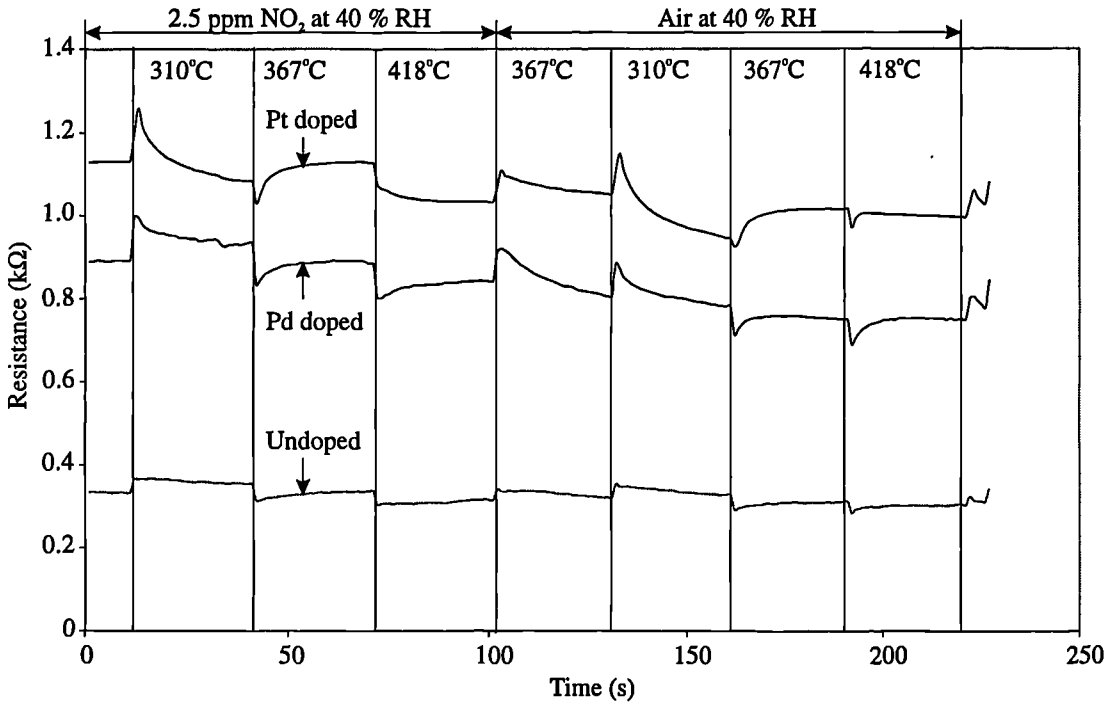

Figure 8.19 Response of thin film SnO_2 chemoresistors (e.g. undoped, Pd doped and Pt doped) to a sequence of 30 s temperature pulses at 367°C, 310°C, 367°C, 418°C, 367°C, 310°C, 367°C and 418°C in 2.5 ppm NO_2 and air at 40 % RH.

These characteristics serve to demonstrate the suitability of temperature pulsing the thin film SnO_2 chemoresistors. The response times are shown to be ~ 30 s, for the higher sampling rate used here.

8.3.2 Thick Film SnO_2 Chemoresistors

Undoped, Pd doped and Pt doped thick film SnO_2 chemoresistors were fabricated with the SRL125/MOS SADs, as described in Chapter 4. The characterisation of the thick film SnO_2 chemoresistors to NO_2 and CO are described in this Section.

The response of the thick film SnO_2 chemoresistors to low concentrations of NO_2, at 38 % RH and 355°C are shown in Figure 8.20. The standard test conditions consisted of alternate pulses of low NO_2 concentrations (15 minutes) and air (10 minutes), where the NO_2 concentration sequence was 0.3125 ppm, 0.625 ppm, 1.25 ppm, 2.50 ppm, 5.00 ppm and 6.25 ppm.

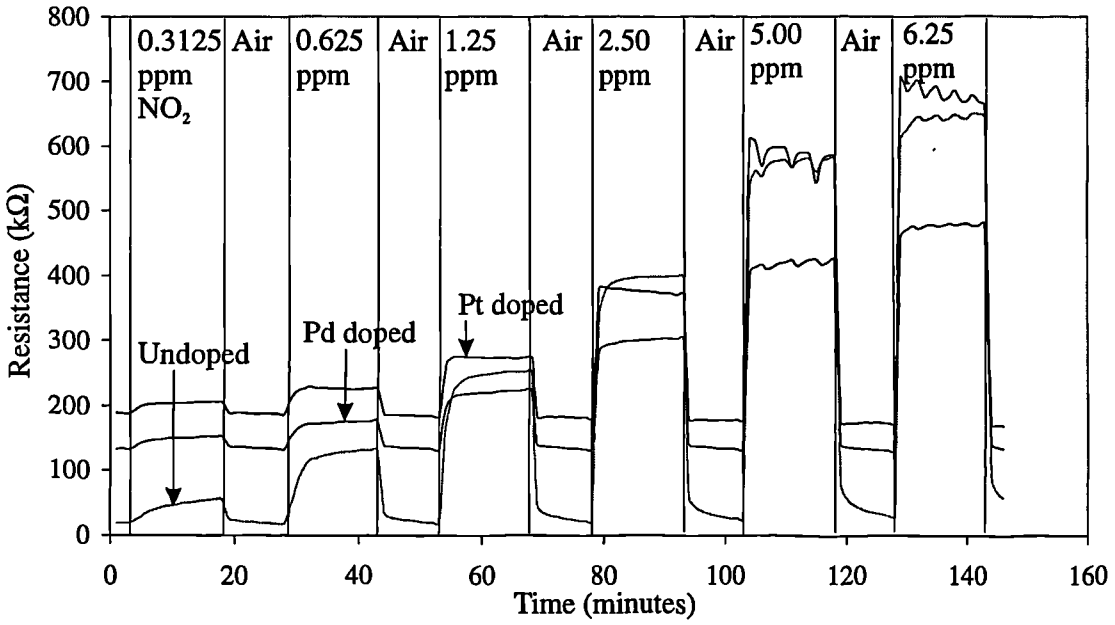

Figure 8.20 Response of undoped, Pd doped and Pt doped thick film SnO_2 chemoresistors to different NO_2 concentrations (e.g. 0.3125 ppm, 0.625 ppm, 1.25 ppm, 2.50 ppm, 5.00 ppm and 6.25 ppm) at 38 % RH and at an operating temperature of 355°C.

The general characteristics shown in Figure 8.20 are typical of that expected for both the undoped and doped SnO_2 chemoresistors i.e. an increase in resistance upon exposure to NO_2. However, it is uncertain, as to whether the instability in sensor resistance at higher concentrations (e.g. > 5.00 ppm) of NO_2 is due to mechanisms occurring within the sensor or within the test system. The base-line stability is better than that observed for the same materials on ceramic former (i.e. Taguchi Series 8 type sensor) [8.2].

The effect of RH on the response of the thick film SnO_2 chemoresistors to low concentrations of NO_2 was also investigated. The steady-state response (fractional change in resistance) for undoped, Pd and Pt doped SnO_2 chemoresistors are shown in Figure 8.21. The pulses of different NO_2 concentrations were the same as that used to obtain the data shown in Figure 8.20. The responses from the undoped and doped chemoresistors were acquired at 0 %, 21 %, 38 %, 52 %, 61 % and 68 % RH.

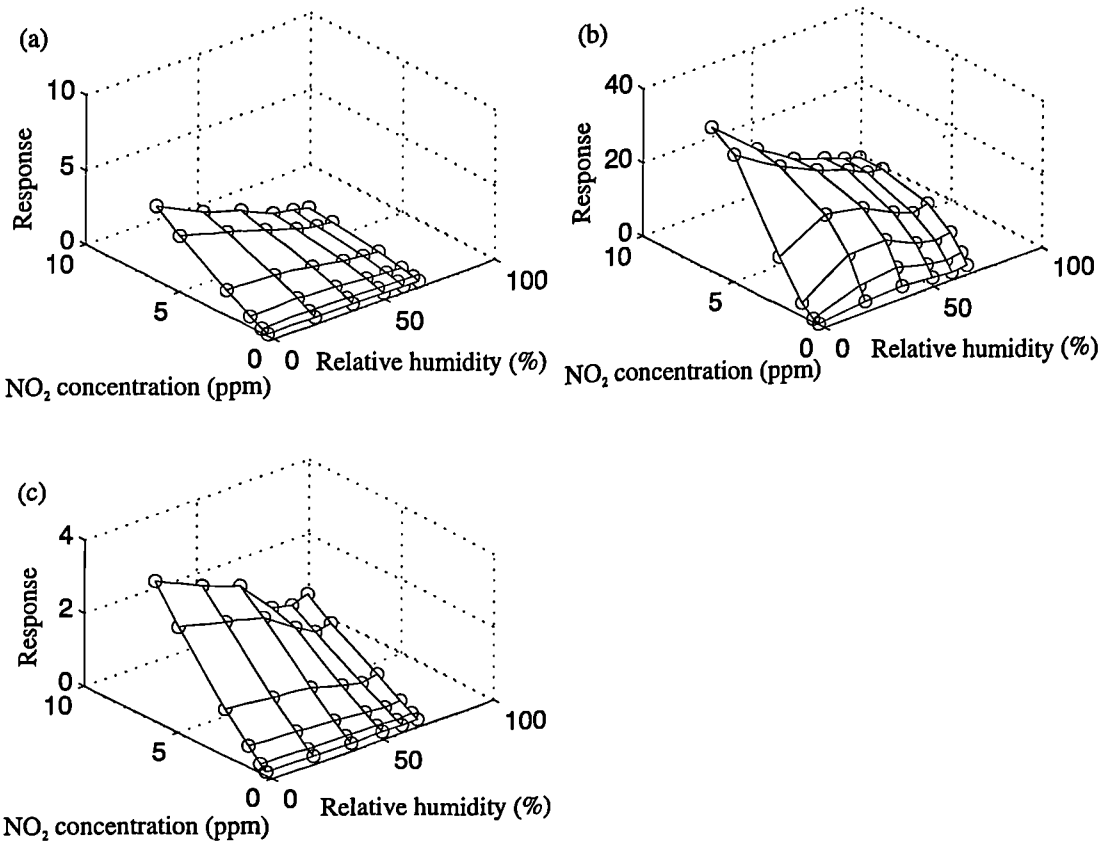

Figure 8.21 Response (fractional change in resistance) of the thick film SnO_2 sensors , (a) undoped, (b) Pd doped and (c) Pt doped, to changes in NO_2 concentration and RH at 355°C.

It is apparent from the data shown in Figure 8.21 that the response of the undoped and Pt doped thick film SnO_2 decreases with increasing RH. The characteristics for the Pd doped SnO_2 does not show any systematic relationship to RH over the NO_2 concentration range investigated. At NO_2 concentrations up to 2.50 ppm the response forms a maximum at around 35 % RH, whereas, at higher NO_2 concentrations the response clearly decreases with increasing RH.

It is interesting to note that under these test conditions, there is a linear relationship between the NO_2 concentration and the response for both the undoped and the Pt doped chemoresistors. The characteristics of the Pd doped SnO_2 chemoresistor for response against NO_2 concentration as shown in Figure 8.21 (b), did not give a good fit to any of the adsorption isotherms investigated in Chapter 5.

The temperature dependence of the response was investigated by varying the operating temperatures between test sequences, with otherwise identical test conditions. The NO_2 concentration sequence was the same as that used to obtain the

data shown Figure 8.20. Likewise the RH was maintained at 38 %. The response of an undoped SnO_2 chemoresistor at four different temperatures (e.g. 170°C, 235°C, 295°C and 330°C) is shown in Figure 8.22 under the conditions described above.

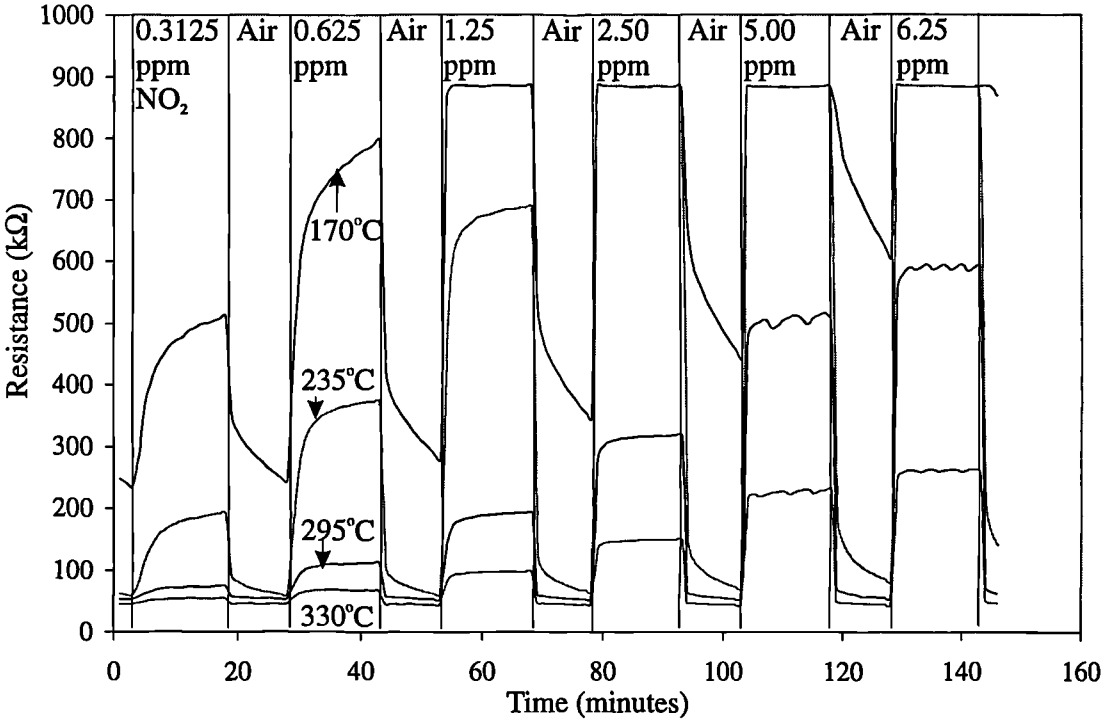

Figure 8.22 Four responses of undoped thick film SnO_2 chemoresistor at different temperatures to changes in low concentrations of NO_2 at 38 % RH.

The response of the undoped SnO_2 chemoresistor at lower temperatures is shown to have a greater sensitivity compared to the response obtained at higher temperatures. The sensitivity is so large that the output signal from the static rig saturates for the responses obtained at 170°C and 235°C at NO_2 concentrations greater than 1.25 ppm and 2.5 ppm, respectively. The same trend was found for the Pd doped chemoresistor as is shown in Figure 8.23.

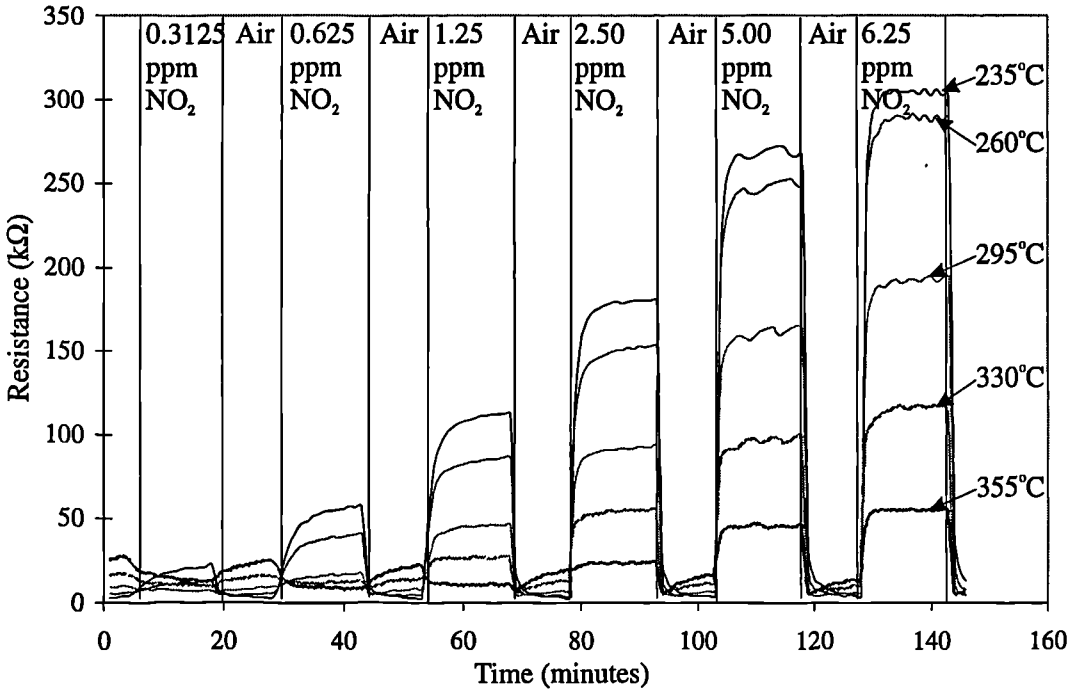

Figure 8.23 Responses of Pd doped thick film SnO_2 chemoresistor at different temperatures (e.g. 235°C, 260°C, 295°C, 330°C, 355°C) to changes in low concentrations of NO_2 at 38 % RH.

The Pt doped chemoresistor gave a similar trend, to such a large extent, that saturation of the sensor signal from the static rig reduced the temperature range over which the measurement could be made. Nevertheless, the temperature dependence of the response (fractional change in resistance) for the three types of thick film SnO_2 chemoresistor are shown in Figure 8.24.

It was noted from the data shown in Figure 8.24 that there is maximum in the response of the undoped and Pd doped chemoresistors to NO_2 at approximately 210°C.

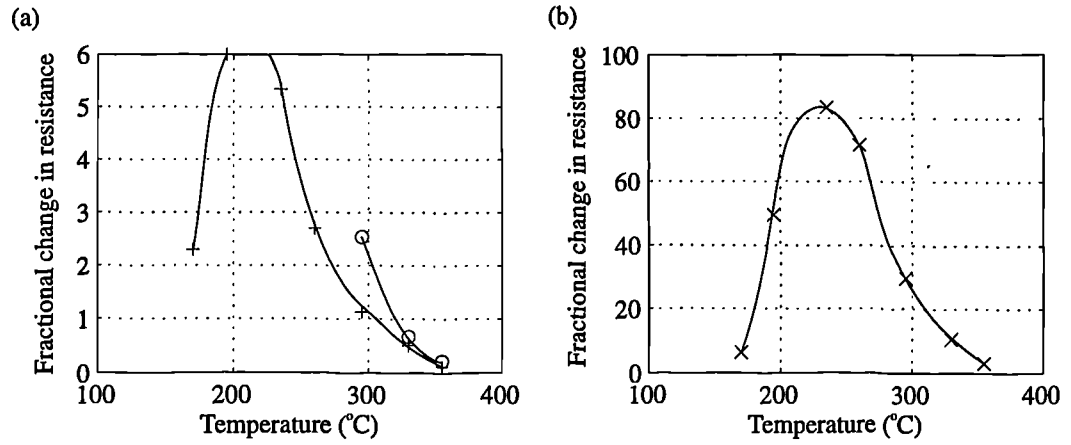

Figure 8.24 Temperature dependence of the response of (a) undoped and Pt doped, and (b) Pd doped thick film SnO_2 chemoresistors to low concentrations of NO_2 at 38 % RH. The response was defined as the fractional change in resistance, '+' is the response data points of an undoped sensor to 0.625 ppm NO_2, 'x' is the response data points of a Pd doped sensor to 6.25 ppm and 'o' are the data points for a Pt doped sensor to 1.25 ppm.

The tests so far described for the thick film SnO_2 chemoresistors were repeated to characterise the response to CO. The response of the undoped and doped thick film chemoresistors to changes in low concentrations of CO, at 295°C and 40 % RH, are shown in Figure 8.25. The response from a Pd doped chemoresistor is shown in Figure 8.26.

All three types of thick film SnO_2 chemoresistor showed a decrease in resistance (i.e. increase in conductance) upon exposure to CO, with a response time of < 2 minutes. The same sequence of CO concentrations were run at 295°C at different RHs e.g. 15 %, 29 %, 40 %, 52 %, 62 %. The response (e.g. fractional change in conductance) to the different RHs are shown in Figure 8.27. A Freundlich isotherm was found to describe the characteristics, because plotting logarithmically the fractional change in conductance against the logarithm of concentration produced a straight line, as is shown in Figure 8.28.

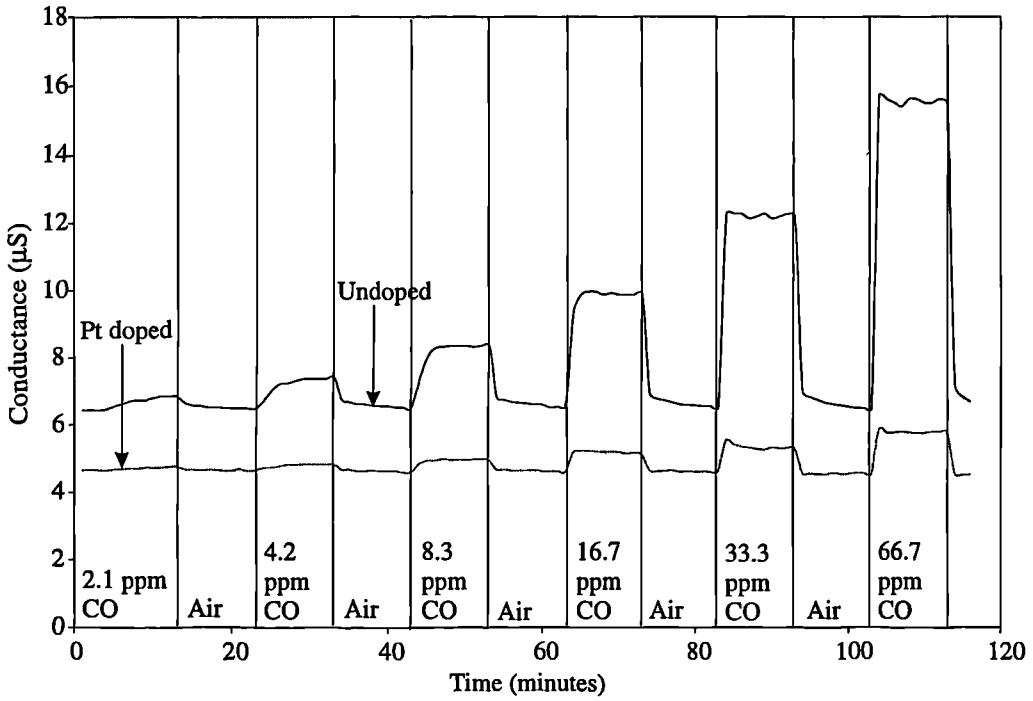

Figure 8.25 Response of undoped and Pt doped thick film SnO_2 chemoresistors to alternate pulses (10 minutes) of low concentrations of CO (e.g. 2.1 ppm, 4.2 ppm, 8.3 ppm, 16.7 ppm, 33.3 ppm and 66.7 ppm) at 295°C and 40 % RH.

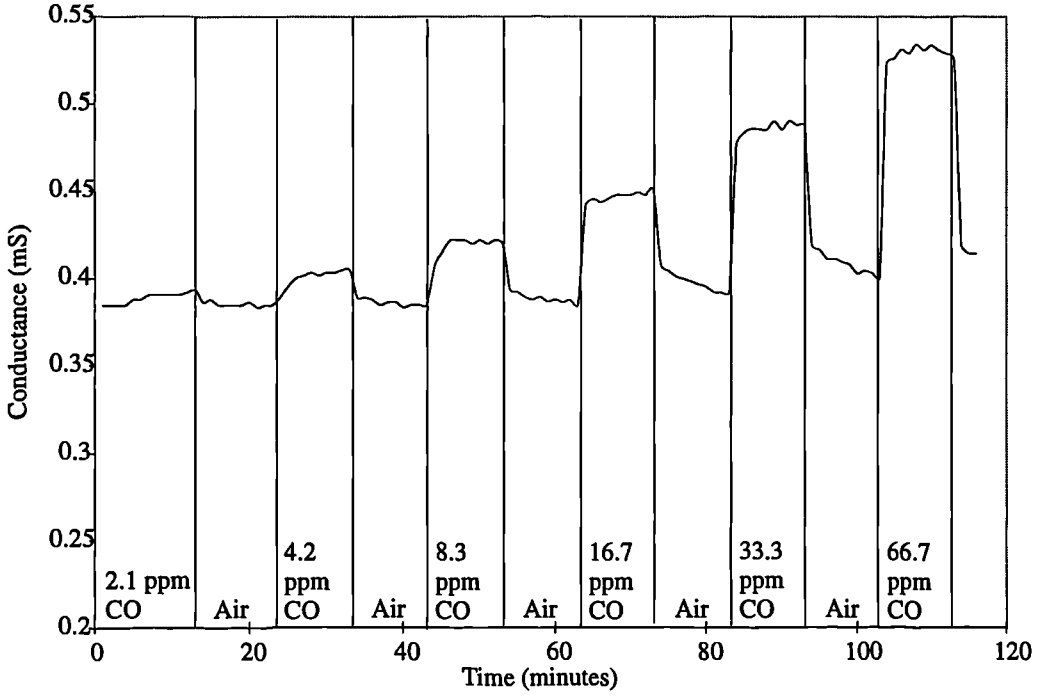

Figure 8.26 Response of a Pd doped thick film SnO_2 chemoresistors to alternate pulses (10 minutes) of low concentrations of CO (e.g. 2.1 ppm, 4.2 ppm, 8.3 ppm, 16.7 ppm, 33.3 ppm and 66.7 ppm) at 295°C and 40 % RH.

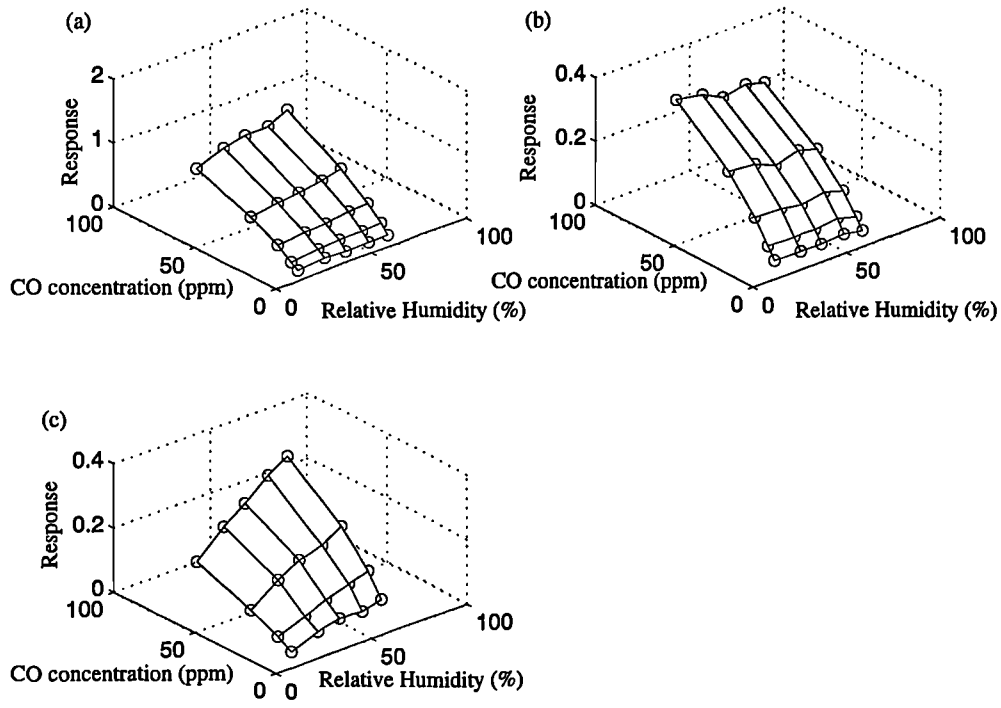

Figure 8.27 Response of (a) undoped, (b) Pd doped and (c) Pt doped thick film SnO_2 chemoresistors to different CO concentrations and RHs at 295°C. The response is defined as the fractional change in conductance.

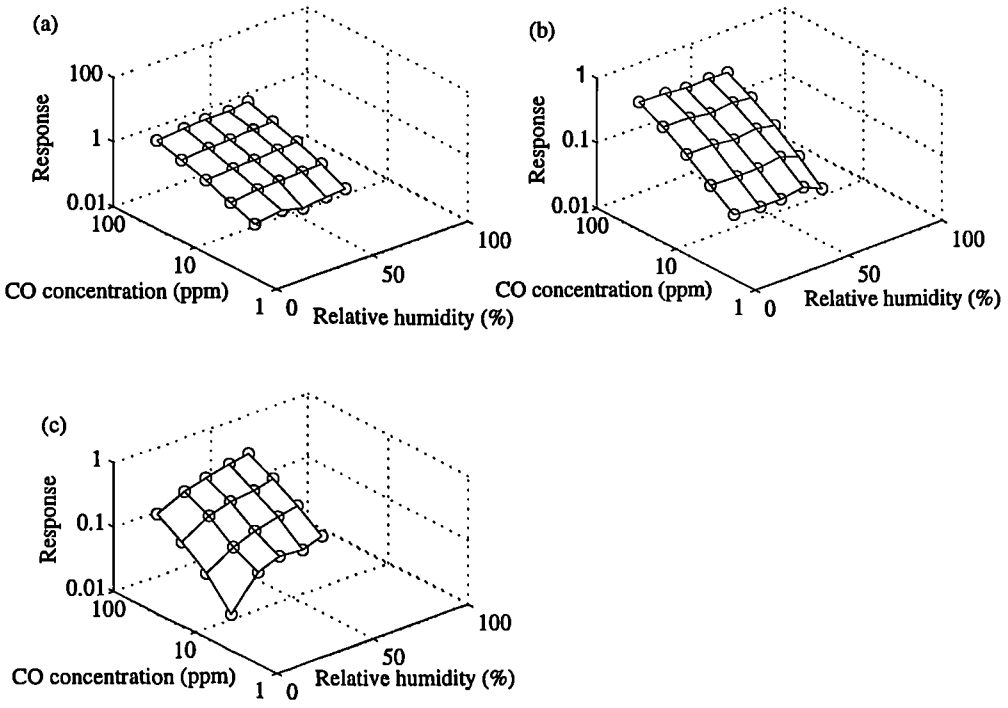

Figure 8.28 Re-representation of the data shown in Figure 8.27 to show the linear characteristics of the logarithm of the response is plotted against the logarithm of concentration.

It is apparent that the data shown in Figure 8.27 that the response for the undoped and Pt doped thick film SnO_2 increases with increasing RH. Whereas, the response of Pd SnO_2 is independent of RH.

The data presented in Figure 8.28 can be represented by equation 8.4. The variation of the power coefficient (β) and the constant coefficient (K) with humidity has been derived for each of the test runs carried out at different humidities, as shown in Figure 8.29.

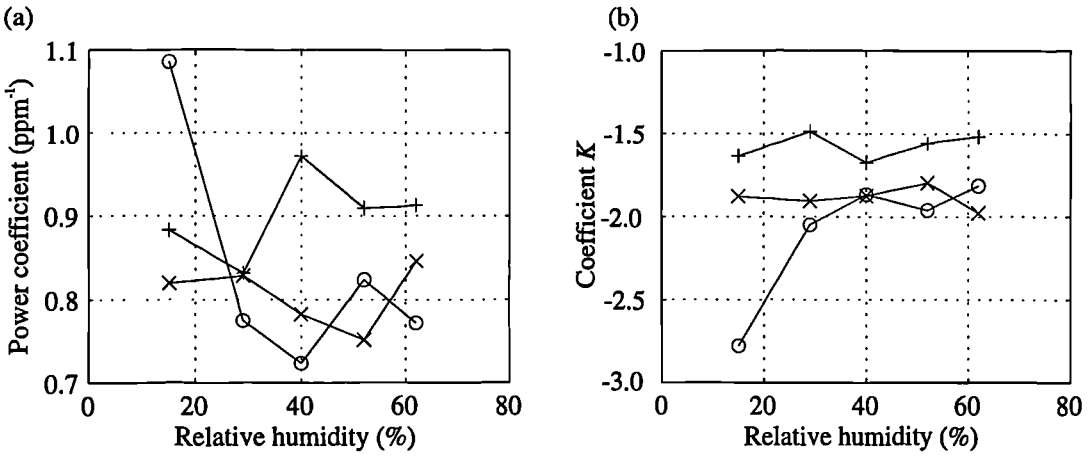

Figure 8.29 Variation of the (a) power coefficient (β) and (b) constant coefficient (K) with RH at 295°C. '+' are the data points for an undoped chemoresistor, 'x' are the data points for a Pd doped chemoresistor and 'o' are the data points for a Pt doped chemoresistors.

No distinct relationship was established between these adsorption isotherm coefficients and humidity for the response to CO by the thick film SnO_2 chemoresistor.

The temperature dependence of the response from the thick film SnO_2 chemoresistors to low concentrations of CO was investigated at 235°C, 260°C, 295°C, 330°C and 355°C. Alternate pulses (10 minutes) of 2.1 ppm, 4.2 ppm, 8.3 ppm, 16.7 ppm, 33.3 ppm and 66.7 ppm with air, at 40 % RH were exposed to the sensors. A comparison of the response of the Pt doped chemoresistor at different temperatures (e.g. 260°C, 295°C, 330°C and 355°C) is shown in Figure 8.30.

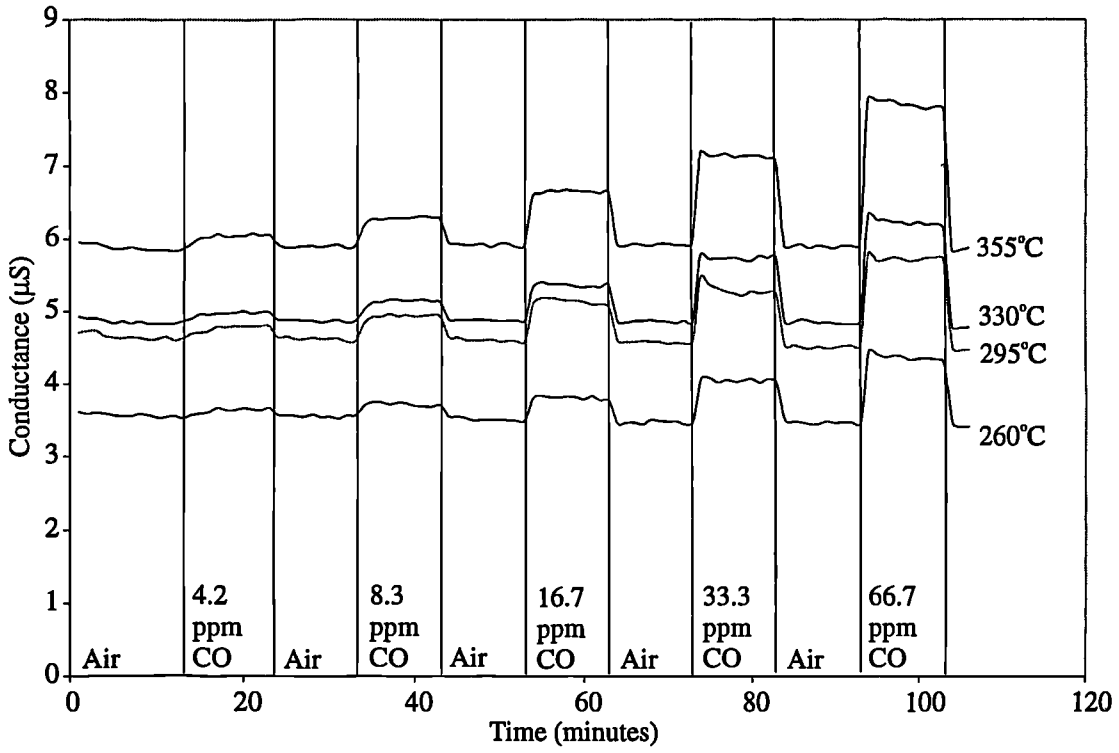

Figure 8.30 Response (conductance) of a Pt doped thick film SnO_2 chemoresistor to pulses of low concentrations of CO at 40 % RH.

It is shown in Figure 8.30 that the response time is longer (~ 4 minutes) when the chemoresistor is exposed to 4.2 ppm CO, however, the response time decreases to < 1 minute at higher concentrations (e.g. > 33.3 ppm) at any of the operating temperatures shown. For each type of thick film SnO_2 chemoresistor the fractional change in conductance has been calculated for exposure to 66.7 ppm at each of the operating temperatures, and hence describing the temperature dependence, as is shown in Figure 8.31.

It is apparent that the response of the doped chemoresistors to 66.7 ppm increases up to 360°C. However, the response of the undoped sensor shows a peak at ~ 310°C.

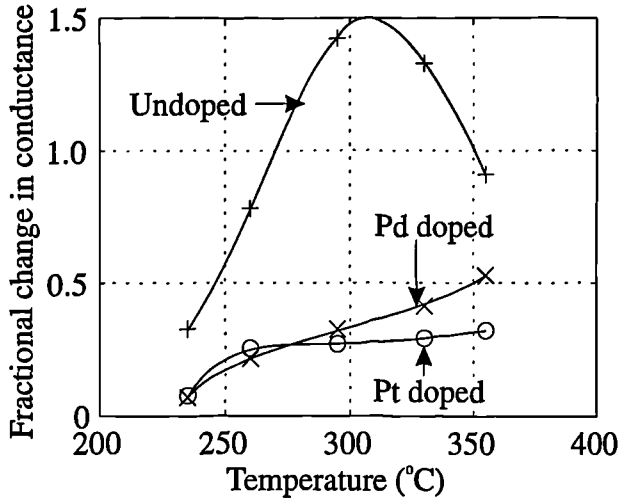

Figure 8.31 Temperature dependence of the response of undoped, Pd doped and Pt doped thick film SnO_2 chemoresistors exposured to 66.7 ppm CO and 40 % RH. The response is defined as the fractional change in conductance.

8.4 Characterisation of the Dual Sensor Device

In Chapter 5 the theoretical operation of a dual sensor device was introduced, in which the response from a pair of structurally dissimilar chemoresistors may be used for a poisoning diagnostic. Such a potentially important feature led to the incorporation of the theoretical design into the SRL125/dual SAD as described in Chapter 3. This structure consists of a pair of planar chemoresistors located under the same gas-sensitive film, where one sensor has an inter-electrode gap (10 μm) much greater than the active film thickness, while the second chemoresistor has an inter-electrode gap (≤ 1 μm) much less than the active film. Chapter 4 outlines the fabrication of such a structure. This Section describes the tests carried out, and the results obtained in an attempt to validate the theory.

The theoretical operation of the dual device was considered for two limiting cases, in which the target gas would produce either a uniform (type I) or a moving-boundary (type II) gas concentration profile. In Chapter 5 the type of concentration profile is determined by the gas-sensitive material. Both PPy/PSA/H_2O (type I) and thick SnO_2 (type II) materials have been investigated with the gas sensor test system described in Chapter 7.

Testing of the CP coated SRL125/dual SAD involved the exposure of propanol[†] at RT. Unfortunately, no useful results were obtained because of either membrane fracture or CP cracking and peeling during very high vapour exposure. A likely explanation would be due to swelling induced stress caused by the geometrical changes in the CP film expected during a high levels of vapour sorption. An example of the CP cracking is shown in Figure 8.32. It has been noted that CPs have been grown and tested on other SADs successfully, without fracture.

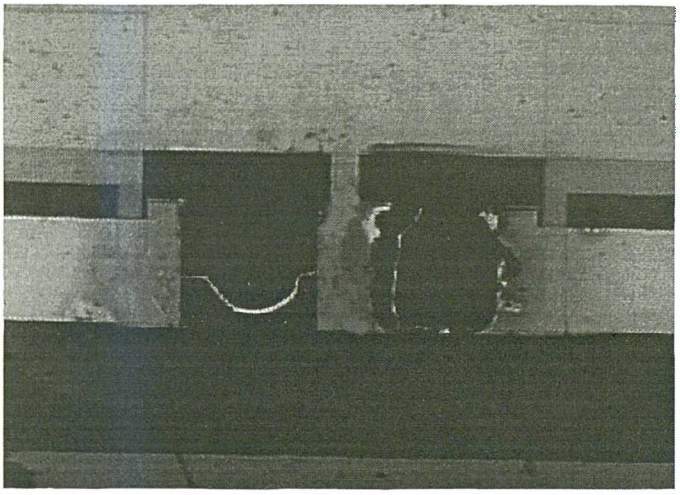

Figure 8.32 Cracked CP as a result of swelling induced stress.

Characterisation of the thick SnO_2 SRL125/dual to changes in CO proved more successful. The MHPs were operated at 400°C and exposed to alternating 10 minute pulses of CO and then dry air. The CO concentration was varied from 50 ppm to 300 ppm in steps of 50 ppm. A dry gas supply was maintained throughout the test. The data collected were processed in order to express the chemoresistors steady-state response as a fractional change in conductance, so as to be consistent with the theoretical response. The fractional change in conductance for both the wide-gap chemoresistor and the narrow-gap chemoresistor are shown in Figure 8.33.

[†] The concentration was controlled by bubbling air through pure propanol and dilution with the dry air supply.

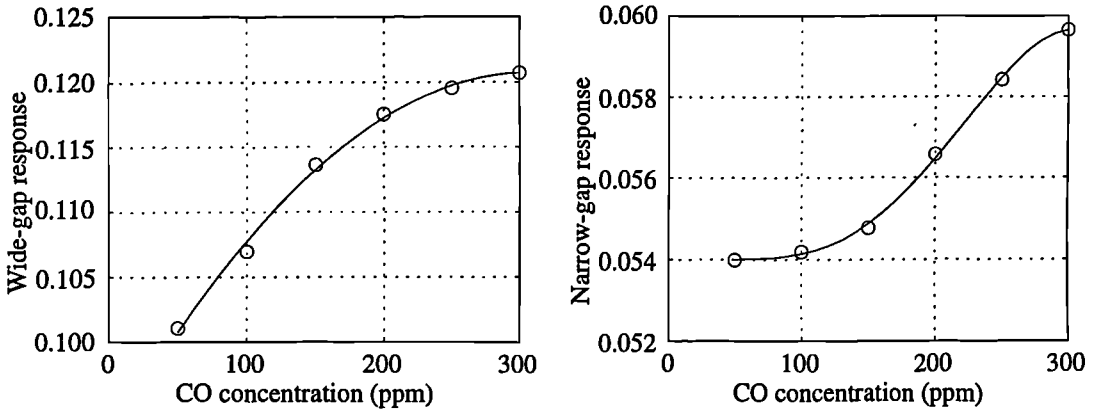

Figure 8.33 Fractional change in conductance for (a) wide-gap device (b) narrow-gap device. A best fit line is shown to the data points.

The data can now be expressed in a form which represents the characteristic response of a dual sensor device by plotting the wide-gap sensor response (x-axis) against the narrow-gap sensor response (y-axis) as shown in Figure 8.34.

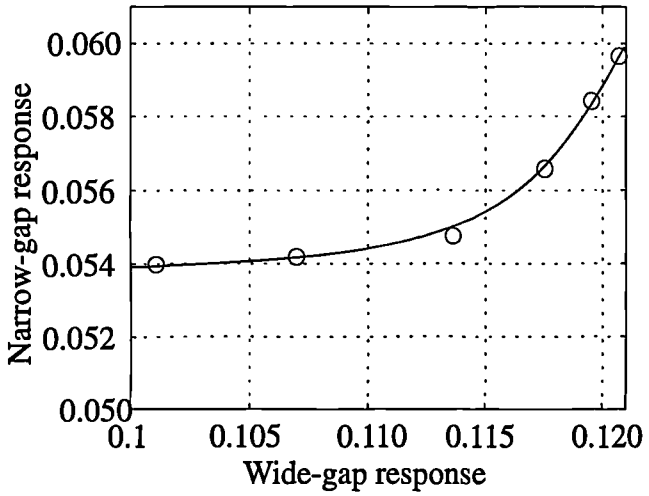

Figure 8.34 Response of a thick film SnO_2 dual sensor device at 400°C in dry conditions. A best fit line is shown to the data points.

These characteristics are of the same form as the moving-boundary theory described in Section 5.6 of Chapter 5. Below 150 ppm CO the narrow-gap sensor does not show a significant fractional change in conductance, whereas the wide-gap sensor responds at lower CO concentrations. Drawing comparisons with the theory it may be suggested that the gas boundary had not reacted far enough into the film to affect the narrow-gap sensor. Whereas, above 150 ppm CO, the gas-sensitivity of the

narrow-gap sensor rapidly increases. The dual sensor response shown in Figure 8.34 is typical of moving-boundary, however, the characteristics do not indicate the concentration at which the gas is uniform through the film thickness.

8.5 Typical Characteristics for CP Chemoresistors

SADs, discrete and bridge chemoresistors employing films of PPy and PAn with different counter-ions have been characterised to certain vapours (e.g. propan-2-ol, ethanol, toluene). Characteristic variations to temperature and RH have also been investigated. A typical response of a chemoresistor employing PAn/PSA/H_2O to varying concentrations of toluene at 30.4°C and 20 % RH is shown in Figure 8.35.

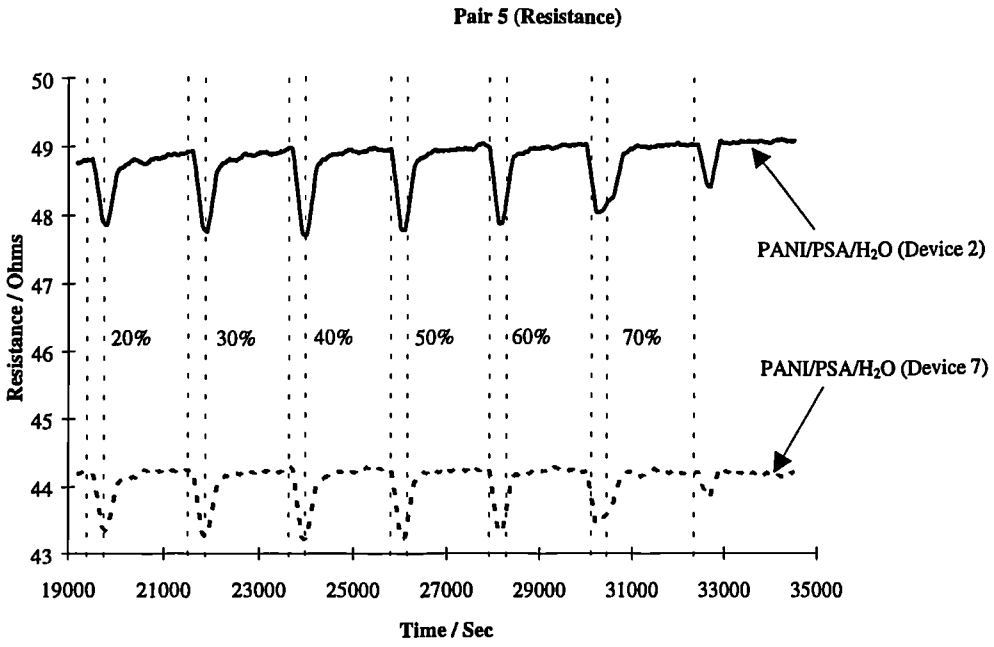

Figure 8.35 The response of two PAn/PSA/H_2O chemoresistors to different concentrations of toluene at 30.4°C and 20 % RH (from P. Ingleby), where the different concentrations are expressed in % of saturated toluene vapour (yet to be calculated for the conditions used).

These results have been collected by Mr Paul Ingleby and form part of his PhD studies.

8.6 Conclusions

This Chapter has described the characterisation of XPc, SnO_2 and intelligent dual SADs.

Characterisation of the XPc chemoresistors was limited by membrane fracture. However, those results obtained for as-deposited MgPc exhibited a response time (~ 1 hour), which would be impractical for implementation into a hazardous-gas early-warning instrument. An on-chip annealing process was investigated which gave a response for a PbPc chemoresistor with a response time of ~ 1 minute to detect 1 ppm of NO_2.

The thin and thick film SnO_2 chemoresistors produced a characteristic increase in resistance when exposed to low concentrations of NO_2 (< 10 ppm). A summary of the key characteristics are shown in Table 8.4.

Both the thin and thick film SnO_2 chemoresistors have shown a characteristic decrease in resistance when exposed to low concentrations of CO (e.g. < 100 ppm). A summary of the key characteristics are shown in Table 8.5.

The response of thick and thin SnO_2 chemoresistors to NO_2 and CO were sensitive at concentrations much less than the long-term exposure limits (see Table 1.1), which suggests that with additional characterisation they could be employed easily in an early warning instrument for a single target gas. In general the base-line resistance (R_0) of thin film SnO_2 chemoresistors (e.g. $150 > R_0 > 900\ \Omega$ at 367°C) was less than that of the thick film SnO_2 chemoresistors (e.g. $10 > R_0 > 200\ k\Omega$ at 355°C). Also the change in resistance was typically larger for thick films of SnO_2 as suggested by the measured sensitivity shown in Table 8.4 and Table 8.5. Considering application of the SnO_2 sensors investigated in an instrument for detecting NO_2 and CO mixtures, it is important to note that the chemoresistors exhibit cross-sensitivity to both target gases but of opposite sign. This is undesirable as the oxidising effects of NO_2 may cancel the reducing effect of CO. However, the temperature dependence of each SnO_2 chemoresistor response was more specific e.g. an undoped thick film SnO_2 chemoresistor shows a maximum response to low concentrations of NO_2 at ~ 210°C and a maximum response to low concentrations of CO at ~ 310°C. Therefore, to demonstrate the suitablity of the SADs to a temperature pulsed mode of operation, the fast thermal response times of the MHPs were exploited in tests on thin film SnO_2.

Further results are required to determine quantitatively the response characteristics to RH.

The initial results acquired from a dual sensor device coated with a thick film of SnO_2 was of the same form as the theory described in Chapter 5.

Table 8.4 Summary of characteristics of SnO_2 chemoresistors to NO_2.

SnO_2 sensor type	Relative sensitivity (ppm^{-1})	Response time (min)	Temp. of highest sensitivity	Response Dependence on RH	Isotherm type
Thin undoped	0.07 (at 367°C, 6.25 ppm)	~ 5	310°C	Insufficient data	Freundlich (see Table 8.2)
Thin Pd doped	0.10 (at 367°C, 6.25 ppm)	< 1	367°C	Independent trend	Freundlich (see Table 8.2)
Thin Pt doped	0.08 (at 367°C, 6.25 ppm)	< 1	310°C	Third order expression	Freundlich (see Table 8.2)
Thick undoped	6.1 (at 355°C, 1.25 ppm)	~ 2	195°C	Response decreases with RH	Not recognised
Thick Pd doped	0.6 (at 355°C, 1.25 ppm)	~ 1	235°C	Insufficient data	Not recognised
Thick Pt doped	0.5 (at 355°C, 1.25 ppm)	~ 1	< 250°C	Response decreases with RH	Not recognised

Table 8.5 Summary of characteristics of SnO_2 chemoresistors to CO.

SnO_2 sensor type	Relative sensitivity (ppm^{-1})	Response time (min)	Temp. of highest sensitivity	Response Dependence on RH	Isotherm type
Thin undoped	4.8×10^{-3} (at 367°C, 31.3 ppm)	~ 0.5	418°C	Third order expression	Freundlich (see Table 8.3)
Thin Pd doped	4.2×10^{-3} (at 367°C, 31.3 ppm)	~ 0.5	418°C	Independent trend above 21 % RH	Freundlich (see Table 8.3)
Thin Pt doped	4.0×10^{-3} (at 367°C, 31.3 ppm)	~ 0.5	367°C	Independent trend	Freundlich (see Table 8.3)
Thick undoped	26×10^{-3} (at 295°C, 33.3 ppm)	~ 1	295°C	Response increases with RH	Freundlich (see Figure 8.28)
Thick Pd doped	7.7×10^{-3} (at 295°C, 33.3 ppm)	~ 1	355°C	Independent trend	Freundlich (see Figure 8.28)
Thick Pt doped	0.5 (at 295°C, 33.3 ppm)	~ 1	355°C	Response increases with RH	Freundlich (see Figure 8.28)

8.7 References

8.1 T.A. Jones, B. Bott and S.C. Thorpe, Fast Response Metal Phthalocyanine-Based Gas Sensors, *Sensors and Actuators*, **17** (1989) 467-474.

8.2 N. Bârsan, Private Communication.

Chapter 9

9. Conclusions

9.1 Research Approach to Achieve Objectives

The general aim of my research was to develop hazardous-gas microsensor technology suitable for application in a portable instrument. Of particular interest was the detection and early warning of harmful levels of NO_2, CO and VOC in air. Silicon technology was employed in the design of chemoresistive gas sensors to realise miniaturised low-power devices. The approach taken to fulfil the gas detection requirements is described in Chapter 2 and involved investigating existing gas-sensitive material technology. The desire to detect NO_2 and CO led to the investigation of SnO_2 (e.g. undoped, Pd and Pt doped) and XPc (e.g. PbPc, MgPc and CuPc) materials, while an interest in VOCs led to the investigation of CP films. An integrated heater was an essential part of the chemoresistor devices incorporating MOS and XPc films that operate at high temperatures. To meet the low power requirements of a portable instrument, both conventional planar thin film technology and micromachining techniques were used to integrate miniaturised chemoresistors with a thermally insulated MHP structure.

Chemoresistors employing MOS, XPc and CP films often suffer from poor specificity and poor long-term stability. The approach taken to overcome these problems here was to fabricate an array of low-power sensors suitable for operation with a microprocessor that can apply a chemometric program to solve the multicomponent problem. The implementation of such an intelligent sensor system will be outlined in more detail later, however, at present it is important to note that its performance will be determined by the distinctiveness of different fingerprints associated with a particular gas mixture. Therefore, the choice of sensor elements in the array and the mode of operation of each sensor is a critical part in the design of an

intelligent sensor system. The SADs were specifically designed to investigate just one class of gas-sensitive material. However, it is expected that a suitable SAD for a multicomponent gas instrument would combine the different sensor technologies investigated (i.e. hybrid sensor). The fabrication processes employed were suitable for the fabrication of a hybrid sensor, as described in Chapter 4.

Although the design and fabrication of discrete and bridge CP chemoresistors has been described, the large amount of research required to establish the most suitable CPs for a hybrid SAD, has meant that this work has been undertaken in collaboration with other researchers at the Universities of Warwick and Southampton. The results arising from these sensors will be published elsewhere. However, the characterisation of the SnO_2 and XPc chemoresistors was undertaken by me (see Chapter 8). Any further discussion on the design of a portable hazardous gas monitor is therefore concerned with NO_2 and CO.

The performance of the SnO_2 and XPc chemoresistors are known to be highly dependent on temperature. The integration of three MHPs on each SAD enables a rapid control of the device operating temperature. The temperature cycle of the SAD can then be chosen to optimise the performance of the array device in a so-called intelligent sensor system. In order to improve the design of my MHPs thermal modelling of these structures has been carried out and is reported in Chapter 6 together with the thermal performance (e.g. power consumption and response time).

Researchers have developed models to describe the different gas-sensing mechanisms in chemoresistive gas sensors. In Chapter 5 I have described these models for SnO_2, XPc and CP chemoresistors. Moreover, in Chapter 5 I provide the background behind the theoretical model proposed for an intelligent dual sensor device, which in theory could give a poisoning diagnostic. The dual sensor was incorporated into the SRL125/dual SAD, in an effort to improve chemoresistor stability (for which poisoning is a main cause). The characterisation of this device has also been described in Chapter 8.

The main research objectives have been achieved, namely, I have designed and fabricated a number of silicon SADs for use in low power gas monitors, and characterised a number of gas-sensitive materials of potential application. Even though time did not permit the production of a portable instrument, our improved knowledge of the SAD functionality allows the proposal of a general block structure

for a portable instrument. Furthermore, the research described in this thesis has developed microsensor technology to the position in which it could be employed to make a multi-mode hybrid SAD. The conclusions from my research are therefore based on the analysis of these novel devices for application in portable instruments, as described in the following Section. My work has led to a series of silicon sensors that are being used by other researchers in a range of application areas.

9.2 Conclusions from the Characterisation of SADs

Three different types of chemoresistor were characterised with the automated gas sensor test system; those based on XPc films, SnO_2 films and the intelligent dual sensor.

Two problems limited characterisation of the XPc chemoresistors; firstly, the SRL125/XPc MHPs exhibit a thermal hot spot and secondly, stresses were induced during tests which frequently led to membrane fracture. Those results obtained showed that the response times of as-deposited MgPc to low concentrations of NO_2 were too slow for use in an early-warning instrument. However, a response time of ~ 1 minute was achieved for a PbPc chemoresistor to 1 ppm NO_2 after an on-chip annealing process (e.g. 200°C for 1 hour). It would appear that the XPc annealing process improves the gas-sensing characteristics, and thus produces chemoresistors suitable for use in a hybrid SAD. Unfortunately, not enough results were obtained to warrant the further development of a more mechanically stable XPc chemoresistor. It should be noted, however, that to improve MHP mechanical stability with the employed technology would require a thicker membrane, which would consequently increase the thermal power losses.

Characterisation of thick and thin films of SnO_2 showed properties which were suitable to detect low concentrations of NO_2 and CO and more stable than identical coatings on other substrates. Moreover, it was noted that the temperature dependence of the response to NO_2 and CO were different, for both thick and thin film SnO_2 chemoresistors. For example, an undoped thick film SnO_2 chemoresistor was shown to have a maximum sensitivity to NO_2 at approximately 210°C, and a maximum sensitivity to CO at approximately 310°C. This indicates the potential application of running similar chemoresistors at different temperatures to enhance discrimination of CO and NO_2 mixtures. The very rapid thermal time constant (~ 5 ms) of the MHP

also allows very short pulses of different operating temperature to be used. It was demonstrated for a thin film SnO_2 chemoresistor that the rapid control of the reaction kinetics on the gas sensor surface, may provide information on the gas-sensing mechanisms. The response to a sequence of different temperature pulses of varying duration makes possible an alternative signal for gas mixture analysis. Another advantage of pulsing the operating temperature is that it consumes less power, compared to a constant operating temperature mode. The excellent thermal properties of the MHPs makes this multi-mode operation of the chemoresistors very attractive. The power consumption of the SRL125/MOS MHP was 175 mW to heat two SnO_2 chemoresistors to 400°C, taking ~ 15 ms to reach thermal equilibrium. A pulsed mode of operation could reduce the average power consumption to less than 1 mW.

The characterisation of an intelligent dual sensor device coated with a thick film of SnO_2 showed an encouraging verification of the theoretical operation. The results indicate that if the effects of poisoning occur a short distance into the active film, then only the wide-gap sensor response will decrease. This situation would cause a shift in the characteristic dual sensor response, which could be used as a diagnostic tool. Before incorporation of such sensors in a hybrid SAD, more characterisation is required to verify further the validity of the theory and to calibrate poisoning effects.

The initial results are encouraging with respect to suitable detection of NO_2 and CO, using a temperature pulsed SAD consisting of chemoresistors employing different SnO_2 films. The operating temperature of the sensors can be controlled by low power MHPs. The fabrication of a hybrid device would be straightforward using the technologies and materials described in Chapter 3 and Chapter 4.

9.3 Proposal of an Intelligent Sensor System

It is proposed in this discussion that a SRL108/MOS device coated with undoped, Pd doped and Pt doped SnO_2 would be suitable for detection of CO and NO_2 in an intelligent sensor system. However, further characterisation of the SnO_2 chemoresistors is required to determine quantitative discrimination between NO_2 and CO using a chemometric PARC algorithm. The use of thin film SnO_2 materials may simplify the instruments interface electronics, because of the lower base-line resistances and lower range of expected resistance excursions, compared to thick

SnO_2 films. The general block architecture for a portable gas monitor using the SAD described above is shown in Figure 9.1.

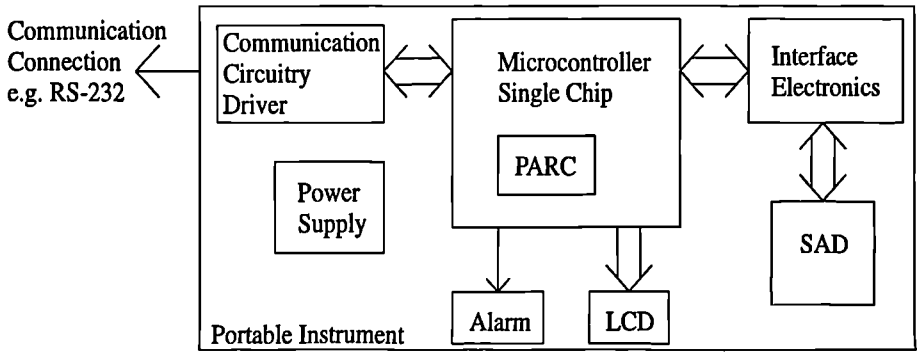

Figure 9.1 General block diagram of a portable instrument employing a SAD.

The system operation would involve the microcontroller acquiring the conditioned sensor data while controlling the SAD operating temperatures. The microcontroller can apply a PARC program to the sensor data to extract the CO and NO_2 concentrations. The measurement could then be displayed on a LCD, or if the gas concentrations approach the OES an alarm could be triggered. The performance of the instrument is greatly influenced by the choice of the PARC and preprocessing algorithms employed by the microcontroller [9.1]. Previous work at Warwick has identified artificial neural networks (ANNs) as a suitable PARC method of identifying mixtures of gases and vapours. An example of the type of predictive classifier employed would be a two-layer back-propagation network [9.2].

ANNs are biologically inspired from studies of neural organisation in the brain which are modelled within the ANN network configuration and algorithms. For an ANN to extract the gas concentrations from the acquired data set requires that the program has been previously 'taught' the distinguishing features of the sensor response to known concentrations of CO and NO_2. The SAD calibration could be carried out by a PC and electronic hardware which emulates the operation of the PARC program and simulates the operation of the portable instrument [9.3]. By placing the SADs in the automated test gas system the environment can be controlled during calibration. This would allow the PARC network weights (coefficients) to be determined. The portable instrument would then be loaded with the SAD. A communication connection (e.g. RS-232, CAN or I^2C) to the external PC allows the

PARC program and weights to be down-loaded to the microcontroller, as well as providing a means of checking instrument calibration.

To warn against a short-term exposure hazard requires that the sequence of data acquisition and data processing should take much less than 10 minutes. It has been shown in Chapter 8, that the very rapid thermal time constant (~ 5 ms) and the fast response time (~ 30 s) of the thin film SnO_2 chemoresistors can be exploited for thermal cycling. The results obtained (see Chapter 8) suggest that three steady-state data points can be acquired at different temperatures within 2 minutes, as shown in Figure 9.2.

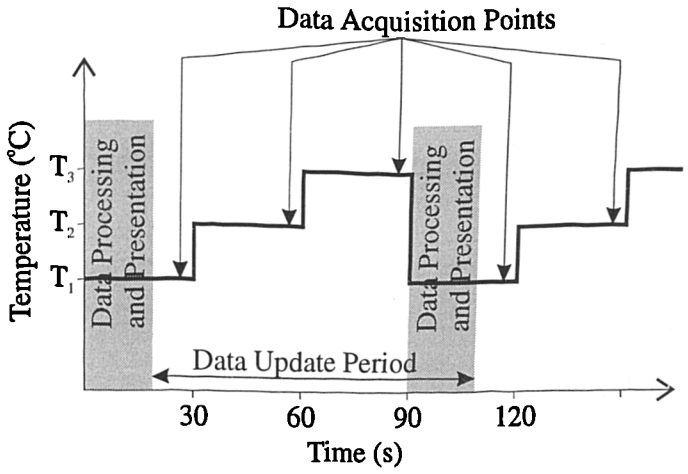

Figure 9.2 Sequence of temperature cycling and sequence of data sampling.

Applying this sequence of three temperature levels to the MHPs, the six sensor outputs from the hex SAD forms a 6×3 data set matrix. Interface electronics are needed to provide the measurement of six chemoresistive outputs, a temperature sensor and the three microheater resistances, while it needs to set the three MHP operating temperatures. The resistance measurement of the microheaters allows closed-loop temperature control. The temperature cycling is based on acquiring steady-state sensor data at different temperatures as rapidly as possible. This mode of operation is assumed for the portable instrument proposal discussed below. However, it is important to note that the operating temperature can also be rapidly pulsed (~ 10ms) at the same levels once over the same period (2 minutes) to obtain non-

equilibrium data information. Temperature pulsing would dramatically reduce the MHP power consumption to approximately less than 1 mW per chemoresistor.

A portable instrument must have a very low power consumption to prolong the battery life. To define the power consumption of such a system, requires that the system hardware is described in greater detail. The rapid advancement in microelectronics, is increasing the level of integration of features into single packages, which makes the following system description speculative. However, a basic instrument outline with typical devices (where known) serves to assess the SAD power consumption. An 8-bit microcontroller (e.g. the low power 80CL31 family by Philips) with 32 I/O lines would be adequate for the slow I/O sampling rate (30 s). 32 k ROM and 128 bytes of RAM would provide necessary memory for the two-layer back-propagation ANN, weights and the instrument's operating system.

Separate ADCs and DACs are proposed for the portable instrument, so as to provide the I/O signals to the microcontroller at a 12-bit accuracy. The general architecture of the interface circuitry is as shown in Figure 9.3. The analogue features of this interface circuitry were based on that proposed by Dyer and Gardner [9.4] for a hybrid electronic nose.

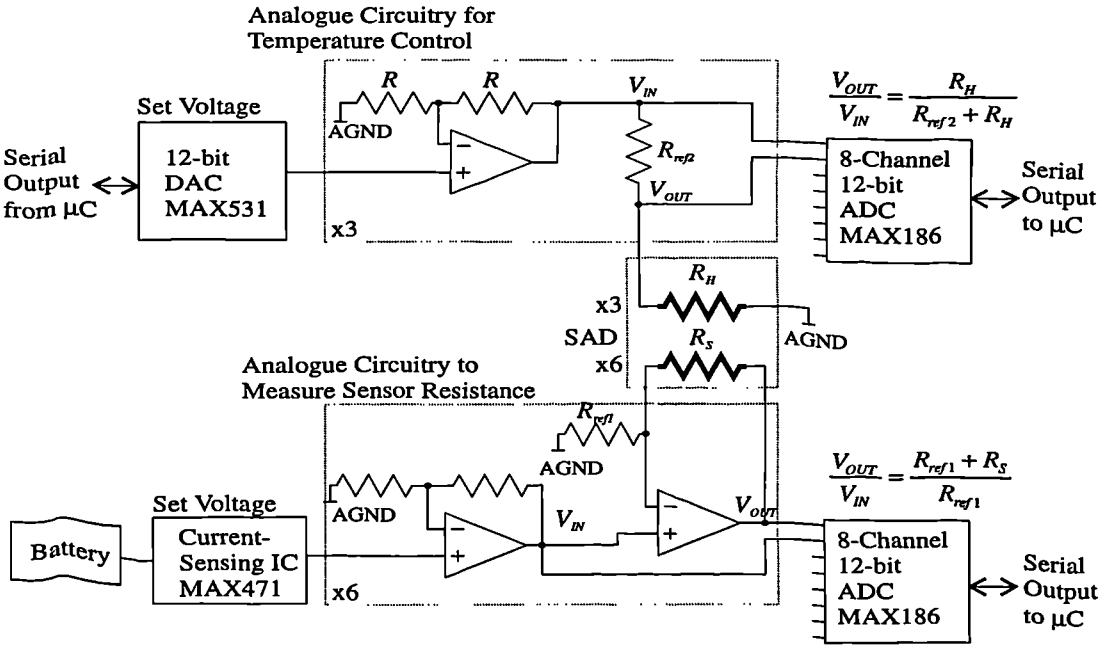

Figure 9.3 General lay-out of interface circuitry for a proposed portable sensor system.

The maximum voltage required in the system is to drive the microheaters up to approximately 7 V, although the heater resistance can be decreased (in future designs) to reduce the drive voltage to the desired rating. The digital electronics can operate from a 5 V supply. The battery pack is a key part of any portable instrument, which has led to the advancement of battery technology. Lithium based cells have exhibited very high energy densities and higher terminal voltages (e.g. 3.6 V) compared to nickel based cells. Current technology is leading to smart battery systems which allows cell maintenance and measurement functions for portable instruments [9.5]. However, for this proposal, I have assumed the use of two non-rechargeable lithium thionyl chloride cells (size AA, RS Components Ltd.) in series. This power source provides a supply voltage of 7.0 V and a combined nominal capacity of 4.2 Ah.

To warn against a low battery supply, a current-sensing IC (e.g. MAX471, Maxim Integrated Products Ltd.) could be used to measure battery discharge.

To measure the sensor resistances, the analogue interface circuitry is arranged so as each sensor element forms a feedback resistor (R_S) in a noninverting amplifier. Another amplifier sets the input voltage (V_{IN}) to the noninverting amplifier which is also connected to the input of an 8-channel ADC (MAX186, Maxim Integrated Products Ltd.). The output voltage (V_{OUT}) from the noninverting amplifier is also connected to the ADC. This allows V_{OUT}/V_{IN} to be measured, which is equal to $R_{ref1}+R_S/R_{ref1}$. The value of R_{ref1} can be matched to the sensors base-line resistance prior to the instrument's calibration. The MAX186 is a micropower 12-bit ADC which has an 8-way MUX integrated into the package [9.6].

For microheater temperature control, an ultra-low power serial DAC (MAX531, Maxim Integrated Products Ltd.) can produce an analogue voltage with a 12-bit accuracy [9.7]. This voltage can then be amplified up to 7 V using a discrete power amplifier capable of supplying a current of up to approximately 24 mA to provide the thermal power requirements of the MHPs (e.g. 158 mW produces an operating temperature of 418°C). The microheater (R_H) is arranged electrically as part of a potential divider with a reference resistor (R_{ref2}), as shown in Figure 9.3. The input and output voltages are measured from the potential divider with an ADC (MAX186). Again the ratiometric voltage from the potential divider provides a means of measuring R_H, as highlighted in Figure 9.3.

The low sampling rate of data acquisition and change in operating temperature required by the system, allows power savings in the electronics. Typical power requirements of some of the components of the portable instrument are summarised in Table 9.1.

Table 9.1 Power requirements of key components in the proposed portable instrument.

Device	Description	Supply Current	Power (mW)	Ref
MAX186	Micropower, 8-channel 12-bit ADC	10 μA	0.05	[9.6]
MAX531	12-Bit, 5 V, Serial DAC	<300 μA	<1.5	[9.7]
80CL31	Low-power Single-chip 8-bit micro-controller at 8 MHz.	<8 mA	≈ 40	[9.8]
MAX471	Single-IC that measure battery discharge current	<100 μA	<0.5	[9.9]
MAX3223	RS-232 Transceiver with automatic-shutdown circuitry	10 μA	0.05	[9.10]
LCD	160 characters with LED back lighting	2 mA	10	[9.11]

If the thin film SnO_2 SAD is temperature cycled as shown in Figure 9.2 with T_1, T_2 and T_3 as 310°C, 367°C and 418°C, respectively, then the heater drive currents are 19.6, 21.7 and 23.3 mA, respectively. The corresponding heater drive voltages are 5.1, 6.0 and 6.8 V, which consumes an average power consumption of 129 mW per heater. Even though the cycled temperature operation can reduce the power consumption, the three microheaters on the SRL108/MOS are still a major power consuming component. The power consumption of the analogue components will be undefined until circuit production, but the future possibility of applying ASIC technology will reduce power consumption of the microelectronics even further.

Considering the continuous current supply to the various components, it seems reasonable to assume that the whole system could draw less than 100 mA. Using the battery pack described earlier with a capacity of 4.2 Ah. This suggests that the portable instrument may be operated for approximately 40 hours (or one working

week) with one set of batteries, and perhaps many times longer in pulsed current mode.

It can be concluded that the power consumption of my silicon micromachined chemoresistive gas sensors and the excellent stability of them, makes their application in future portable instrumentation a distinct possibility.

9.4 Future Work and Outlook

The success of my work has provided the foundation for future research effort with the aim of developing a portable instrument for gas detection. The sensor technology produced here is also being employed in other collaborative research, with the aim of improving the performance of electronic nose technology. Details of on-going research are given below:

Both the SAD and the discrete devices are being used to further characterise CP materials. The encouraging results obtained so far, may lead to the CP SADs being employed in portable electronic nose instruments. The CP chemoresistors have also provided characteristics which are suitable for inclusion onto a hybrid SAD proposed for a collaborative European project.

The MHP structures employed in this research have been incorporated into microcalorimetric gas sensors designed at Warwick. The characterisation and modelling of the MHPs has provided a basis for this work. An objective of this research is to reduce further the MHP power consumption, while improving the isothermal property of the active region.

Directly relating to the production of a portable gas-sensing instrument, is the continuing development of a microcontroller-based instrument employing temperature pulsed SADs and the development of a low-power interface ASIC chip. Current collaborative work with the Electronics Department at Southampton University is developing an ASIC chip for use in a three chip instrument, which includes an ASIC, microcontroller and an array of bridge devices (see Chapter 3).

The research presented in my thesis has demonstrated that microsensor array devices may be used in intelligent portable instruments for the detection of gases and vapours. With the likelihood of the complexity of circuit integration increasing and production unit costs decreasing, it is envisaged that intelligent gas sensor systems such as described here should be a commercial reality in the 1990s.

9.5 References

9.1 J.W. Gardner, Detection of Vapours and Odours from a Multisensor Array Using Pattern Recognition Part 1. Principal Component and Cluster Analysis, *Sensors and Actuators B*, **4** (1991) 109-115.

9.2 J.W. Gardner, E.L. Hines and H.C. Tang, Detection of Vapours and Odours from a Multisensor Array Using Pattern-Recognition Techniques Part 2. Artificial Neural Networks, *Sensors and Actuators B*, **9** (1992) 9-15.

9.3 E.L. Hines and J.W. Gardner, An Artificial Neural Emulator for an Odour Sensor Array, *Sensors and Actuators B*, **18-19** (1994) 661-664.

9.4 D.C. Dyer and J.W. Gardner, High Precision Intelligent Interface for a Hybrid Electronic Nose, To be presented at *Eurosensors X*, Leuven, 1996.

9.5 M. Brown, Safety First in Smart Battery Management, *New Electronics on Campus Spring 1996*, p. 14-15.

9.6 Analog Design Guide, A/D Converters (7), *Maxim Data Sheet*, 6th Edition.

9.7 12-Bit 5V DACs have World's Lowest Power Consumption, *Maxim Engineering Journal*, **13**, p. 17.

9.8 *80C51-Based 8-Bit Microcontrollers, Data Handbook IC20*, Philips Semiconductors, March 1995.

9.9 Analog Design Guide, OP Amps, Video and Comparators (3/8), *Maxim Data Sheet*, 6th Edition.

9.10 New RS-232 ICs Feature 1μm Supply Current, ±15 kV ESD Protection, and 3 V Operation, *Maxim Engineering Journal*, **16**, p. 3.

9.11 Alphanumeric Dot Matrix Liquid Crystal Displays with Backlighting, *RS Data Library F14071*, November 1992.

Appendix A

Sensor Design Cells

This appendix contains the design cells relating to layout patterns required to produce the sensor structure. There are five design cells required to produce each of the SADs and three design cells required for the discrete and bridge devices.

I. SAD Cells

There were two batches of sensor array devices fabricated. The SRL108/CP SADs were fabricated in the first batch, while the SRL125/MOS, CP, XPc and dual SADs were fabricated in the second batch. The overall dimensions for the design cells are 16.2 mm × 4.25 mm and 16.05 mm × 4.4 mm for the first and second batch, respectively.

SRL108/CP SAD Cells

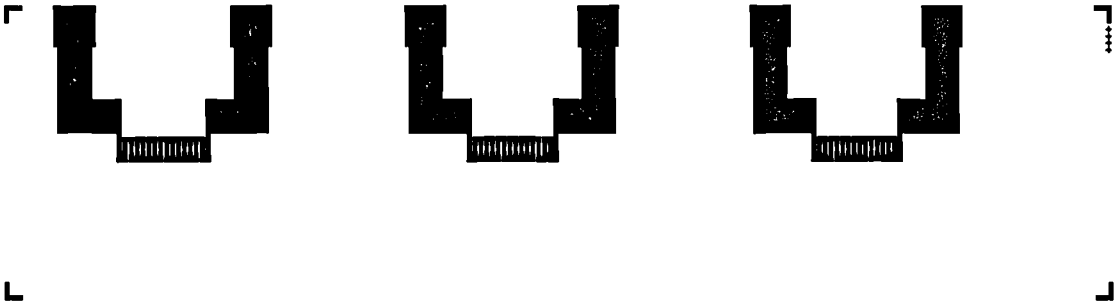

Pt microheater design layout.

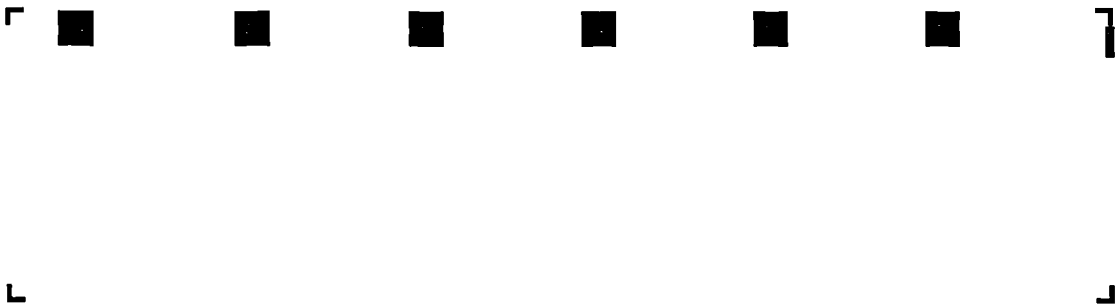

Layout of etch windows required in the thin film of Si_3N_4 to expose the microheater contact pads.

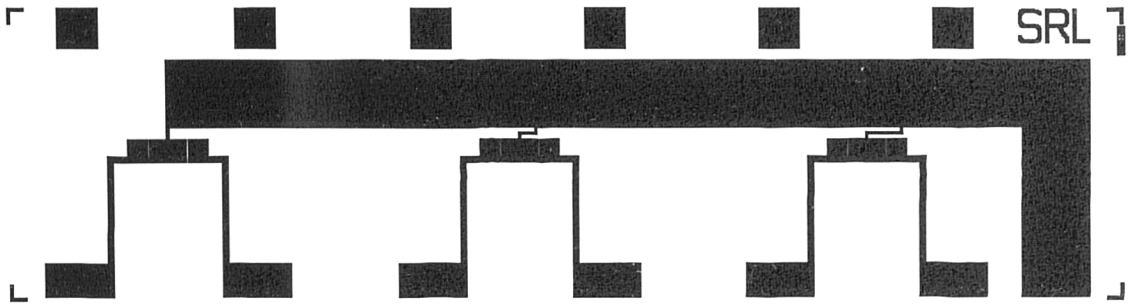

Layout of Au electrode geometry defining six sensor elements grouped in three goups of two. Each sensor element has a 10 μm inter-electrode gap.

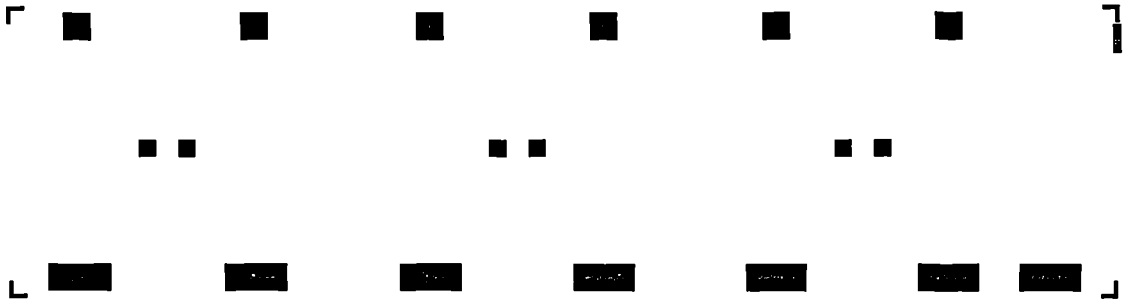

Layout of windows through protective photoresist to reveal electrodes and contact pads. The window above the electrode defines an aspect ratio of 25.

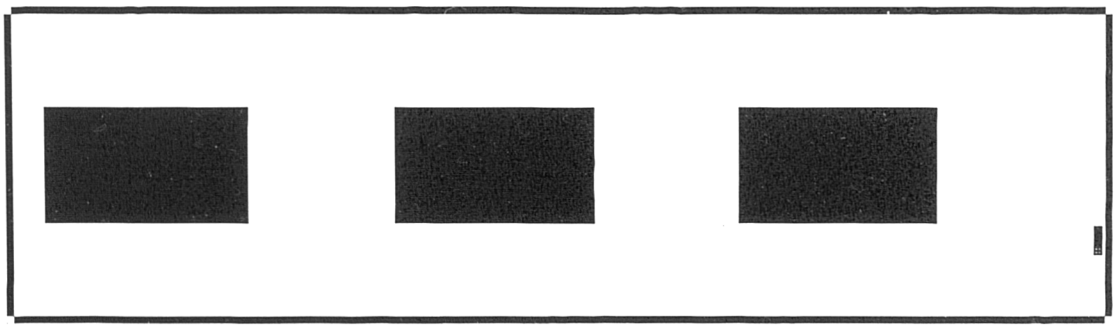

Layout of back-side KOH mask which defines the subsequent sensor structure after anisotropic etching.

SRL125/CP SAD Cells

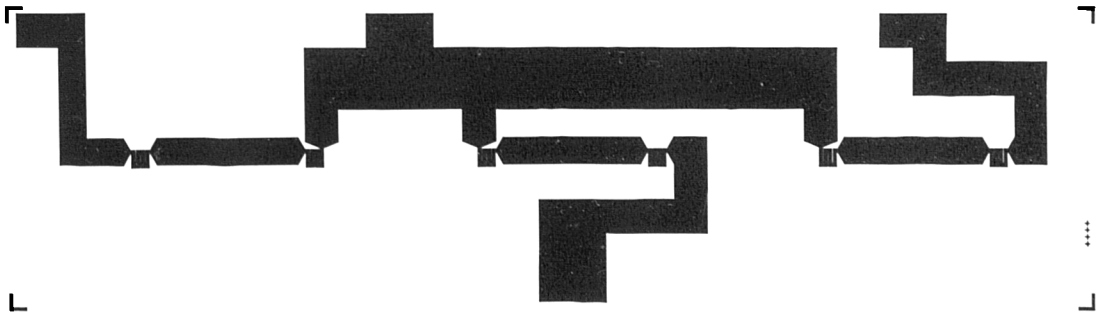

Pt microheater design layout.

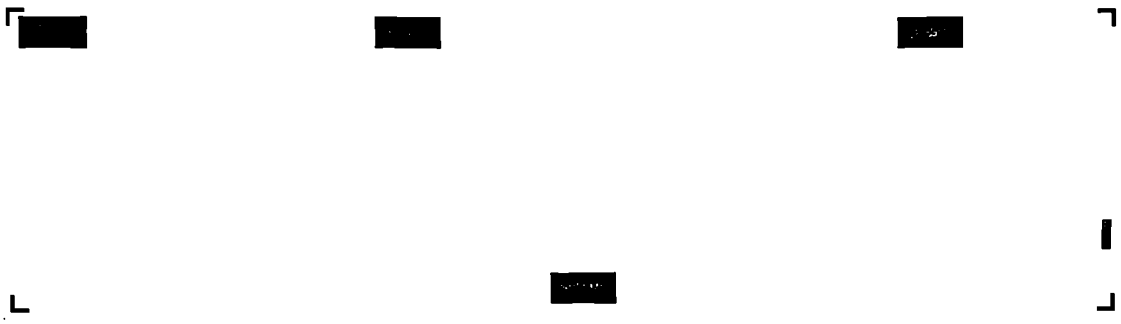

Layout of etch windows required in the thin film of Si_3N_4 to expose the microheater contact pads.

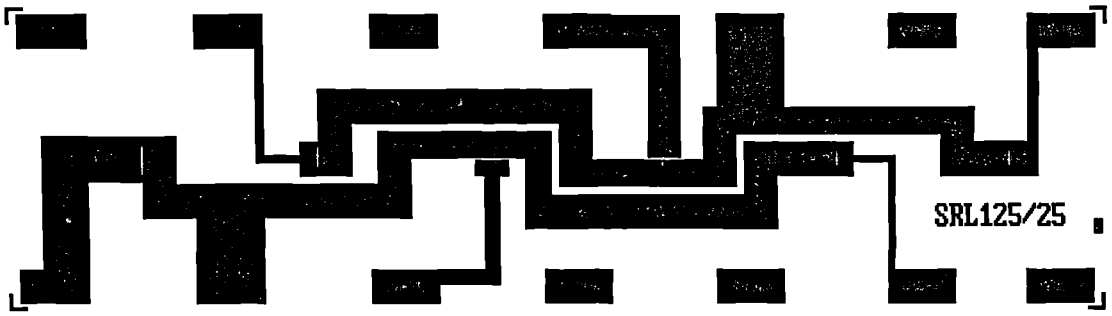

Layout of Au electrode geometry defining six separate sensor elements. Each sensor element has a 10 μm inter-electrode gap.

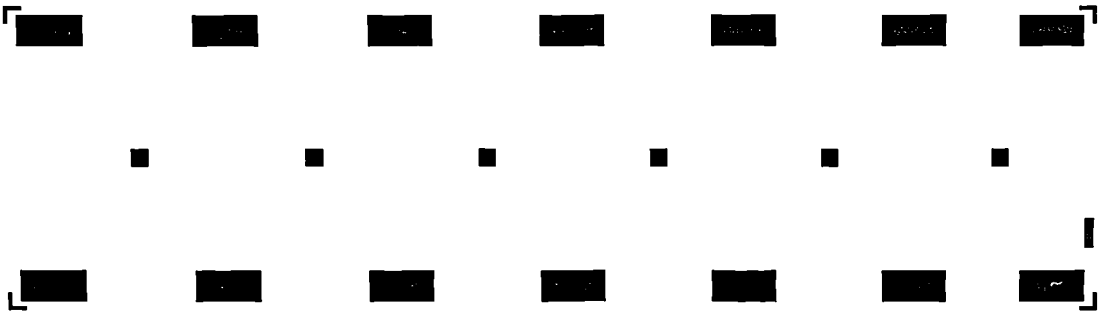

Layout of windows through the protective photoresist to reveal electrodes and contact pads.

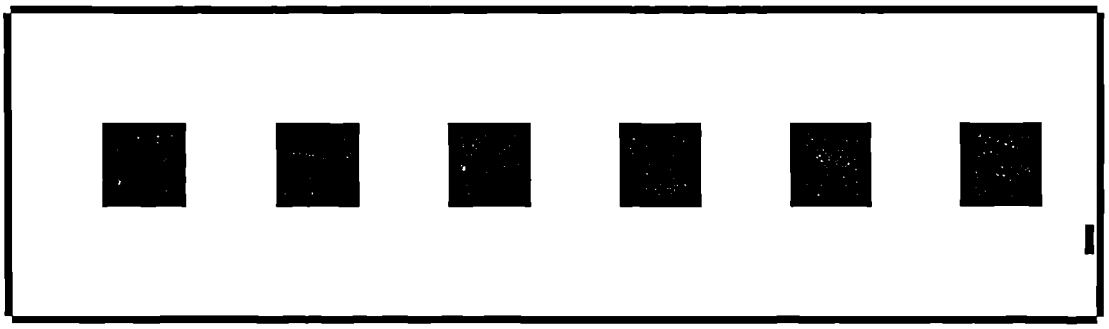

Layout of back-side KOH mask which defines the subsequent sensor structure after anisotropic etching.

SRL125/MOS SAD Cells

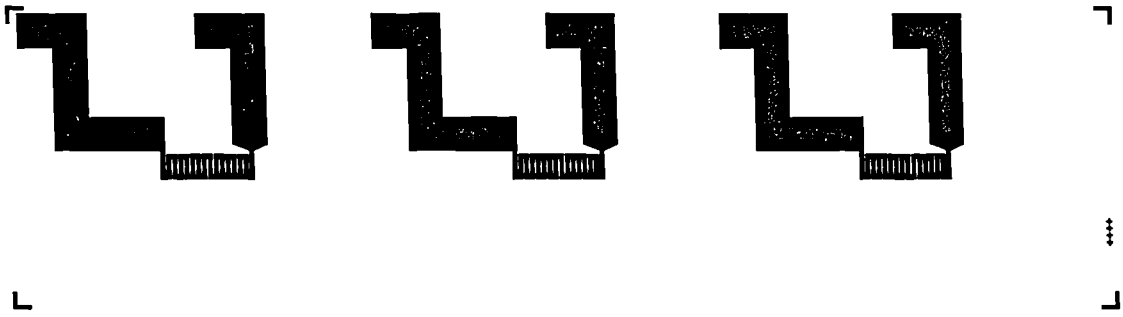

Pt microheater design layout.

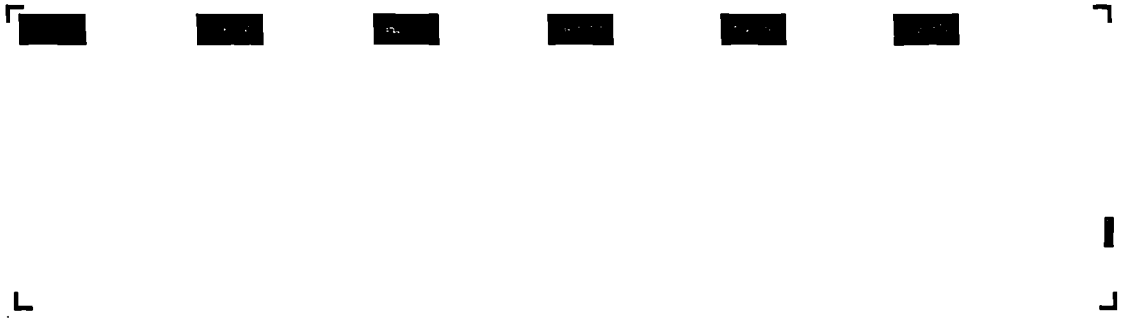

Layout of etch windows required in the thin film of Si_3N_4 to expose the microheater contact pads.

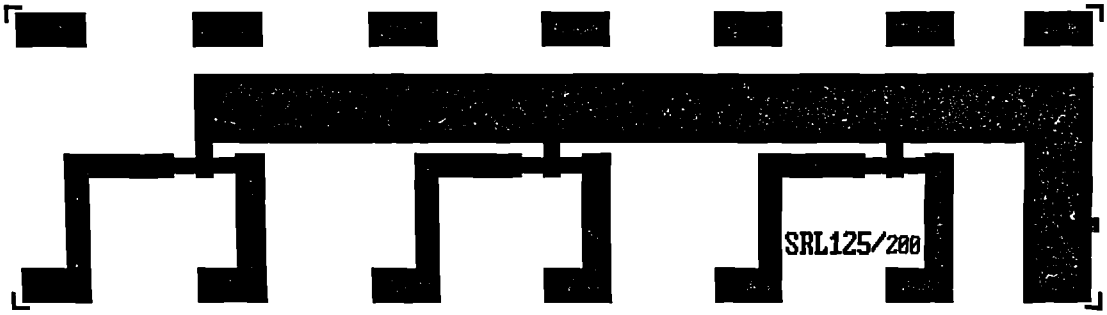

Layout of Au electrode geometry defining six sensor elements grouped in three groups of two. The electrode aspect ratio is approximately 200.

Layout of windows through the protective photoresist to reveal membrane area and contact pads.

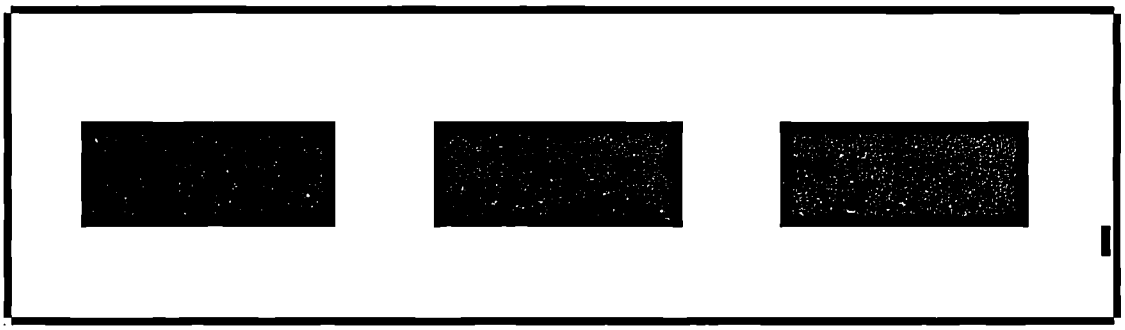

Layout of back-side KOH mask which defines the subsequent sensor structure after anisotropic etching.

SRL125/XPc SAD Cells

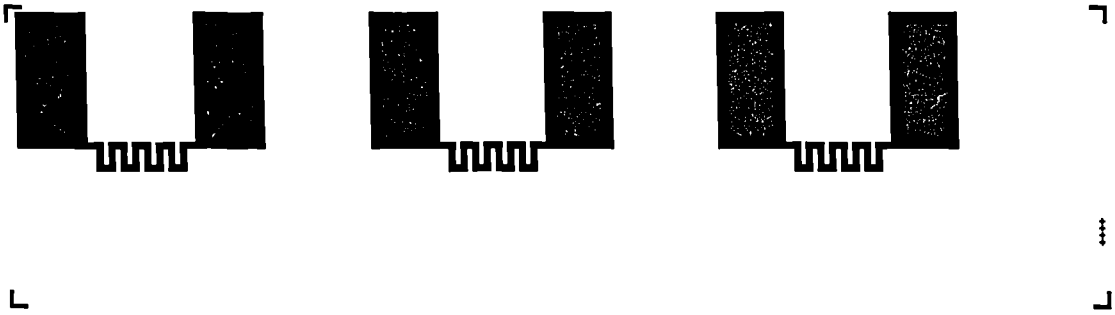

Pt microheater design layout.

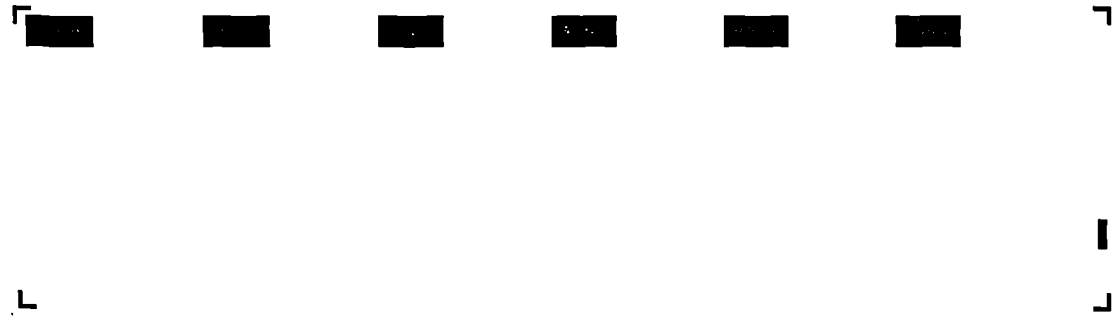

Layout of etch windows required in the thin film of Si_3N_4 to expose the microheater contact pads.

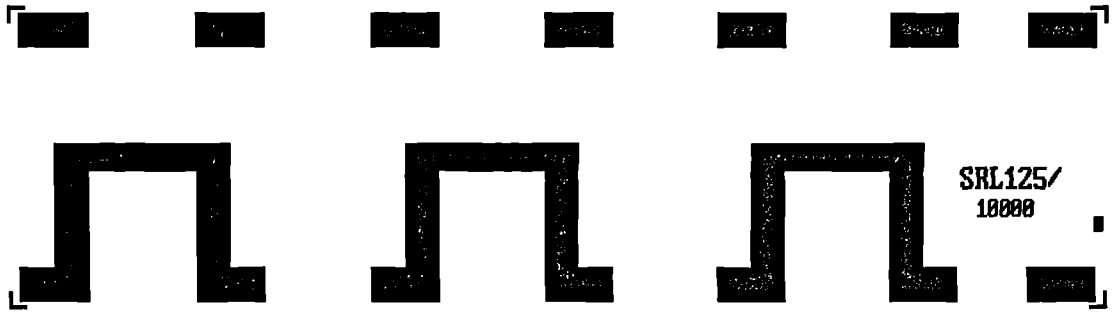

Layout of Au electrode geometry defining three sensor elements, with an aspect ratio of 10,000.

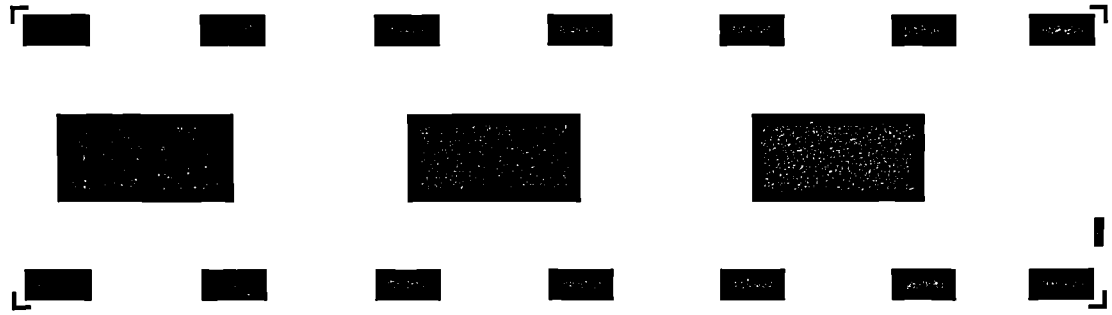

Layout of windows through protective photoresist to reveal membrane area and contact pads.

Layout of back-side KOH mask which defines the subsequent sensor structure after anisotropic etching.

SRL125/dual SAD Cells

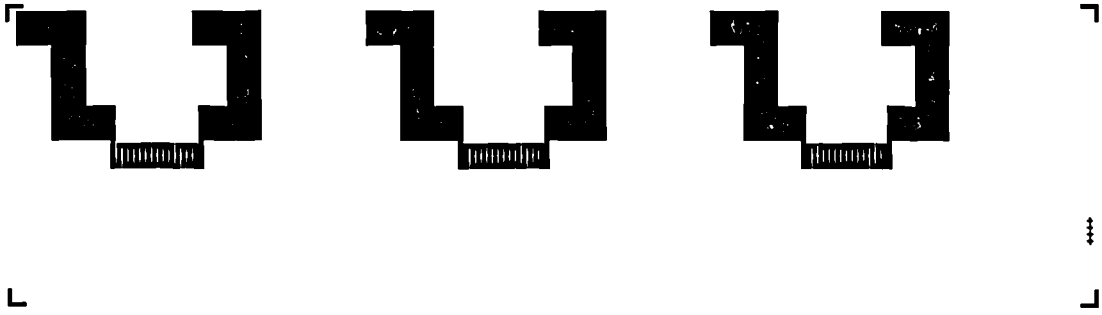

Pt microheater design layout.

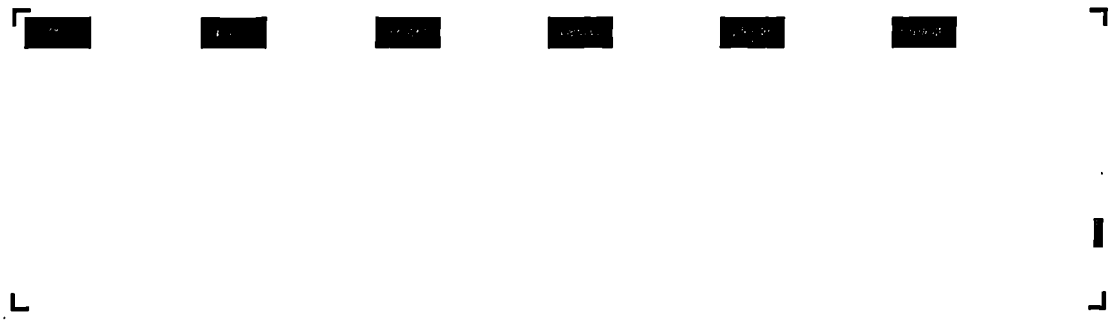

Layout of etch windows required in the Si_3N_4 thin film to expose the microheater contact pads.

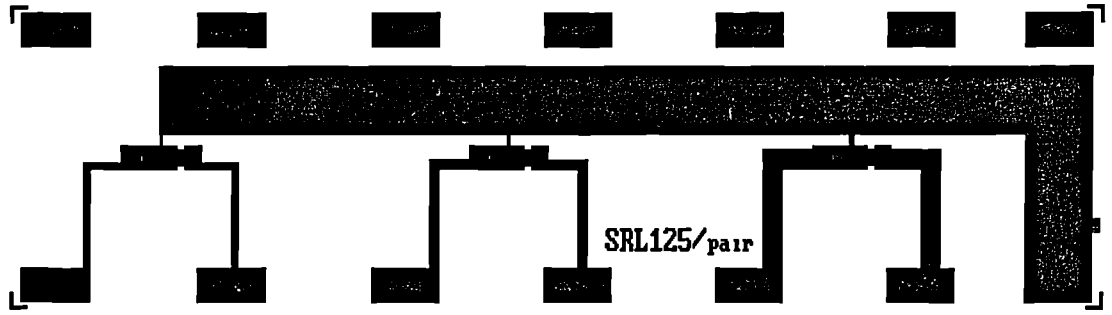

Layout of Au electrode geometry defining three sensor pairs. One sensor has a 10 μm inter-electrode gap while the second inter-electrode gap in the sensor pair is processed with FIBM after the silicon processing.

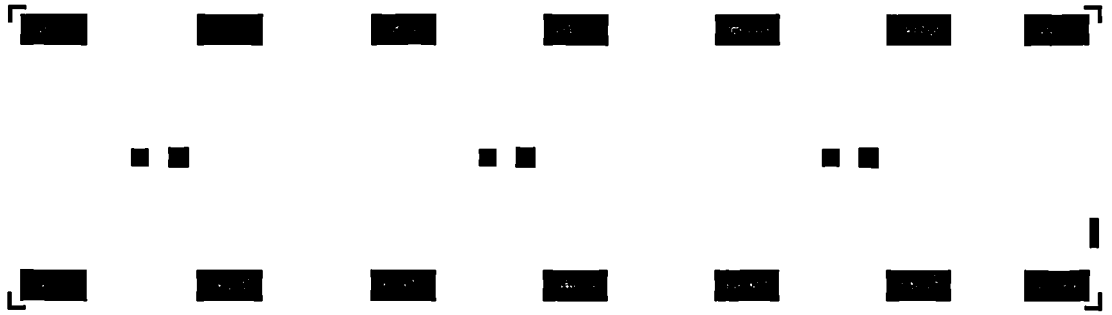

Layout of windows through protective photoresist to reveal electrode area and contact pads.

Layout of back-side KOH mask which defines the subsequent sensor structure after anisotropic etching.

II. Discrete Sensor Design Cells

There are four discrete sensor designs. Two square designs (A) have a side length of 4 mm, while the two extended designs (B) have dimensions of 10 mm × 4 mm.

Discrete Square Design Cells

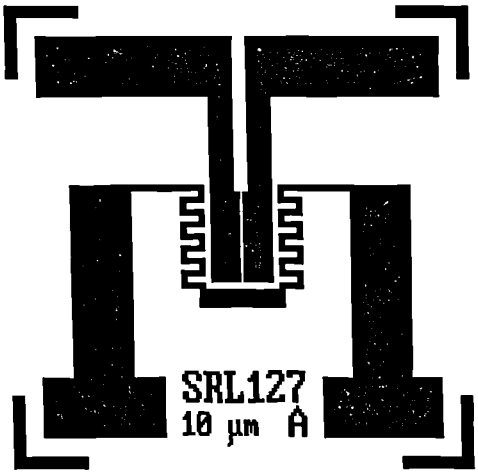

Au layout for design A cell which defines planar heater and 10 µm gap electrode geometry.

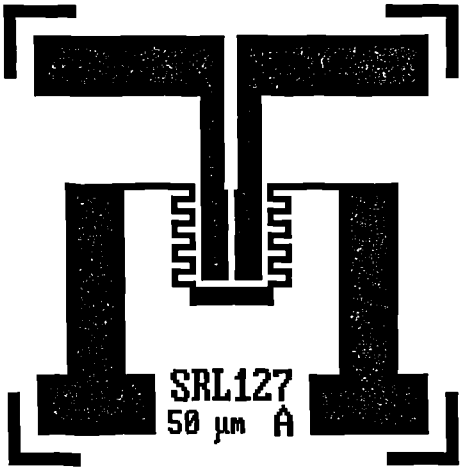

Au layout for design A cell which defines planar heater and 50 µm gap electrode geometry.

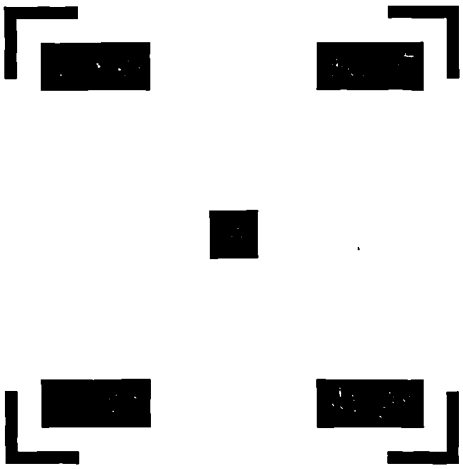

Layout of windows through protective photoresist to reveal electrodes and contact pads.

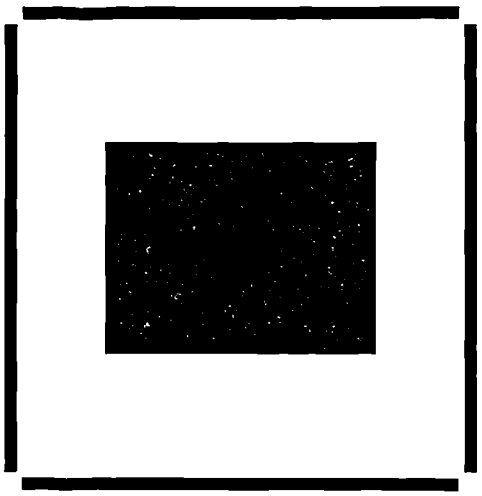

Layout of back-side KOH mask which defines the subsequent sensor structure after anisotropic etching

Discrete Long Design Cells

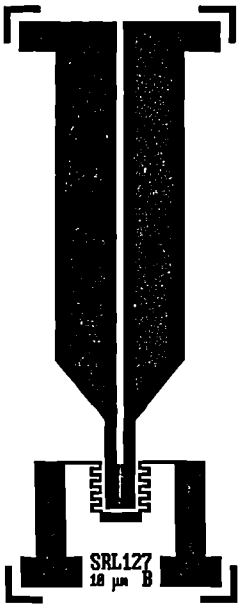

Au layout for design B cell which defines the planar heater and 10 µm gap electrode geometry.

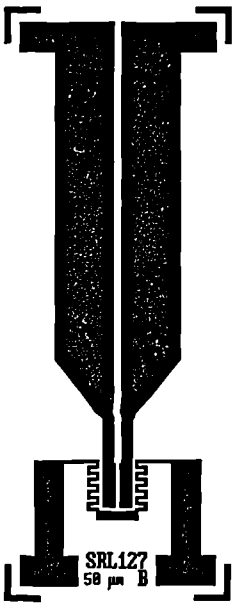

Au layout for design B cell which defines the planar heater and 50 µm gap electrode geometry.

Layout of windows through protective photoresist to reveal electrodes and contact pads.

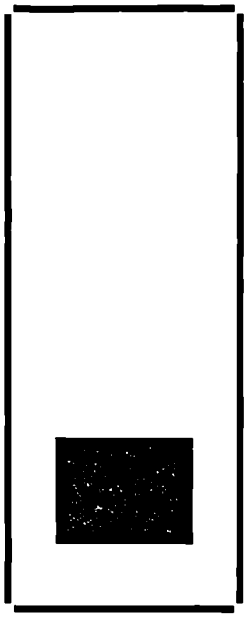

Layout of back-side KOH mask which defines the subsequent sensor structure after anisotropic etching.

III. Bridge Designs Cells

Layout of Au bridge geometry with four 10 µm inter-electrode gap chemoresistors.

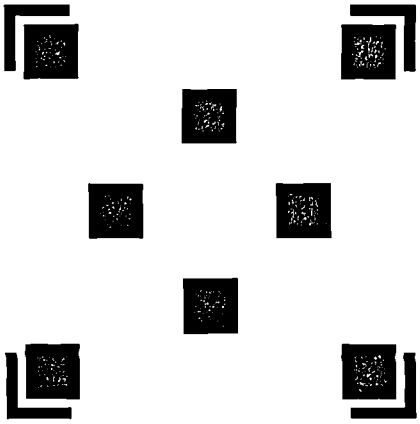

Layout of photoresist windows to expose electrodes and contact pads.

Appendix B

Sensor Design Fabrication Masks

This appendix contains the sets of mask images used for the wafer processsing of the SADs, discrete and bridge devices. There are two sets of five masks for the SADs and a three mask set for the discrete and bridge devices. The data on all masks were produced in the darkfield unless otherwise stated, i.e. the background polarity was lightfield.

First Batch of Masks for SADs

This first batch of masks were used to fabricate the SRL108 SADs.

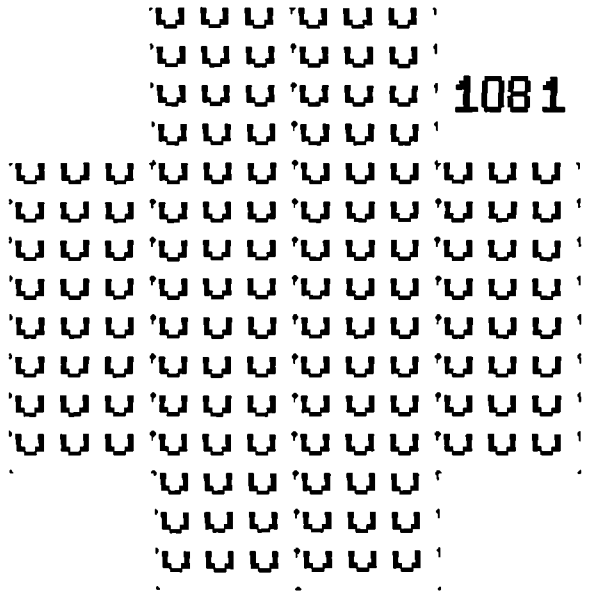

Mask 1 patterns the Ta/Pt film to form the microheaters.

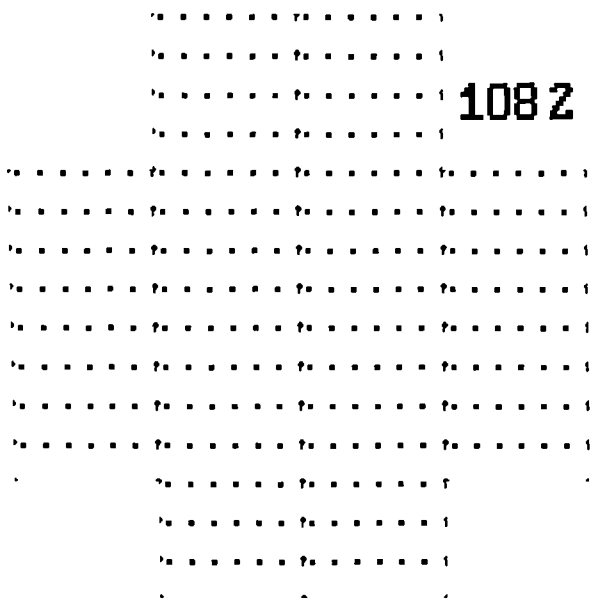

Mask 2 opens windows in the Si_3N_4 layer to expose the heater contact pads.

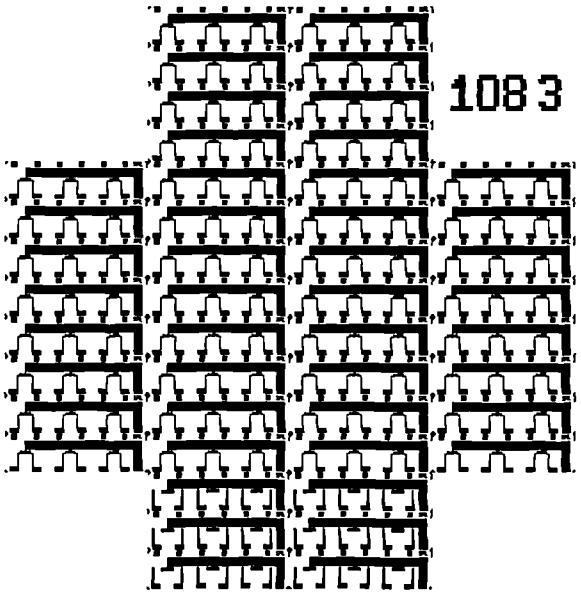

Mask 3 patterns Ti/Au films to create the electrode geometry.

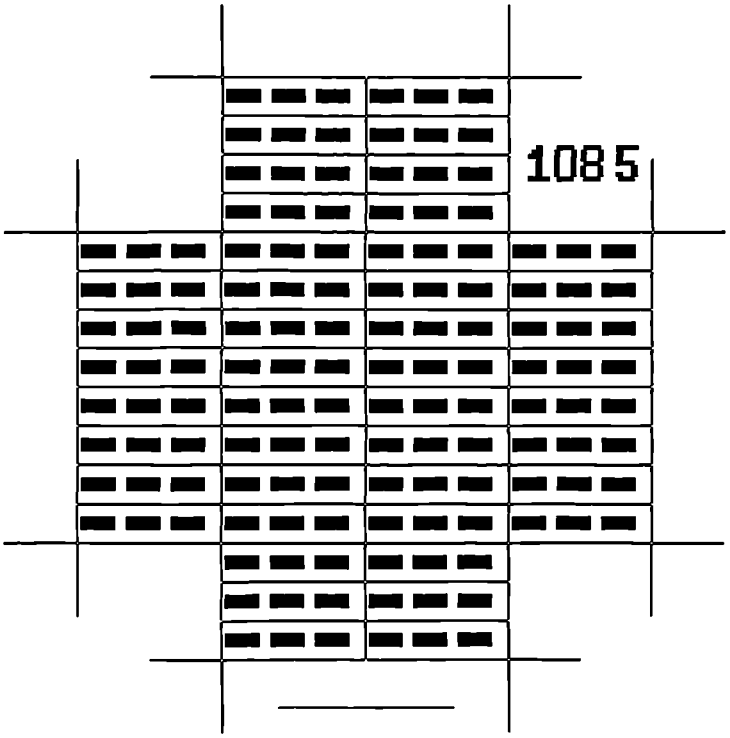

Mask 4 patterns the back-side Si_3N_4 to generate a KOH mask. The actual mask produced is a mirror of this image, because it is used to process the wafer back-side.

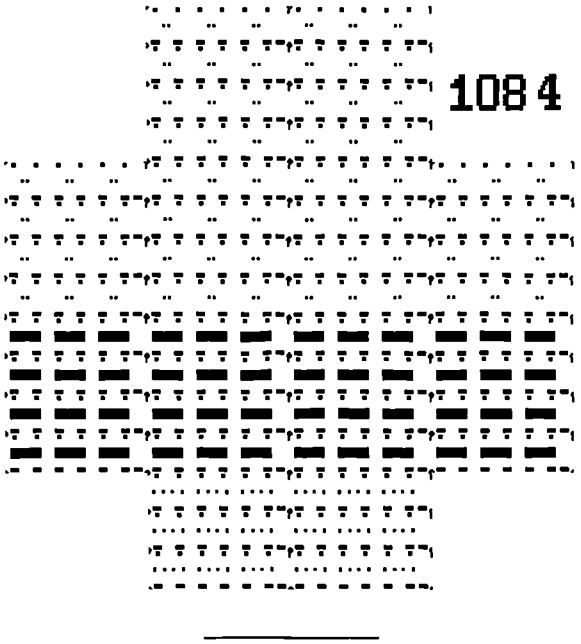

Mask 5 patterns the protective photoresist to reveal contact pads and electrode area.

Second Batch of Masks for SADs

This second batch of masks were used to fabricate the SRL125 SADs.

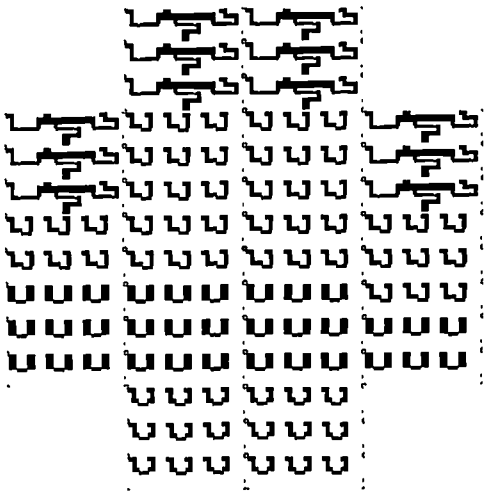

Mask 1 patterns the Ta/Pt film to form the microheaters.

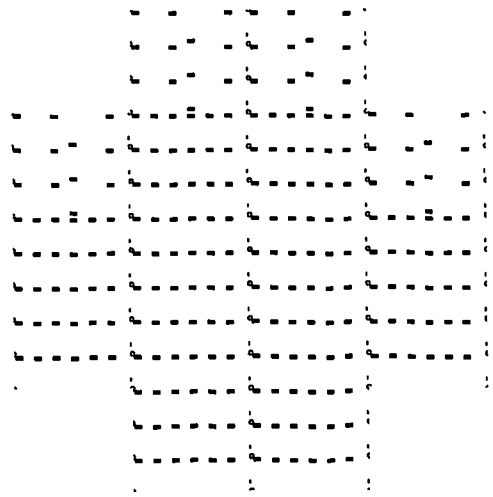

Mask 2 opens windows in the Si_3N_4 layer to expose the heater contact pads.

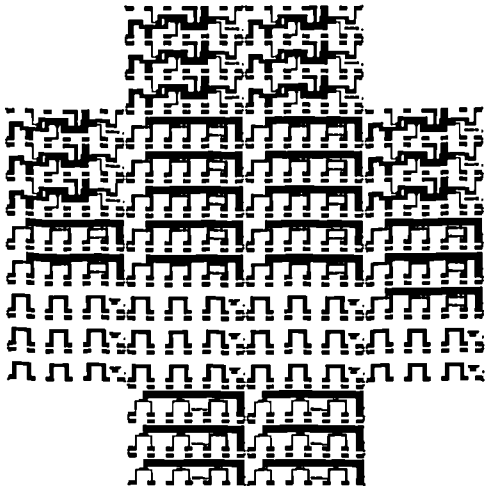

Mask 3 patterns Ti/Au films to create the electrode geometry.

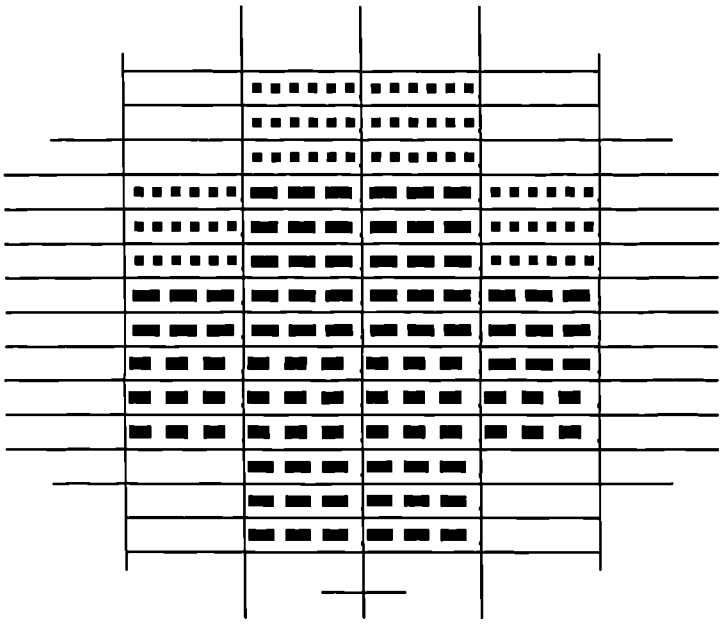

Mask 4 patterns the back-side Si_3N_4 to generate a KOH mask. The actual mask produced is a mirror of this image, because it is used to process the wafer back-side.

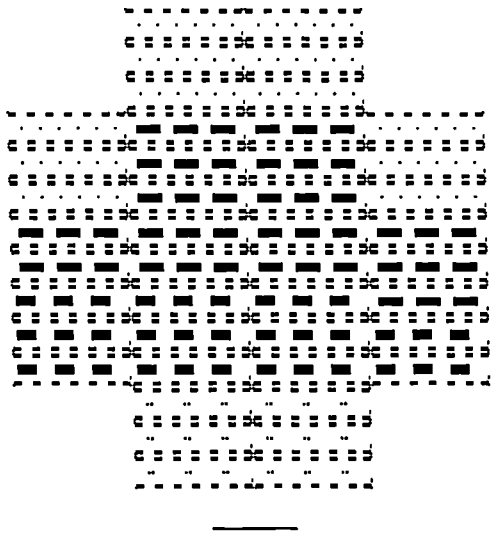

Mask 5 patterns the protective photoresist to reveal contact pads and electrode area.

Masks for Discrete and Bridge Devices

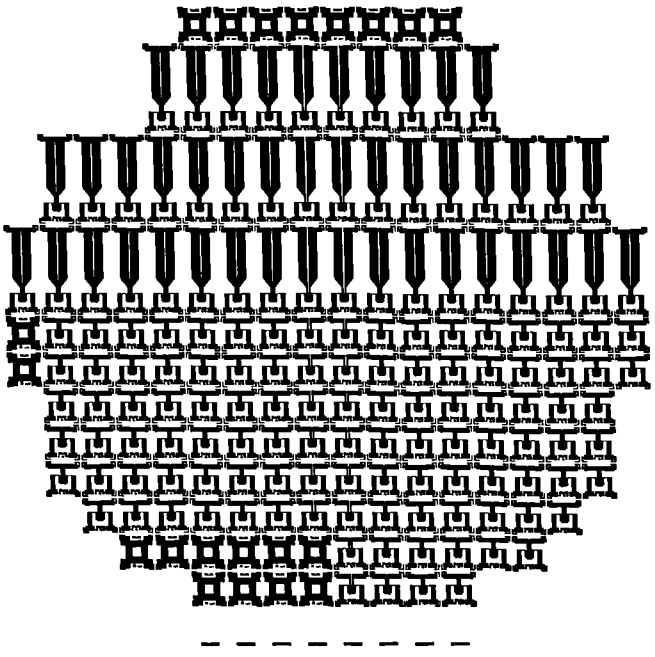

Mask 1 patterns Ti/Au metallisation to form the electrode geometry. The actual mask produced is lightfield.

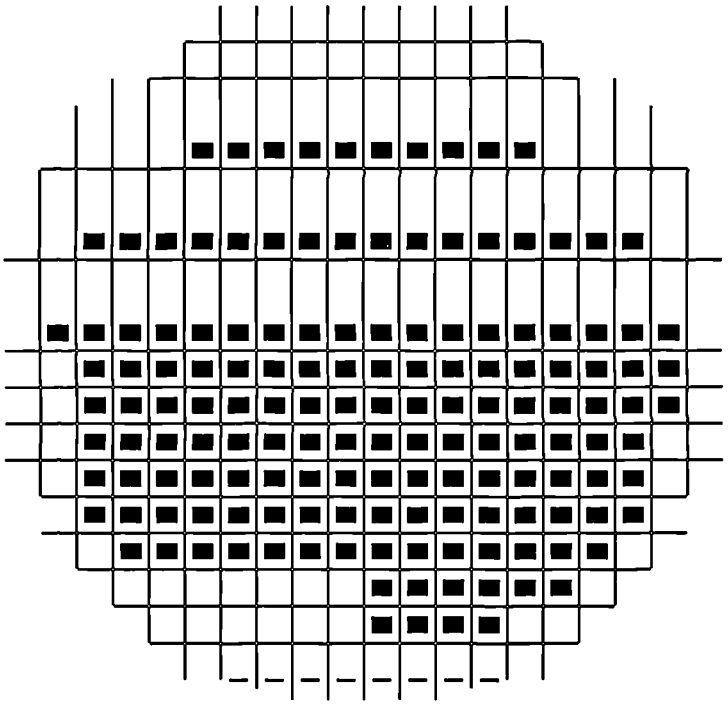

Mask 2 patterns the back-side oxynitride to create a KOH mask. The actual mask produced is a mirror of this image, because it is used to process the wafer back-side.

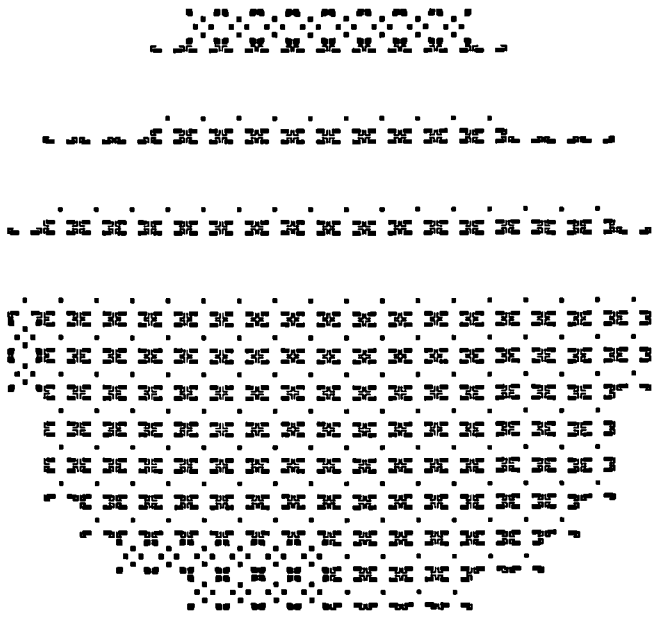

Mask 3 patterns the protective photoresist layer.

Appendix C

DAQ Specification

This appendix lists the specification of the National Instruments® DAQ card at 25°C.

Analogue Input

Input Characteristics

Number of channels	16 single-ended or 8 differential, jumper-selectable
Resolution	12 bits, 1 in 4096
Max sampling rate	100 kS/s
Input signal ranges	Board Range (Jumper Selectable): ±10 V; ±5 V; 0 to 10 V
Input coupling	DC
Max working voltage	Within 12 V of AIGND
Overvoltage protection	±35 V power on, ±20 V power off
FIFO buffer size	16 samples

Transfer Characteristics

Relative accuracy	±0.9 LSB typical, ±1.5 LSB max

Amplifier Characteristics

Input impedance	1 GΩ in parallel with 50 pF
Input bias current	±25 nA
Input offset current	±15 nA

Dynamic Characteristics (Gain = 1)

Bandwidth (-3 dB)	650 kHz
Settling time to full-scale step	10 μs
Slew rate	5.0 V/μs

Stability

Recommended warm-up time	15 min

Analogue Output

Output Characteristics

Number of channels	2 voltage
Resolution	12 bits, 1 in 4096
Max update rate	250 kS/s
Type of DAC	Double-buffered, multiplying

Transfer Characteristics

Relative accuracy (Unipolar range)	±0.5 LSB typical, ±1.0 LSB max

Voltage Output

Ranges	±10 V, 0 to 10 V,jumper selectable
Output impedance	≤ 0.2 Ω
Current drive	± 2 mA max
Protection	Short-circuit protection

Dynamic Characteristics

Settling time to 0.024 % of full scale	4 µs for a 20 V step
Slew rate	30 V/µs
Noise	1 mVrms, DC to 1 MHz

Digital I/O

Number of channels	8 I/O
Compatibility	TTL

Digital logic levels

Level	Min	Max
Input low voltage	0 V	0.8 V
Input high voltage	2 V	6 V
Input low current (V_{in} = 0.4 V)		-20 µA
Input high current (V_{in} = 2.7 V)		20 µA

Output low voltage (I_{out} = 24 A)		0.5 V
Output high voltage (I_{out} = -2.6 A)	2.4 V	

Data transfers — Programmed I/O

Timing I/O

Number of channels	3 counter/timers, 1 frequency scalers
Resolution	
Counter/timers	16 bits
Frequency scalers	4 bits
Base clocks available	1 MHz, 100 kHz, 10 kHz, 1 kHz, 100 Hz
Base clock accuracy	±0.01 %
Min source pulse duration	70 ns

Triggers

Digital Triggers

Compatibility	TTL
Response	Falling edge
Pulse width	50 ns min